The Mcpt5-Cre mouse model for studying mast cells in the brain

DISSERTATION

zur Erlangung des akademischen Grades

doctor rerum naturalium (Dr. rer. nat.)

von M.Sc. Hanna Josephine Edler
geb. am 19.01.1994 in Stendal

genehmigt durch die Fakultät für Naturwissenschaften der Otto-von-Guericke-Universität Magdeburg

Gutachter:
Prof. Dr. rer. nat. Anne Dudeck
Prof. Dr. rer. nat. Ana Zenclussen

eingereicht am:
28.02.2023

verteidigt am:
29.11.2023

“He who has made a mistake and does not correct it, has made another mistake"

(Confucius)

Table of Contents

List of Figures

Supplemental Figures

List of Tables

Supplemental Tables

Abbreviations

α	antibody against
5-HT	serotonin
AB	Astra blue
Ab	antibody
AB/SO	Astra blue and/or safranin O
ABSO	Astra blue safranin O (mixed type)
AlcB	Alcian blue
AM	arachnoid mater
AP	area postrema
arachn	arachnoid
Ba	basophils
BBB	blood brain barrier
BCFSB	blood cerebrospinal fluid barrier
BM	bone marrow
BMMC	bone marrow-derived mast cells
c	caudal
CCRs	CC chemokine receptor
CD88	C5a anaphylatoxin chemotactic receptor 1
cDNA	cyclic desoxyribonucleic acid
cf.	compare
c-kit	*cf. Kit*
cMMC	cultured mucosal-like mast cell
CNS	central nervous system
cp	capillary plexus
CP	choroid plexus
CRH	corticotropin releasing hormone
CSF	cerebrospinal fluid
C_T	threshold cycle
CTMC	connective tissue-type mast cell
CUBIC	“clear, unobstructed brain/body imaging cocktails” protocol
CVO	circumventricular organ
CXCRs	CXC chemokine receptor
d	dorsal
DC	dendritic cell

dcLN	deep cervical lymph nodes
DCM	dichloromethane
DEG	differentially expressed genes
DG	dentate gyrus
DGE	differential gene expression
di	distal
dist.	distilled
DM	dura mater
DNA	desoxyribonucleic acid
DNase	desoxyribonuclease
EAE	experimental autoimmune encephalomyelitis
ECM	extracellular matrix
eCtrl	endogenous control
EDTA	ethylenediaminetetraacetic acid
Eo	eosinophils
Ep	epithelial cells
ER	estrogen receptor
EtOH	ethanol
f	female
Fc	fragment crystallizable
FcγRI	Fc gamma receptor I
FcεRI	Fc epsilon receptor I
FCS	fetal calf serum
FGF	fibroblast growth factor
FITC	fluorescein isothiocyanate
FMO	fluorescence minus one
FP	fluorescent protein
FRC	fibroblast reticular cells
GFAP	glial fibrillary acidic protein
GMCSF	granulocyte macrophage colony stimulating factor
GN	granulocyte
GOI	gene of interest
H_4R	histamine receptor 4
Hc	hippocampus
HCl	hydrochloric acid
HEPES	2-[4-(2-hydroxyethyl)piperazin-1-yl]ethanesulfonic acid
HSC	hematopoietic stem cell

IL-33	interleukin 33
IL-4	interleukin 4
IL-Rs	interleukins
Kit	stem cell factor receptor
l.	like
lam	laminin
le	left
LPS	lipopolysaccharide
LSFM	light sheet fluorescent microscopy
LTB_4	leukotriene B4
LTC_4	leukotriene C4
lz	lateral zone
m	male
MC	mast cell
MCSF	macrophage colony stimulating factor
me	medial
ME	median eminence
MEChi	thymic medullary epithelial cells
MF	macrophages
MHCII	major histocompatibility complex II
MMC	mucosal mast cell
MMPs	matrix metalloproteases
Mo	monocyte
MRGPRX2/b2	Mas-related G-protein coupled receptor X2/b2
mRNA	messenger ribonucleic acid
N.A.	not available/ not determined
NGF	nerve growth factor
NH	neurohypophysis
NK	natural killer
nu	nucleus
OB	olfactory bulb
oc	outer shell
OVLT	organum vasculosum of the lamina terminalis
P2X7R	purinoreceptor 7
PAS	periodic acid–Schiff
PBS	phosphate buffered saline
PCA	principal component analysis

PCR	polymerase chain reaction
PDGF	platelet derived growth factor
PEGASOS	polyethylen glycol associated solvent system
PGD_2	prostaglandin D2
PI	propidium iodide
PM	pia mater
PSF	point spread function
PVS	perivascular space
QC	quality control
(q)RT-PCR	(quantitative) reverse transcriptase polymerase chain reaction
r	rostral
r.	receptor
ri	right
RMCP	rat mast cell protease
RNA	ribonucleic acid
RNase	ribonuclease
rpm	rounds per minute
RPMI	Roswell Park Memorial Institute
RT	room temperature
SAB	subarachnoid barrier
SAS or sas	subarachnoid space
SCF	stem cell factor
SEM	scanning electron microscopy
SFO	subfornical organ
SG	secretory granules
Siglec-8	sialic acid-binding Ig-like lectin 8
SLC	solute carrier
SNR	signal-to-noise ratio
ST2	IL-33 receptor
t-SNE	t-distributed stochastic neighbor embedding
TB	toluidine blue
TEM	transmission electron microscopy
TGFβ	transforming growth factor beta
THF	tetrahydrofuran
TLR4	toll-like receptor 4
TLRs	toll-like receptor
TNF	tumor necrosis factor

TRIS	Tris-(hydroxymethyl)-amino methane
v	ventral
VEGF	vascular endothelial growth factor
VEGFR	VEGF receptor
VIP	vasoactive intestinal peptide
vSMC	vascular smooth muscle cell

Abstract

Mast cells (MCs) are sentinel and effector cells of the innate immune system and in that role, they are strategically positioned at almost all body-environmental interfaces. They are known for their diverse phenotypes depending on the local microenvironment. Due to their unique staining features, MCs were discovered very early in brain tissue as well, preferably residing at brain-periphery interfaces in the meninges, the choroid plexus (CP) and alongside parenchymal blood vessels. There, they are part of the blood-brain barrier (BBB) and blood-cerebrospinal fluid barriers (BCSFB) which allow them to spread effector molecules over the whole organ and beyond. Hence, they have a strong effect, even if rare in number, and were described to play important pro- or anti-inflammatory roles in the context of several neurological pathologies. The small cell number of brain MCs and the lack of an appropriate MC-specific mouse model may be reasons why little is known so far about sub-organ differences, molecular functions and their interactions with other cells in this specialized organ.

Hence, this thesis aimed at elucidating the characteristics and functions of MCs in three different sub-organ localizations of the brain as part of a complex neuro-immune cell network. Therefore, the Mcpt5-Cre mouse model, popular for its high connective-tissue MC (CTMC)-specificity in peripheral tissues [1, 2], was used. Since it was never investigated for the brain, the usefulness and reliability of this mouse model was addressed as well in this context. To detect the rare cells in their native environment, an appropriate clearing and light sheet microscopy protocol for Mcpt5-Cre EYFP mouse brains was developed. Both, light sheet microscopy and transcriptome profiling revealed that, in the brain, the EYFP expression is not restricted to MCs. Further fluorescence microscopy methods identified mainly neurons to be targeted in the brain parenchyma, but also certain cell types of the CP and meninges. Astra blue safranin O (AB/SO) staining, a classical sequential MC detection method supported the above findings on histological slices and meningeal whole mounts. Surprisingly, it emerged that AB/SO allows not only to distinguish MC subtypes as it is usually used for, but also for detecting MC activation. This was finally evidenced by single cell transcriptome profiling of meningeal MCs and an activation assay designed for this specific purpose.

Collectively, this thesis confirms the existence of MCs in cerebral tissues and presents a transcriptome profile for dura mater MCs which indicates connective-tissue like characteristics. Additionally, it displays limitations of the Mcpt5-Cre mouse line as a CTMC-specific model system and finally shows that the classical sequential MC staining method AB/SO identifies MC activation.

Zusammenfassung

Mastzellen (MZ) sind Wächter- und Effektorzellen des angeborenen Immunsystems und als solche sind sie strategisch sinnvoll an beinahe allen umweltexponierten Körperstellen angesiedelt. Sie sind bekannt für ihre verschiedenen, von der lokalen Mikroumgebung geprägten, Phänotypen. Aufgrund ihrer einzigartigen Färbeeigenschaften wurden Mastzellen auch schon früh im Gehirn entdeckt, wo sie bevorzugt an den Übergängen von Gehirn und Peripherie, also in den Hirnhäuten, den Plexi choroidei und an parenchymalen Blutgefäßen vorkommen. Dort sind sie Teil der Bluthirnschranke und der Barrieren zwischen Blut und Zerebralflüssigkeit, was es ihnen ermöglicht, Effektormoleküle innerhalb des Gehirns und darüber hinaus zu verteilen. Trotz ihrer geringeren Anzahl, haben sie daher einen großen Einfluss, welcher als pro- oder antiinflammatorisch im Zusammenhang mit verschiedenen neurologischen Erkrankungen beschrieben wurde. Die geringe Anzahl an zerebralen MZ und das Fehlen eines geeigneten MZ-spezifischen Mausmodells mögen Gründe dafür sein, dass bisher nur wenig über intra-organelle Unterschiede, deren molekulare Funktionen oder ihre Interaktionen mit anderen Zellen des Gehirns bekannt ist.

Daher hat diese Arbeit zum Ziel, Eigenschaften und Funktionen von MZ als Teil eines komplexen neuroimmunologischen Netzwerks an drei verschiedenen Gehirnregionen aufzuklären. Dafür wurde das Mcpt5-Cre-Mausmodell verwendet. Dieses ist dafür bekannt, in peripheren Organen sehr spezifisch Bindegewebsmastzellen zu adressieren, was bisher jedoch nicht fürs Gehirn gezeigt wurde. Daher wurde das Mausmodell zuallererst auf seine Nutzbarkeit und Verlässlichkeit in diesem sehr speziellen Organ untersucht. Um die wenigen Zellen in ihrer natürlichen Umgebung detektieren zu können, wurde ein geeignetes Protokoll zur Gewebeklärung und anschließende Lichtblattmikroskopie für Mcpt5-Cre EYFP-Mausgehirne entwickelt. Sowohl die Lichtblattmikroskopie, als auch Transkriptomanalysen haben gezeigt, dass die Expression des gelb fluoreszierenden Proteins (EYFP) in diesen Mäusen nicht nur auf MZ beschränkt ist. Weitere fluoreszenzmikroskopische Methoden identifizierten zusätzlich vor allem Neuronen, aber auch andere Zellen des Plexus choroideus und der Hirnhäute. Astrablau und Safranin O (AB/SO)-Färbungen, als klassische sequenzielle MZ-Färbungen, unterstützten dabei die obigen Ergebnisse an histologischen Schnitten und intakten Hirnhäuten. Überraschenderweise zeigte sich dabei, dass die AB/SO-Färbung nicht nur die Unterscheidung von MZ-Subtypen ermöglicht, wofür sie üblicherweise verwendet wird, sondern auch MZ-Aktivierung widerspiegeln kann. Letzteres konnte abschließend anhand von Einzelzellsequenzierungen meningealer MZ und einem eigens dafür entwickelten Aktivierungsassay belegt werden.

Zusammengefasst bestätigt diese Arbeit die Existenz zerebraler Mastzellen und präsentiert ein Transkriptomprofil für meningeale Mastzellen, was denen anderer Bindegewebs-MZ

ähnelt. Außerdem zeigt sie Limitationen der Mcpt5-Cre-Mauslinie als MZ-spezifisches Modellsystem auf und verdeutlicht schlussendlich, dass die klassische AB/SO MZ-Färbung auch MZ-Aktivierung anzeigen kann.

1 Introduction

1.1 The Ehrlich Story – a historical outline

Even scientific stories may start long time ago and sometimes take curious ways. Two discoveries born in the same mind, made their ways separately, were brought into contact decades later and still keep some secrets after about 150 years of research – such a story is the one of mast cells (MCs) and the blood-brain barrier (BBB).

It was the young German physician Paul Ehrlich (1854 – 1915) who discovered MCs during tissue staining approaches for his doctorate at Leipzig University. His interest in histological dyes made him observe aniline-positive cells around blood vessels in connective tissues, filled up with metachromatically reacting granules [3]. He called them “Mastzellen” using the German word „Mast” (*engl.* fattening) to describe their overfed appearance.
This fascination in dyes led him to another important observation. During his early career, he performed several injection experiments and tested acidic or basic compounds of different colors and in varying body locations and species. Thereby, he noticed a selective or even impossible staining of the brain (except of the choroid plexuses (CPs)) when applying the dye subcutaneously. The same finding was made by his contemporary Edwin Goldmann [4, 5] and later by other authors, too. Even if Ehrlich never believed in a BBB which was named and described decades later by other scientists, its discovery is attributed to him [6]. Ironically, it would have helped him to understand why he could not cure trypanosome-infected rodents and thus never succeeded in developing a potent drug for patients suffering from ‘sleepiness disease’. These pathogens can hide inside the brain, making advantage of a special location beyond the BBB: the immune-privileged area of the brain [7].

The term of an immune-privileged area was shaped in the second half of the 20th century and describes a part of the body in which tissue grafts are not rejected as a result of an immune response [8, 9]. Such areas can be found in the brain, eye or testis of the human body [10-12]. But immune-privileged does not mean the complete absence of immune cells. Despite the existence of microglia, which are brain resident macrophages, it was shown, that under certain circumstances, lymphocytes or monocytic cells may enter the neuropil depending on their activation state [13-15]. Moreover, already in the 60’s and 70’s of the last century, MCs were detected in the brain and meninges of a multitude of mammalian species [16-18].

The understanding of an immune-privileged area was recently revisited for the central nervous system (CNS) when Louveau *et al.* and Aspelund *et al*. 'rediscovered' in 2015 lymphatic vessels surrounding the brain [19, 20]. Lymphatic vessels return extracellular fluid back to circulation and transport lipids and fatty acids. Additionally, they are an important part of the immune system. They guide immune cells and antigens to draining lymph nodes and secondary lymphoid organs [21] which was a surprising finding for an immune-privileged area and led to intensive scientific discussions in this field. On the other hand, it explains how the brain-invading leukocytes may find back their way to periphery.

A large proportion of the lymphatic network is located along the sinusoid structures of the dura mater (DM) which make this area a favorable place for brain-immune interactions. It is no longer surprising, that MCs were identified alongside the sinuses, too, given the fact that they preferably reside along vasculature. A very recent publication showed higher numbers of activated meningeal MCs along the sagittal and transverse sinuses compared to the hemisphere- and cerebellum-covering areas [22]. They stated that sinusoidal MCs are in a pole position for modulating T cell recruitment. But this is only one study describing MCs as mediators in brain-peripheral immune interactions of the innate and adaptive immunity. The state-of-the-art knowledge about the interfaces of the brain and the involvement of MCs in CNS-barrier regions is summarized in the following sections.

1.2 Blood-Brain Barriers and Interfaces

Brains need a lot of oxygen and nutrients which is provided continuously via the bloodstream. Blood enters the head via the common carotid artery ascending from the aortic arch. The common carotid artery branches in the internal carotid artery nourishing the brain and in the external carotid artery which supplies for example the face, ears, skull and most of the meninges. Since the blood transports not only nutrients, but toxic compounds, hormones, signaling molecules or pathogens, the CNS needs proper protection to avoid cross-over of substances causing severe damage, uncontrolled activation or life-threatening inflammation. Varying barriers and interface regions [23], creating the so-called immune-privileged area, can be distinguished, all of them with distinct features, functions, limitations and unsolved secrets.

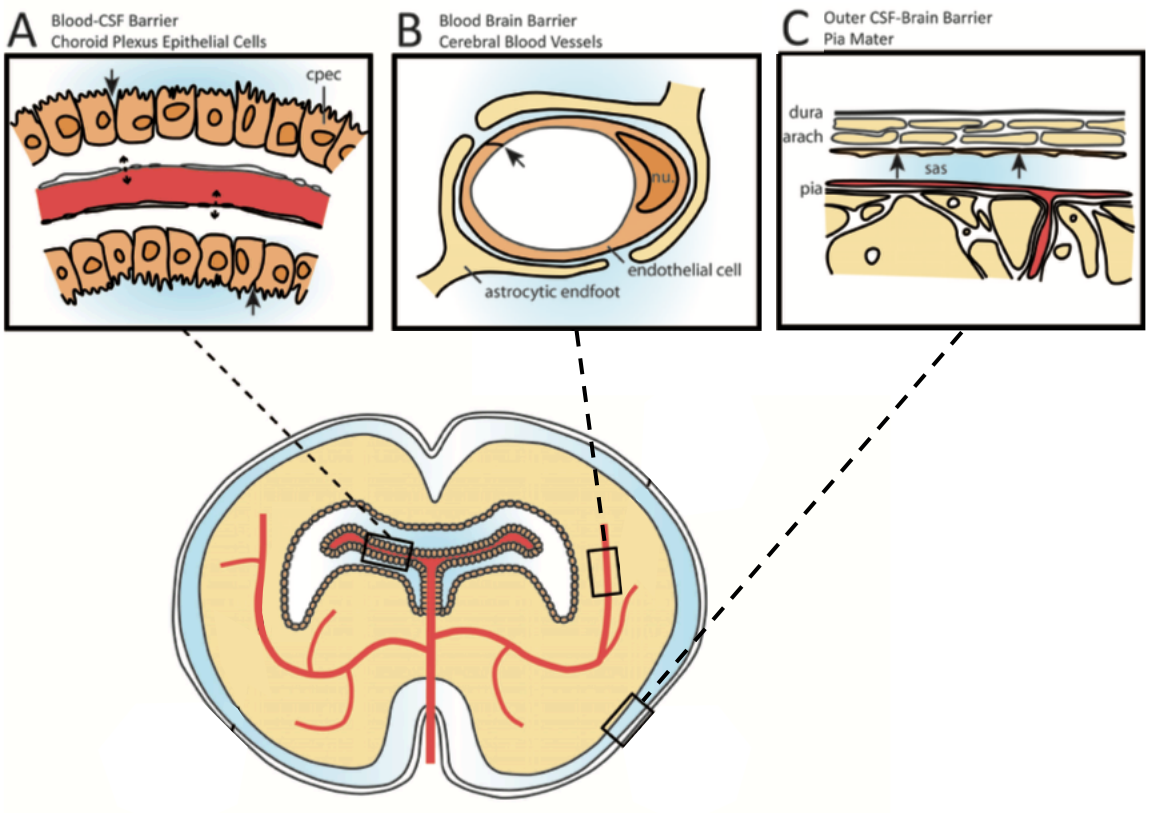

Figure 1-1 Location of the brain-periphery barriers

The scheme by Liddelow [24] was modified and represents the three barrier systems of a mammalian brain. The “true barriers” which are cell layers formed by tight junctions are displayed in orange. **A** For the CP blood-cerebrospinal fluid (BCSF) barrier, it consists of CP epithelial cells. **B** The BBB around parenchymal vessels is formed by endothelial cells. In the meninges, the BCSF true barrier is composed of arachnoid mater epithelial cells. Arach – arachnoid mater, BBB – blood brain barrier, CP – choroid plexus, cpec – CP epithelial cells, CSF – cerebrospinal fluid, nu – nucleus, sas – subarachnoid space

1.2.1 Meningeal blood-cerebrospinal fluid barrier

The meninges form the outer barrier and interface of the brain and therefore line the inside of the skull bone. They are composed of three layers, DM, arachnoid mater (AM) and pia mater (PM) [25] as displayed in Figure 1-1**C**.

The outermost and toughest layer is the DM. In human, its thickness is 500 to 600 µm and in mice about one-tenth [26]. On the outside, one or several layers of fibroblasts and collagen attach the DM to the skull bone (periosteal layer) and on the inside, dural border cells, a thin fibroblast layer, connect it to the second meningeal layer, the AM [23, 27]. Consisting of one layer of epithelial-like cells connected by tight junctions [27], the AM forms a true barrier to the below floating cerebrospinal fluid (CSF). It is therefore called blood-cerebrospinal fluid barrier

(BCSFB). Proximally to its epithelium, the AM is lined by fibroblasts which form trabeculae in the CSF-filled subarachnoid space (SAS) and attach it to the PM [27], as drawn in Figure 1-2**A**. In mice, the SAS is very thin and almost not apparent, that trabeculae are thought to be absent [25]. AM and PM form together the so-called leptomeninges [15]. The PM is a thin fenestrated layer of fibroblasts and basement membrane which separates the CSF and the brain parenchyma [15, 25, 27]. Some authors describe an underlying subpial space, located between PM and brain surface which can be entered by certain compounds or even cells of the CSF [25, 28].

The highly collagenous DM consists of blood vessels, lymphatics, and is highly innervated [15]. The blood, which reaches the DM, derives from the periphery passing the aortic arch, common carotid artery and the internal and external carotid branches [29, 30]. It transports nutrients and oxygen, but also immune cells, hormones, mediators, toxins or pathogens which can enter the CNS-close tissue easily via fenestrations in the dural vessels. As a result, an efficient drainage system is needed as well. In the mouse skull, proximally to the sagittal and lambdoid suture of the calvaria, both dural layers separate and form the sagittal and transverse venous sinuses [23, 25], already mentioned above. They transport collectively deoxygenated blood, metabolites and CSF remnants over the jugular vein back to systemic blood circulation [19]. A very recent study describes them as a neuroimmune interface where T cells scan the tissue for antigen-presenting cells (APCs) loaded with brain and CSF-derived antigens and become activated [31]. These triggered immune cells leave the DM subsequently via lymphatics juxtaposed to the sinuses and the middle meningeal artery to the deep cervical lymph nodes (dcLN) [15].

The BCSFB of the arachnoid epithelium seals the dural layer to protect the brain. Like a wall around a castle, the epithelial layer shields the parenchyma against this blood-nourished environment. Staying with this allegory, the SAS which is filled with CSF build up the castle moat. This special fluid acts as a shock absorber and transport medium for nutrients, signaling molecules and waste compounds for the brain. Evaginations of the SAS, so-called granulations or arachnoid villi, reach into the venous sinuses of the DM allowing efficient efflux of the CSF remnants [25]. Also in the SAS, but on the PM surface, pial vessels build a network which is distinct from the dural vasculature [32]. The big arteries which derive from the internal carotid artery traverse the SAS, before invading the brain parenchyma to feed the cortical tissues [15]. Within the neuropil, they narrow and branch in arterioles and capillaries. As soon as the capillaries release oxygen and take up carbogen, they become venules and emerge as pial veins back on the brain surface to transport the carbogen-rich blood back to heart.

These so-called pial or leptomeningeal vessels are made up of non-fenestrated endothelial cells covered by vascular smooth muscle cells (vSMCs), basal laminae, both forming the

arterial tunica media, and a pial-like sheath of fibroblasts, named “leptomeningeal lining cells”, sheathing a space of connective tissue, the adventitia [27, 28, 33]. Tunica media and adventitia form the perivascular space (PVS). Abbott *et al.* describe, that leptomeningeal cells contain pores, termed stomata, which allow the CSF to enter the PVS. As soon as the arteries dive into the parenchyma, accompanied by tunica and adventitia, the CSF follows the vessels inside this space. By passing the PM and entering the parenchyma, a second space emerges: the paravascular or Virchow-Robin space (VRS) [33]. It is restricted on the outside by the glia limitans, the last protective brain interface formed by parenchymal cells itself. Astrocytic processes (“endfeet”) shields the CNS at all surfaces by inducible tight junctions [34] and a dense basement membrane [10, 15]. On the inside, the VRS is bounded by the leptomeningeal lining cells. In rodents, this leptomeningeal layer eventually does not continue below the PM [35, 36], allowing the perivascular and paravascular spaces to fuse. This fusing happens anyway, when the arterioles narrow to become capillaries and lose their sheathing (except of the endothelial basal membrane) to enable exchange of substances with the brain environment. Once the capillaries broaden to venules and veins, the peri- and paravascular spaces expand again [33]. A recent review states that the PVS disappears when the vascular basement membrane and the glia limitans basal lamina fuse around the capillaries [37], others describe the PVS as continuous [33]. These localizations of fluid-filled cavities and fluid flows in the brain are non-uniformly described [10, 11, 27, 33]. The pial or cortical veins can finally enter the venous sinuses which drain the venous blood into the internal jugular vein back to the heart [19].

1.2.2 Blood-brain barrier

Due to its unique features, the BBB have been gained a lot of research, but also public, interest for a long time and still keeps some secrets. The BBB is localized around most of the capillaries inside the brain parenchyma (Figure 1-1**B**) and strongly restricts the exchange of blood-borne materials with “neural” cells beyond the glia limitans [11, 28, 38]. It is of vital importance to keep the special micromilieu under homeostatic conditions and protect the essential organ from infections. According to Abbott and Friedman, active “neural” cells are neurons, macroglia (astrocytes and oligodendrocytes) and microglia [38]. They populate the parenchyma inside the glia limitans surrounded by interstitial fluid (ISF).

The BBB is primarily consisting of tightly connected endothelial cells encircling the vascular lumen. Nowadays, it is recognized that the BBB is not only a simple cell layer, but a complex composition of endothelial, glial and immune cells, but also neurons and basal laminae which work together as the so-called neurovascular unit (NVU) [37, 38]. The cellular composition changes with the discrete functions in different brain areas and at different stages of the

cerebrovascular tree of larger and smaller vessels, arteries, capillaries and veins [37]. Since the broad composition of the larger vessels were already described above, this section focuses on the more general NVU composition of small capillaries (Figure 1-2**C**). As already mentioned before, the capillary lumen is lined by endothelial cells, building the true BBB by their tight junctions. They are surrounded by mural cells, which are pericytes around the capillaries, and vSMCs along larger vessels [28, 39]. The next cell layer is composed of astrocyte endfeet, but can be reached by microglia or neuronal processes as well. Basement membranes separate but also connect the different cell types, like cement in a brick wall. As part of the “enhanced” NVU, some immune cells are present as well. Erickson and Banks describe the existence of perivascular macrophages, residing inside the PVS and protecting the brain for example against infections [40]. Furthermore, MCs were identified in the PVS of some brain regions. The release of MC mediators following activation, can cause BBB disruptions [40, 41] (cf. Figure 1-2**A** and **B**).

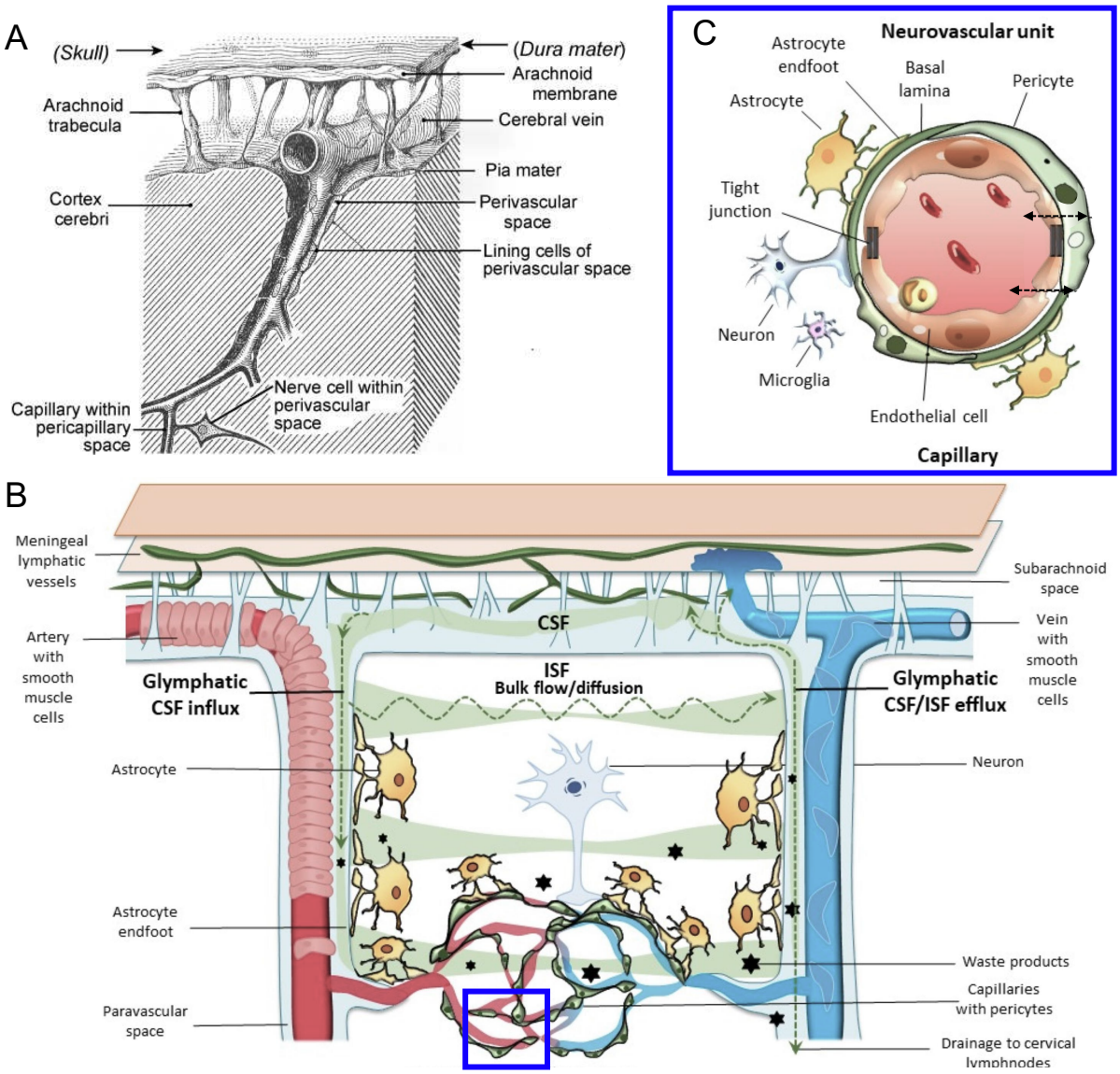

Figure 1-2 The brain vascular system

A The drawing of canine meninges from the 1920s shows all three layers, DM, AM and PM. The SAS, traversed by trabeculae is probably absent or very narrow in mice [25]. Pial vessels penetrate the parenchyma, accompanied by PVS. **B** More recently, the perivascular spaces inside (PVS) and outside (paravascular or VRS) of the perivascular lining cells (tunica adventitia) were discriminated. When pial arteries enter the parenchyma, below the tunica adventitia, they are covered by vSMCs (tunica media). The arteries narrow to arterioles and further to capillaries which lack these outer layers. Capillary endothelial cells are only covered by pericytes and basal membrane with contact to parenchymal cells. This so-called NVU (**C**) allows a highly selective exchange of oxygen and carbogen, but also nutrients and waste products. A limited and size-dependent exchange of molecules probably also happens directly between the ISF of the neuropil and the CSF inside the peri- and paravascular spaces. Along this way, waste products can be drained by meningeal lymphatic vessels (= 'glymphatic system'). Images B and C were taken from [42] and modified.

The BBB is present throughout the whole brain in varying compositions except of the circumventricular organs, which will be described in 1.2.4.

1.2.3 Choroid plexus blood-cerebrospinal fluid barrier

A second BCSFB can be found in the CP tissues inside the brain ventricular system (Figure 1-1**A**). The ventricles are lined with ependymal cells, epithelial-like cells from which the CP epithelium evolves during early stages of development [43]. They form veil-like or lobular structures of an epithelial cell layer (Figure 1-3**D**) covering a network of highly anastomosed, fenestrated capillaries (Figure 1-3**E**) and filled with connective tissue (stroma) [43-45]. The epithelial cells are cuboidal in shape [46], polarized and connected by tight junctions (Figure 1-3**F**) [44, 47] restricting the transition of blood-borne solutes, cells or pathogens in the surrounding CSF [23, 48]. On the apical side, microvilli maximize the epithelial surface inside the ventricular lumen and thus, optimize numerous functions in CSF secretion, nutrient supply or retrograde transport of remnants and toxins [23, 45, 47]. Therefore, epithelial cells are rich in mitochondria to meet the high energy demand for barrier crossing processes [47]. The choroidal epithelium is considered as a “leaky” barrier by some authors [44, 47, 49-51]. Not immediately obvious, this refers to the electrochemical properties due to the high ion permeability, since for large organic compounds or cells, the CP is a properly sealed, potent and highly selective barrier [44]. But indeed, it can be better described as an active interface than an inert barrier. About 65% of the almost 400 identified solute carrier (SLC) transporters were found to be expressed by the choroidal epithelium [45]. They assist in secreting 80% of the CSF [52], maintaining brain homeostasis and providing nutrients, signaling molecules, hormones, growth factors, bioactive polypeptides and cytokines [44]. The repertoire of molecules can differ by sexes, between the ventricles [44] and even during day/night cycle [47]. Men and mice possess four ventricles, *left lateral* and *right lateral*, *third* and *fourth,* each containing a CP (Figure 1-3**A**-**C**) which differ not only in appearance and secretion but in the tissue composition and transcriptome profile [53]. The ventricles are filled with CSF and connected with each other and with the SAS surrounding the brain. CSF is produced continuously by the CPs and renewed 3-4 times a day in humans [47, 52]. Taking responsibility for nutrient supply and waste removal, the CSF follows certain flow routes which were described in detail by [50] recently.

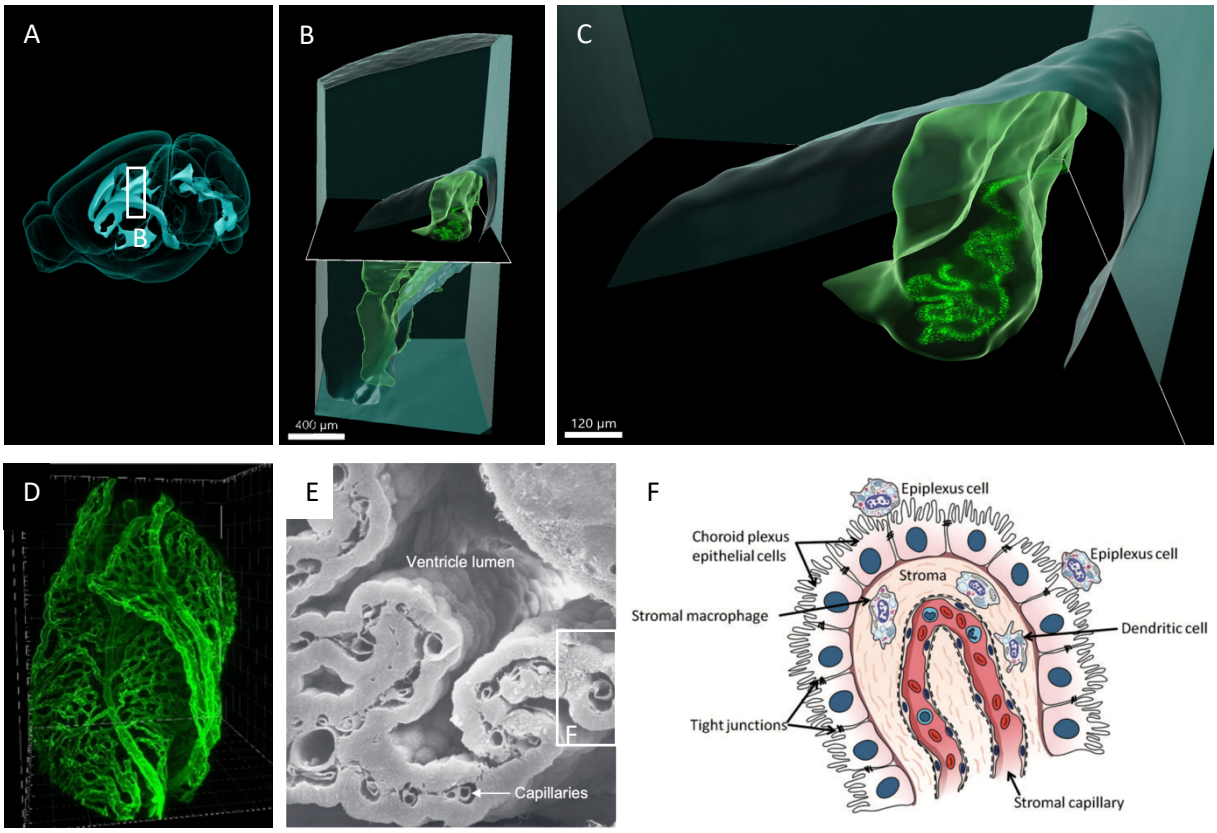

Figure 1-3 The CP of the rodent brain

A A schematic image created with the Scalable Brain Atlas tool [54, 55], shows the murine brain ventricular system. An exemplary area shown in B is marked with a white square. **B** A piece of the murine brain cortex (cyan), including a part of the lateral ventricle, was acquired with light sheet microscopy and processed with Imaris software. Inside the ventricle, the large leaf of the lateral CP is shown in transparent green as a three-dimensional object. One slice represents the arrangement of the single cells based on a nuclear stain (green) in a two-dimensional projection which is magnified in **C**. **D** displays three-dimensionally the vascular network of a rat lateral CP, acquired by light sheet microscopy [44]. A cross-section of a murine CP is depicted in **E**. The cryo-fractured preparation for electron microcopy shows the capillaries, surrounded by the epithelial sheath, located in the ventricular lumen, according to [52]. An area which is comparable with the drawing in F is marked with a white square. **F** An exemplary area of the schematic drawing by [47] is marked in E. The tight junctions between the CP epithelial cells form the blood cerebrospinal fluid barrier (BSCFB). Inside (dendritic cells and stromal macrophages) and outside (epiplexus cells) of the barrier, immune cells are located under homeostasis. Stromal capillaries inside the CP lumen are fenestrated.

1.2.4 Circumventricular organs

The CVOs are described as areas in the brain which are not sealed from peripheral influences by a tight BBB. Coming back to the dye injection experiments of P. Ehrlich, these areas took up the dye as the CP did, whereas the rest of the brain remained pale [43]. In rodents, three

sensory and two secretory CVOs can be distinguished. The sensory CVOs are the subfornical organ (SFO), organum vasculosum of the lamina terminalis (OVLT) and the area postrema (AP), whereas the neurohypophysis (NH) and the median eminence (ME) have secretory properties. All of these areas are characterized by fenestrated capillaries, relatively large PVS and specialized ependymal cells [56]. They show strong angiogenic potential which is due to relatively high levels of vascular endothelial growth factor (VEGF).

In the distal part of the CVOs, tanycyte- or astrocyte-like cells shield the CSF-soaked environment from the brain neuropil [52] and therefore form a third type of BCSFB [43], as depicted in Figure 1-4**B**. These cells were identified as specialized neural stem cells which cover the capillaries in the CVO center with cellular protrusions, but mainly form a barrier in the distal regions being connected by tight junctions. They can differentiate into new neurons or glial cells which populate the CVO itself but also other brain regions [56].

Sensory CVOs are important to maintain body fluid homeostasis by sensing electrolyte levels and osmotic changes. The large number of highly interconnected neurons sense hormones or mediators like ghrelin or angiotensin in the CSF or in the blood. Microglia inside these regions are highly responsive to lipopolysaccharide (LPS) and rapidly proliferate [56].

Secretory CVOs release hormones and mediators, like oxytocin or arginine-vasopressin in the blood. In females, they undergo neurovascular or neuroglial plasticity during estrous cycle or lactation [56].

Due to the lack of endothelial tight junctions, CVOs can serve as entry sides for lymphocyte or macrophage invasion into the brain or CSF [11].

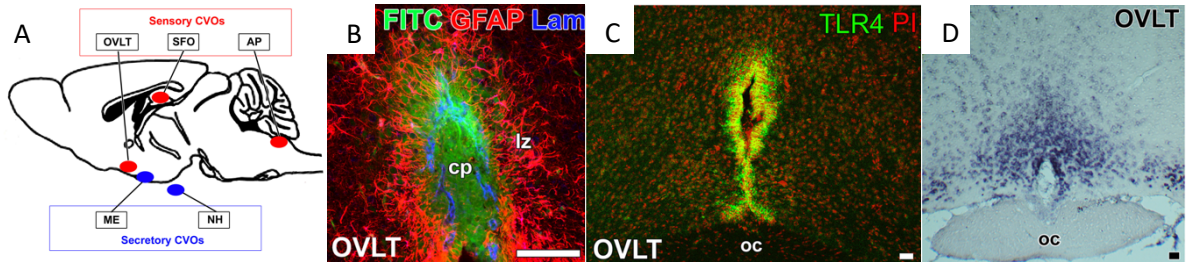

Figure 1-4 The CVOs of the rodent brain

A The scheme displays the locations of the sensory (red) and secretory (blue) CVOs in the rodent brain. **B** GFAP-positive astrocyte-/tanycyte-like cells (red) surround the capillary plexus of the OVLT and therefore shields the brain parenchyma from the CSF-containing CVO (green) by forming tight junctions. Their cellular processes may reach into the center and contact the capillaries. **C** Sensory CVOs as the OVLT are rich in TLR4 expression (green) on microglia and GFAP$^+$ cells. **D** *In situ* hybridization revealed high *Vegf* mRNA expression (dark blue) within the OVLT which explains the continuous angiogenesis in CVOs. CVO – circumventricular organ, OVLT – organum vasculosum of the lamina terminalis, AP – area postrema, NH – neurohypophysis, ME – median eminence, cp – capillary plexus, lz – lateral zone,

oc – outer shell, FITC – fluorescein isothiocyanate, GFAP – glial fibrillaric acidic protein, Lam – laminin,TLR4 – toll-like receptor 4, PI – propidium iodide. Scale bars 50 µm. Images were taken from [56].

1.3 Brain-Immune interaction

1.3.1 Immune cells in the brain

Even under homeostatic conditions, immune cells of the innate and adaptive system populate the meninges, the CP and to a less extent the peri- or paravascular spaces [23, 28, 31]. Resident APCs constantly scan their environment and present self or foreign peptides to patrolling T cells. Once activated, the latter are drained by the dural lymphatics to the cervical lymph nodes (cLNs) and trigger an immune response [15].

Very early during development or later via bloodstream, immune cells enter the DM connective tissue to provide immunosurveillance for the CNS [15]. Van Hove *et al.* identified 15 immune cell populations in the healthy murine DM via single-cell RNA sequencing [57], among them monocytes, macrophages, dendritic cells (DCs), neutrophils, MCs, natural killer (NK) cells, B and T cells. Recent studies could show, that myeloid cell reservoirs in the skull and vertebrae bone marrow (BM) can supply the DM with myeloid cells [58-60] and B cells [61] in homeostasis and disease via direct bony vascular connections. In disease progression, these cells are able to pass the arachnoid BCSFB and enter the CSF or the parenchyma [60].

In the CP, immune cells reside mainly in the stroma, between blood endothelium and outer epithelial cells. DCs were described to form dendrites through the epithelial barrier and sample the surrounding CSF constantly for antigens [23]. Macrophages are located inside the epithelium (stromal macrophages) and on the outside (epiplexus or Kolmer cells) as depicted in Figure 1-3**F**. Stromal macrophages can pass the epithelium trans- or paracellularly. All of them express major histocompatibility (MHC) molecules which allow them to serve as APCs for patrolling T cells [47]. Dani *et al.* published in 2021 a cellular map of the murine CPs and identified additionally neutrophils, plasma cells, MCs and lymphoid B and T cells [53] depending on the individuum`s age. Furthermore, they detected differences in the cellular composition and gene expression across the four ventricles and during development and aging.

In case of brain injury, infection or certain diseases, both blood-brain interfaces can serve as entry routes for leukocytes into the CSF and subsequently, into the parenchyma. As reviewed,

it depends on the cell subtypes and the pathological state or infection type where the immune cells prefer to enter [23, 62]. It seems, that only a distinct portion of cells have a ‘key’ for a certain ‘gate’, whereas others have to use another trafficking route [63]. Regardless of their migration route, the meningeal or CP barrier, the activated immune cells populate the CSF which aids in transporting and distributing them to the inflammation site. Healthy human CSF already contains about 1,000 to 3,000 leukocytes per milliliter [23] which can dramatically increase in a pathological state [64].

1.3.2 Mast cells populate the brain

1.3.2.1 Mast cells as sentinels at major body interfaces

MCs are tissue-resident effector cells of the innate immunity with diverse pro- and anti-inflammatory roles. As sentinels, they are preferably abundant in body-environment interfaces such as skin, respiratory, intestinal and urogenital tracts. In healthy individuals and under normal physiological circumstances, the multifunctional roles of MCs are barely recognized – but their influence in inflammatory conditions can have disastrous outcomes. Under homeostatic conditions, their proteases act in the protection against bacterial peptides, alarmins, venoms [65] and itch-inducing molecules [66]. Moreover, they are involved in tissue turnover or remodeling during pregnancy [67] and in wound [68] or bone fracture healing [69, 70]. Additionally, MC mediators promote angiogenesis [71] and neuronal communication [72, 73].

In a pathological state, MCs can act pro- or anti-inflammatory and are probably best known for their involvement in IgE-dependent allergic inflammation. But far beyond that, they have several roles in the innate and adaptive immune response. As first responders, MCs can react on varying external stimuli, including venoms, toxins, chemicals, bacteria, pathogens, commensals or viruses [65, 74]. Additionally, they respond to endogenous molecules like alarmins, cytokines, adenosine triphosphate (ATP) or neurotransmitters as a result of tissue damage or stress [72, 75].
Therefore, MCs are equipped with a diverse tissue-specific set of receptors (Figure 1-5**B**). Once activated, they can degranulate, resulting in the release of a plethora of mediators and signaling molecules which are stored in secretory granules (SG), summarized in Figure 1-5**C**. MCs can react that fast because most of the signaling compounds are preformed and set free immediately. Additionally, mediators can be newly synthesized as a result of receptor stimulation and will be released with delay of minutes or hours [76]. The degranulation events

can be regulated in a way that SG are released partially or entirely [77] which is described in 1.3.2.1.1 below.

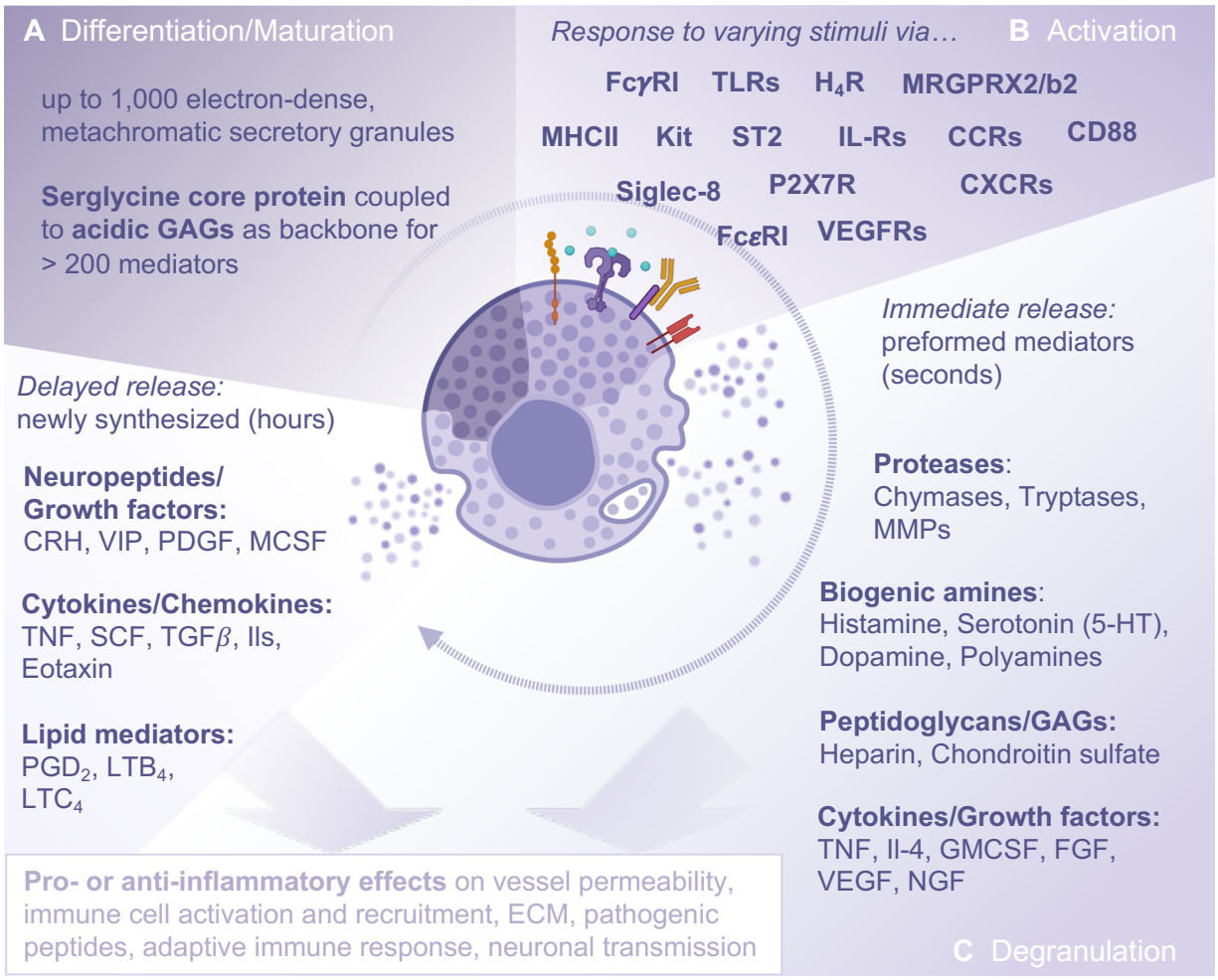

Figure 1-5 Mast cells are diverse effector cells of the innate immunity

A MCs enter their target tissues as progenitor cells and differentiate tissue-specifically. During maturation, they synthesize and store up to 1,000 SGs [78], containing more than 200 mediators [79] tightly attached to strongly acidic glycosaminoglycans (GAGs) on a serglycine backbone [80]. **B** MCs respond to different stimuli depending on their locally diverse repertoire of surface receptors [81, 82] **C** Prior to activation, MCs release their SGs partially or entirely, called degranulation. Prestored mediators are let go stepwise but immediately, whereas others will be newly synthesized resulting in delayed release. Depending on the tissue and the cause of inflammation, MCs may have pro- or anti-inflammatory effects [65, 80]. The figure was created according to [83] with Biorender.com

CCRs – CC chemokine r., CD88 – C5a anaphylatoxin chemotactic r. 1, CRH – corticotropin releasing hormone, CXCRs – CXC chemokine r., ECM – extracellular matrix, f. – factor, FcγRI – Fc r. gamma I, FcεRI – Fc r. epsilon I, FGF – fibroblast growth f., GMCSF – granulocyte macrophage colony stimulating f., H_4R – histamine r. 4, IL-4 – interleukin 4, IL-Rs – interleukins, Kit – Kit r., LTB_4 – leukotriene B4, LTC_4 – leukotriene C4, MCSF – macrophage colony stimulating f., MHCII – major histocompatibility complex II, MMPs – matrix metalloproteases, MRGPRX2/b2 – mas-related G-protein coupled r. X2/b2, NGF –

nerve growth f., P2X7R – purinoreceptor 7, PDGF – platelet derived growth f., PGD_2 – prostaglandin D2, r. – receptor, SCF – stem cell f., Siglec-8 – Sialic acid-binding Ig-like lectin 8, ST2 – IL-33 r., TGFβ – transforming growth f. beta, TLRs – Toll-like r., TNF – tumor necrosis f., VEGF – vascular endothelial growth f., VEGFRs – VEGF r., VIP – vasoactive intestinal peptide

MCs contain up to 1,000 single SGs per cell reaching diameter sizes of 300 – 1,000 nm [78], which collectively store more than 200 different compounds [79]. They are responsible for the unique overfed appearance of this cell type and subsequently their naming as described in 1.1 above. The molecular repertoire of SGs varies dependent on tissue localization, function, subtypes, sex and species. The release of these signaling compounds results predominantly in proinflammatory effects like pathogen clearance, vasodilatation, effector cell recruitment or T cell activation [65]. On the other hand, anti-inflammatory mediators aid in terminating the inflammation by degrading certain cytokines, signaling molecules or infection remnants and finally in tissue repair and build up [84].

Since MCs are such powerful in their action spectrum with a great sphere of influence, they are also involved in a broad range of diseases reaching from contact dermatitis, allergy and asthma to arteriosclerosis and cardiovascular pathologies, diverse neuronal diseases, migraine, autoimmune diseases or life-threatening systemic anaphylaxis and cancer [65, 68, 85].

1.3.2.1.1 MC secretory granules

SGs are a unique morphological feature of MCs, which led to their discovery in the 19th century as reported in 1.1. and are visualized with either cationic dyes or electron-microscopy. The reason behind this phenomenon is their special composition described below.
The main component is the ‘core protein’, a proteoglycan of the serglycine type. Its eponymous Ser-Gly repeat domain binds covalently glycosaminoglycans (GAGs) by forming O-glycosidic bonds (Figure 1-6**C**). Depending on the MC subtype, which will be described in detail in 1.3.2.1.2, the major GAG chains are composed of heparin or chondroitin sulfate. Heparin is exclusively synthesized by MCs. It is built up by repeating trisulfate disaccharide units which make them strongly anionic. Chondroitin sulfates consist of disaccharide units with one or two sulfations and are therefore less negatively charged [80]. The high degree of sulfation is expressed in the metachromatic characteristic of MC granules when stained with cationic dyes as toluidine blue (TB) (Figure 1-6**A**). Under a transmission electron microscope (TEM), SGs are electron-dense and appear very dark (Figure 1-6**B**), which is a unique feature for MCs when identified in a specimen. The overall GAG composition per protein backbone, a single

granule, the MC type or earlier stimuli determines the mediator composition. Based on electrostatic interactions, the mainly cationic signaling molecules are bound to the acidic GAG ‘arms’ of the serglycin. This binding is strong inside the acidified lysosome-like vesicles, but facilitates the rapid release in the surrounding tissue of a neutral pH as soon as exocytosed. Some compounds seem to prefer certain GAGs [80] and the binding of one distinct molecule may affect the association of a second [86].

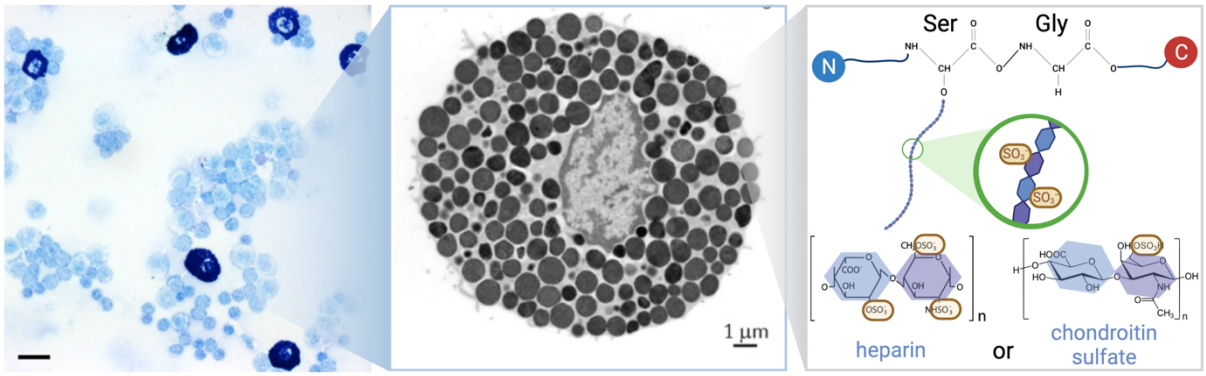

Figure 1-6 Mast cell secretory granules

A The strongly acidic SG of MCs show metachromasia when stained with cationic dyes like TB. Image taken by [87]. Scale bar 20 µm **B** TEM reveals the electron-dense vesicular structures in the cytoplasm of a mature resting MC. Image taken by [80]. **C** Every single SG is tightly packed with serglycine proteoglycans, covalently coupled to highly (heparin) or less sulfated (chondroitin sulfate) GAG chains. The negative charges capture mediators by electrostatic interactions. Created with Biorender.com.

MC degranulation can be regulated. During full exocytosis and compound exocytosis, the vesicles fuse with the plasma membrane and the intact granule, defined as the unit of mediators and scaffold, is set free. Full exocytosis means that only one vesicle fuses and subsequently empties its material (Figure 1-7**F**). The vesicular membrane fuses with the plasma membrane and can be recycled. Compound exocytosis may happen multigranularly or sequentially. Multigranular compound exocytosis is characterized by merging of several granules before fusing with the plasma membrane and as a result releasing a huge amount or even the whole entity of granules (Figure 1-7**D**). This mechanism is preferably used for allergic reactions and provides an enormous number of mediators very fast. During sequential compound exocytosis, first one vesicle fuses with the membrane, followed by connecting with a second which is continued to membrane-distant granules of the MC. This mechanism allows even centrally located SG to be passed through a tunnel-like system in the surrounding environment (Figure 1-7**E**).

In contrast, kiss-and-run and cavicapture describe mechanisms, in which vesicular compounds are only selectively released by forming pores between SG and cell membrane. Whereas

during kiss-and-run, the pore can be only passed by small compounds like amines (Figure 1-7**A**), cavicapture allows also proteins to leave the SG (Figure 1-7**B**). A sixth regulated mechanism is the piecemeal degranulation. During this process, a SG within the cytoplasm enlarges and buds a smaller vesicle, filled with a special compound. This smaller vesicle shuttles to the cell membrane to release its content in the surrounding environment (Figure 1-7**C**). [77]

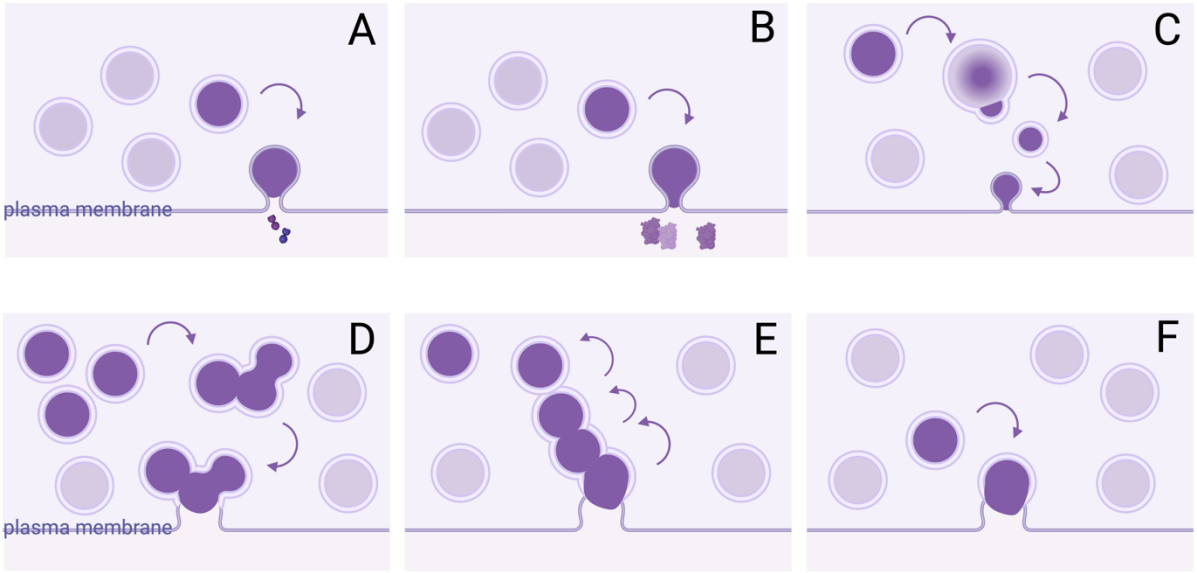

Figure 1-7 Mast cell exocytosis regulation

A The kiss-and-run mechanism is defined by selective release of small molecules, whereas larger cargos are secreted by cavicapture exocytosis (**B**). In **C**, the piecemeal degranulation process is shown, in which a smaller vesicle is bud and transports material to the plasma membrane. Multigranular compound exocytosis (**D**) and sequential compound exocytosis (**E**) are characterized by granule fusions prior to release. **F** shows the event of full exocytosis, when single intact granules are released by membrane fusion. Created with Biorender.com and according to [77].

During degranulation, the tightly packed proteoglycan-mediator bundles are released. As soon as the granular content is set free in the surrounding tissue, two circumstances aid in detaching the stored mediators. First, the proteoglycans hydrate and swell like a gel matrix. And second, the neutral pH outside of the cells reduces the electrostatic interactions between GAGs and mediators resulting in dissociation of the latter. [78]

1.3.2.1.2 MC subtypes and heterogeneity

MCs are one of the most heterogenous cell types of the immune system [88]. They can be classified in order to their anatomical location, staining characteristics or developmental origin. The current understanding for the murine and human system is summarized in this section.

MCs were originally thought to derive from hematopoietic stem cells (HSCs) of the fetal liver during early embryogenesis and from BM HSCs postnatally. HSCs develop to MC progenitor cells and use the bloodstream to enter their target tissues, respectively. Depending on the tissue environment, they come into contact with signaling molecules which stimulate their adhesion, differentiation and proliferation into mature, tissue-specific MCs. The skin, as a MC-rich tissue is probably best studied in this context. Leist *et a*l. showed in 2017, that the contact of MC progenitors with perivascular fibroblasts in the skin is important to induce the expression of typical mature MC genes for proteases or bioamine synthesis. The authors suggest, that membrane-bound stem cell factor (SCF) plays the major role in MC survival, proliferation and maturation. On the other hand, progenitor homing genes, like *Itgb7*, *Cxcr2* or *Cx3cr1*, are downregulated which let the cells settle preferably along blood vessels [89].
In 2018, two studies revealed a second population of skin MCs: yolk-sac derived, prenatally occurring MCs [90, 91]. A dual hematopoietic origin was only known for macrophages so far, but was a revolutionary finding for MCs. Depending on the tissue kinetics, these 'primitive' yolk-sac-derived MCs are replaced during embryogenesis by 'definite' (HSC-derived) MCs. Using differential gene expression analysis, Gentek *et al.* found, that primitive and definite MCs form two subtypes with distinct transcriptome profiles [90] and most probably different functions. Wolf and Goodridge point out, that the gene expression profile of the primitive MCs suggests a role in neuronal and vascular development [92].
But even in adults, primitive MCs can still exist, as it was shown for the murine skin [90]. Moreover, the authors found out, that for adult skin MC replenishment, no precursors from BM are needed and suggest that they maintain themselves by skin-resident precursors. Whether MCs of different developmental origin are present also in other tissues, needs to be further investigated.

Skin MCs are plenty, long-lived and belong to the most prominent MC type described in rodents, the constitutive serosal or connective-tissue type MCs (CTMCs). They were discovered first due to their strong metachromatic features and their presence in the connective tissue of almost all organs [93]. The strong metachromasia is attributed to their high heparin content as the major GAG component inside the granules [80, 94]. After improving the tissue fixation techniques for MC histology, a second MC subtype was discovered in the intestine, the mucosal MCs (MMCs) [95]. They were identified as short-lived [96] and inducible in response to T cell mediated type 2 inflammation [97]. As such, the MMC number can fluctuate, with an enormous increase upon intestinal inflammation [86]. MMCs are named by their preferred location at mucosal surfaces and lack heparin, resulting in poor staining or selective binding of only some cationic dyes after special non-aldehyde fixation [79]. Instead, they have

chondroitin sulfate coupled to their serglycine backbone. The less anionic properties make them not only challenging to detect with cationic dyes and electron microscopy, but also leads to an altered mediator composition. CTMCs are bigger, with many granules of homogenous size, rich in histamine [89], and serotonin [98]. In contrast, MMCs are smaller, contain less granules of variable diameters and less histamine [98]. The presence or absence of serotonin is diversely described [98, 99].

Whereas the MC classification in rodents is based on the cell localization, human MCs are distinguished by their protease expression.
Murine CTMCs are rich in carboxypeptidase A (MC-CPA, gene name Cpa3) and the MC proteases (mMcpt) 4, a chymase, mMcpt6 and 7, which are tryptases, and mMcpt5, an elastase (specialized chymase) [88, 97, 98]. They may also express mMcpt2 to a lesser extent [86]. It was shown, that the expression of these molecules can impact each other: The protein expression of the MC proteases is dependent on heparin, and the presence of MC-CPA influences the translation of Mcpt5 [86]. MMCs were identified to express the chymases mMcpt1 and 2, low levels of MC-CPA, but no mMcpt4, 5 or 6. mMcpt7 is completely absent in C57BL/6 mice due to a naturally occurring mutation and can therefore be used as a constitutive Mcpt7 knockout model [100, 101].
In human and mice, the gene coding for MC-CPA (CPA3 and Cpa3) is highly conserved [86], but for the MC proteases, less human isoforms exist. Thus, the murine classification is not transferable to the human system and comparing the subtypes and their functional impact and relevance should be done with caution. Human MCs are classified as either tryptase-containing (MC_T) or tryptase- and chymase-containing (MC_{TC}). Some authors add also chymase-containing MCs (MC_C) but they seem to be less abundant [88, 102, 103]. Since skin MCs express tryptases and chymases, whereas lung and intestinal mucosa MCs express only tryptases, one should think about a homology to rodent CTMCs and MMCs. But the discrimination based on localization is not as clear as in rodents and mixtures exist [99]. Human MCs express α- and β-tryptases. Functional studies with knockout mice have revealed mMcpt6 as the closest homolog to the human β-tryptase [100]. For the human chymase, it is less obvious, since four isoforms exist in mice: mMcpt1, 2, 4 and 5. Intensive research emerged mMcpt4 as the functional homolog, since mMcpt5 is structurally closer, but shows elastase-like activity [104]. The expression of MC proteases in human and mice is summarized in Table 1-1 according to [100, 105].

A recent transcriptional study challenged this simple MC classification system. Dwyer *et al.* compared 14 immune cell subsets from varying body locations and identified MCs as the most variable subset among them [106]. Moreover, by including only CTMCs, but from five different

anatomical locations, he could show a clear interorgan CTMC heterogeneity. Two years later, Akula *et al.* confirmed this finding of specialized MCs in different tissues using absolute quantification methods [107].

All in all, MCs form an extremely heterogenous immune cell population [102] making their identification as an entity and functional investigations substantially challenging. Lots of effort has been made since their discovery to improve detection methods and develop appropriate mouse models. The current achievements and limitations are described in detail in the following two sections.

Table 1-1 Mast cell proteases of the murine and human system

	Human		**Mouse**			
Enzyme	**ortholog**	**subtype**	**ortholog**	**subtype**	**gene name**	**enzymatic activity**
Exopeptidase	MC-CPA	both	MC-CPA	mainly CTMC	*Cpa3*	CPA-like
Chymases	CMA1	MC_{TC}	mMcpt1	MMC	*Mcpt1*	Chymotrypsin-l.
			mMcpt2	mainly MMC	*Mcpt2*	Unknown
			mMcpt4	CTMC	*Mcpt4*	Chymotrypsin-l.
			mMcpt5	CTMC	*Cma1*	Elastase-l.
			mMcpt9	uCTMC*	*Mcpt9*	Chymotrypsin-l.
Tryptases	α-tryptase	both	mMcpt7	CTMC	*Tpsab1*	Trypsin-like
	β-tryptases (I, II, III)	both	mMcpt6	CTMC	*Tpsb2*	Trypsin-like

*preferably uterine CTMCs, l. – like

1.3.2.2 Mast cell detection methods for murine subtypes

As mentioned in the beginning, MCs were first characterized by their metachromatic staining properties. Metachromasia describes the ability of a specimen to shift the color of a dye after binding. MCs possess this ability due to their heavily acidic SGs and can be clearly identified within the tissue as a result. The dye reacts with the negatively-charged sulfated GAGs of the backbone of granules [108]. Obviously, the quality of the staining depends strongly on 1. the existence of granules inside the cells and 2. their acidity. Over the years, the spectrum of MC detection methods grew continuously resulting in the discovery of more and more subtypes, as described in 1.3.2.1.2. It is important to keep in mind that all of these methods still have limitations. They demand the presence of distinct compounds, characteristics or receptors but within the heterogenous class of MCs, there seem to be no method addressing the entity of MCs in an organism yet. Thus, detection methods should be chosen carefully for the species,

tissue, MC type and maturity and the scientific interest or hypothesis of a study. When comparing different studies and their results, the underlying techniques should be considered and critically questioned. The following section summarizes only MC detection methods, which allow to distinguish subtypes at least in mice.

Toluidine blue (TB) or 'aniline purple' is an aniline derivate which was used by P. Ehrlich to identify MCs first [108, 109]. Whereas the surrounding tissue stains blue, the metachromatic granules of CTMCs stain deeply purple (Figure 1-6**A**). TB is still frequently used for MC detection but the staining procedure was improved over the years. An appropriate non-aldehyde fixation of the tissue (Carnoy´s fixative [110]) and an acidic pH (0.3 – 4) of the solution itself is recommended to visualize a broader spectrum of MCs. The longer the tissue is incubated in the TB solution (2 – 5 days), the more of the less acidic (MMCs) or less granule-containing (immature) MCs will be stained [79]. Hence, TB is principally able to stain both CTMCs and MMCs in rodents which depends strongly on the protocol. Thereby, a standardized protocol is absolutely necessary when comparing MC counts or distributions between studies. Additionally, it is important to know, that other acidic tissue components like cartilage, some granules in macrophages or basophils and goblet cells of the intestine may show metachromatic behavior, too [79, 111].
Other metachromatic dyes as Romanowsky stains, color MCs based on the same principle and produce comparable results in a more elaborate process [112]. Several variations, as **Giemsa**, **May-Grünwald-Giemsa** or **Wright-Giemsa** are available and may distinguish CTMCs and MMCs as well depending on the distinct protocol or treatment [79].

A dye combination further improved the differential staining of CTMCs and MMCs. **Astra blue** or **Alcian blue**, both phthalocyanine dyes, combined with **safranin O** bind to polyanions like GAGs with different affinities. Due to their highly sulfated GAG heparin, murine CTMCs stain positive for safranin (brick red), but poorly with Alcian blue [108]. In contrast MMCs stain blue with one of the cyanine dyes but require a proper non-aldehyde fixation. Carnoy´s fixative, an acidic chloroform-ethanol mixture, differentiates clearly CTMCs (red) and MMCs (blue) when sequentially stained [110]. Moreover, immature MCs show affinity for Alcian blue/Astra blue as well and can therefore be distinguished from the safranin-positive mature MCs in which they develop [108, 113]. Limitations are obviously that immature CTMCs (and MMCs) and mature MMCs can barely discriminated. Additionally, this two-color staining procedure impedes a combination with other dyes or antibodies.

Apart from metachromasia and histological dyes, antibodies against MC-specific surface proteins or granular material are frequently used. They are utilized in immunohistochemistry

(IHC) or immunofluorescence (IF) detection methods. Both methods require either direct labeling by a primary antibody or indirect detection by a secondary antibody which further enhances the signal. IHC is based on an enzyme, coupled to the primary or secondary antibody, which catalyzes a chromogenic chemical reaction to detect the target. In IF, a fluorophore is used for labeling and a fluorescent microscope is needed for detection.
Since, MCs are the only mature tissue-resident hematopoietic cells still expressing **c-kit (CD117)** on their surface [114], it is a frequently chosen protein to identify MCs in tissue sections. C-kit is a transmembrane tyrosine kinase receptor for the SCF, necessary for the homing and self-renewal of hematopoietic progenitor cells in the BM [114, 115]. MCs need the SCF signal for differentiation and maturation, but also for survival or activation [89, 114]. When using c-kit as a marker, one should keep in mind, that for example melanocytes, germ cells, stem cells [108], hippocampal neurons [116], but also some (activated) immune cells [114] stain positive for c-kit, whereas some MCs in the bladder, stomach, lung [108] or brain [117] did not. Studies using exclusively c-kit to detect MCs should be carefully interpreted. Combining antibodies against c-kit with at least one antibody against another MC protein should therefore be considered.
One possibility could be to add an antibody against one of the **mMcpt1 – 7**. Applying IF, more than two antibodies against different targets can be combined when coupled to fluorophores of different emission spectra. The more antibodies can clearly be distinguished, the better described is the cell (sub-)type. Unfortunately, not for all Mcpt, specific antibodies are commercially available.
Another option was discovered already very early [118], but gained new attention for *in vivo* imaging approaches [119]: staining MCs with **avidin**. When coupled to a fluorophore, this protein with strong affinity to heparin stains CTMCs highly effective and allows to distinguish resting and degranulated MCs. Due to the strong binding characteristics and improved fluorophore intensities, single granules are detectable within the tissue and of note, via specialized flow cytometry techniques even within the blood [120]. Disadvantageous, MMC granules cannot be stained due to their lack in heparin content, whereas other acidic (cartilage) or metabolically active tissues (CP) may bind avidin as well (personal observation).

Today, it is known that there is a huge diversity of MCs, based not only on the tissue and environment, but also among sex [121-123], species [18, 117, 124-126] and strains [127, 128]. During differentiation and maturation, the MCs surface receptor and granule composition undergoes alterations. Moreover, acute or chronically activated, as well as replenished MCs can change their repertoire of surface receptors and granular compounds [129]. MC detection methods should therefore be chosen carefully and considered specifically for a certain approach.

1.3.2.3 Mast cell mouse models

As discussed above, there is no single MC-specific marker to address specifically the entity of MCs in an organism. For the development of mouse models to investigate MC functions, this is at least as challenging as to stain them definitely. Already in the '70s of the last century, a so-called 'Kit mutant' mouse model with profound MC deficiency was identified [130]. But in addition to the MCs, these mice have other deficits. They were named $Kit^{W/W\text{-}v}$ due to their white ("W") spotted fur. These spots are caused by severe deficits in melanocytes. Since homozygous W mutations in C57BL/6 mice would be lethal [131], $Kit^{W/W\text{-}v}$ mice have one allele preventing Kit expression (*W*), whereas the other allele expresses a functionally impaired receptor [82]. As a result, the Kit-SCF pathway, which plays an important role during development, is diminished affecting strongly fertility, pigmentation and hematopoiesis [114]. Moreover, Kit was identified to play a role in the nervous system, gut motility [114] and inner ear development [132].
A second Kit mutant mouse, paving the way for MC research, was the $Kit^{W\text{-}sh/W\text{-}sh}$, 'sash', mouse model. 'Sash' mice are born with MCs but show severe deficiency when grown up [133] due to a mutation which impairs c-kit expression [134]. These Kit mutants have normal germ cells, but completely lack melanocytes. Increased blood basophils, enhanced myelopoiesis and cardiac hypertrophy were observed in addition [133]. They were important to reach the first milestones in MC research, but due to the several other deficits, it was recommended to compare always Kit mutant, wild-type and Kit mutant mice reconstituted with wild-type MCs ("MC knock-in mice"). This approach should ensure that the observed effects can be reduced to MCs only. But this system bears still limitations. It is difficult or even impossible to make certain that the reconstituted MCs are equal in number, anatomical distribution and phenotype compared with the wild-type situation [133]. Consequently, the development of more specific MC knock-out systems was indispensable.

With the commonly termed 'new transgenic models of MC deficiency' which are independent of Kit mutations, a new era of MC research begun. Most of them are based on the Cre/*loxP* genetic system (cf. 1.3.2.3.1) and show either constitutive or inducible MC deficiencies. These mice have two major advantages: First, they can be used for tissue investigations where MC reconstitution is expected to be difficult or incomplete [114], faced by [84, 135] for CNS tissue, and second, the Cre/*loxP* system opens new cross-breeding possibilities. For example, when MC-specific Cre expression is combined with *loxP* flanked reporter genes, MCs can be labeled for detection and interaction studies. As summarized in Table 1-2 in accordance with [119, 133, 136], two constitutive Cre-based knockout models were developed under the control of the *Cpa3* promotor in 2011. Cpa3 is one of the four highest expressed MC transcripts [107],

but also abundant in basophils to a lower extent. For the "Cre-Master" (*Cpa3*$^{Cre/+}$) mouse, developed by Feyerabend *et al.* [137], this is reflected in complete absence of CTMCs and MMCs, but also reduced basophil numbers in the spleen. The "Hello Kitty" (*Cpa3-Cre Mcl*$^{fl/fl}$) mouse model, generated by Lilla *et al.* [138], shows almost complete reduction in CTMCs and MMCs, except of some splenic MCs, and dropped basophil numbers in blood, spleen and BM [133].

An alternative constitutive MC deficiency model, published in the same year, is based on Cre expression under the control of the *Mcpt5* promotor. Whereas the Mcpt5-Cre mouse was developed by Scholten *et al.* in 2008 [139], members of the same group crossed them to Rosa26-DTA mice aiming for selective deficiency of Mcpt5 expressing CTMCs [1]. The Mcpt5-Cre mouse model plays a remarkable role in the present study and thus will be described in detail in 1.3.2.3.2.

For the sake of completeness, the inducible MC knockout models are implemented in Table 1-2 as well. These models are based on MC depletion mechanisms when applying or injecting diphtheria toxin. Mice are in general resistant to this toxin, but the MCs are genetically modified to make them selectively sensitive, subsequently leading to depletion. For the present thesis, these models are unsuitable, since it is not clear, if and how MCs in the brain are accessible by toxin injection and therefore will not be described in detail.

Table 1-2 Mast cell mouse models

Name	Background	characteristics	Ref.
MC knock-out mouse models (constitutive)			
WBB6F$_1$-*Kit*$^{W/W-v}$	WB x C57BL/6	1% of normal MC numbers in skin and no MCs in other tissues, Lack melanocytes, interstitial cells of Cajal, germ cells, ↓ γδ T cells, anemia, moderate neutropenia, 75–90% reductions in basophils in blood and spleen [133]	[130]
C57BL/6-*Kit*$^{W-sh/W-sh}$, 'sash'	C57BL/6	adults lack MCs, ↑ myelopoiesis with ↑ myeloid-derived suppressor cells, Cardiac hypertrophy, lack interstitial cells of Cajal and melanocytes, γδ T cells, neutrophilia, megakaryocytosis, thrombocytosis, ↑ basophils in blood [133]	[140, 141]

Cpa3$^{Cre/+}$, 'Cre-MASTER'	BALB/c or C57BL/6	Absence of CTMCs/MMCs (skin, peritoneum, intestine), cell-intrinsic defects 60% reduction in spleen basophils (basophil status in blood and BM not reported), *Cpa3* expressed in other cell types [133]	[137, 142]
Cpa3-Cre^{+} *Mcl-1*$^{fl/fl}$, 'Hello *Kit*ty'	C57BL/6	marked reductions (92–100%) in CTMCs/ MMCs in the skin, trachea, lung, peritoneum, digestive tract, etc., but no reduction in small numbers of splenic MCs, Reductions in basophil numbers in spleen (58%), blood (74%), and BM (75%), reduced IgE- and basophil-dependent chronic allergic inflammation of skin, *Cpa3* expressed in other cell types [133]	[138]
Mcpt5-Cre^{+} *DTA*$^{fl/+}$	C57BL/6	marked reductions in peritoneal (98%) and skin (89–96.5%) MCs; MMCs unlikely to be depleted, presence of MMCs, basophils not assessed [133], reduced numbers of a subset of uterine NK cells [67]	[1] [143]
MC knock-out mouse models (inducible)			
Mcpt5-Cre^{+} i*DTR*$^{fl/+}$	Probably C57BL/6	1 week after 4-weekly i.p. and 2 s.c. DT treatments, deficient in peritoneal and skin MCs (97.5%); stomach and intestinal MMCs present, BM basophils not affected 1 week after 4-weekly i.p. treatments with DT, basophil function not assessed [133]	[1]
Mas-TRECK		3 days after 5-daily i.p. DT treatments: deficient in peritoneal, skin, stomach, and mesenteric window MCs, transient > 95% ↓ in blood basophil numbers 5 days after start of DT treatment with recovery 12 days after the last DT treatment, markedly ↓ features of IgE- and basophil-dependent chronic allergic inflammation of skin (induced 2 days after 5 daily i.p. treatments with DT) [133]	[144]
RMB (Red MC and Basophil Mouse)	Probably C57BL/6	basophil- and MC-deficient at day 6 posttreatment with DT, or basophil-sufficient but MC-deficient at day 12 posttreatment, blood cell populations (red blood cells, CD19^{+} B cells, CD4^{+} and CD8^{+} T cells, neutrophils, eosinophils, monocytes) not depleted (+ tdTomato FP expression, cf. below) [119]	[145]

MC reporter mouse models			
Mcpt5-Cre^{+} EYFP$^{fl/fl}$	C57BL/6	EYFP fluorescence signal specifically in peritoneal and skin MCs [131], 12% EYFP^{+} blood NK cells [132], <20% EYFP^{+} splenic CD11b^{+}/ ~30% EYFP^{+} splenic NK cells [146]	[1, 139]
Mcpt5-Cre^{+} Ai6 (or ZsGreen)	C57BL/6 x C57BL/6J	ZsGreen expression under the control of Mcpt5-Cre promotor (not further characterized)	[147]
Mcpt5-Cre^{+} tdRFP$^{fl/fl}$	C57BL/6	expressing the RFP specifically in peritoneal and skin MCs	[148]
Mcpt5-Cre^{+} tdTomato$^{fl/fl}$ (or Ai9)	C57BL/6	tdTomato expression under the control of Mcpt5-Cre promotor (not further characterized)	[120]
RMB (Red MC and Basophil Mouse)	Probably C57BL/6	FcεRI^{+}KIT^{+} PMCs and FcεRI^{+}KIT^{-}CD49b^{+} blood/splenic basophils highly tdTomato^{+} (+ DT inducible ko, cf. above), knock-in [119]	[145]
MC protease knock-out models (conventional)			
mMcpt1$^{-/-}$	BALB/c	mMCP-1 required for clearance of *T. spiralis* infections (but not for *N. brasiliensis*)	[149]
mMcpt4$^{-/-}$	C57BL/6	Inactive mMCP-4, no effect on other mast cell proteases/ number of MCs/ MC morphology, complete loss of chymotryptic activity in peritoneum and ear tissue	[150]
mMcpt5$^{-/-}$	C57BL/6 or BALB/c	↓ muscle injury after ischemia reperfusion	[151]
mMcpt6$^{-/-}$	C57BL/6	lack mMCP-6 protein in tissue MCs and BMMCs, no Mcpt4/Mcpt5/Mcpt7 knock-out	[152]
C57BL/6 (mMcpt7$^{-/-}$)	-	Ear/skin MCs and BMMCs do not express mMCP-7	[101]
Mc-cpa$^{-/-}$	Backcrossed to C57BL/6	CPA3 and mMCP-5 deficient, no defects in degranulation in vitro or PCA in vivo	[86]

DT – diphtheria toxin, FcεRI^{+} – Fc epsilon receptor I i.p. – intraperitoneally, PCA – passive cutaneous anaphylaxis

For the investigation of the individual MC protease functions, murine knockout models for Mcpt1 [131], Mcpt4 [150], Mcpt5 [151], Mcpt6 [152] and Cpa3 [86] were developed (Table 1-2). When using these, one should know that some of them does not come singly. C57BL/6 mice naturally lack Mcpt7 [90]. Consequently, MC protease knock-out mice of C57BL/6 background need to be tested for mMcpt7 mutation. Surprisingly, for mMcpt6$^{-/-}$ mice on C57BL/6 background it was noticed that mMcpt7 expression is detectable anyway [152]. Moreover, the expression or storage of MC proteases can influence each other. Thus, it is not surprising, that Mc-cpa$^{-/-}$ MCs show an inability to store Mcpt5 and *vice versa*. Furthermore, *Ndst-2* null mice,

deficient in a key enzyme for heparin biosynthesis, were shown to lack Mcpt4, 5, 6 and mature Cpa3 [86] in addition. The same was observed for *Srgn*$^{-/-}$ mice, deficient in the protein component of the granular backbone molecule [80].

1.3.2.3.1 Cre/*loxP* system

The Cre/*loxP* system was developed in the 1980s [153-155] and is a frequently used genetic tool to create conditional knockout mice. Therefore, the gene for Cre-recombinase, an enzyme from bacteriophage, is inserted into the gene of interest to control its expression by a specific promotor. This can either be done as an external DNA construct which will be inserted randomly in the mouse genome or directly brought into the native reading frame by gene targeting methods [156]. Cell-specific expression of the gene of interest, leads to selective Cre expression.
For the conditional gene targeting, a second mutation is needed. So-called *loxP* sites, the recognition elements of the Cre-recombinase, are inserted, flanking the target gene sequence [157]. Depending on how the *loxP* sequences are brought into a gene of interest, either full or partial knockouts of the genes' function can be reached. In reporter systems, usually STOP cassettes upstream to a fluorescent protein (FP) gene are *loxP* flanked ('floxed'). Once Cre-recombinase is expressed, the floxed sites are recognized and the flanked fragment is deleted from the genome. For STOP cassette-restricted FP expression, this means, that the STOP segment is removed which allows the downstream transcription of the FP gene [156]. The combination of these two mutations enables highly cell type- or cell state-specific gene expression or knockouts [157, 158].

Nevertheless, this system should be used with care, considering some limitations. When establishing new Cre-driver lines, they are often crossed with reporter lines to see how specific and how efficient the driver works. Usually, these results are transferred to all other target genes, even if efficiency and specificity can differ dramatically. All experimental target genes have their own sensitivity to recombinase and depending on where they are located in the genome the enzymatic accessibility and the integration in enhancer and promotor regions most likely vary and needs to be tested properly [157]. Additionally, randomly integrated into the genome, the mutated genes can disrupt original reading frames [156].
Further "unspecific" or "ectopic" effects can be observed when the Cre-driver gene is transiently expressed during, often very early, states of development [156]. FPs, once expressed, can remain in the cells for years, even if the driver gene is not transcribed any more. Another problem which can be observed when mutant Cre-driver and target allele are inherited together by one adult is the rare case of germline recombination. This can cause

deletion of the *loxP* flanked sequence in germline leading to a loss of the targeted allele in offspring [156].
Moreover, proper controls are necessary to exclude that the observed effect after site-specific recombination is caused by the targeted knockout gene and not due to Cre expression itself [157]. In this line, homozygous Cre expressing cells may develop artefacts due to an altered cell homeostasis. Such phenomena are known as 'Cre toxicity' and can influence the cells health or force them to undergo apoptosis. Another important point in breeding these mice is to avoid mating Cre^+ females. Maternal oocytes are able to transfer Cre-recombinase to the new generation and only few molecules may cause a site-specific recombination [156].

1.3.2.3.2 Mcpt5-Cre mouse model

The Mcpt5-Cre mouse model, as mentioned in 1.3.2.3, was developed in 2008 by [139] to overcome the limitations of kit mutants like $Kit^{W\text{-}sh/W\text{-}sh}$ and $Kit^{W/W\text{-}v}$ and to reduce non-MC effects. Taking advantage of the Cre/*loxP* system, described above, the authors created a bacterial artificial chromosome (BAC) construct which contained an entire *Mcpt5* gene. The first exon of the gene was substituted by an 'improved Cre' complementary DNA (cDNA). Following purification, this construct was injected into pronuclei of oocytes from C57BL/6 female mice.
The resulting 'founder animals' were mated to reporter mice expressing EYFP under the control of a *loxP* flanked STOP cassette (Rosa26EYFP) [159]. EYFP expression in the offspring was investigated to evaluate recombination efficiency and specificity. In addition, Cre toxicity was verified in an *ex vivo* assay.

The authors observed an almost perfect recombination rate of 99% $EYFP^+$ peritoneal MCs ($CD117^+Fc\varepsilon RI^+$). A comparable rate, they described for skin MCs ($CD117^+CD45^+$). Regarding specificity, they observed less than 1% $EYFP^+$ cells in non-hematopoietic populations in the skin and only 1 - 3% recombination in hematopoietic (non-mast) cells. Therefore, they investigated cell suspensions from peritoneal lavage (macrophages) and spleen (macrophages, basophils, DCs, eosinophils, neutrophils, B and T cells). Only one of the eight mice showed higher ubiquitously recombination, hypothesized as accidental early promotor activity.
Cre recombinase genotoxicity could not be observed since *ex vivo* proliferation was not affected.

In 2011, the same group added experimental data to their model for skin and blood leukocytes [1]. They observed on the one hand 97.5% $EYFP^+$ cells in the ear skin MC population

(CD117$^+$FcεRI$^+$), and on the other hand 97.3% MCs (CD117$^+$FcεRI$^+$) among the EYFP$^+$ cells in ear skin. For blood leukocytes, they found EYFP$^+$ cells only in a minor fraction of NK cells (12% of NK1.1$^+$CD49b$^+$).

All in all, this mouse model is well accepted and established in the field and frequently used due to its high (CT)MC-specificity. Since its development in 2008, the Mcpt5-Cre mouse was used to generate different conditional reporter lines, but also constitutive and inducible knockouts (summarized in Table 1-2).

1.3.2.4 Cerebral mast cell research

MCs are sentinels and therefore preferably populate body-environment interfaces, as already mentioned above. As such, they have a junctional role in connecting innate and adaptive immunity but also monitor the healthy individuum. Thus, they are able to communicate with other cells in their direct environment or over far distances inside the body. Cerebral MCs probably act in both ways. They reside at brain-periphery interfaces, as they have been detected in PVS of the brain parenchyma, in the meninges and the CP [23, 41]. At these locations, they are able to sense danger signals or foreign antigens under pathological conditions. When activated, their released bioactive mediators influence BBB permeability or breakdown and recruit immune cells from elsewhere in the body. In contrast, during homeostasis, they monitor the environment and provide signaling molecules. It was shown for rats, that 50% of total brain histamine derive from MCs [160]. By providing neuropeptides, MCs may enhance neural signaling but also allow a crosstalk with peripheral body regions by acting on nerve endings [73, 161]. In addition, dural MCs can sense and react on several compounds in the periphery [162].

Cerebral MCs, their locations and functions in healthy and pathological conditions are still insufficiently studied. The knowledge about their location is based on different methods, sexes, health conditions and species. Especially the last mentioned seem to have a great impact, thus transferring the knowledge from one animal model to a second and finally to human beings should be done with care. The sex seems to play a role in cerebral MC numbers, distribution, but also function [22, 121, 122, 163]. The following two sections will provide an overview of the state-of-the-art knowledge.

1.3.2.4.1 Mast cell detection and localization in the brain

MCs were detected very early in the brain of varying mammalian species [18]. The inter- and intraspecies differences are strikingly which makes it challenging to draw plausible conclusions regarding their functions in general. Moreover, different detection methods, described in more detail in 1.3.2.2, aggravate the comparability of the experiments. A summary of MC detection studies over almost half a century is displayed in Table 1-3. It is remarkable that TB is the most frequently used MC stain. The protocol, especially the pH, may vary, but TB was used in 17 out of 20 studies including four different species. Most of the experiments were performed using at least two detection methods in combination. Interestingly, there is an inconsistency, whether c-kit is expressed on murine parenchymal MCs [128, 164] or not [117]. In mice, MCs were identified in the ventricles (ependyma, CP epithelium), leptomeninges, hippocampal formation (dentate gyrus), and dural meninges. In contrast to studies on C57BL/6 mice [117, 164, 165], Hendrix *et al.* [128] could not identify a single MC in the thalamus of B10.PL mice. Interestingly, most of the parenchymal MCs in rats are located in the thalamus. Some were detected in the preoptic area and hippocampus. In addition, MCs were identified in leptomeninges and DM. In humans, cerebral MCs are rare and studies are few ([124], [166]). They were detected in the ventricles (ependyma, CP) and in the pineal gland. For all of these studies, it cannot be excluded that the understanding of the anatomical regions differs.

Table 1-3 Mast cells detected in the brain of varying species

Year [Ref.]	Method	Species	Located in …
1978 [124]	TB, AlcB, AlcBSO, PAS (no protocols)	Frog	ventricles: ependyma, CP epithelial cells, tongue, CP connective-tissue, leptomeninges,
		Mice (albino)	Ventricles: ependyma, CP epithelial cells, tongue, leptomeninges,
		Humans (3 females)	Ventricles: ependyma, Pineal organ, area postrema, CP connective-tissue
1984 [163]	TB (neutral) TB (pH2.3) TB in EtOH, restained with AB enzymatic assay which accounts for histamine	Rat	Brain (>98% in thalamus, mostly lateral habenular nucleus, 2% in parietal cortex, optic chiasm) tongue
1998 [117]	AlcB + c-kit	Mouse (C57BL/6J)	inferior colliculus medial/lateral geniculate Dorsal/ventral thalamic nuclei
		Dove	Forebrain Habenula Around CVOs

		Rat	Diencephalon Olfactory bulb
1999 [167]	TB Berberine sulfate SEM TEM α-ER α-histamine α-RMCP-I/II	Rat (m)	DM (sub-calvarial)
2006 [128]	Giemsa TB (0.5N) Avidin α-c-Kit	Mice (B10.PL)	Hippocampal formation (Hc/entorhinal cortex) thalamus
2007 [168]	TB (pH2) Avidin	Rats (up to one months old pups, 4 months old m)	Thalamus and overlying PM
2010 [135]	TB (acidified) PE (pinacyanol erythrosniate)	Mice	DM (sub-calvarial) PM (removed from brain) CNS spleen LN
2010 [164]	May-Grünwald-Giemsa c-kit	Mice (C57BL/6, 8w, f)	habenula border, thalamus, increase in EAE
2011 [162]	TB	Rat	thalamus Spinal DM
2012 [165]	TB (pH2)	Mice ($Kit^{W\text{-}sh/W\text{-}sh}$ $Kit^{W\text{-}sh/+}$ C57BL/6)	Hc parenchyma, leptomeninges, CP
2014 [169]	TB	Mice (diverse)	DM (after formalin fixation, removed from brain surface), thalamus/Hc (not whole brain)
2017 [116]	Avidin c-kit	Mice (*Mcpt**5**-Cre*$^{+}$ *DTA*$^{fl/+}$, *Mcpt**5**-Cre*$^{-}$ *DTA*$^{fl/+}$, C57BL/6)	Hippocampal fissure/formation, meninges
2018 [166]	TB AlcB α-tryptase	Human (17-68y)	Pineal gland, Capsule/septae, among pinealocytes, close to vessels Same for CP
2018 [122]	TB (pH2) AlcBSO (0.7N, 0.125N) IHC: α-ER-a α-5-HT α-Histamine α-FcεR1 α-RMCPII	Rats	Preoptic area and (ventral) leptomeninges (fixed brain removed from skull) *Velum interpositum* adjacent to hippocampus
2018 [170]	TB (acidic)	Mice (*Kit*$^{W\text{-}sh/W\text{-}sh}$ *Kit*$^{W/KitW\text{-}v}$)	Lateral ventricles, dentate gyrus, meninges
2019 [72]	TB (pH2)	Mice (C57BL/6, 10-12w, m)	Freshly isolated meningeal MCs, DM

2019 [171]	TB (70%EtOH, pH2)	Rats	hypothalamus
2020 [172]	Beta-tryptase Avidin AlcBSO in acetic acid	Rats Mice (*Kit*$^{W\text{-}sh/W\text{-}sh}$)	Hc
2022 [22]	TB (0.5N)	Mice (C57Bl/6J)	DM (sub-calvarial)

5-HT – serotonin, α – "antibody against", AB – Astra blue, Ab – antibody, AlcB – Alcian blue, CP – choroid plexus, CVO – circumventricular organ, DM – dura mater, EAE – experimental autoimmune encephalomyelitis, ER – estrogen receptor, EtOH – ethanol, f – female, FcεRI – Fc epsilon receptor 1, Hc – hippocampus, LN – lymph node, m – male, PAS – Periodic acid–Schiff, PVS – perivascular space, RMCP – rat mast cell protease, SEM – scanning electron microscopy TB – toluidine blue, TEM – transmission electron microscopy

Even if cerebral MCs are sometimes specified as a third major subtype [41, 109], the studies using TB suggest that cerebral MCs are in most features connective-tissue type-like: they show deep metachromasia without special fixation. For the meninges, this was verified by Mcpt1$^+$ MCs in rat DM [167], SO$^+$ MCs in the cortical meninges in rats [122] and avidin$^+$ MCs in murine meninges [116] and rat thalamic pia mater [168], all indicative for CTMCs. Avidin$^+$ MCs were also detected in the mouse and rat hippocampus [128, 172], and rat thalamus [168]. Only MCs in the rat preoptic area identified by Lenz *et al.* [122] were defined as mucosal-like (AB$^+$, SO$^-$, Mcpt2$^+$).

1.3.2.4.2 Functional mast cell studies in the mouse brain

Until now, there are only few studies addressing the functional role of MCs in the murine CNS. A representative summary of publications in Table 1-4 delineates that most approaches are based on 'Kit mutant' mice. The impact of MCs was investigated in EAE (experimental autoimmune encephalomyelitis, a mouse model for multiple sclerosis pathology), LPS-induced inflammation, stroke, meningitis and spinal cord injury (SCI). Furthermore, Nautiyal and colleagues described a MC effect in adult neurogenesis, spatial learning and memory by performing cognitive tests [165]. The observed influence of MCs is as diverse as the murine and functional models used. MCs were shown to promote inflammation in the context of stroke and LPS treatment. These proinflammatory effects are mediated by BBB breakdown, T cell activation, cytokine release or microglia activation. For EAE, contradictory observations were made with MCs playing a proinflammatory [135, 173] or redundant role [137]. Mcpt knockout models reveal that the proinflammatory effect in EAE is at least partially mediated by Mcpt4. On the other hand, after traumatic SCI, Mcpts play an anti-inflammatory role by promoting scar extracellular matrix (ECM) remodeling. In pneumococcal meningitis, MCs seem to be not involved.

Table 1-4 Functional mast cell studies in the murine brain

MC mouse model	Study (year [ref.])	Functional model	MC effect
C57BL/6	2010 [164]	EAE	MC number ↑
WBB6F$_1$-*Kit*$^{W/W\text{-}v}$	2010 [135]	EAE	Proinflammatory: T cell activation, BBB breakdown
	2011 [137]	EAE	No effect
	2014 [169]	Stroke	Proinflammatory: ↑ infarct size and pathology
	2018 [170]	Pneumococcal meningitis	No effect
Kit$^{W\text{-}sh/W\text{-}sh}$	2012 [165] (C57BL/6 bg)	Cognitive tests	Impaired spatial learning, memory, adult neurogenesis in MC deficient mice
			No effect
	2018 [170] (C57BL/6 bg)	Pneumococcal meningitis	Proinflammatory, microglia activation
	2019 [171] (unknown bg)	LPS inflammation (i.p.)	Proinflammatory (less strong than in C57BL/6): TNFα, IL1β, IL6, IL5 ↑, IL4 ↓, microglia activation, ↑ BBB permeability
	2020 [172] (~87% C57BL/6 bg)	LPS inflammation	
Cpa3$^{Cre/+}$, 'Cre-MASTER'	2011 [137]	EAE	No effect
Cpa3-Cre^{+} *Mcl-1*$^{fl/fl}$, 'Hello *Kit*ty'	2014 [169]	Stroke	Proinflammatory: ↑ infarct size and pathology
Mcpt5-Cre^{+} *DTA*$^{fl/+}$	2017 [116]	MCs affect adult neurogenesis?	No effect
Mcpt4$^{-/-}$	2016 [173]	EAE	Proinflammatory effect of Mcpt4 in early EAE

	2019 [174]	SCI	Anti-inflammatory, Mcpt4 modulate scar formation
Mcpt6$^{-/-}$	2016 [84]	SCI	Anti-inflammatory, Mcpt6 improves recovery, modulates scar formation

BBB – blood-brain barrier, bg – background, EAE – experimental autoimmune encephalomyelitis, IL – interleukin, LPS – lipopolysaccharide, SCI – spinal cord injury, TNF – tumor necrosis factor

Using kit mutant mouse models, as discussed already in 1.3.2.3, bears certain limitations. Therefore, it is strongly recommended to always use 'knock-in' mouse models as controls [133, 136]. But when used for brain studies, Vangansewinkel *et al.* faced the problem that reconstituting MCs in the CNS is incomplete [84]. Also, Fritscher *et al*. noticed BMMC engraftment is less efficient in the brain ventricles, than in meninges [170]. Moreover, the genetic background of the mouse models is missing in some of the studies above.

Hence, it is surprising that studies on brain MCs using the new transgenic mouse models are few. Cpa-based mouse strains were used in two cases to confirm the results obtained with kit mutants in the same approach [137, 169]. In only one study, authors made use of the *Mcpt5-Cre*$^{+}$ *DTA*$^{fl/+}$ mouse model for studying MCs in the brain [116]. In contrast to Nautiyal *et al.*, who hypothesized in 2012 that MCs contribute to cognitive brain functions and adult neurogenesis using C57BL/6-*Kit*$^{W\text{-}sh/W\text{-}sh}$ mice [165], Wasielewska *et al.* could not verify this effect [116]. They proposed that the observation in neurogenesis is more likely caused by a disrupted SCF/c-kit signaling in general in the neurogenic niche. On the other hand, they agree that MCs may affect cognitive brain function by their ability to rebuild ECM and cellular environments in brain regions of neuronal plasticity and adaptive rewiring [116]. All in all, the function of brain MCs and their role as immune cells in this specialized organ needs to be further investigated and therefore, was targeted in this thesis.

1.4 Aim of the study

MCs, as first responders of the immune system, are strategically positioned at environmental surfaces of the body. In probably the same role as sentinel and effector cells, they were found at brain-periphery interfaces as well. Together with other immune cells, like macrophages, MCs were identified at the meningeal and CP BCSFB and the BBB of brain parenchyma. They seem to be part of a complex neuro-immune cell network, since their pro- or anti-inflammatory effects were described in the context of several neurological diseases. For brain macrophages, at least three different subtypes can be discriminated, which differ in their transcriptome and predicted functions [15, 44, 175]. For brain MCs, the function in a certain sub-organ localization and their interaction with other immune cells at brain barriers is barely understood. A major limitation to investigate their role in this context was the lack of an appropriate MC-specific mouse model.

The aim of this study was to investigate the role of cerebral MCs as part of a complex neuro-immune cell network. It pursued to elucidate their involvement in brain-periphery barrier formation and their interaction with immune and non-immune cells of the NVU, inside the CP and as a component of the meninges. Therefore, the Mcpt5-Cre mouse model should be used due to its high CTMC-specificity observed in peripheral organs [1, 2]. As the Mcpt5-Cre mouse model was already used in a brain-related study, but the MC-specificity for this organ was not tested in this context [116], the usefulness and reliability of the Mcpt5-Cre mouse model should be addressed first.

Hence, the Mcpt5-Cre EYFP reporter mouse should be used to characterize the transcriptome profile of $EYFP^+$ MCs cells at brain-periphery interfaces. In addition, the localization, spatial distribution and MC numbers should be studied in the intact reporter mouse brains by means of light sheet microscopy. This three-dimensional microscopy technique allows to resolve the spatial distribution even of rare cell types in a native environment and thereby, it has a major advantage to previous mechanical tissue sectioning methods.

In addition, observations in the three-dimensional data should be complemented with classical histological MC staining and immune fluorescence microscopy on brain slices and meningeal whole mounts. Finally, state-of-the-art full-length transcriptome profiling should support the microscopic findings for meningeal $EYFP^+$ cells with single cell resolution.

2 Materials

2.1 Chemicals

Table 2-1 Reagents

Reagent	Manufacturer	Order#
100 bp DNA ladder	Invitrogen, Thermo Fisher Scientific, Waltham, USA	#15628050
2-Mercaptoethanol	Thermo Fisher Scientific, Waltham, USA	#21985023
Acetic acid, glacial	Sigma Aldrich, St. Louis, USA Merck, Darmstadt	#695092
Acetone	J.T. Baker, Philipsburg, USA	#8002
Alexa Fluor™ 647 Protein Labeling Kit	Thermo Fisher Scientific, Waltham, USA	#A20173
Astra Blue FM	Carl Roth, Karlsruhe	# T129.1
Avidin, egg white	Thermo Fisher Scientific, Waltham, USA	#A2667
bovine serum albumin (BSA)	GERBU Biotechnik, Heidelberg	#1503.0500
Chloroform	Sigma Aldrich, St. Louis, USA Merck, Darmstadt	#288306
Dichlormethane (DCM)	Carl Roth, Karlsruhe	#8424.1
Ethanol, absolute	Th. Geyer GmbH und Co. KG, Berlin	#2246.1000
Ethidium bromide (1%)	Carl Roth, Karlsruhe	#2218.1
Ethyl cinnamate	Sigma Aldrich, St. Louis, USA	#112372
ethylenediaminetetraacetic acid (EDTA)	Carl Roth, Karlsruhe	#8043.2
Fetal calf serum (FCS)	Sigma Aldrich, St. Louis, USA	#S0615
Glycine	Carl Roth, Karlsruhe	#3908.2
HCl 5M	AppliChem GmbH, Darmstadt	#1821091211
Heparin	Sigma Aldrich, St. Louis, USA	#H3149-25KU
HEPES buffer solution (1M)	Gibco, Thermo Fisher Scientific, Waltham, USA	#15630-056
Isopropanol (2-Propanol)	Carl Roth, Karlsruhe	#CP41.2
KCl	Carl Roth, Karlsruhe	#6781.3
KH_2PO_4	CHEMSOLUTE®	#16480250
$KHCO_3$	Carl Roth, Karlsruhe	#p748.1
Methanol	Carl Roth, Karlsruhe, Karlsruhe	#8388.1
Methyl-β-cyclodextrin	Sigma Aldrich, St. Louis, USA	#332615-5G

Methylbutane	Carl Roth, Karlsruhe	#3927.1
murine RNAse inhibitor	New England Biolabs, Ipswich, USA	#M0314S
Na_2EDTA		
Na_2HPO_4 x $2H_2O$	CHEMSOLUTE®	#8622
NaCl	CHEMSOLUTE®	#13671000
NH_4Cl	Carl Roth, Karlsruhe	#p726.1
Normal goat serum	Sigma Aldrich, St. Louis, USA Merck, Darmstadt	#G9023-10ML
Nuclease-free water	Qiagen, Hilden	#129114
Orange G (C.I. 16230)	Carl Roth, Karlsruhe	#0318.1
Paraformaldehyde (PFA)	AppliChem GmbH, Darmstadt	#A3813.1000
Penicillin-Streptomycin	PAN Biotech, Aidenbach, Bayern	#P06-07050
Percoll	GE Healthcare, Chicago, USA	
Phytagel	Sigma Aldrich, St. Louis, USA	#P8169-100G
Protaqs® Clear Intermedium	quartett GmbH, Berlin	#400301105
Protaqs® PARAmount	quartett GmbH, Berlin	#BP-167H
RPMI 1640 Medium	PAN Biotech, Aidenbach, Bayern	#P04-18500
Safranin O	Carl Roth, Karlsruhe	#5165.1
SDS	AppliChem	#A2572,0250
Sodium azide (NaN_3)	Carl Roth, Karlsruhe	#4221.1
Sodium pyruvate	PAN Biotech, Aidenbach, Bayern	#P04-43100
Streptavidin	Jackson ImmunoReserach, West Grove, USA	#016-000-084
Sucrose	Carl Roth, Karlsruhe	#4621.1
Tissue freezing medium	Leica Biosystems, Wetzlar	#14020108926
Toluidine blue O	Carl Roth, Karlsruhe	#0300.2
trans-1-Acetyl-4-hydroxy-L-proline	Sigma Aldrich, St. Louis, USA	#441562-10G
Tris-(hydroxymethyl)-amino methane (TRIS)	Carl Roth, Karlsruhe	#4855.2
Triton X-100	Carl Roth, Karlsruhe	#3051.4
UltraPure™ DNase/RNase-Free Distilled Water	Invitrogen (Thermo Fisher Scientific, Waltham, USA)	#10977015
Vectashield® Mounting Medium	Vector Laboratories, Burlingame, USA	#H-1000

2.2 Enzymes

Table 2-2 Enzymes

Enzyme	Manufacturer	Order#
Collagenase D	Roche Diagnostics, Basel	#11088866001
Collagenase/Dispase	Roche Diagnostics, Basel Sigma Aldrich, St. Louis, USA	#10269638001 #COLLDISPRO
DNase	Sigma Aldrich, St. Louis, USA	#DN-25
DNase I	Sigma Aldrich, St. Louis, USA	#10104159001
Hyaluronidase	Sigma Aldrich, St. Louis, USA	#H3506
Liberase TM	Sigma Aldrich, St. Louis, USA	#5401119001
Proteinase K	Carl Roth, Karlsruhe	#7528.5

2.3 Kits

Table 2-3 Kits

Kit	Manufacturer	Order#
DreamTaq Green DNA Polymerase	Thermo Fisher Scientific, Waltham, USA	#EP0711
ILL DNA Library Prep Tagmentation LV	Illumina, San Diego, USA	
Quick-RNA™ Microprep Kit	ZymoResearch, Irvine, USA	#R1051
Reliance One-Step Multiplex Supermix	Bio-Rad Laboratories, Hercules, USA	#12010220
SingleShot Cell Lysis Kit	Bio-Rad Laboratories, Hercules, USA	#1725080

2.4 Antibodies and labeling reagents

Table 2-4 Antibodies and Dyes

Antibody/Dye	Manufacturer	Order#	
Antibodies			
CD3ε Monoclonal Antibody	eBioscience™, San Diego, USA	#12-0033-83	Fluorophore: PE Clone: eBio500A2
FluoTag®-X4 anti-GFP	NanoTag Biotechnologies, Göttingen	#N0304	Fluorophore: AbberiorStar635P, Blend of two single domain antibodies
goat anti-rat	Jackson ImmunoReserach, West Grove, USA	#112-605-003	Fluorophore: Alexa Fluor® 647 Clone: polyclonal
rat anti-CD117	Biolegend, San Diego, USA	#135101	Fluorophore: purified Clone: ACK
Dyes			
Avidin Alexa Fluor 647	Self-made*		Fluorophore: Alexa Fluor® 647
Hoechst 33342	Sigma Aldrich	#82261	Ex.: 350 Em.: 461
NeuroTrace™	Thermo Fisher Scientific, Waltham, USA	#21479	Ex.: 435 Em.: 455
TO-PRO™-1 iodide	Thermo Fisher Scientific, Waltham, USA	#T3602	Ex.: 515 Em.: 531
TO-PRO™-3 iodide	Thermo Fisher Scientific, Waltham, USA	#3605	Ex.: 642 Em.: 661

*The avidin Alexa Fluor 647 was generated using egg white Avidin and the Alexa Fluor™ 647 Protein Labeling Kit (both Thermo Fisher Scientific) according to manufacturer´s instructions. The final concentration was not determined since the spectrophotometer used for protein measurements cannot measure protein coupled to a fluorophore. Instead, varying dilutions were tested for optimal staining results in IHC and IF prior to use in experiments.

2.5 Primers and probes

2.5.1 Primers for genotyping

Table 2-5 Genotyping primers

Primer name	Internal number	Manufacturer	Sequence
GOI: Rosa26STOP (EYFP$^{fl/fl}$)			
R26stopDO1	**#63**	Eurofins Genomics, Ebersberg	5'GCG AAG AGT TTG TCC TCA ACC
ROSA26-DO2	**#62**	Eurofins Genomics, Ebersberg	5'GGA GCG GGA GAA ATG GAT ATG
ROSA26-UP	**#61**	Eurofins Genomics, Ebersberg	5´CCA AAG TCG CTC TGA GTT GTT ATC
GOI: Mcpt5-Cre			
M5/M6-Cre DO	**#43**	Eurofins Genomics, Ebersberg	5'GTC AGT GCG TTC AAA GGC CA
Mcpt5-Cre UP	**#42**	Eurofins Genomics, Ebersberg	5'ACA GTG GTA TTC CCG GGG AGT GT
Mcpt5-Ex1 DO3	**#41**	Eurofins Genomics, Ebersberg	5'TGA GAA GGG CTA TGA GTC CCA
GOI: tdTomato$^{fl/fl}$			
tomato mut fwd	**#111**	Invitrogen (Thermo Fisher Scientific, Waltham, USA)	5'GGC ATT AAA GCA GCG TAT CC
tomato mut rev	**#112**	Invitrogen (Thermo Fisher Scientific, Waltham, USA)	5'CTG TTC CTG TAC GGC ATG G
tomato wt fwd	**#109 / #117**	Invitrogen (Thermo Fisher Scientific, Waltham, USA)	5'AAG GGA GCT GCA GTG GAG TA
tomato wt rev	**#110**	Invitrogen (Thermo Fisher Scientific, Waltham, USA)	5'CCG AAA ATC TGT GGG AAG TC

2.5.2 Assays and templates for qPCR

Table 2-6 qPCR assays and templates

Product name and number	Unique ID	gene
PrimePCR Template #10031285	qMmuCEP0052849	*Kit*
	qMmuCEP0054703	*Cma1*
	qMmuCEP0054865	*Mcpt2*
	qMmuCEP0056041	*Cd3e*
	qMmuCEP0056394	*Tpsb2*
	qMmuCEP0060067	*Mcpt4*
	qMmuCIP0031356	*Fcer1a*
PrimePCR Probe Assay, FAM 500R #10031225	qMmuCEP0054703	*Cma1*
	qMmuCEP0054865	*Mcpt2*
	qMmuCEP0056041	*Cd3e*
	qMmuCEP0056394	*Tpsb2*
	qMmuCEP0060067	*Mcpt4*
PrimePCR Probe Assay FAM 200R #12001950	qMmuCEP0052849	*Kit*
	qMmuCIP0031356	*Fcer1a*

2.6 Consumables

Standard consumables as reaction tubes, cannulas, petri dishes, syringes and pipette tips were used from varying manufacturers.

Table 2-7 Consumables

Product	Manufacturer	Order#
96 Well 0.2 mL 8-Transformer Plate	Biozym Biotech Trading GmbH, Wien	#712540
BD Vacutainer, Safety Lok blood collection set (21G)	Becton Dickinson and Company, Franklin Lakes, NJ, USA	#367282
Craft cotton swabs, triangular, extra small	Tamiya, Shizuoka, Japan	#300087105
Menzel-Gläser SUPERFROST® PLUS	G. Menzel B.V. & Co. KG, Braunschweig	#J1800AMNZ

MicroAmp® Fast 96-Well reaction plate (0.1 mL)	Applied biosystems (Thermo Fisher Scientific, Waltham, USA)	#4346907
MicroAmp™ Optical Adhesive Film	Applied Biosystems (Thermo Fisher Scientific, Waltham, USA)	#4311971
PCR SingleCap 8er-SoftStrips (0.2 mL)	Biozym Biotech Trading GmbH, Wien	#710980
twin.tec PCR plate 96	Eppendorf AG, Hamburg	#0030 128.648 #951020401

2.7 Equipment, microscopes, machines

Table 2-8 Lab equipment and machines

	Manufacturer
BD FACSAria™ III cell sorter	Becton Dickinson, Franklin Lakes, USA
Centrifuge 5415 R	Eppendorf AG, Hamburg, Germany
DNA/RNA UV-Cleaner Box UVT-B-AR	Biosan, Riga
GFL Shaking incubator 3031	Gesellschaft für Labortechnik, Burgwedel, Germany
Heraeus Multifuge 3SR+ Centrifuge	Thermo Fisher Scientific, Waltham, USA
Herolab E.A.S.Y B-445-F camera	Herolab, Wiesloch, Germany
Herolab Transilluminator	Herolab, Wiesloch, Germany
Illumina NextSeq 500	Illumina, San Diego, USA
Illumina NovaSeq 6000	Illumina, San Diego, USA
Leica CM 1950 Cryotome	Leica Biosystems, Wetzlar, Germany
MICRO CENTRIFUGE	Fisher scientific, Thermo Fisher Scientific, Waltham, USA
NanoZoomer Slide scanner	Hamamatsu Photonics, Shizuoka, Japan
neoLab-Rotator	neoLab, Heidelberg, Germany
Neubauer Hemacytometer	P. Marienfeld, Germany
Platform shaker Duomax 1030	Heidolph instruments, Schwabach, Germany
QuantStudio3	Applied Biosystems (Thermo Fisher Scientific, Waltham, USA)
Stereomicroscope GZ6	Leica Biosystems, Wetzlar, Germany
Thermocycler T3000	Biometra GmbH, Göttingen, Germany
ThermoMixer C	Eppendorf AG, Hamburg, Germany
Microscopes	
Leica DMI8, inverted whitefield microscope	Leica Biosystems, Wetzlar, Germany

Leica DMIL, inverted phase contrast microscope	Leica Biosystems, Wetzlar, Germany
- SPOT INSIGHT color camera 3.2.0	Visitron systems GmbH, Puchheim, Germany
UltraMicroscope II	LaVision Biotech GmbH, Bielefeld, Germany
UltraMicroscope Blaze	Miltenyi Biotec, Bergisch Gladbach, Germany
- Objective lenses/dipping caps: **1.1x NA 0.1 MI Plan, DC57 WD17 O** **4x NA 0.35 MI Plan, DC57 WD16 O1**	Miltenyi Biotec, Bergisch Gladbach, Germany
- SuperK FIANIUM (white light laser)	NKT Photonics, Birkerød, Denmark

2.8 Software

Table 2-9 Software

Software and version	Manufacturer/ Reference
bcl2fastq2 2.20.0	Illumina, San Diego, USA
Cutadapt v2.10	Published by [176]
E.A.S.Y Win32 Software	Herolab, Wiesloch, Germany
FastQC v0.11.8	Published by [177]
Fiji	Published as open-source platform by [178]
GraphPad Prism (for Windows) v9.0.0	Dotmatics Limited
Imaris 9.7	Bitplane, Zürich, Schweiz
ImspectorPro 7.3.6	LaVision Biotech GmbH, Bielefeld, Germany
Leica Application Suite (LAS) X	Leica Biosystems, Wetzlar, Germany
NDP.view 2	Hamamatsu Photonics, Shizuoka, Japan
Photoshop	Adobe Inc., SanJosé, USA
Qlucore Omics explorer	Qlucore, Lund, Sweden
QuantStudio Design and Analysis software	Applied Biosystems (Thermo Fisher Scientific, Waltham, USA)
R package Seurat v4.0.5	Published by [179]
R package Subread v2.4.3	Published by [180]
SPOT advanced	SPOT Imaging, Sterling Heights, USA
STAR v2.7.8	Published by [181]

2.9 Buffers, solutions and fixatives

Astra blue solution

1% (w/v) Astra blue (powder) was dissolved at RT in 0.7N HCl while stirring at RT

Materials

Carnoy´s fixative

60% (v/v) Ethanol, absolute
30% (v/v) Chloroform
10% (v/v) Acetic acid, glacial

Cell culture medium

RPMI1640 supplemented with
10% v/v FCS
1% v/v Penicillin/Streptomycin
1% v/v sodium pyruvate
50 µM β-mercaptoethanol

Erytrocyte lysis buffer (1x)

20.73 g NH_4Cl
2.5 g $KHCO_3$
93 mg EDTA
2.500 L distilled water

0.125N HCl

2.5% (v/v) 5M HCl
In distilled water

0.7N HCl

14% (v/v) 5M HCl
In distilled water

Lysis buffer (RNA sequencing experiments)

1.9 µL 0.2%(v/v) Triton-X 100 in nuclease-free water
0.1 µL murine RNAse inhibitor (NEB, PN M0314S)

Orange G solution

0.5% (w/v) Orange G powder was dissolved in absolute ethanol. A very small volume of glacial acetic acid helped to acidify the solution.

10xPBS

2 g	KCl
2 g	KH_2PO_4
14.42 g	Na_2HPO_4 x $2H_2O$
80 g	NaCl

Filled up to 1 L using dist. H_2O. For 1xPBS, 10xPBS is diluted 1:10 and pH adjusted to 7.2 – 7.4, if not indicated differently.

Permeabilization buffer

0.02 g trans-hydroxy-L-proline (Sigma)
0.5 mL Methylcyclodextrin stock solution 10 mM
50 µL NaN_3 stock solution 10%
0.5 mL Triton 10%ig in PBS
→ filled up to 10 mL with 1xPBS

4% PFA solution

40 g PFA
100 mL 10xPBS
Filled up to 1L using dist. H_2O, heating (<70°C) and stirring until dissolved, pH adjusted to 8.5 using NaOH when cooled to RT.

Safranin O solution

0.5% (w/v) safranin O (powder) was dissolved in 0.125N HCl while stirring at RT

Tissue lysis buffer

100 mM	TRIS (pH 8.6)
5 mM	Na_2EDTA
0.2%	SDS
200 mM	NaCl

in distilled water

Distilled water was generated using a Milli-Q® water purification system (Merck, Darmstadt).

3 Methods

3.1 Mouse husbandry

All mice were bred and housed in the Central Animal Facility ("Zentrale Tierhaltung", ZTH) on the Medical Campus, Otto-von-Guericke University Magdeburg in a pathogen-controlled environment. All strains were originally purchased from Jackson laboratories, summarized in Table 3-1. Usually, two females (Cre^{-}) and one male (Cre^{+}) were combined to breed. Females gave birth naturally and pups were weaned at the age of 2 – 4 weeks. They were marked with ear holes and grew up separated in males and females in small groups of up to six animals. All mice had *ad libitum* access to food and water, wooden bedding and enrichment in their cages. If not stated differently, female mice at the age of 12 weeks were used for experiments, according to the Aktenzeichen 42502-2-1539UniMD, approved by the Landesverwaltungsamt Sachsen-Anhalt. Male mice (12 weeks of age), were only used for organ dissections. Mice used in this study were all let to acclimate in the laboratory at least 24 hours prior to experiment. Animal handling was conducted calm and carefully, in accordance with the institutional guidelines on animal welfare.

Table 3-1 Mouse strains in this study (double mutant reporter mice)

Mouse strain	Official name(s), JAX stock#	Short form	Ref.	phenotype
Mcpt5-Cre^{+} EYFP$^{fl/fl}$	Tg(Cma1-cre)ARoer (stock# NA), B6.129X1-Gt(ROSA)26Sortm1(EYFP)Cos/J (stock#006148)	Mcpt5-Cre EYFP	[139] [1]	EYFP expression in CTMCs (under the control of *Mcpt5/Cma1* promotor) Ex.: 513 Em.: 527
Mcpt5-Cre^{+} tdTomato$^{fl/fl}$ (or Ai9)	Tg(Cma1-cre)ARoer (stock# NA), B6.Cg-Gt(ROSA)26Sortm9(CAG-tdTomato)Hze/J (stock#007909)	Mcpt5-Cre tdT	[120] [182]	tdTomato expression in CTMCs (under the control of *Mcpt5/Cma1* promotor) Ex.: 554 Em.: 581

Em. – emission maximum, Ex. – excitation maximum (according to fpbase.org)

3.2 Mouse genotyping

All mice were tested for their genotype twice, once after weaning by using the punched bioptates from ear marking and once after sacrifice by using a tiny piece of the tail tip.
The bioptate is lysed using 300 µL (ear tissue) or 600 µL (tail tips) tissue lysis buffer (cf. 2.9) and 3 or 6 µL proteinase K in a 1.5 mL reaction tube. After at least 2 hours of incubation at 56°C and 800 rpm in the ThermoMixer C (Eppendorf AG, Hamburg), the lysate is centrifuged for 10 min at 16,000 g. The supernatant is transferred in a fresh 1.5 mL reaction tube and an equal volume (300 µL) isopropanol is added. The tubes are carefully mixed and centrifuged again for 10 min at 16,000 g when DNA is precipitated. The supernatant is discarded and DNase-free 70% ethanol solution is added for washing the DNA precipitate. The closed tubes are inverted carefully followed by 5 min centrifugation at 16,000 g. The supernatant is discarded again, and tubes containing DNA are air-dried. The dried DNA pellet is finally dissolved in 50 µL DNase-free water (Quiagen, Hilden), which is completed over night at 37°C and 800 rpm in the ThemoMixer C. DNA is stored at 4°C until used for polymerase chain reaction (PCR).

PCRs are conducted according to the expected inherited mutations. 16 µL-PCR reactions are performed in 0.2 mL reaction tubes of nuclease-free Transformer plates (Biozym, Wien). Therefore, PCR reagents are united (14 µL) and the DNA template generated above is added (2 µL), as summarized in Table 3-2. The primers for each gene of interest are mixed prior to use and diluted to 10 µM (for each primer). The PCR program is given in Table 3-3.

Table 3-2 Pipetting scheme for genotyping PCR

Component	Volume (µl)	final concentration
10x Dream-Taq Green buffer	1.6	1x
dNTPs (10 mM)	0.32	0.2 mM
DreamTaq DNA Polymerase (5 U/mL)	0.064	0.3 U
Nuclease-free water	13.056	–
Primer (10 µM each)	0.32 (mixture)	0.2 µM each
DNA Template (~100-500 ng)	2	NA

DNA – desoxyribonucleic acid, dNTPs – desoxyribonucleic triphosphates, NA – not determined, U - units

Table 3-3 PCR program „TOUCH“ for genotyping

Step	Temperature [°C]	time [s]	
Initiation	95	240	
Denaturation	95	30	x2
Annealing	60	30	
Elongation	72	45	
Denaturation	95	30	x2
Annealing	58	30	
Elongation	72	45	
Denaturation	95	30	x2
Annealing	56	30	
Elongation	72	45	
Denaturation	95	30	x34
Annealing	54	30	
Elongation	72	45	
Termination	72	600	
Hold	15	∞	

PCR products are separated in a 2% (w/v) agarose gel in 1x TAE buffer. The gel is incubated afterwards in 1x TAE containing 1 µg/mL ethidium bromide which binds to DNA and allows to visualize fragments under UV illumination (Transilluminator, HeroLab). To determine the DNA fragment size, a 100 bp DNA ladder (Invitrogen, Thermo Fisher Scientific) is included once per row.

3.3 Estrous cycle determination

The estrous cycle phases of female mice were determined according to [183]. Therefore, subsequently after sacrifice for experiments, a very small cotton swab was inserted in the vaginal opening for 0.5 to 1 mm and turned carefully to collect a mucosal smear. This smear was spread out on a microscope slide and air dried. To visualize the mucosal cells and enhance the contrast, the slides were stained for 15 min in a 0.5% aqueous toluidine blue solution. Afterwards, the slides were washed with tap water, the smears protected with a cover slip and immediately imaged using a DMIL (Leica Biosystems, Wetzlar). Five representative images per mouse were acquired with a SPOT INSIGHT camera for cell counting. According to [183], three cell populations were distinguished, counted and calculated as percentages for every single image: nucleated epithelial cells, cornified epithelial cells and leukocytes. Nucleated epithelial cells are characterized as big, almost square, rich in cytoplasm and have a single blue-stained nucleus. Cornified epithelial cells have a similar appearance, but lack a

bluish nucleus. Instead, they are pale and have a ghost-like shadow where the nucleus was. Leukocytes, mainly neutrophils, are comparably small, deeply stained with the blue dye and often polynuclear. The percentages of the three cell types were determined per mouse manually. Estrous cycle phases were finally determined using the “Mouse estrous cycle identification tool” by [183] as depicted in Figure 3-1**A**.

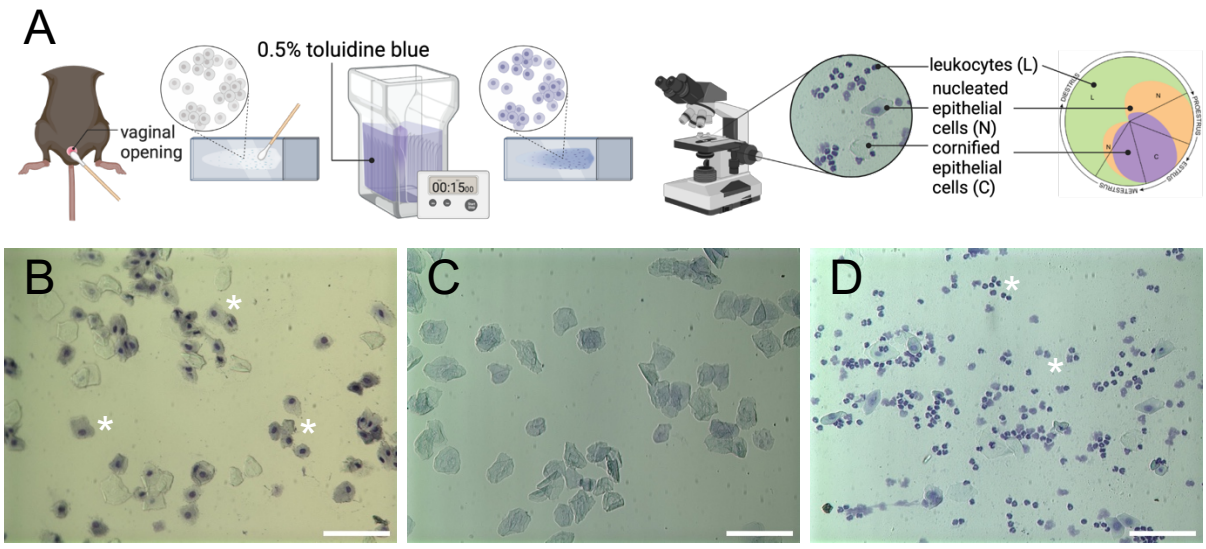

Figure 3-1 Estrous cycle determination
The estrous cycle phases of female mice used for experiments were determined following the scheme in **A**. Vaginal swabs were taken after sacrifice, air-dried and stained with an aqueous solution of toluidine blue. Three cell populations were distinguished using light microscopy and percentages determined manually. The right-most “Mouse estrous cycle identification tool” by [183] was used to categorize into the four stages of the female cycle. **B** shows a representative smear of the proestrus phase, containing 66% nucleated epithelial cells (white asterisks) and 34% cornified epithelial cells. **C** is a representative image of a smear with exclusively cornified epithelial cells, taken during proestrus phase. The image in **D** contains all three cell types, cornified and nucleated epithelial cells and mainly leukocytes (white asterisks), which represents the diestrus phase of the murine estrous cycle. Scale bars 100 µm. Scheme created with Biorender.com

3.4 Tissue dissociation for FACS

Mice were euthanized in a chamber by increasing the carbon dioxide concentration to a lethal dose. Organ dissection started when the mice showed no pedal reflexes anymore. Table 3-4 provides an overview which tissues and mice were used for which experiment.

Table 3-4 Overview organ dissection per experiment

Experiment (section)	Mice	Organs/tissues
Bulk RNA Sequencing (4.1)	Mcpt5-Cre^{+} EYFP	DM, CP, parenchyma, peritoneal lavage
	Mcpt5-Cre^{-} EYFP (only gating control)	peritoneal lavage
qPCR (4.2)	Mcpt5-Cre^{+} EYFP	DM, CP, parenchyma, peritoneal lavage, ear skin, spleen
	Mcpt5-Cre^{-} EYFP (only gating control)	peritoneal lavage
	C57BL/6	Bone marrow
Single cell RNA Sequencing (4.7)	Mcpt5-Cre^{+} EYFP	DM
	Mcpt5-Cre^{-} EYFP (only gating control)	DM

3.4.1 Peritoneal Lavage

Peritoneal MCs (pMCs) were obtained via peritoneal lavage. Therefore, the very first step was to open the skin on the ventral side to expose the peritoneum. The abdominal cavity should be still covered by the inner layer of the abdominal wall (parietal peritoneum). 5 mL sterile 1xPBS (ice-cold) was injected carefully in the abdominal cavity using a syringe and a 19G cannula. Inner organs or blood vessels should not be punctured. Then, the fluid was moved in the cavity by kneading the belly carefully. Finally, the fluid was pulled back in the syringe and filtered through a 100 µm mesh size in a 50 mL tube. Only 1 mL of the cell suspension was transferred in a round-bottom tube and centrifuged for 5 min at 400g and 4°C. The supernatant was discarded and the cell pellet was ready for staining.

3.4.2 Dura mater, brain and choroid plexus

3.4.2.1 Perfusion and tissue isolation

For the isolation of the brain tissues, the mice have to be cleared from blood by perfusion. Therefore, the thorax was opened carefully above the sternum. Starting with the diaphragm, the rib cage was opened posteriorly to anteriorly on the left and right side until the heart is exposed. A so-called butterfly cannula (21G) as part of a blood collection set (Becton Dickinson, Franklin Lakes) was inserted into the left ventricle of the heart and a cut with sharp scissors opened the right atrium. This allowed to flush the blood vessel system using maximal 60 mL sterile ice-cold 1xPBS manually with a syringe before the organs of interest were isolated for further dissociation.

Isolation and dissociation of brain tissues for the bulk RNA sequencing and qPCR (except of the meninges) was carried out by Lorena Morton (Institute for Inflammation and Neurodegeneration, OvGU Magdeburg) according to [184]. Therefore, the skull was scalped and mandible removed. The brain was isolated carefully from the ventral side of the skull. Both brain and emptied skull are placed in a petri dish in 1xPBS separately. The sub-calvarial meninges, which consists usually of DM and arachnoid barrier [25], were carefully stripped from the inside of the skull. CPs were isolated from all four ventricles and pooled for the digestion procedure. From the whole brain, olfactory bulb and caudal region (cerebellum and midbrain) were removed before dissociating parenchymal cells. All three brain tissues were enzymatically digested at 37°C in RPMI1640 (Roswell Park Memorial Institute) medium containing 2% (v/v) FCS, 2 mM HEPES (2-[4-(2-hydroxyethyl)piperazin-1-yl]ethanesulfonic acid), 2 mg/mL DNase I and 0.4 mg/mL collagenase D. Ethylenediamine tetra acetic acid (EDTA) was added to a final concentration of 5 mM to stop digestion. Subsequently, cells were washed and filtered through a 70 µm (bulk RNA Sequencing) or 100 µm (qPCR) cell strainer. Cells were finally suspended in 1xPBS for fluorescence activated cell sorting (FACS) and kept on ice. Only some of the processing details differ among the tissues and will be described below.

3.4.2.2 Brain processing

The brain was split in two hemispheres which were minced in small pieces individually. Both pieces were unified in a 50 mL reaction tube containing digestion buffer as described above. The brains were digested for 30 min at 37°C and 650 rpm, followed by carefully homogenizing the suspension with a pipette. As described in [185], the homogenate was cleaned up on a discontinuous 30-70% Percoll gradient to remove the myelin. The cleaned cell suspension was filtered prior to FACS as mentioned above.

3.4.2.3 Choroid plexus processing

The four CPs were individually extracted and directly transferred in digestion buffer. They were incubated for 20 min at 37°C and 650 rpm and subsequently homogenized using a pipette. Finally, the homogenates were washed three times and filtered prior to FACS.

3.4.2.4 Dura mater processing

In the literature, murine sub-calvarial meninges, isolated from the inside of the skull as described above, are usually referred to as DM, even if they most probably contain also the arachnoid epithelium [25]. In the context of this thesis, I stick to the term DM, but I cannot exclude the presence of other meningeal layers.

For bulk RNA sequencing, the isolated DM was directly transferred in digestion buffer. It was incubated for 50 min at 37°C and 650 rpm and subsequently homogenized by pipetting. Finally, the homogenates were washed three times and filtered prior to FACS.

For qPCR and single cell RNA sequencing, the isolated DM was directly transferred in a 2 mL reaction tube containing 1 mL RPMI1640 medium supplemented with 2% (v/v) FCS and 2 mM HEPES and an enzyme mix of 1 mg/mL DNase (Sigma) and 1 mg/mL Collagenase/Dispase (Roche). The tubes were incubated for 40 min at 37°C in the ThermoMixer C (Eppendorf AG, Hamburg) shaking at 300 rpm. To stop the digestion, samples were subsequently placed on ice and filtered through 100 µm cell strainer in a round-bottom tube. The 2 mL tubes and the filters were washed with 1 mL 1xPBS and centrifuged for 5 min at 365g and 4°C. The supernatant was discarded and the cell pellet finally resuspended in 1xPBS for FACS in a round-bottom tube.

3.4.3 Ear

For the outer ear skin digestion, 2 mL tubes with 500 µL RPMI were prepared. The pinnae were dissected distally to the cartilaginous regions of tragus and scapha and afterwards separated in two halves along the medial cartilage layer. Both halves were minced in small pieces using a scalpel by cutting a grid-like pattern. The pieces were transferred in the prepared RPMI medium and another 500 µL RPMI containing the enzyme mix were added to each tube to reach a final concentration of 198 U/mL DNase I (Sigma-Aldrich), 31.25 µg/mL Liberase TM (Sigma-Aldrich) and 0.25 mg/mL Hyaluronidase (Sigma-Aldrich). These tubes were than incubated for 45 min at 37°C in the ThermoMixer C (Eppendorf AG, Hamburg), shaking at 1,400 rpm. To stop the digestion process after the 45 min, the tubes were subsequently placed on ice and filtered through 100 µm mesh size in a round-bottom tube. The 2 mL tubes and the filters were washed with 1 mL 1xPBS and centrifuged for 5 min at 400g and 4°C. The supernatant was discarded and the cell pellet finally resuspended in 1xPBS for FACS.

3.4.4 Spleen

$CD3\varepsilon^+$ splenic T cells were used as negative control for MC gene expression. To isolate them, spleens from the same Mcpt5-Cre EYFP mice were smashed through a 70 or 100 µm cell strainer in 1xPBS in a petri dish. This cell suspension was transferred in a 50 mL reaction tube and centrifuged for 5 min at 400 g and 4°C. The supernatant was discarded and the cell pellet was resuspended in 3 mL erythrocytes lysis buffer. After 60 s incubation, the reaction was stopped by adding 10 mL 1xPBS and cell suspension was centrifuged again for 5 min at 400g and 4°C. Once the supernatant was discarded, the cell pellet was dissolved in 1 mL 1xPBS (for FACS) and transferred in a round-bottom tube. Following another centrifugation step and decantation of the supernatant, the cell pellet was resuspended in 1xPBS for FACS.

3.5 Fluorescence-activated cell sorting (FACS)

Cell pellets generated in 3.4 were resuspended carefully in 1 mL 1xPBS. For the reporter mice, Mcpt5-Cre EYFP, additional staining was not needed, when only $EYFP^+$ cells were counted or sorted. The cell suspension was filtered again using 100 µm mesh size prior to cell sorting to avoid plugging of the sorting machine.
The splenocytes used as negative control in qPCR were stained against CD3ε. Therefore, 0.1 µg PE-labeled anti-CD3ε (Invitrogen) was added to 100 µL of the cell suspension and incubated for 15 min at 4°C in the darkness. The staining reaction was stopped by adding 1 mL 1xPBS. A final washing step by centrifuging as above, discarding supernatant and adding 1 mL 1xPBS again, was followed by a last filtering through a 40 µm cell strainer. After centrifuging and discarding again as above, the samples and controls were ready for measurement or sorting by adding 100 µL of the 1xPBS and homogenizing the cell suspension thoroughly.

The BD FACSAria™ III cell sorter was equipped with an 85 µm or 100 µm-nozzle (single cell RNA sequencing), sterile 1xPBS and cooled down to 4°C. The sorting process was conducted by Dr. Roland Hartig (Multi-parametric bioimaging and cytometry (MPBIC), OvGU Magdeburg). Gating for EYFP was based on Mcpt5-Cre^- EYFP littermates. The sorting gate for PE^+ cells was set by using unstained Mcpt5-Cre^+ EYFP splenocytes. The gating strategy is displayed in Figure 3-2.

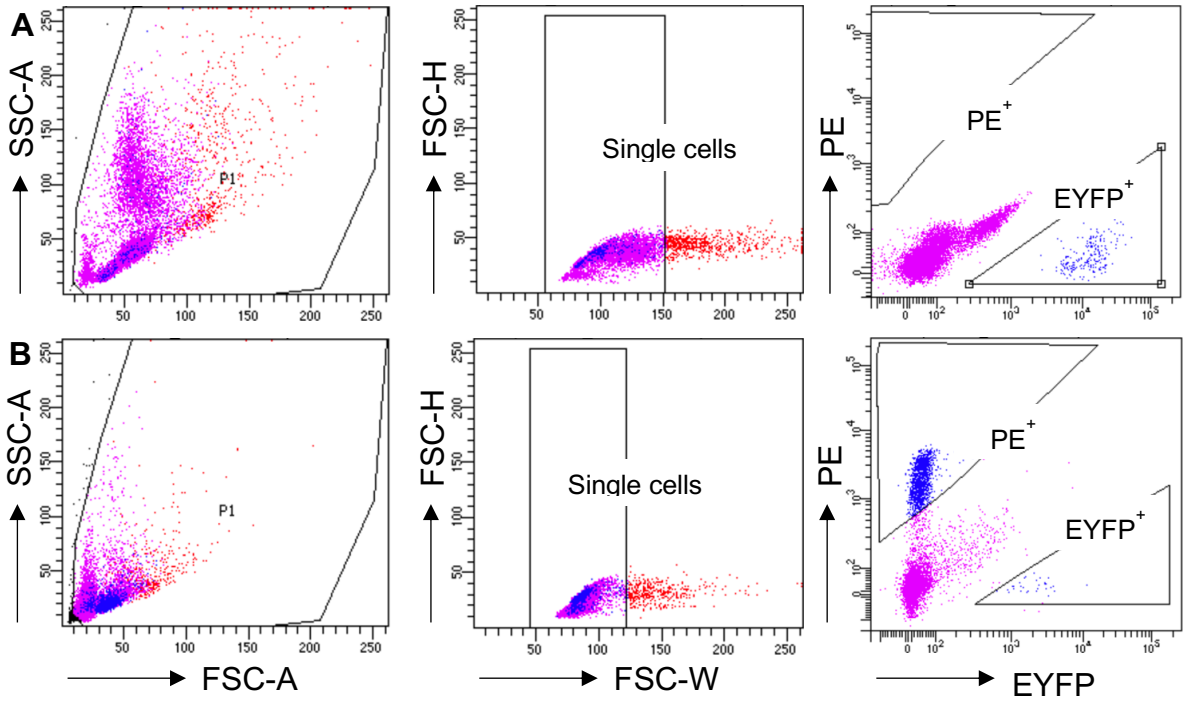

Figure 3-2 Gating strategy for FACS

A EYFP$^+$ cells were sorted by 1. excluding cell debris in a, 2. gating on single cells and 3. collecting EYFP$^+$ cells in the FITC channel (Ex.: 488 nm, Em.: 530/30 nm). The EYFP$^+$ gate was placed based on a Mcpt5-Cre$^-$ EYFP control (pMCs). **B** For the detection of PE-labeled anti-CD3ε$^+$ splenocytes, pre-gating on single cells is followed by collecting cell inside the PE$^+$ gate using the PE channel (Ex.: 561 nm, Em.: 582/15 nm). Em. – emission filter, Ex. – extinction wavelength, EYFP – enhanced yellow fluorescent protein, FITC – fluorescein thiocyanate, FSC – forward scatter, FSC-A – FSC (area), FSC-W – FSC (width), PE – phycoerythrin, SSC –, sideward scatter

3.6 Bulk RNA sequencing

Cell suspensions from CP, brain parenchyma, DM and peritoneal lavage were generated as described in 3.4. EYFP$^+$ cells were sorted as outlined in 3.5, following the gating strategy in Figure 3-2 for EYFP$^+$ cells. 50 cells were pooled in 2 µL lysis buffer (cf. 2.9), considered as one sample. Three peritoneal, three meningeal, five parenchymal and five CP samples were sorted and subsequently frozen at -80°C until send to the DRESDEN-concept Genome Center (DcGC), Dresden on dry ice for further processing. Messenger ribonucleic acid (mRNA) amplification, library preparation (ILL DNA Library Prep Nextera Low Input) and sequencing (75 cycles, 75 bp single-end, NextSeq 500, Illumina) was performed by the DcGC following a SMART-Seq2 protocol. Three samples were degraded and excluded from library preparation. One sample (“s3”) showed a low RNA yield and was excluded later due to saliences in further analysis.

Mapping and initial quality control (QC) metrics were performed by Dimitra Alexopoulou (DcGC, Dresden). With using the mm10 reference mouse genome, she identified more than 69% uniquely aligned fragments. The dataset was normalized with DESeq2 [186], resulting in a size factor normalized fragment count matrix which allows to discover differentially expressed genes (DEGs) among samples and served as the basis for Pearson correlation. This matrix I used for further analysis. In Qlucore Omics Explorer (QOE), the matrix is reduced by standard deviation filtering (s/s_{max} = 0.54) to the 160 most variable genes and log2 transformed. Dimensionality reduction resulted in the principal component analysis (PCA) and t-distributed stochastic neighbor embedding (t-SNE) plots in Figure 4-1. For the heatmap in Figure 4-2, a multi-comparison test (ANOVA) was used to detect DEGs over all tissues ($q < 0.05$).

3.7 Mast cell cultures for qPCR

3.7.1 Bone marrow-derived mast cells (BMMCs)

Mice were euthanized by a lethal dose of isoflurane inhalation, followed by cervical dislocation. The hint limbs were moisturized and cleaned using 70% ethanol. Skin and muscles were peeled off the leg bones. Left and right bones were harvested by dislocating the hip joints and removing the paws carefully to keep the joint heads intact. Under sterile conditions, the latter were cut off with sharp scissors and femur and tibia were separated. Both bones of one leg were placed in a sterile 0.5 ml microcentrifuge tube with a hole in the bottom and placed in a second, 1.5 ml microcentrifuge tube. This second tube contained 100 µl sterile 1xPBS in which the BM is collected by centrifuging at 16,000 g for 15 seconds. The collected cell pellet was carefully resuspended in 1 ml sterile 1xPBS and filtered through a cell strainer (pore size 100 µm) to remove bone remnants or cell aggregates. Containing erythrocytes were removed after precipitating at 365g and 4°C for 5 min by resuspending the precipitate with 1 ml erythrocyte-lysis-buffer. After incubation for 1 min at RT, the lysis was stopped by administering 9 ml sterile 1xPBS. Following a final centrifugation step at 365g and 4°C for 5 min, the BM cells of one mouse were resuspended in 20 ml culture medium (RPMI1640 supplemented with 10% (v/v) FCS, 1% (v/v) Penicillin/Streptomycin, 1% (v/v) sodium pyruvate and 50 µM β-mercaptoethanol, cf. 2.9) with 10 ng/ml recombinant murine IL-3 (PeproTech) and transferred in a 75 cm² cell culture flask. The BMMCs were cultured at 37°C and 5% CO2 under humid atmosphere for four weeks to enrich MCs. Flasks and medium were replaced twice a week. Prior to use, the cells were harvested by centrifugation at 365g for 5 min.

3.7.2 Cultured mucosal-like mast cells (cMMCs)

Cultured MMCs were generated according to [97]. Therefore, the 4-weeks old BMMCs generated in 3.7.1 were harvested and counted using a Neubauer counting chamber. $2.5x10^6$ cells were suspended in 5 mL culture medium (cf. 2.9), supplemented with 10 ng/mL transforming growth factor beta (TGFβ) 1 and 100 ng/mL stem cell factor (SCF), and transferred in each well of a 6-well plate. After 72h, the cells were harvested by centrifugation (365g for 5 min) for cell sorting.

3.8 Quantitative RT-PCR (qPCR)

3.8.1 Sorting

For qPCR, 12-weeks old Mcpt5-Cre EYFP female mice were euthanized and cell suspensions from peritoneal lavage, ear skin, spleen, DM, CP and whole brain were generated as described in 3.4. 50 $EYFP^+$ cells per tissue from Cre^+ mice were sorted for each sample. Cre^- littermates were used as unstained controls, processed identically and used to adjust the gates for FACS. First, 0.2-mL PCR SingleCap 8er-SoftStrips (Biozym, Wien) were prepared with 50 µL SingleShot cell lysis buffer (Bio-Rad SingleShot Cell Lysis Kit) in an RNase-free environment (UV-Cleaner Box, biosan). According to the manufacturer´s instructions, 48 µL buffer were mixed with 1 µL of the containing Proteinase K solution and 1 µL of the containing DNase solution. Cell sorting was done with a BD FACSAria™ III cell sorter using an 85-µm nozzle in a temperature-controlled environment at 4°C. In each well, 50 cells were sorted directly in the lysis buffer, either CD3-PE^+ splenocytes, $EYFP^+$ cells from all other tissues or unstained cells from bone-marrow cell cultures as described in 3.7. Subsequently, the tubes were separated as pairs of two, the caps closed and cells spun down quickly using a microcentrifuge with an 8-well stripe adapter to immediately freeze them at -20°C and avoid RNA degradation. As soon as all samples were sorted, the frozen tubes were processed following manufacturer´s instructions for the SingleShot cell lysis kit. Therefore, they went through the lysis program (Table 3-5) in the T3000 Thermocycler (Biometra). Subsequently, the lysed samples were frozen immediately at -80 °C and stored for less than 12 months until qPCR was performed.

Table 3-5 SingleShot cell lysis program

Temperature (°C)	Time (min)
25	10
37	5
75	5

3.8.2 RNA isolation

RNA from the frozen samples were isolated using the Quick-RNA™ Microprep Kit (ZymoResearch). Therefore, 50 µL pure lysis buffer from the previously used SingleShot Cell Lysis Kit (Bio-Rad) was added to each frozen sample to thaw it in an RNase-free environment (UV-Cleaner Box, biosan). The samples were mixed well by pipetting up and down. By adding 100 µL 100% ethanol (kept RNase-free since opening) , the isolation protocol starts according to manufacturer´s instructions. After mixing well again by pipetting up and down, the mixture was transferred into a Zymo-Spin™ IC Column in a Collection Tube and centrifuged at 16,000g for 30 s at RT. The flow-through was discarded. Before DNase treatment, the column was washed by applying 400 µL RNA Wash Buffer on the column and centrifuged again as in the previous step. The flow-through was discarded again and a mix of 5 µL DNase I in 35 µL DNase Digestion Buffer was added on each column. After a 15 min incubation time at RT, 400 µL RNA Prep Buffer were added on the column and centrifuged again at 16,000g for 30 s at RT. The flow-through was discarded and 700 µL RNA Wash Buffer were added, followed by centrifugation as before and discarding the flow-through. The washing step was repeated by adding 400 µL RNA Wash Buffer on the column and repeat the centrifugation step at 16,000g for 1 min to ensure complete removal of the wash buffer from the column. Finally, the column is transferred carefully in an RNase-free 1.5 mL tube in an RNase-free environment. By adding 15 µL RNase free water per step directly on the column and holding a few minutes at RT, followed by a further centrifugation step, the RNA was rinsed from the column matrix in two elution steps to increase yield. Both eluates were unified and either frozen immediately at -80 °C or preferably used directly for qPCR.

3.8.3 qPCR

For qPCR reaction, the Reliance One-Step Multiplex Supermix (Bio-Rad) was used in combination with the PrimePCR probe assays (Bio-Rad, Hercules) for the genes of interest (GOIs), listed in Table 3-6 and following the manufacturer´s recommendations. All genes for each sample were measured in duplicates in 10 µL reactions. Since the RNA yield out of 50 cells is low, the Relative Standard Curve Method according to [187] was used for calculation which allows to circumvent absolute RNA mass determination and saves eluted template.

Therefore, a **standard curve** was created to interpolate the unknown target quantities out of the measured C_T values (minimal cycle number at which the amplification reaches an exponential phase). For the standard curves, the PrimePCR templates of all genes (listed under Table 2-6) were unified to one "template mix" and diluted five times by 10^{-1} with nuclease-free water.

Standard curve dilution steps were either measured in duplicates or triplicates and in 10 µL reactions as well. On each plate, all tissue samples from maximal two mice and two genes were measured in singleplex reactions, resulting in four plates for each experiment.

To increase comparability between plates of one experiment, a so called "run control" (duplicate) was included on all plates. Therefore, a certain amount of "template mix" was added to the Rps18 (housekeeping gene) master mix and 10 µL of the mixture were added into each of the four plates twice. The PCR program is summarized in Table 3-7.

Table 3-7 qPCR program

Step	Temperature (°C)	Time (s)	Cycles
Reverse transcription	50	600	
Initiation	95	600	
Denaturation	95	10	50x
Annealing and Elongation	60	30	

3.8.4 Analysis

For the analysis, first, the four plates per experiment were first normalized with the help of the **run control**. In most experiments, the C_T value (mean of duplicate values) of the run control on the first plate (Rps18 and Cma1) showed a difference > 0.5 compared to plate two to four (Table 3-8). If this is the case, the C_T values are corrected (per plate) as shown in the following example:

Table 3-8 Determination of plate correction (exemplary for one sample)

	Plate 1 (*Rps18+Cma1*)	**Plate 2 (*Cd3e+Mcpt2*)**	**Plate 3 (*Mcpt4+Tpsb2*)**	**Plate 4 (*Kit+Fcer1a*)**
C_T Run control 1	20.127	22.289	22.302	22.271
C_T Run control 2	20.156	22.282	22.279	22.247
Median (all plates)	22.275			
Mean of duplicates	20.141	22.286	22.290	22.259
Difference mean to median	2.134*	-0.010	-0.015	0.016

Raw data	$C_T(Rps18)_1$	= 31.535	$C_T(Rps18)_2$	= 31.088
(of plate 1):	$C_T(Cma1)_1$	= 32.125	$C_T(Cma1)_2$	= 31.961
Corrected means:	$C_T(Rps18)_{mean}$	= (31.535 + 31.088)/2 – **2.134***		= 29.178
	$C_T(Cma1)_{mean}$	= (32.125 + 31.961)/2 – **2.134***		= 29.909

* **red**: difference mean to median > 0.5 (used to correct raw C_T values on each plate)

For the **standard curves** C_T values were only accepted when duplicates differed < 1.5 or triplicates (highest vs. lowest value) < 1 to plot their mean values. Standard curves were only plotted with at least four "ACCEPTED" data points, with "ACCEPTED" means:

- $C_T(Rps18)$ < 35 (mean) and < 36 (single raw)
- Duplicates (triplicates) of C_T with difference < 1.5 (< 1).

Plotted curves were only used for further analysis when

- slope m with $3.1 \leq m < 3.9$ and
- $R^2 \geq 0.95$.

Otherwise the corresponding gene expression was not determined and marked as "NA" (black-colored in Figure 4-8**B**). According to [187], gene expression for the **GOI** was calculated with help of the standard curve by interpolation and represented as fold difference to housekeeping gene expression (Table 3-9).

Table 3-9 Calculation of gene expression from standard curves (exemplary for one sample)

Standard curves (C_T means of duplicates)							
	1:10⁴	**1:10³**	**1:10²**	**1:10**	**m**	**n**	**R^2**
Rps18	30.208	25.623	21.846	20.458	-3.3026	42.698	0.9531
Cma1	32.853	28.373	24.718	21.839	-3.6697	47.129	0.9906
With y = m*x + n, where m and n result from standard curve, y represents the measured C_T value and x represents the amount of template, x is interpolated from the C_T values for housekeeping gene and GOI separately. Non determinable C_T values (no gene expression) are considered to be 50 as 50 is the maximal number of cycles.							
$C_T(Rps18)_{mean}$ = 29.178			x = (y – n)/m = (29.178 – 42.698)/(-3.3026) = 4.09				
$C_T(Cma1)_{mean}$ = 29.909			x = (y – n)/m = (29.909 – 47.129)/(-3.6697) = 4.69				
Fold difference (*Cma1*)			**= 4.09/4.69 = 1.15**				

3.9 Clearing and Light sheet microscopy

3.9.1 Clearing

I developed an appropriate clearing protocol over years, resulting in a final version which combines most aspects of the organic clearing protocols by [188] and [58]. The initial step is the fixation via transcardial perfusion. Therefore, 25 mL 1xPBS containing 10 U/mL heparin (RT) were perfused, followed by 150 mL ice-cold 4% PFA/PBS solution. The mice were decapitated and scalped, facial muscles and lower jaw removed. The skull was postfixed for two hours in 4% PFA/PBS on ice and afterwards decalcified in 50 mL of a 0.225 M ethylenediaminetetraacetic acid (EDTA) in PBS, by shaking for two days on a platform shaker. After washing the skulls three times for 30 min in 1xPBS (shaking), the brains were isolated carefully from the softened skull bone. They were subsequently transferred in permeabilization buffer in a 5 mL reaction tube. Following one day of incubation by gentle shaking at 37°C in a shaking incubator, the permeabilization buffer is replaced and enriched with an AbberiorStar635P FluoTag®-X4 anti-GFP (Nanotag technologies) 1:1,000. The brains are incubated in the nanobody-containing permeabilization buffer for three to five days at 37°C by gentle shaking before the solution is changed. When changed, the solution is enriched with the nuclear dye TO-PRO™-1 iodide (Thermo Fisher Scientific), 1:5,000. After further incubation for at least five days at 37°C (gentle shaking), the brains were washed. Therefore, they were transferred in 14 mL reaction tubes filled with 0.1% (v/v) Triton X-100 in PBS. For washing, the tubes rotated, using the neoLab-Rotator (neoLab, Heidelberg), at RT for two hours. The washing was repeated two times and once overnight. The next day, washing is continued as before by using only 1xPBS, three times per day and once overnight. After washing, the brains were dehydrated in a volume of 14 mL each step and by continuous rotation. The first day, brains were transferred in 50% ethanol (EtOH) in distilled (dist.) water. Following overnight incubation, they are transferred once a day in 70%, EtOH/dist. water, 100% EtOH and once more 100% EtOH (absolute), before delipidated for three to four hours in 5 mL dichloromethane (DCM). Afterwards, they were carefully transferred in 5 mL pure ethyl cinnamate for clearing. When incubated for one day at RT (rotating), the ethyl cinnamate is exchanged. Cleared brains were stored in 5 mL ethyl cinnamate in a desiccator over silica gel in a humidity-reduced environment until imaged.

3.9.2 Light sheet microscopy

Light sheet fluorescence microscopy (LSFM) of the cleared mouse brains was conducted with the Ultramicroscope II by LaVision Biotec (Figure 4-10) or the UltraMicroscope Blaze by

Miltenyi Biotec (Figure 4-11 to Figure 4-15). Prior to imaging, the light sheets were correctly oriented using the alignment tool provided by the manufacturer. Filter settings for the detecting of AbberiorStar635P and TO-PRO™-1 is displayed in Table 3-9. The brain is carefully fixed in the sample holder by using cleared phytagel blocks, generated as described in [189]. Therefore, two blocks were placed in front of the screws and the brain was placed in between (Figure 3-3). Cavities in the phytagel allow to pocket the olfactory bulb and the spinal cord inside the blocks. By gently tighten the screws of the specimen holder, the brain is fixed and the image will not be disturbed by shadows of the screws.

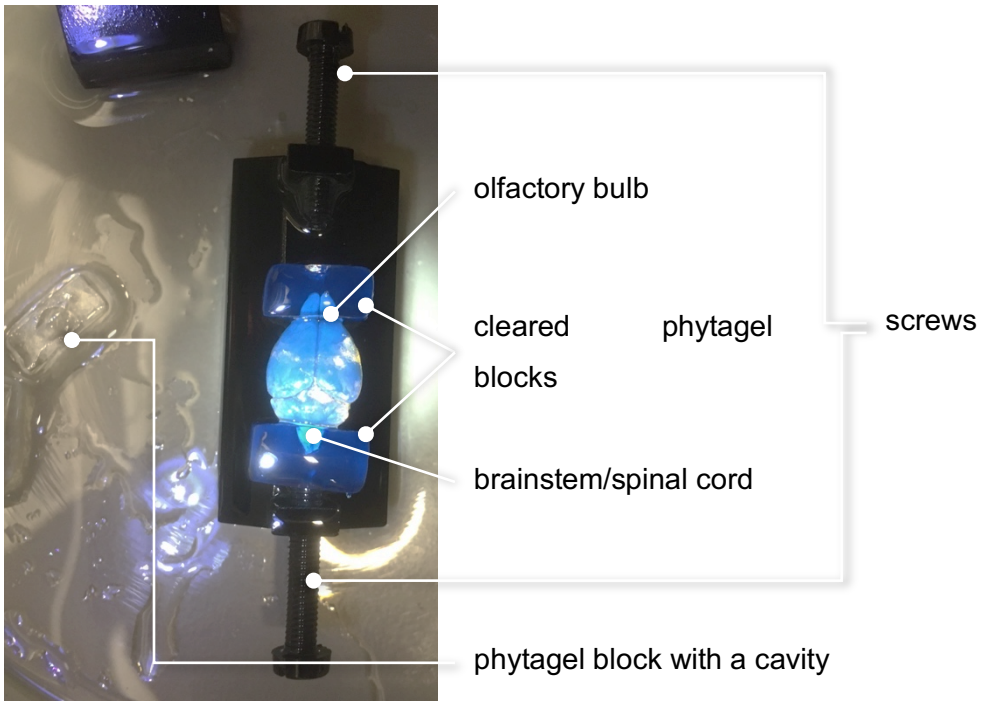

Figure 3-3 Fixation of the brain on the specimen holder

The brain is carefully fixed inside the screws of the specimen holder, protected by cleared phytagel blocks. Olfactory bulb and brain stem/spinal cord are placed in cavities inside the gel blocks. The brain is orientated with the midline on a virtual line between both screws. For better visualization of the cleared, transparent components, a UV light is used for illumination.

Images for Figure 4-11 to Figure 4-15 were acquired using the 1.1x or 4x objective and light sheets from both sides with 80% sheet width (dynamic focusing with recommended step size). The sheet NA was adjusted until light sheet thickness of 5 – 6.1 µm was reached. Tiles of a tile scan have an overlap of 10% (fixed blending, blend over mosaic). Step size in Z direction was 4 µm. Laser power of the SuperK FIANIUM white light laser (NKT Photonics) was set to 60% (78 MHz) and exposure time of the camera to 100 ms.

Table 3-10 Filter settings for LSFM

Fluorochrome	Excitation [nm]	Emission [nm]
AbberiorStar635P	640/30	680/30
TO-PRO™-1	510/20	540/20

3.10 Brain harvesting for brain slices

Brains were harvested and prepared for cryosections as followed. Mice were euthanized in a carbon dioxide-filled chamber as described in 3.4. They were transcardially perfused using 100 mL ice-cold 4% PFA in PBS and the isolated brain was post-fixed for two hours in the same fixative on ice (cf. 3.4.2 and 3.9.1). Afterwards, the brains are transferred in a 30% (w/v) sucrose/PBS solution and kept for at least three days at 4°C (reporter mouse brains protected from light). When sunken to the bottom of the solution, the brains were frozen using methyl butane, cooled down to -80 °C. Therefore, they are carefully placed in a plastic pan filled with cooled methyl butane. When completely chilled (no bubbling, homogenously white color), the brains were kept at -80 °C until sectioned.

For sectioning the brains, they were slowly thawed in the cooled chamber (-22 °C) of the Leica CM1650 cryotome. They were properly oriented (coronal, sagittal, horizontal) and frozen on the sample holder (-20 °C) using tissue freezing medium (Leica Biosystems, Wetzlar). 30 - 50 µm sections were cut and transferred with a brush on Menzel-Gläser SUPERFROST® PLUS slides (Menzel, Braunschweig). Brain sections were air-dried and directly used or stored for one day at 4 °C, protected from light.

3.11 Fluorescence immunohistochemistry staining

For fluorescence immunohistochemistry (IHC), either brain sections (as prepared in 3.10) or DM whole mounts were used. Last mentioned were prepared as described in 3.12.1 using 25 - 50 mL fixative for perfusion.

3.11.1 NeuroTrace™ and nuclear staining of brain slices

Air-dried brain sections were moistened with 1xPBS for 30 min at RT. Following permeabilization for 10 min at RT using 0.1% Triton X-100 in PBS, the slides are washed carefully two times for 5 min with 1xPBS. NeuroTrace™ (Thermo Fisher Scientific, Waltham, USA) was diluted 1:200 in 1xPBS and subsequently used to incubate the specimen for 20 min

at RT. The slides are washed afterwards with 0.1% Triton X-100 in PBS for 10 min at RT, followed by 1xPBS for two hours. TO-PRO™-3 iodide (Thermo Fisher Scientific, Waltham, USA), a nuclear dye, was diluted 1:2,000 in 1xPBS and applied to the sections for 15 min at RT. Finally, the slides were washed with 1xPBS and mounted with Vectashield® Mounting Medium (Vector laboratories, Burlingame) and a cover glass.

Without staining NeuroTrace™, Hoechst 33342 was used for nuclei detection. Therefore, the sections were moistened with 1xPBS and incubated for 5 min with Hoechst 33342 1:1,000 in 1xPBS at RT. After washing, the sections were mounted as described above.

3.11.2 Anti-c-kit and nuclear staining of dura mater

Air-dried DM whole mounts were moistened with the blocking buffer, containing 2% (v/v) normal goat serum, 1% (v/v) bovine serum albumin (BSA) and 1xPBS. The primary rat anti-mouse CD117 antibody (Biolegend, San Diego) was diluted in the blocking buffer and the mixture was applied on the specimen for 2 hours at RT in a wet chamber. The slides were washed three times for 5 min with 1xPBS before the secondary antibody, a goat anti-rat Alexa Fluor® 647 (Jackson ImmunoResearch, West Grove), 1:100 diluted in the blocking buffer was added. After 60 min incubation, the slides were washed three times for 5 min with 1xPBS and Hoechst 33342, diluted 1:1,000 in 1xPBS was added and incubated for 15 min at RT. After a final washing step with 1xPBS, the specimens were mounted with Vectashield® Mounting Medium (Vector laboratories, Burlingame) and a cover glass.

3.11.3 Staining of the dura mater with fluorescently-labeled avidin

The air-dried DM whole mounts were permeabilized for 10 min with an ice-cold methanol-acetone mixture (1:1). After washing for 5 – 10 min with 1xPBS, 100 mM glycine in 1xPBS were added for 30 min at RT. Following washing with 1xPBS, streptavidin (Jackson ImmunoResearch) is dissolved in 1xPBS to 0.5 µg/mL and applied on the slides, where it incubates for 60 min. Subsequently, fluorescently labeled avidin (generated as described in 2.4) was diluted 1:1,000 in 1xPBS and applied on the slides for 60 min at RT. Following a further washing step, Hoechst 33342, diluted 1:2,000 in 1xPBS, is added on the slide and incubated for 15 min at RT. After a final washing step with 1xPBS, the slides were mounted with Vectashield® Mounting Medium (Vector laboratories, Burlingame) and a cover glass.

Table 3-11 Filter setups in the widefield microscope DMI8 for detection of the fluorophores

Fluorochrome/Fluorophor	Ex. Wavelength [nm]	Ex. Filter [nm]	Em. Filter [nm]	DC [nm]
Hoechst 33342	385	391/31	425/30	415
NeuroTrace™	435	436/28	473/22	459
Alexa Fluor® 488	460	480/40	527/30	505
tdTomato	550	479/33	519/25	500
TO-PRO™-3	594	554/24	594/32	572
DyLight™ 649/ Alexa Fluor® 647	635	638/32	695/58	660

DC – dichroic mirror, Em. – emission, Ex. – excitation

3.12 Sequential Histological staining

3.12.1 Tissue preparation

Sequential **A**stra **b**lue **S**afranin **O** (AB/SO) staining can be conducted using either Astra blue (AB) or Alcian blue. I decided to use AB due to highly selective MC staining characteristics without giving background [79].

AB/SO staining of DM or brain slices was done as described in Strobel *et al.* 1981 [110], only slightly modified. First, the tissues were fixed in vivo, directly after euthanizing the mice (cf. 3.4). Therefore, 25 mL of an ice-cold 4% PFA solution (cf. 2.9) was transcardially perfused (Figure 3-4**A**). The DM was isolated carefully in 1xPBS from the inside of the calvaria and transferred on a glass slide, where it is flattened and air-dried (Figure 3-4**B**). The whole brains were isolated, frozen and sectioned as described in 3.10. For combined IHC and AB/SO staining, the cover glasses from already imaged slices or DM explants from section 3.11 were carefully removed and specimens washed with 1xPBS followed by air-drying at 4°C.

3.12.2 Tissue staining

Carnoy´s fixative (cf. 2.9) was prepared freshly and air-dried specimen were incubated for 60 min to fix the tissue in a strongly acidic environment (Figure 3-4**C**). Subsequently, they were stained in the first dye, Astra blue solution, for 30 min, washed in 0.7N HCl by moving up and down carefully and stained in the second dye, safranin O solution, quickly (< 30 s). Slides with specimen were transferred directly in an ascending ethanol series (50%, 70%, 80%, 90% in distilled water), where they dehydrated for 5 min in each dilution (not shown in Figure 3-4). Before they were transferred in absolute ethanol, they are quickly dipped in the Orange G solution, which provides a better contrast and helps the slide scanner to identify and focus the samples on a slide (Figure 3-4**D**). After final dehydration in absolute ethanol for 5 min, the

slides stay in Protaqs® Clear Intermedium for 10 min to reach transparency. Finally, they air-dried and were mounted in Protaqs® PARAmount using a cover glass.

As soon as the mounting medium was hardened, the slides were scanned with the NanoZoomer slide scanner (Hamamatsu Photonics, Shizuoka), by Michael Seidel (Institute of Pathology, University Hospital Magdeburg). Whereas the Orange G stains the collagen fibers pale yellowish to provide a clear tissue background staining, both Astra blue and Safranin O stain the mast cells (Figure 3-4**E**). The combination of both cationic dyes and by additionally using the acidic Carnoy´s solution as a fixative allow to distinguish 'blue' MMCs and 'red' CTMCs [110], as described in more detail in 1.3.2.2.

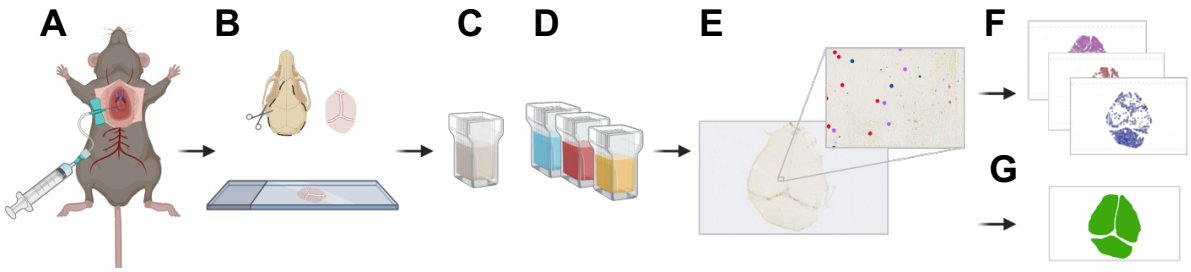

Figure 3-4 Sequential mast cell staining and quantification

For sequential AB/SO staining of MCs, the mice are transcardially perfused with 4%PFA solution to fix the MCs *in situ* (**A**). **B** DM is isolated from calvarial skull bone and flattened and dried on a slide. **C** The dried specimens are fixed in strongly acidic Carnoy´s fixative. **D** Slides are stained by three dyes, AB, safranin O and Orange G and subsequently dehydrated. **E** The stained meninges are imaged using a NanoZoomer slide scanner (Hamamatsu Photonics) and converted to .psb files. Photoshop allows to count "red" (SO^+), "blue" (AB^+) and mixed type ($ABSO^+$) MCs manually on separate layers and mark the counted area. These layers can be exported for automatic cell counting with Imaris (**F**) and area quantification in Fiji (**G**). Created with Biorender.com

3.12.3 Mast cell counting in dura mater

In order to quantify the AB/SO stained cells in the murine DM, they cells were counted manually. Therefore, all scanned images were opened in NDP.view 2 and exported from the slide scanners original file format .ndpi to full-resolution .jpeg image files. In Photoshop, layers for each cell type ("red", "blue", "red-blue") were added by creating a .psb file. All cells were counted and hence, marked in the corresponding layer (Figure 3-4**F**). Additionally, one layer per area ("right hemisphere-covering", "left hemisphere-covering", "cerebellum-covering") was added and the counted areas (excluding regions in which the thin tissue overlaps, as along the edges and sinusoid structures) were filled (Figure 3-4**G**). All of these areas were exported separately in .jpeg files of original size. In Fiji, images were binarized and a scale bar based

on pixel size is inserted (10,893 px == 5 mm). Areas were calculated using the “analyze particles” tool. For determine the cell numbers, binarized images of cell counts were saved in .tiff image format and converted in an .ims file to open with Imaris (Bitplane). In Imaris, the spot detection wizard tool was used (XY diameter = 0.02 µm, mean and center intensity 255, quality = 50%) to count the marked cells. Finally, the cell counts per mm^2 were calculated for each cell type. Distribution patterns were created by exporting snapshots of the detected spots in Imaris, separated again by cell types (Figure 4-25**C**).

The decision whether a stained MC is ‘red’, ‘blue’ or ‘red-blue’ was slightly different between the first (section 4.6) and second experiment (section 4.8). In 4.6, only the cell color was taken into account. ‘Red’ MCs were considered to be ‘red’ once they are mostly red stained. The same holds true for ‘blue’ cells. ‘Red-blue’ was referred to cells, either stained clearly in both colors or which show no distinct red or blue coloring (pale, shaded). For 4.8, the cell morphology was additionally taken into account. ‘Red’ cells were clearly red, with an intact and distinct cell boundary. In contrast, ‘blue’ cells were exclusively blue and a clear boundary often got lost. Some of the ‘blue’ cells show a ruptured morphology losing a typical cell shape. All cells which could not be categorized as ‘red’ (intact) and ‘blue’ (degranulated), were considered to be ‘red-blue’ (partially degranulated).

3.13 Single cell RNA Sequencing

Single $EYFP^+$ cells from Mcpt5-Cre EYFP mice were sorted (described in 3.5) as one cell per well in twin.tec 96-well PCR plates (Eppendorf, Hamburg) containing 2 µL lysis buffer. From four female Mcpt5-Cre EYFP mice, 46 single cells and a bulk sample (50 cells) were collected. The plates were spinned down quickly (300g) and sealed with MicroAmp™ Optical Adhesive Film (Thermo Fischer Scientific). Library preparation and sequencing was conducted by the DRESDEN-concept Genome Center (DcGC), Dresden. Briefly, DNA libraries were generated using an Illumina® DNA Library Prep Tagmentation LV kit. SMART-Seq2 [190] was performed with an Illumina NovaSeq 6000 (Illumina Inc., San Diego) and fastq files were generated using the bcl2fastq2 2.20.0 software (Illumina Inc., San Diego).

The resulting fastq files were further processed by GeneVia technologies (Tampere, Finland). Cutadapt v2.10 was used to trim Illumina Nextera adapters [176]. In addition, base-quality trimming retained reads with a minimum PHRED score of 20, minimum length of 20 bases and maximum error rate of 10%. The quality of raw and trimmed reads was inspected using FastQC, version 0.11.8 [177] with observing no saliences.

Trimmed reads were aligned using STAR (v2.7.8, using default parameters) in paired-end mode to produce one BAM file per cell [181]. A custom reference was generated from the NCBI GRCm38 reference genome and ERCC spike-in sequences using STAR (--runMode genomeGenerate).

The count per gene matrix was obtained using featureCounts in the R package Subread (v2.4.3, -t exon) [180].

The cell-gene matrix was subsequently filtered using the R package Seurat (v4.0.5) [179] with parameters to keep cells with mitochondrial read 0.1-1.6%, number of detected genes 3000-5000 and number of counts per cell 0.9-1.75 million (Figure 3-5). The filtering resulted in keeping 133 cells (28 - 42 cells per mouse) out of the initial 184 cells and 22,552 of the initial 55,510 genes.

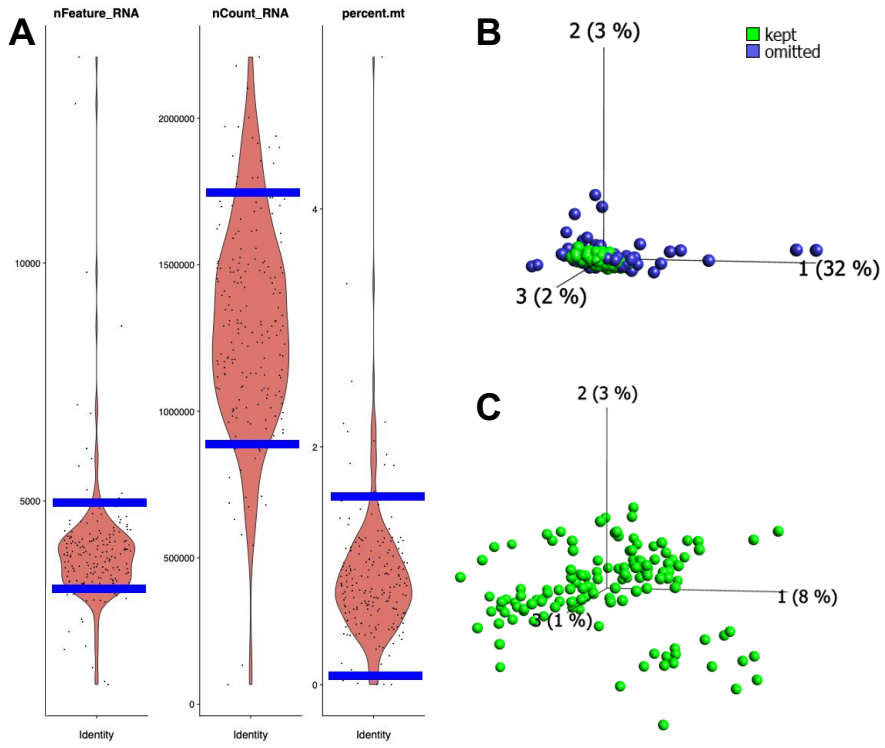

Figure 3-5 Pre-filtering of the single cells using Seurat

A The violin plots (red) show the distribution of single cells (presented by a black dot) regarding number of genes per cell (nFeature_RNA), number of raw counts per cell (nCount_RNA) and percentage of mitochondrial reads per cell (percent.mt). Cells below and above the horizontal lines (blue) were omitted by Seurat (parameters customized for the datasets). **B** The three-dimensional PCA plot visualizes, how the dataset 'opens' when outliers (dark blue) are removed (**C**).

For further analysis, I used the filtered gene count matrix file (provided by GeneVia), containing genes in rows and cells in columns, to load in Qlucore Omics explorer (QOE). The dataset was collapsed (duplicate exclusion) and variance filtering was applied with $s/s_{max} = 0.35$.

For identifying the cell clusters in my single cell dataset, I used the publicly available immune cell dataset GSE37448 [106, 191]. Two-group comparison ($q \leq 0.05$) in QOE between the 20 MC subsets (esophageal, peritoneal, skin, tracheal, tongue) and NK cells identified 205 genes upregulated in NK cells (termed “NK cell signature genes”) and 281 genes upregulated in MCs (termed “MC signature genes”). To determine further immune cell signatures, a multi-group comparison test (ANOVA, $q < 1x10^{-26}$) of all immune cell subsets revealed genes almost exclusively upregulated in B cells, basophils, epithelial cells, fibroblast reticular cells (FRCs) and γδT cells. From all of these individual signature gene subsets, gene lists were created (Supplemental Table 1 and Supplemental Table 2). These lists were used to mark genes in the volcano plot in Figure 4-26**E**.

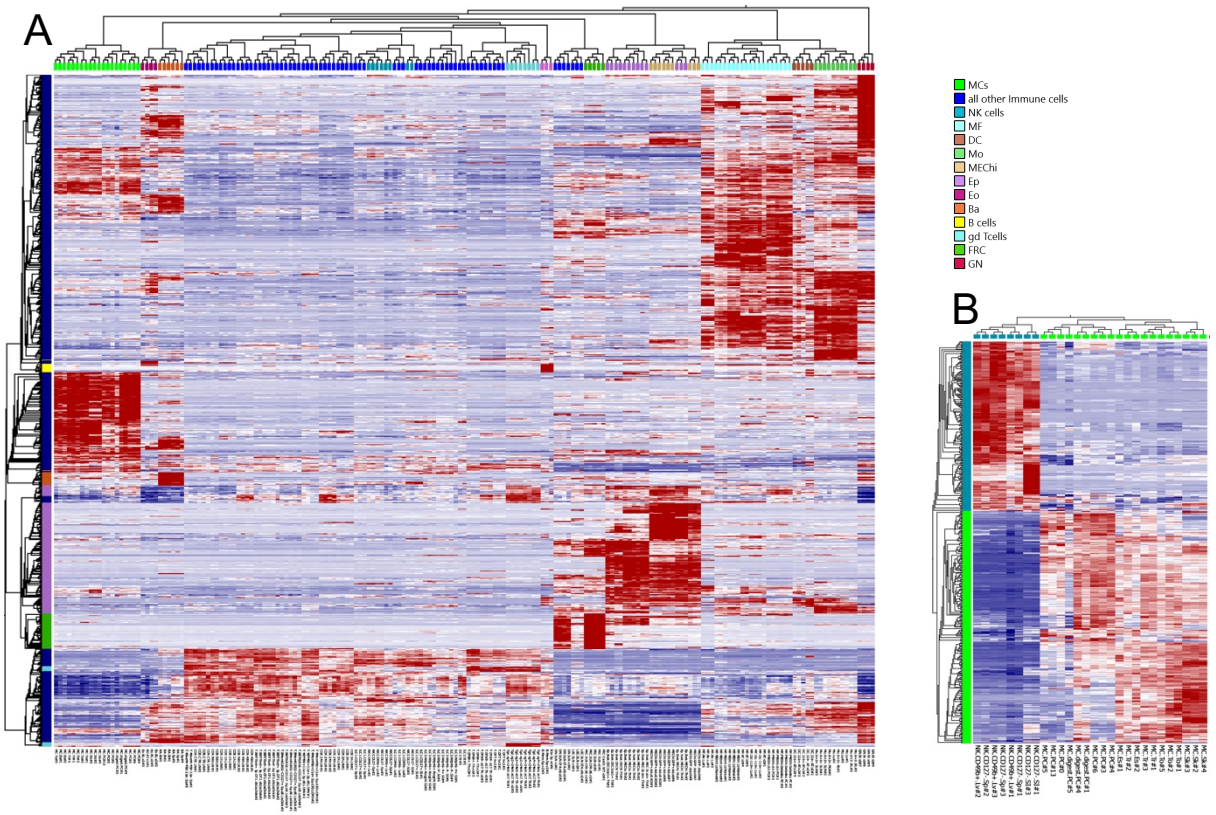

Figure 3-6 Immune cell signatures

Immune cell signature gene lists were generated based on the dataset GSE37448 [106, 191]. **A** Multi-group comparison (ANOVA, $q < 1x10^{-26}$) over all tissues revealed unique gene sets upregulated preferably in certain immune cell subtypes, as B cells (yellow), basophils (orange), epithelial cells (purple), fibroblast reticular cells (FRCs, green) and γδT cells (cyan). The gene lists are available in

Supplemental Table 1. **B** To determine the differences in gene expression between MCs (light green) and NK cells (turquoise), a two-group comparison (T-Test) was performed ($q \leq 0.05$). MC signature genes (light green) and NK cell signature genes (turquoise) were exported as gene lists as well (Supplemental Table 2). Ba – basophils, DC – Dendritic cell, Eo – eosinophils, Ep – thymic epithelial cells, FRC – fibroblast reticular cells, GN – granulocytes, MF – Macrophages, MEChi – thymic medullary epithelial cells, Mo – Monocytes

4 Results

4.1 Transcriptional profiles of cerebral EYFP$^+$ cells from MC reporter mice

As peripheral MCs are located on environmental surfaces and barrier regions, CNS MCs populate the brain barrier regions, the blood-brain barrier (BBB) of the brain parenchyma and the blood-cerebrospinal fluid barriers (BCSFB) of the CP and the meninges [40, 41, 53, 165, 170, 192].
Aiming to investigate tissue-derived effects on MCs in these three CNS barrier regions that may results in a MC heterogeneity, as already known for macrophages [15, 44], we isolated EYFP$^+$ cells from CP, DM and brain parenchyma of Mcpt5-Cre EYFP reporter mice (Figure 4-1). Additionally, peritoneal EYFP$^+$ cells were used as CTMC control to compare with.

As depicted in a representative dot plot in Figure 4-1**A**, 50 EYFP$^+$ single cells were sorted directly into lysis buffer and were immediately frozen. The further processing, like library preparation, sequencing and fragment alignment was realized by the DRESDEN-concept Genome Center (DcGC), Dresden and initial quality control (QC) metrics were performed by Dimitra Alexopoulou (DcGC, Dresden). Three of the 16 samples could not be used for library preparation due to low RNA yield or degradation and were omitted. To visualize the relation between the remaining 13 samples, Dimitra performed a Pearson correlation based on the normalized counts. In the resulting Pearson correlation matrix plot (Figure 4-1**C**), closely correlated samples, which represent similar expression values for the genes, were brought into proximity. This is indicated by a connection line on top of the plot and a dark blue color. Correlation coefficients are color-coded (dark blue: strong correlation, light blue: low correlation). Strongest correlation could be observed between the CP samples (light green), with coefficient values higher than 0.99. Three of the parenchymal samples (grey) correlated comparably strong, but all parenchymal samples together had correlation coefficients higher than 0.75. The two peritoneal control samples (blue) showed high similarity with one meningeal sample (red) whereas the other two meningeal samples were in between, correlating with coefficient values of up to 0.72 with the peritoneal-and-meningeal cluster and with up to 0.6 with the parenchymal and CP samples.

For further data analysis, I used the visualization and analysis software Qlucore Omics Explorer. Based on the DESeq2 normalized counts matrix, generated by Dimitra, I created a three-dimensional principal component analysis (PCA) plot, which is shown in Figure 4-1**D**. Whereas all samples clustered clearly by tissue, the meningeal sample “s3” separated from all

the others. Since s3 already showed less detected genes per million fragments than all the others in a previous QC plot, which mirrored less complexity of the sample (Figure 4-1**B**), I decided to omit s3 from further analysis. The resulting t-SNE plot (Figure 4-1**E**), including three CP, five parenchymal, and two meningeal and peritoneal samples each, displayed a strong clustering by tissue and a clear separation between the tissue samples. As it was apparent already in the Pearson correlation, the CP and parenchymal samples were closer related and more distinct from the meningeal and peritoneal, which formed a separate cluster.

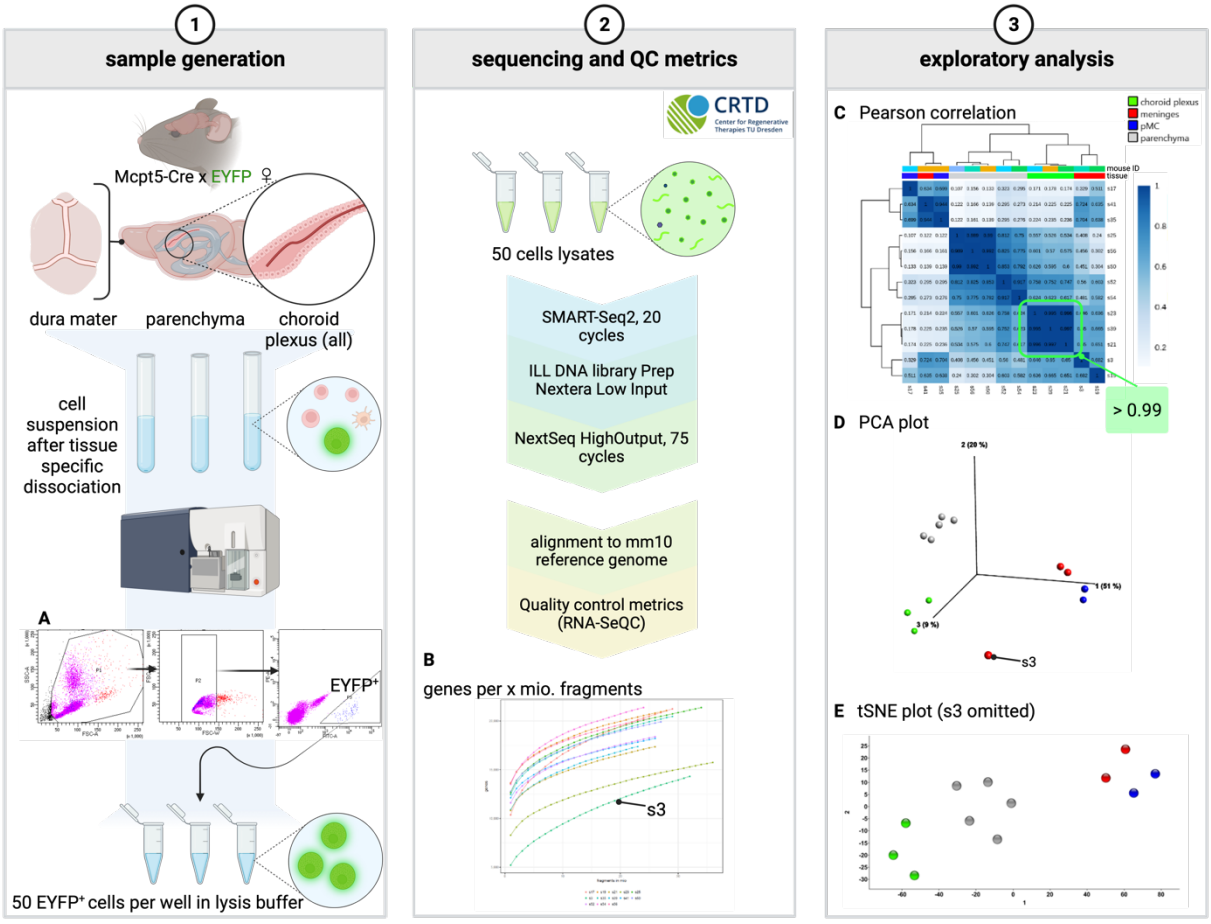

Figure 4-1 Transcriptome analysis of cerebral EYFP⁺ cells

The above figure displays the whole process of tissue dissociation and FACS (1), sequencing, quality control analysis (2) and exploratory data analysis (3) of bulk RNA sequencing from EYFP⁺ cells of the three brain regions (DM, CP, parenchyma) and the peritoneum (control, not shown) of Mcpt5-Cre⁺ EYFP mice. **A** shows the gating strategy for sorting. First, cell debris was excluded (SSC-A vs. FSC-A). Second, plotting FSC-H vs. FSC-W was used to identify single cells. In the third plot, the target cell gate included only EYFP⁺ cells and was set based on a Mcpt5-Cre⁻ EYFP control mouse. In **B**, genes per million uniquely aligned fragments were plotted for all 13 sequenced samples. The resulting 'complexity plot' showed lowest complexity for the meningeal sample 3 (s3) which was most different from all other samples. **C** The Pearson correlation histogram of all samples displayed strongest correlation between the CP (light green) samples (> 0.99). Parenchymal samples (grey) clustered with a correlation coefficient > 0.75. Meningeal (red) and peritoneal (pMC, blue) samples together formed a third, but less

distinct correlation cluster. Correlation coefficients are color-coded (dark blue: strong correlation, light blue: low correlation). The resulting three-dimensional PCA plot in **D** showed a clear separation between the tissues but a strong clustering of samples from the same origin. Meningeal (red) and peritoneal (blue) samples were close with greatest distance to CP samples (green). Only s3 separated from all others and was therefore omitted in the final t-SNE plot (**E**). Created with Biorender.com.

To discover differences in the transcriptome between the tissue clusters, I compared all samples via a multi-comparison analysis (ANOVA) over all tissues. 131 differentially expressed genes (DEGs) over all tissues showed significant differences with an adjusted p-value (q-value) below 0.05 and were displayed in a heatmap in Figure 4-2, the deeper the color, the higher the expression of the certain genes in a sample. Hierarchical clustering of the samples showed, in accordance with the dimensionality reduction plots in Figure 4-1**D** and **E,** a clear clustering of all samples from the same tissue or location. The closest inter-tissue relation was observed between the meningeal EYFP$^+$ cells and the pMCs whereas parenchymal and CP cells showed more differences, respectively.

More than one third of the listed genes were upregulated in parenchymal and CP EYFP$^+$ cells compared to the meningeal and peritoneal samples. Among them, there were many genes which maintain brain homeostasis and facilitate the transport of certain substances: *Enpp2*, *Ttr* and *Kl* (highly expressed in CP and surrounding CSF), six SLC transporter genes, *Ptgds* (responsible for brain maturation and homeostasis), *Clu* (a chaperone coding gene), Car genes (responsible for fluid secretion, pH adjustment), *Otx2* (involved in brain development) and P2ry genes (coding for purinergic receptors). Immune cell genes as *Itm2a*, Klr genes, *Ncr1*, *Gzma*, *Ly6c2* and *Ccl3* and *Ccl4* were upregulated mainly in the meningeal and parenchymal samples and at least some of them also in one CP sample. Others, as *Tnf* or *Egr2* were upregulated in all except of the CP samples, which showed very low expression of these genes.

Surprisingly and in contrast to the strong correlation of the CP samples observed in the Pearson correlation, there were 17 out of the 131 genes, which were highly expressed in one of the three CP samples, but close to zero in the other two. Interestingly, these genes were highly expressed in all tissues and samples, except of these two CP samples. Among them, there were typical MC signature genes, like *Cpa3, Cma1, Mcpt4, Tpsb2* and *Tpsab1*, all coding for MC proteases as summarized in Table 1-1. Additionally, it affects the genes *Egr1, Egr3, Fos, Junb* and *Nr4a1*, which code for transcription factors and *Ccl7*, coding for a chemokine with heparin-binding ability, secreted by, amongst others, MCs as well [193] (cf. Supplemental Figure 1).

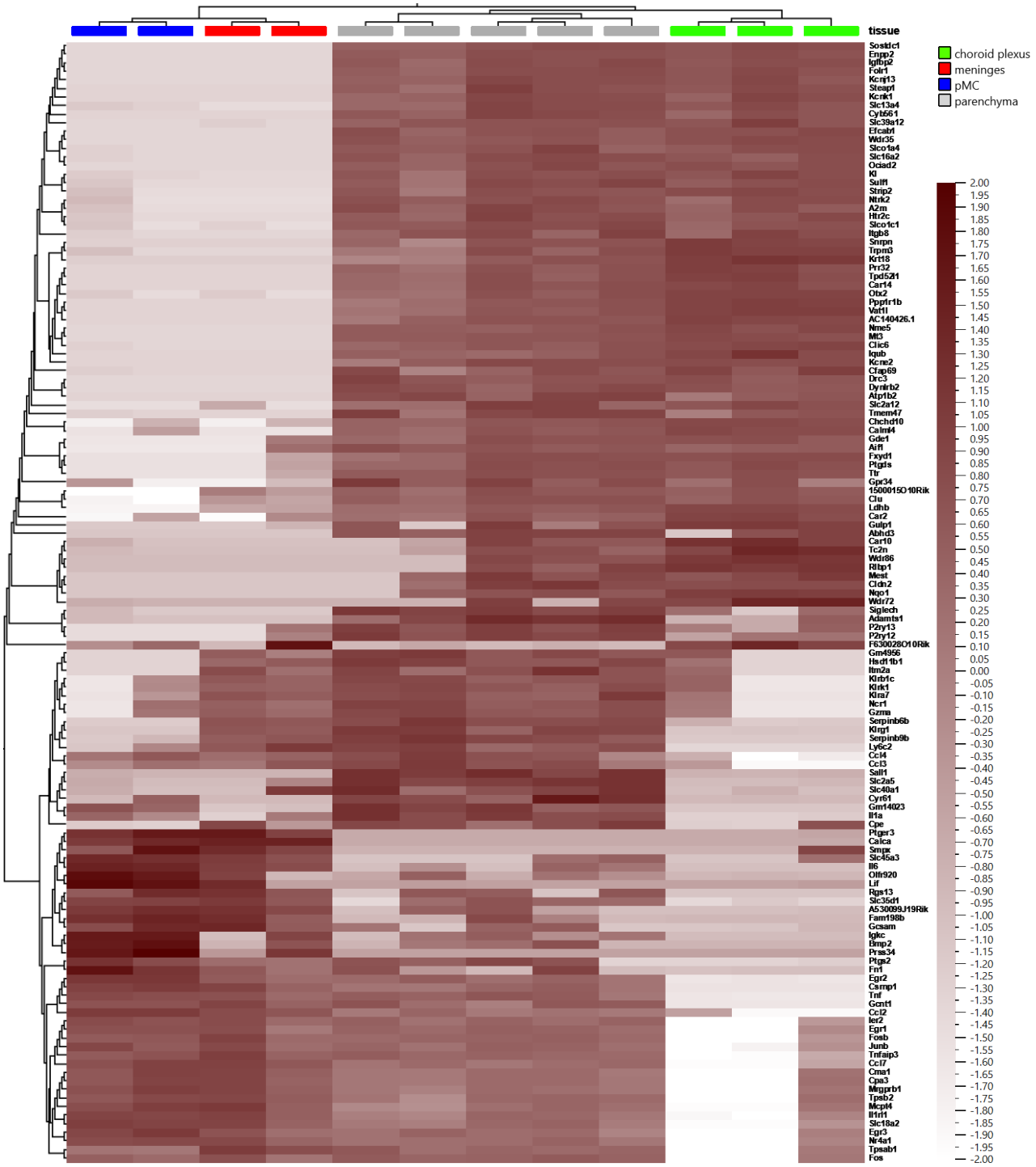

Figure 4-2 Heatmap of 131 DEGs over all tissues

The heatmap comprises of differentially expressed genes (DEGs) over all four tissues with highest significance (> 0.05) when multiple comparison statistical test (ANOVA) was applied in Qlucore Omics Explorer. The normalized color-coding revealed that the lowermost 17 genes are not expressed at all in two of the three CP samples. Official gene names were used.

Next, I created bar charts for all the MC genes separately, aiming to see the dimension of the differences in gene expression (Figure 4-3). Therefore, I plotted the normalized counts for each

sample, grouped by tissue. The resulting charts revealed that MC gene expression could not be detected in these two CP samples at all. Interestingly, the expression was also low in the third CP sample and in all parenchymal samples, compared to MC gene expression in the peritoneal control. *Tpsab1* expression was low in all tissues except of the meninges. Of note, highest MC gene expression was observed in the peritoneal and meningeal sample of the same mouse (#5).

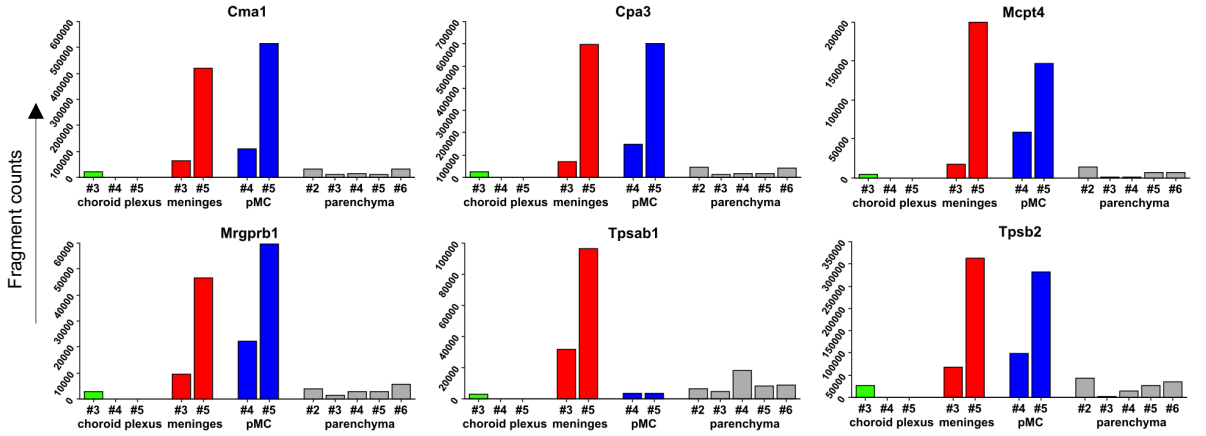

Figure 4-3 MC genes expressed in EYFP⁺ cells at brain interfaces and in peritoneum

For six MC genes of the 17 lowermost genes from the above heatmap, the DESeq2 (size factor) normalized fragment counts were displayed as bar charts. X-axis shows sample number and tissue type. Color code represents the tissue type and is consistent with Figure 4-2.

4.2 Validating the expression of selected target genes

4.2.1 Establishment of appropriate protocols

Since transcriptome profiling mirrors temporary cell states in ongoing cell transitions [194], I established a protocol for quantitative reverse transcription polymerase chain reaction (qRT-PCR). To repeat and verify the above findings, I applied this new method on 50 cells isolated from each tissue. In addition, I established a procedure to determine the estrous cycle stages of the individual mice, to meet the challenge of estrous cycle fluctuations in female mice which potentially affect the transcriptome.

4.2.1.1 Establishment of a stable qPCR protocol for 50 cells

Aiming to directly compare both setups, the RNA sequencing and the qRT-PCR, the tissue dissociation and cell sorting procedure was exactly the same as for the bulk RNA sequencing above. For RNA isolation, I decided to rely on the ZymoResearch "*Quick*-RNA Microprep Kit", which is, according to manufacturer, usable for RNA isolation out of 1-10^6 *in vitro* or *ex vivo* harvested cells. To test this, I isolated murine cells by peritoneal lavage and made a dilution series of 20 to 10^5. Next, I isolated the RNA following manufacturer´s instructions (including DNA digestion as recommended) and determined the RNA concentration using a "UV5Nano" spectrophotometer (Mettler Toledo). The results are depicted in Table 4-1.

Table 4-1 Nucleic acid concentrations after '*Quick*-RNA Microprep Kit' RNA isolation

Cell#	**20**	**50**	**100**	**250**	**500**	**10^3**	**10^4**	**10^5**
c (ng/µL)	21.804	0.431	0.275	2.745	2.510	2.941	4.941	27.255

Additionally, I checked the absorbance spectra for all the samples, especially, since the determined concentrations did not behave proportional to the cell numbers (Table 4-1). However, except of the highest input sample with 10^5 cells (Figure 4-4**B**), I could not observe the typical peak at 260 nm in any other spectrum (Figure 4-4**A**). This peak should occur in the presence of RNA as nucleic acids absorb the passing UV light at 260 nm due to their purine and pyrimidine rings [195].

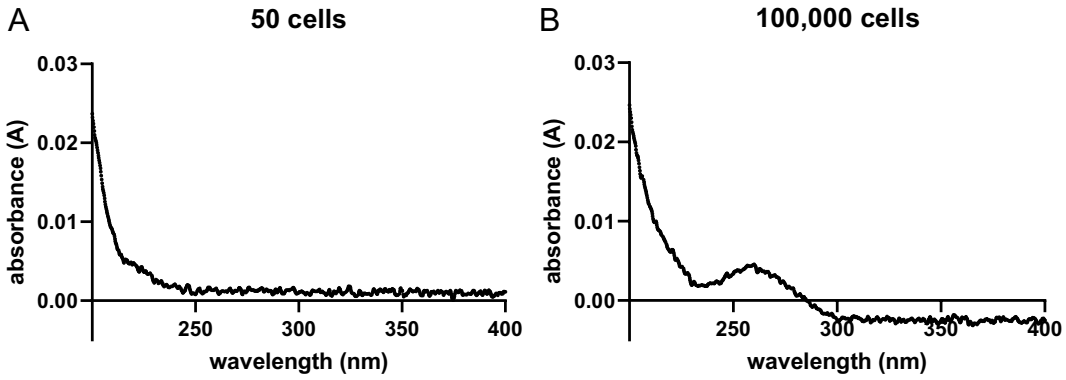

Figure 4-4 Absorbance spectra of nucleic acid determination

The absorbance spectra of eluates after RNA isolation (ZymoResearch "*Quick*-RNA Microprep Kit") from 50 cells (**A**) and 100,000 cells (**B**) are shown. From all measured samples (eluates out of 20 – 100,000 cells), only the highest cell number resulted in the characteristic spectrum of nucleic acids, peaking at 260 nm.

In order to circumvent the problem of determining the very low RNA concentrations, I decided to change the experimental setup. The so-called “Standard Curve Method” for relative quantification of target gene expression allows to interpolate the unknown sample quantities from standard curves [187]. Therefore, standard curves need to be determined on all plates and for all genes. This provides highly accurate quantification results without intense validation of the method. But, on the other hand, the standard curves increase the need of reagents and limit the space for reactions per plate. Therefore, it would have been advantageous to combine the assays for the gene of interest (GOI) and the endogenous control (eCtrl) in one reaction tube as so-called duplex reactions. For duplex reactions, both genes should be expressed on a similar level, otherwise, the higher expressed gene may use up the necessary reaction compounds and slow down the second reaction in the tube as a result.

A second improvement was made to reduce amplification target loss as a result of several pipetting steps: Since it is not necessary to determine and therefore isolate the RNA for standard curve quantification, I tested the so-called “SingleShot Cell Lysis Kit” (Bio-Rad), which allowed to directly sort the 50 cells in a cell lysis buffer and use the lysate without any purification for a combined RT and PCR reaction. This SingleShot Kit, I combined with the iTaq Universal Probes One-Step Kit (Bio-Rad). According to the manufacturer, this kit combines reverse transcription and PCR in one step and is compatible with crude lysate due to high inhibitor tolerance. For the gene detection, I used ready-to-use Taqman probe assays from Thermo Fisher Scientific, which are exon-spanning in contrast to the corresponding Bio-Rad assays. Exon-spanning primers in Taqman assays have the advantage to amplify only cDNA, which consists of only intronic sequences, but no exon-containing genomic DNA.

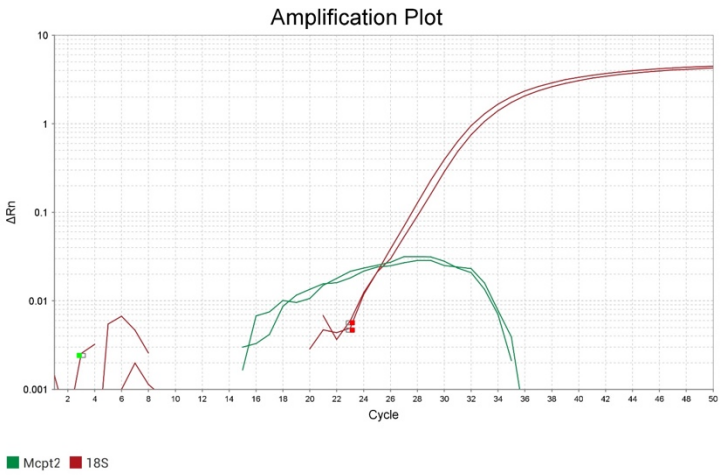

Figure 4-5 Amplification plot of two duplex reactions

In order to test the Bio-Rad Kits in combination with Thermo Fisher Scientific gene assays for duplex reactions, a mixture of peritoneal MC, CD3ε+ splenocyte and cMMC RNA was used as a template. Gene assays for *Cd4*, *Mcpt2*, *Mrgprb2* and *Tpsb2* (all FAM-labeled) were combined in duplex reactions with *Rps18* („18S“, VIC-labeled) as eCtrl. Two duplex reactions for *Mcpt2* (green) and *Rps18* (red), with

varying template concentrations, are displayed. Whereas the eCtrl *Rps18* showed an exponentially increasing slope, the *Mcpt2* slope behaves unusual. ΔRn – difference of normalized signal

Surprisingly, with this setup, I observed an unusual behavior of the slopes in most of the amplification plots. As shown for *Mcpt2* exemplary in Figure 4-5, the ΔRn (difference of normalized signal) dropped with increasing cycle numbers. Investigation of the raw data revealed an unexpected high baseline fluorescence of the VIC (Figure 4-6**A**) and FAM (Figure 4-6**B**) dyes as a cause when compared to the passive reference dye ROX. Such a high baseline fluorescence implies the presence of unbound fluorophores in the reaction mixture, released from the probes during several freeze-thaw cycles or caused by an incompatible buffer. Since Taqman probes from Thermo Fisher Scientific are not optimized for Bio-Rad reagents, I exchanged them by corresponding Bio-Rad probe assays as a consequence.

Besides the high background fluorescence, the raw data plots in Figure 4-6 revealed a different slope for the GOI expression in singleplex than in duplex reactions. While the fluorescence of VIC (eCtrl) increased around cycle 20 in both singleplex (Figure 4-6**A**) and duplex (Figure 4-6**C**), the fluorescence of FAM (GOI) increased around cycle 35 in singleplex (Figure 4-6**B**) but later than cycle 40 in the duplex reaction (Figure 4-6**C**). This can be observed when the first amplification reaction of the higher expressed gene (eCtrl) inhibits the second reaction of the less abundant transcript (GOI).

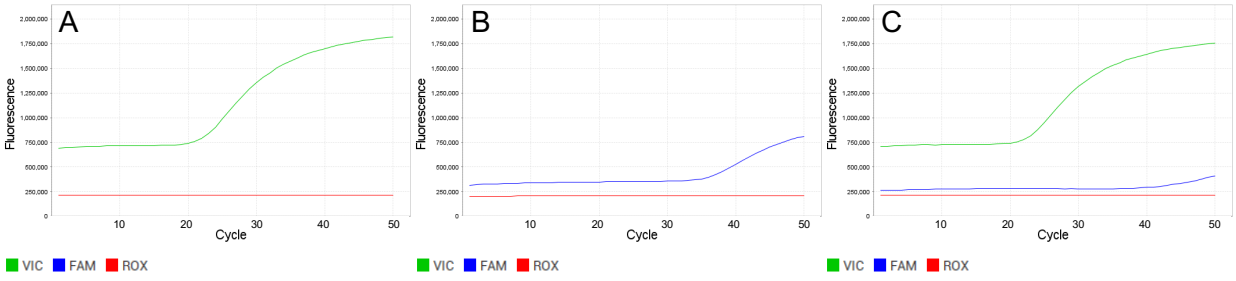

Figure 4-6 Multicomponent plots of singleplex and duplex measurements
So-called Multicomponent plots display the detected fluorescence in each cycle of a real-time PCR for each channel (filter setup). In the VIC channel (green), the signal for the endogenous control (eCtrl) probe was measured, whereas the target gene probe was labeled with FAM (blue). ROX (red) was used as a passive reference dye which should not alter over time. In **A** and **B**, target gene and eCtrl were measured separately in singleplex reactions but probes were combined in a duplex reaction in **C**.

As a consequence, I used the PrimePCR™ Probe Assays by Bio-Rad and exchanged the iTaq Universal Probes One-Step Kit against the Reliance One-Step Multiplex RT-qPCR Supermix (Bio-Rad) which is optimized for multiplex reactions and was claimed to have enhanced

tolerance to inhibitors. With this new setup, I tested 1. if both GOI and eCtrl can be measured together in duplex reactions without affecting each other, 2. whether the reaction volume can be scaled down from 20 µL to 10 µL to save reagents and 3. whether components in the lysate influence the reaction.

As displayed in Figure 4-7**A, B**, I found out, that technical replicates showed higher reproducibility in 10 µL compared to 20 µL reactions which were recommended by the manufacturer. Second, I noticed again, that the amplification of the higher expressed gene seemed to inhibit the second gene in the duplex reaction. Even if the effect was less strong than in Figure 4-6 above, a slight shift of the *Cma1* amplification curve to higher cycle numbers in duplex versus singleplex could be observed in Figure 4-7**C, D**.

To test, whether the PCR was inhibited by the lysate, I used a PrimePCR™ Template for Probe assays (Bio-Rad), a synthetic DNA template specifically for the corresponding gene assay. The template was amplified alone in one reaction and in combination with 4 µL of the RNA lysate in a second reaction. Since the sum of template nucleic acids in the second reaction was expected to be higher, the C_T values should not increase. Surprisingly, they increased by 1 C_T value when MC lysate was added, as shown in Table 4-2. In contrast, when 4 µL splenocytes lysate was used, the C_T values were comparable to the synthetic template only (not shown). This observation may be due to the heparin in lysed MCs which is known to be a potent PCR inhibitor [196] and necessitated an RNA purification step for the final protocol.

Table 4-2 PCR inhibition test

	Template only		**Template + 4 µL lysate (pMCs)**	
Template dilution	C_T *(Cma1)*	32.65	C_T *(Cma1)*	32.43
1:10^3	C_T *(Rps18)*	30.78	C_T *(Rps18)*	31.92
Template dilution	C_T *(Cma1)*	28.20	C_T *(Cma1)*	29.20
1:10^2	C_T *(Rps18)*	26.48	C_T *(Rps18)*	27.89

pMCs – peritoneal mast cells

As a result, I finally decided 1. to isolate the RNA, 2. to run each gene in singleplex reactions, 3. with a reaction volume of 10 µL and 4. by combining the above-named Bio-Rad products. The final procedure was described in 3.8 in detail. Since the RNA eluate volume after the final isolation step limits the number of genes to measure, I maximized the volume by eluting two times à 15 µL. Additionally, I could skip the nucleic acid concentration determination by applying the standard curve method explained above.

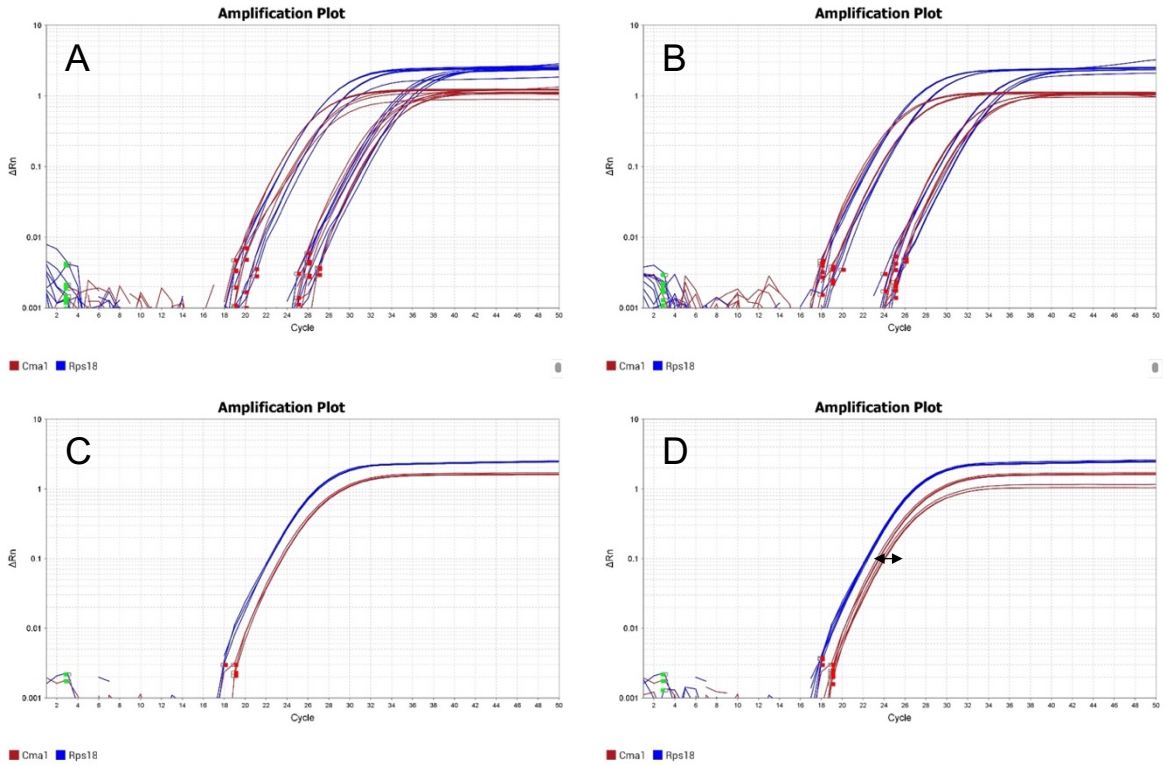

Figure 4-7 Amplification plots in varying reaction setups

While in **A**, 20 µL-duplex reactions (four template concentrations) had a higher standard deviation in technical triplicates, triplicates of 10 µL-reactions showed less variability. When amplified in a singleplex reaction (**C**), *Cma1* had a lower C_T value compared to a duplex measurement (**D**). In **D**, duplex and singleplex results were combined to display the shift in the *Cma1* (red) amplification curve (arrow), whereas *Rps18* (blue) showed no difference.

4.2.1.2 Development of an estrous cycle determination protocol

Female mice and rats undergo their estrous cycle every four to five days [197]. In rats, it was shown that dural MC numbers fluctuate during estrous cycle [121]. In order to exclude any effect of the estrous cycle phase on the MCs, I established a protocol to determine the estrous cycle phases in all mice used in further experiments. Based on the procedure published in 2012 by Byers *et al.* [183], I took vaginal swabs from sacrificed animals. This publication provides an identification tool which I used to count nucleated and cornified epithelial cells and leukocytes in the smears. Subsequently, I calculated the percentages to distinguish between proestrus, estrus, metestrus, diestrus and late diestrus. Aiming to increase the contrast of the cells in the smears and to clearly distinguish nucleated and cornified epithelial cells, I used an 0.5% TB solution as a counterstain. TB is a cationic dye which is able to penetrate cell and nuclear membranes and binds to acidic cell compounds, mucus and strongly to the anionic DNA. Since the TB staining is water-based and fast, I could easily include the staining in all

experimental setups. The whole procedure is described in detail in 3.3 and delineated in the cartoon in Figure 3-1**A**.

4.2.2 Defining the expression patterns of MC-specific genes in EYFP$^+$ cells

With the final qRT-PCR protocol, I was able to proof the RNA sequencing results. Therefore, I measured *Cma1, Mcpt4* and *Tpsb2*, CTMC genes which were expressed in all samples in Figure 4-3 of RNA sequencing, except of the two CP samples. Additionally, I included assays for *Mcpt2*, an MMC gene, *Kit* and *Fcer1a*, which are expressed in both major MC subtypes and *Cd3e*, as a negative control, which is expressed in different T cells as part of the T cell receptor-CD3 complex [198]. *Rps18*, the gene coding for the ribosomal protein S18 (part of the 40S ribosomal subunit), was used as eCtrl.
These genes were measured in lysates of 50 EYFP$^+$ cells from all four tissues included in the RNA sequencing (CP, meninges, parenchyma and peritoneal cavity). Additionally, as delineated in the cartoon in Figure 4-8**A**, I investigated control samples: EYFP$^+$ cells from ear skin (= CTMC control) and Cd3ε^+ splenocytes (= negative control) from the same mice. To complete the controls, Johanna Kotrba (Institute for Molecular and Clinical Immunology, OvGU Magdeburg) kindly provided me BM-derived MCs (BMMC, = immature control) and “cultured MMCs” (cMMCs, = MMC control), generated *in vitro* from wildtype female BM. The cMMCs were BMMCs which express mucosal MC genes when treated for 72 h with TGFβ and SCF according to Derakhshan *et al.* [97].

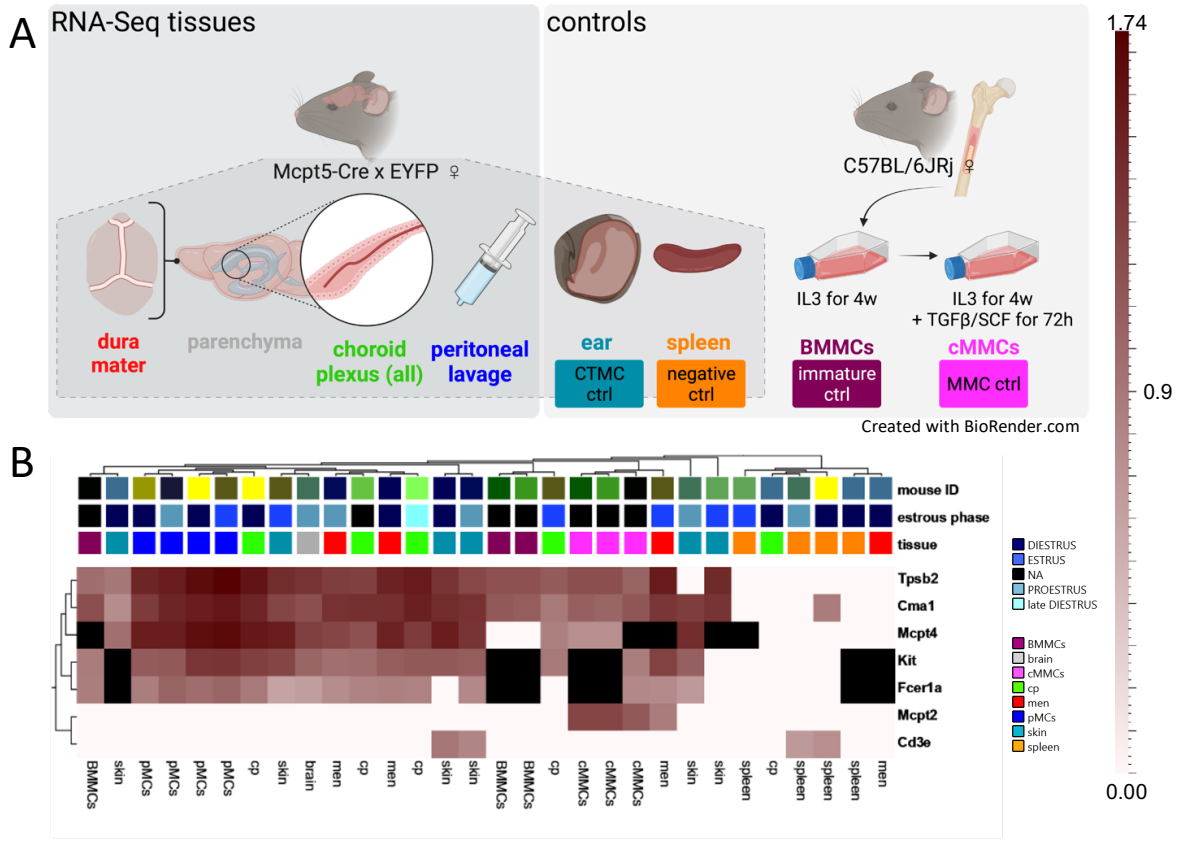

Figure 4-8 Quantitative RT-PCR confirms the RNA sequencing results

A delineates the tissue isolation and control cell generation scheme for the qRT-PCR. Cerebral tissues and peritoneal samples were generated and sorted as for bulk RNA sequencing (Figure 4-1). Ear skin and spleen from the same mice were used to generate a CTMC control and a negative control. Therefore, 50 EYFP$^+$ cells from ear skin lysates and CD3ε$^+$ splenocytes were sorted per sample. BM from C57BL/6 female mice was used to culture BMMCs as a control with immature MC characteristics and cMMCs as a MMC control. 50 cells were sorted for each sample, RNA was isolated and used for qRT-PCR. Created with Biorender.com. The heatmap in **B** presents the qPCR results as fold differences (cf. Table 3-9) for the expression of six MC genes and CD3ε (negative control gene) vs. eCtrl. Samples are color-coded for sample ID, estrous cycle phase and tissue. Black squares – no data (N.A.). cp – choroid plexus, ctrl – control, h – hours, IL3 – interleukin, men – meninges (DM), pMCs – peritoneal mast cells, SCF – stem cell factor, Seq – sequencing, TGFβ – transforming growth factor beta, w – weeks.

In Figure 4-8**B**, the qRT-PCR results are displayed in a heatmap. Samples are colored by mouse ID, estrous cycle stage and origin of cells (tissue).

Tpsb2, the gene which encodes for the MC protease (Mcpt) 6 was detected in all tissues and cell types except of the negative control samples (Cd3ε$^+$ splenocytes), namely parenchyma, pMCs, BMMCs, cMMCs as well as in five out of six skin samples, four out of five CP and three out of four meningeal samples. Thereby, strongest *Tpsb2* expression was observed for pMCs, one CP and one meningeal and skin sample.

Cma1, which encodes for Mcpt5, was expressed in all samples of the above tissues and cell types, but including all of the six skin samples. Strongest expression was observed in pMCs and one CP sample. Additionally, in one negative control, *Cma1* transcripts were detected. *Mcpt4* was detected in all of the quantifiable pMCs, skin, CP, meningeal and parenchymal samples. In regard to the *in vitro* cultured cells, *Mcpt4* was identified in the cMMCs but not in the immature BMMCs. Splenic control cells also lacked transcripts of this gene.

Kit and *Fcer1a*, the genes coding for c-kit and the alpha chain of the FcεRI, could not be quantified for seven samples ("NA", caused by the data selection criteria described in 3.8.4). Among the remaining, *Kit* expression was identified in BMMCs, cMMCs, pMCs, brain parenchyma and all except of one skin and one CP sample. *Fcer1a* RNA was detected in four out of six skin samples, three out of five CP samples, but all of the other cell types and tissues if quantifiable. Neither *Kit* nor *Fcer1a* transcripts were detected in the negative controls.

Mcpt2, which codes for the MMC protease Mcpt2, was expressed in all of the cMMCs and one meningeal sample, with highest expression in cMMCs.

Cd3e, which was expected to be expressed in all control samples, was identified in two skin and two splenic control samples. All in all, MC genes could be detected in all quantifiable tissues or cell types except of two samples: one CP and one meningeal sample did not express any of the determined genes. Even if they showed housekeeping gene expression comparable to all the other samples, MC gene expression was not detectable. Interestingly, both samples derived from the same mouse.

The female mice used for this approach were in different stages of the estrous cycle, with five mice in diestrus or late diestrus, two mice in estrus and three mice in proestrus. For one CP sample and the mice used for *in vitro* cell cultures, the estrous cycle phase was not determined. In general, most of the sample numbers per tissue were too low to allow an adequate comparison. With six samples, the skin was represented best in this dataset. When comparing the skin samples only, two mice were in diestrus but with showed differences in *Tpsb2*, *Mcpt4*, *Cma1* and *Cd3e* expression. The mouse expressing higher levels of *Tpsb2*, *Mcpt4* and *Cma1* clustered closer with a mouse in proestrus phase. This mouse in proestrus further separates from the second mouse in the same phase due to differences in *Tpsb2* and *Cd3e* expression. The last two mice were in the estrus phase. While one expressed *Kit* and *Fcer1a*, the other lacked both. For this small sampling size, all in all, no obvious effect of the estrous cycle phases on the gene expression was identified and differences among individuals were more prominent.

4.3 Anatomic location of EYFP$^+$ cells in the brain of Mcpt5-Cre EYFP mice

Both the bulk RNA sequencing and the qRT-PCR, revealed samples, in which no expression of MC genes – which are usually used to identify and characterize MCs – could be detected at all. In both methods, especially the CP samples seem to be different. To make sure, that the CNS MCs are targeted with our Mcpt5-Cre EYFP reporter mouse model and localized in the brain regions as described several times before, I aimed to identify them with light sheet microscopy. This microscopy method allows to scan a whole organ or organism without any mechanical manipulation and therefore to identify the cells of interest in their (almost) native three-dimensional environment. In contrast to brain slices, no single cell can be missed due to sectioning and even very few cells can be visualized based on their fluorescent reporter protein.

Light sheet fluorescence microscopy (LSFM) is a young method with gaining interest and increasing possibilities and methodical improvements every year. In Figure 4-9, the results of a Pubmed database query are displayed, visualizing the increasing interest in the method, and development of protocols for mouse tissue. Within the last 10 years, between 2012/13 and 2021/22, the increase in publications matching the terms “clearing” AND “light sheet microscopy” AND “mouse” was about 10fold.

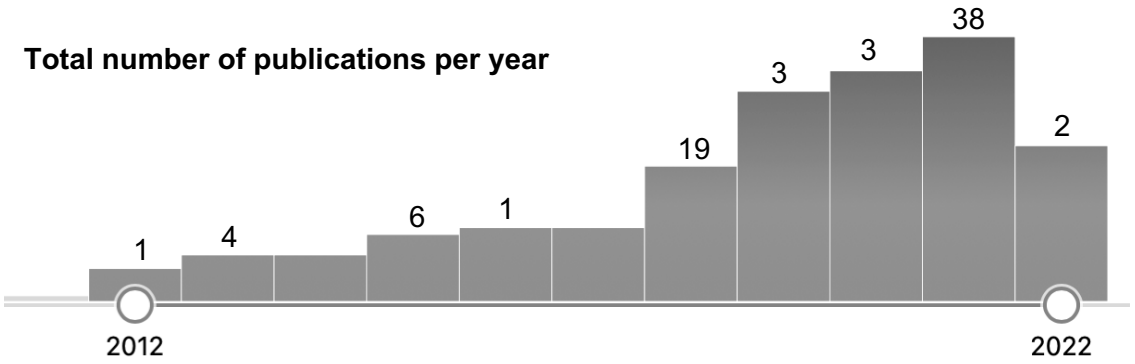

Figure 4-9 A Pubmed query for the terms “clearing”, “light sheet microscopy” and “mouse”
According to a Pubmed database query for the terms “clearing” AND “light sheet microscopy” AND “mouse”, the matching results of publications per year increased between 1 and 4 in 2012 and 2013 up to about 40 in 2021 and calculated for 2022. It demonstrates the growing interest in LSFM within the last 10 years. (as of 28.07.2022)

4.3.1 Establishment of a suitable LSFM protocol

In order to establish an appropriate protocol for Mcpt5-cre EYFP mouse brains, I started with the clearing protocol by Klingberg and colleagues from 2017 [188]. They stated that the endogenous fluorescence of several fluorescent proteins (FP) can be maintained during the clearing procedure and finally be detected with LSFM. In my hands, the expression of neither the EYFP in the Mcpt5-Cre EYFP reporter mice nor the tdTomato FP in the Mcpt5-Cre tdT mice were detectable after clearing. For the first time, I observed tdTomato$^+$ cells (Figure 4-10**B**) after clearing when using tert-butanol instead of ethanol for dehydration, while the EYFP fluorescence seem to suffer still from the procedure. Another problem, however, occurred during dehydration: butanol shrinked the tissue more than ethanol which increased background fluorescence from fiber-rich brain regions. The cells of interest shrunk as well, which make them hard to detect within the high background fluorescence.

To overcome the problem of shrinkage, I performed the so-called CUBIC clearing, which means “clear, unobstructed brain/body imaging cocktails”. The protocol was published by Susaki and colleagues in 2015 [199] and utilize hydrophilic instead of hydrophobic clearing reagents. As a result, the tissue binds a lot of water and expands instead of shrinking. The FP should stay intact and be preserved for subsequent LSFM imaging in a high glucose or oily solution. Indeed, the CUBIC clearing resulted in an optimal signal-to-noise fluorescence of tdTomato$^+$ cells in the Mcpt5-Cre tdT reporter mice (Figure 4-10**C**). The detected cells including their protrusions and different shapes were bright and big enough to observe varying morphologies. But two problems remained: on the one hand, the EYFP fluorescence of the Mcpt5-Cre EYFP mice, used for the previous transcriptome analyses, were still not detectable and on the other hand, the brain tissue became very soft during clearing. Due to the massive water incorporation in the specimen and its expansion, the tissue was soft, sticky, easy to destruct and wobbling in the immersion medium during acquisition. As a result, the image stacks were blurry, unfocused or hard to align. Those problems could be addressed by decreasing the incubation times, but a high transparency *and* proper stiffness of the tissue were hard to balance.

In May 2018, a new method was published by Jing and colleagues [200], which should be able to preserve endogenous fluorescence, clear the whole mouse body and provide cellular level resolution in the mouse brain. I performed this PEGASOS (**P**oly**e**thylen **g**lycol **a**ssociated **so**lvent **s**ystem) method on one hemisphere of the Mcpt5-Cre EYFP reporter mouse brain and for the first time, I could identify some very bright EYFP$^+$ cells in the CP tissue. But, in contrast to what I observed before in the tdTomato reporter mice, I could not detect any EYFP$^+$ cell in

the surrounding parenchyma. On the one hand, according to [157, 201], it could be that the distribution of tdTomato$^+$ cells is different compared to the EYFP$^+$ cells even if the Cre-recombinase is expressed under the same promotor. On the other hand, it could be, that only the brightest cells were detectable which contain the most FP in their cytosol and which seemed to be the case here. Already with the other two methods, I observed that the CP FP$^+$ cells were brighter than the other cells in the parenchyma, even if this phenomenon was not equally apparent in Figure 4-10**B** and **C** as it was in Figure 4-10**D**.
In parallel, I tried to enhance the endogenous FP signal in targeted cells by using a nanobody against the EYFP (FluoTag®-X4 anti-GFP, NanoTag Biotechnologies). According to manufacturer, this nanobody cross-reacts with several green FPs. Hence, I used the second hemisphere and a blocking solution according to manufacturer´s protocol, which contained 10% serum and 0.1% Triton X-100. After staining with a nanobody concentration of 1:500 for 4 d, several washing steps, ethanol dehydration and ethyl cinnamate clearing, I could detect much more signals in many different regions in the whole hemisphere (Figure 4-10**E**). Most of them were very likely cells, a lot of them had dendrites which gave them a neuronal appearence. For the next months, I tried to improve the signal-to-noise ratio (SNR), a homogenous staining throughout the whole brain and to avoid sticking of the nanobody to the surface and in ventricular regions, which made an identification of individual cells in the outer regions almost impossible.

In February 2019, a new clearing procedure was published which significantly improved the nanobody stainings and influenced my final protocol the most. The so-called “vDisco” (v for variable chain, the binding region of an antibody and the only region a nanobody consists of) was an improvement of a previous protocol from the same group, uDisco, and was published by Cai *et al*. [58]. Due to ingredients, which interfere with the collagen structures to loosen them, the whole brains have not been broken during dehydration. Dichloromethane (DCM) delipidated the tissue and tetrahydrofuran (THF) was used for dehydration. Both reagents lead to a substantially improved transparency of the brains compared to all protocols before, and decreased the background fluorescence as a consequence. Incubation times and nanobody concentration were adopted and a second dye was included, TO-PRO™-1 iodide, a nuclear stain. With this protocol for a two-color staining (Figure 4-10**F**), I aimed to distinguish cells from nanobody aggregates. The nuclear dye penetrated well resulting in a homogenous, clear staining. But one problem still persisted: the nanobody staining was brighter on the outer surface and regions surrounding the ventricles. It seemed that the nanobody penetration into the organ still needed improvement.

In 2020, the SHANEL method was published by the same group [202]. The authors stated that this protocol improves the permeabilization in a way that even large mammalian (including human) organs can be stained centimeters-deep with antibodies. I tested the SHANEL clearing protocol, slightly adapted for the smaller mouse tissue, to receive better nanobody penetration and less sticking on the surface or accumulation in ventricular regions. Compared to my previous protocol modified from the vDisco procedure, the nanobody penetration with SHANEL seem to be faster (not shown). But, as it is shown in Figure 4-10**G**, the penetration of the nuclear stain was dramatically reduced. Whereas the outer brain regions were stained strongly, the dye almost have not reached the center of the murine brain. Additionally, the nanobody sticking on the surface was still apparent.

The final breakthrough for this problem was not a change in the protocol, but in the nanobody´s fluorochrome in 2021. I exchanged the FluoTag®-X4 anti-GFP Atto647N nanobody from Nanotag with the FluoTag®-X4 anti-GFP AbberiorStar635P. Obviously, it was the fluorochrome, which prevented the nanobody from staining homogenously. Its sticky behavior led to an accumulation on all parenchymal surfaces which was significantly diminished when using the AbberiorStar635P conjugate (Figure 4-11). Only some well-defined and super-bright aggregates occur, especially in outer regions. Herewith, counterstaining with TO-PRO™-1 iodide, a DNA intercalating dye, aids in distinguishing $EYFP^+$ cells and nanobody aggregates when high magnifications are used and precise alignment (camera, filters and chromatic aberration) is guaranteed (Figure 4-12).

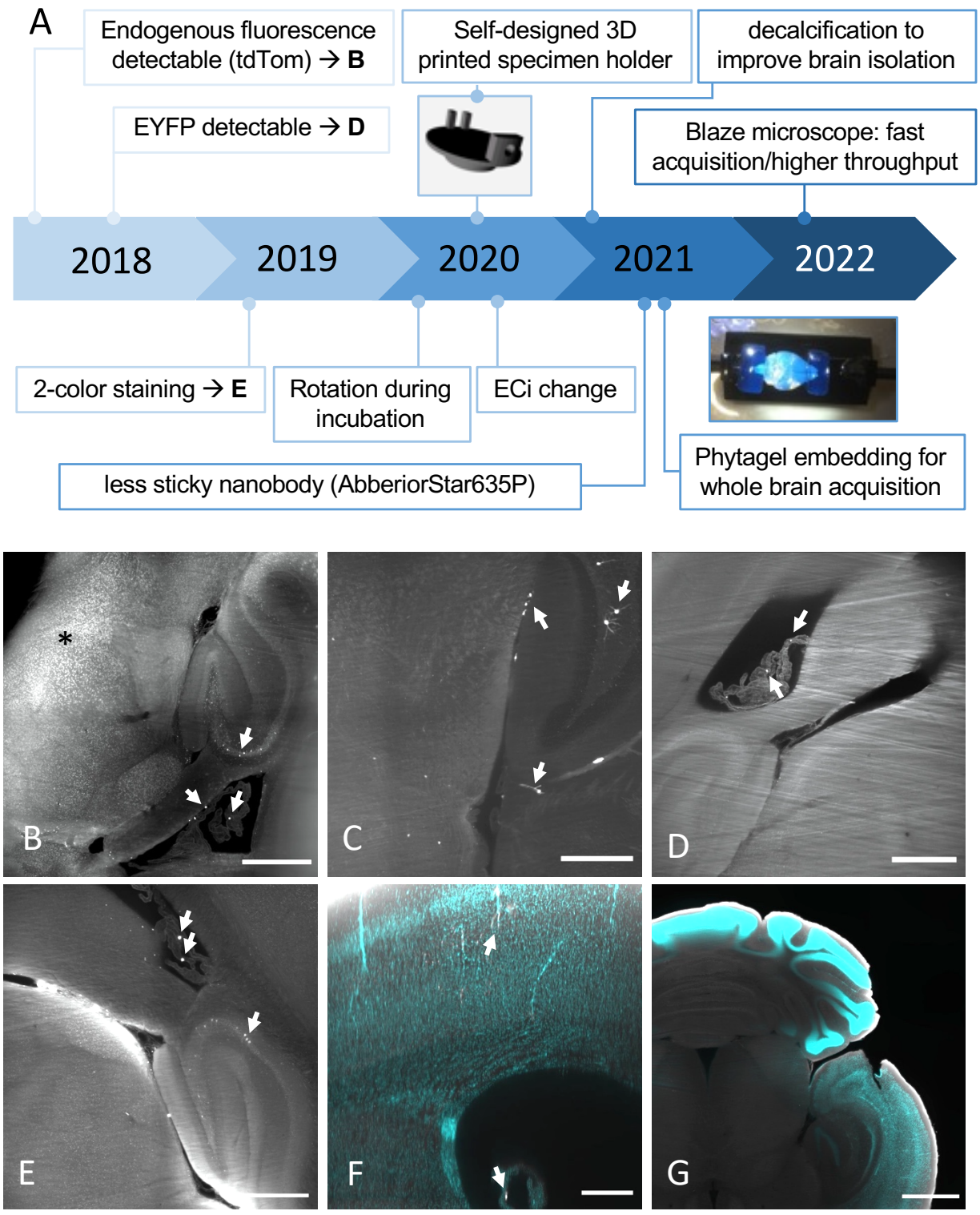

Figure 4-10 Establishment and optimization of an appropriate clearing and LSFM procedure

Prior to using light sheet fluorescence microscopy (LSFM) for the identification of EYFP$^+$ cells in the Mcpt5-Cre EYFP mice, an appropriate clearing protocol was developed. Mcpt5-Cre tdT and EYFP reporter mice were tested. In **A**, the milestones of the establishment process and further improvements in LSFM acquisition are displayed on a timeline. In **B**, the ethyl cinnamate clearing protocol by [188] was

modified by using butanol instead of ethanol for dehydration to preserve the endogenous fluorescence in the reporter mouse brain. tdTomato$^+$ cells in the hippocampus (hc) and CP of an Mcpt5-Cre$^+$ tdT mouse were detectable (arrows). The enormous shrinkage of the tissue caused strong autofluorescence (asterisk). A 50 µm virtual slice is displayed. Scale bar 500 µm. In **C**, the water-based clearing protocol CUBIC [199] was tested. Again, only tdTomato$^+$ cells were clearly detectable (arrows). Scale bar 500 µm. For **D** and **E**, the EYFP fluorescence was detectable for the first time when applying two different protocols each on one hemisphere of the same brain. In **D**, the PEGASOS method [200] preserved the endogenous EYFP fluorescence at least in the brightest cells in the CP (arrows). Scale bar 500 µm. In **E**, an Atto647N-labeled nanobody against green FPs was used to enhance the endogenous EYFP fluorescence and shift the emission to longer wavelengths. Scale bar 500 µm. **F** According to Cai *et al*. [58], the vDisco protocol was used, an improvement of the nanobody-enhancing method in E. To better distinguish cells and nanobody aggregates, a nuclear dye (TO-PRO™-1 iodide in cyan) was included. Scale bar 200 µm. In **G**, the SHANEL method [202] was tested which was claimed to improve antibody penetration into the tissue. Surprisingly, the penetration of the nuclear dye (cyan) decreased dramatically. Scale bar 1 mm. Cells expressing FP in Mcpt5-Cre reporter mouse brains are marked with white arrows.

As summarized in the timeline in Figure 4-10**A**, I dealt with additional obstacles during establishment. Improvements of the procedure were on the one hand in rotation instead of shaking during incubation times, skull decalcification prior to brain harvesting to enable non-destructive organ isolation and prolonged ethyl cinnamate incubation in a larger volume prior to acquisition for highest transparency. On the other hand, an improved specimen holder was developed and finally, the brains were embedded in phytagel blocks for acquisition which allowed to scan the intact brain without quality loss due to fixation with screws or glue. My final protocol which is optimized to visualize the EYFP$^+$ cells in the Mcpt5-Cre EYFP mouse brains is described in section 3.9 above and was used to generate the following data.

4.3.2 Defining the morphologies of EYFP$^+$ cells in distinct brain regions

In Figure 4-11, the results of the above described clearing and LSFM establishment are displayed. Both brains derived from 12-weeks old female Mcpt5-Cre EYFP mice and were treated identically. They are representative for four Cre$^+$ and one Cre$^-$ mice investigated in parallel in this context (cf. Supplemental Figure 3). Whereas in the Cre$^+$ mice, EYFP$^+$ cells could be detected as single cells or in clusters in varying regions, no cells were detectable in the Cre$^-$ mice. Very few nanobody aggregates were visible on the surfaces of both brains, especially on the ventral side, but those could be distinguished from EYFP$^+$ cells with the help of the nuclear stain in the second channel (not shown here). This is displayed exemplary in Figure 4-12.

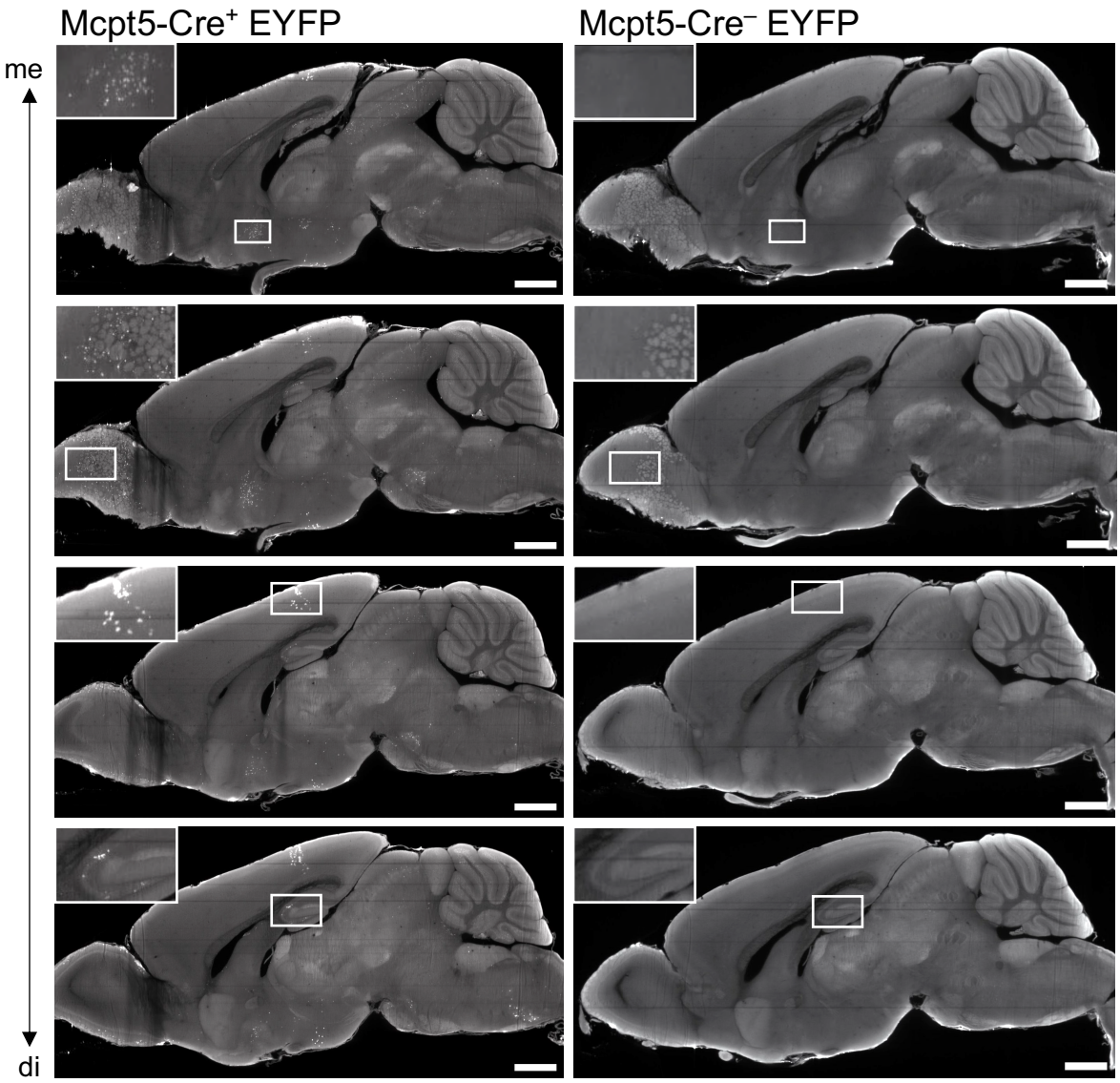

Figure 4-11 The final clearing protocol revealed EYFP$^+$ cells in varying brain regions

The final clearing protocol, slightly modified from vDisco [58], provided a clear SNR owing to the AbberiorStar635P nanobody labeling. Mcpt5-Cre$^+$ EYFP mice showed fluorescently labeled single or clustered cells in varying brain regions (left images), whereas Mcpt5-Cre$^-$ EYFP mice lack them (right images). 20 µm virtual brain slices (sagittal, right hemisphere, for left hemisphere cf. Supplemental Figure 2) are displayed. Scale bars 1 mm. di – distal, me – medial

Surprisingly, in the Cre$^+$ mice, I could detect cells in more regions and in higher cell numbers than expected. Previous studies detected MCs in the murine CP [53, 170], the thalamus and hypothalamus [203], preoptic area [122], entorhinal cortex [128] and hippocampus [165]. In addition to these, I found EYFP$^+$ cells in the olfactory bulb (OB), dorsomedial periaqueductal and cortical regions. EYFP$^+$ cells in the above-named regions appeared in all four investigated mice in almost identical patterns. After magnifying the regions with these cells and switching from sagittal (yz projection) to horizontal (xy projection) to omit the influence of the point spread

function (PSF) distortion in z direction, the real cell shapes became visible. As it is displayed in Figure 4-13**B´**, **C´**, **D´**, these cells had dendrites, some long, some have several, which give them a neuronal morphology.

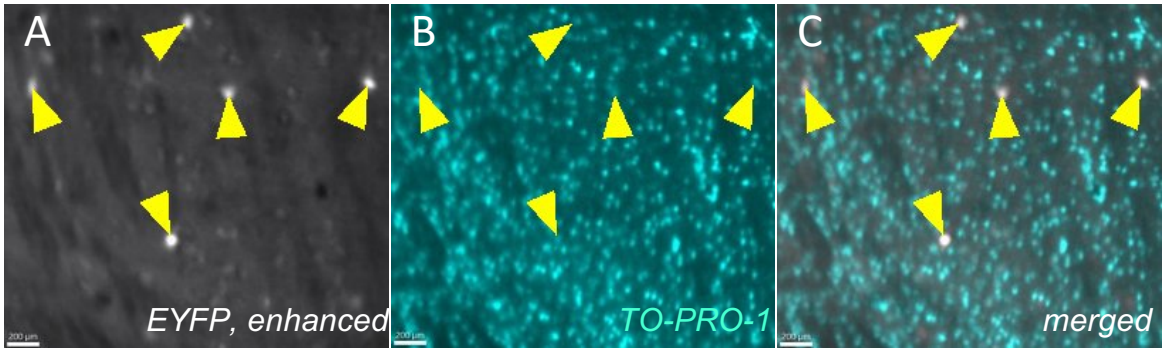

Figure 4-12 A nuclear dye helped to identify single EYFP⁺ cells

TO-PRO™-1 iodide, a DNA intercalating dye, stains nuclei and was used to distinguish EYFP expressing cells and potential nanobody aggregates. High magnifications and precise alignment (camera, filters and chromatic aberration) are necessary for a reliable assessment. EYFP⁺ cells (nanobody-enhanced as described in Figure 4-10) in **A** are marked with yellow arrowheads to identify their nuclei in **B**. **C** represents the merged image with nuclei in cyan and EYFP⁺ cells in grey scale. Scale bar 200 µm.

The three-dimensional insight and a comprehensive investigation of the entire brain revealed many different cell shapes in addition to the neuronal-like. Some of them appeared in all investigated mice, some of them only in one or two. Figure 4-14 shows the cells which were apparent in all mice. In **B**, there are the neuronal-shaped cells in the CA3 region of the hippocampus. In **C,** there are the very bright roundish cells in the CP, which could be visualized already in most of the test experiments during establishment and in **D**, roundish or flatten cells could be identified close to the surface, probably located in the pia mater. In Figure 4-15, examples for cells are displayed, which could be detected only in one or two mice, but not in all. Among them were glia-shaped cells, which seemed to have a net of protrusions or dendrites around the cell body (Figure 4-15**B**). Figure 4-15**C** displays the region between cortex and midbrain (superior colliculus), in which egg-shaped flatten cells could be identified in noticeable numbers. Close to these, pericyte-like EYFP⁺ cells were detected, as depicted in Figure 4-15**D**. Such vessel-enclosing cells were identified in several different regions, which seemed to differ between the mice, but mainly in the cortex or thalamus.

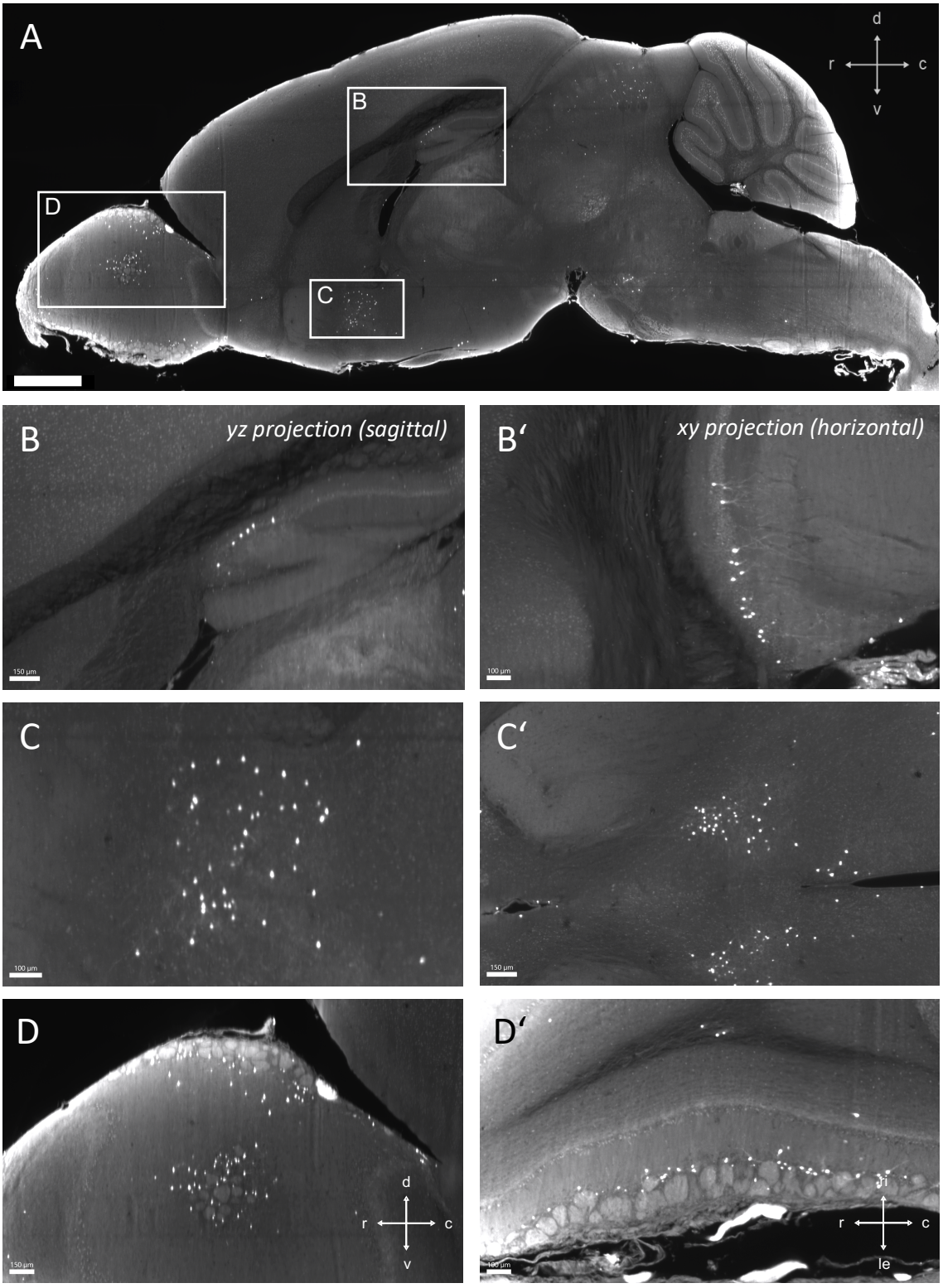

Figure 4-13 Brains show recurrent expression patterns of neuronal-like EYFP⁺ cells

All investigated mice had expression patterns of EYFP⁺ cell clusters e.g. in the hippocampus (**B**), the preoptic area (**C**) and the olfactory bulb (**D**). When investigating these areas in xy projection (horizontally, **B', C', D'**) which has the best resolution, these cells appeared to have a neuronal morphology with long, branched dendrites. Scale bar A 1 mm, B, C', D 150 µm, B', C, D' 100 µm. c – caudal, d – dorsal, le – left, PSF – point spread function, r – rostral, ri – right, v – ventral

All of these LSFM images are optical slices of 50 µm or less which is a comparable thickness reached when physically sectioning the mouse brain with a cryotome (30 – 50 µm). Sectioning the tissue and staining the slices with histological dyes and techniques was the gold standard for MC detection over decades. Due to the special staining characteristics of their granules, MCs can be identified safely in tissues as soon as they are not completely degranulated. If the EYFP fluorescence in the reporter mice appears specifically in (CT)MCs as stated for most peripheral tissues investigated [1, 139], histological MC stains should reproduce the cell clusters observed in the LSFM optical slices. As summarized in [108], there are many different protocols and dyes, but I decided to use the AB/SO staining. As described in 1.3.2.2, AB/SO is a differential staining technique which makes most of the MCs visible based on their granule composition if appropriately fixed: CTMCs and MMCs, immature and mature MCs, all by one protocol [108, 110, 204].

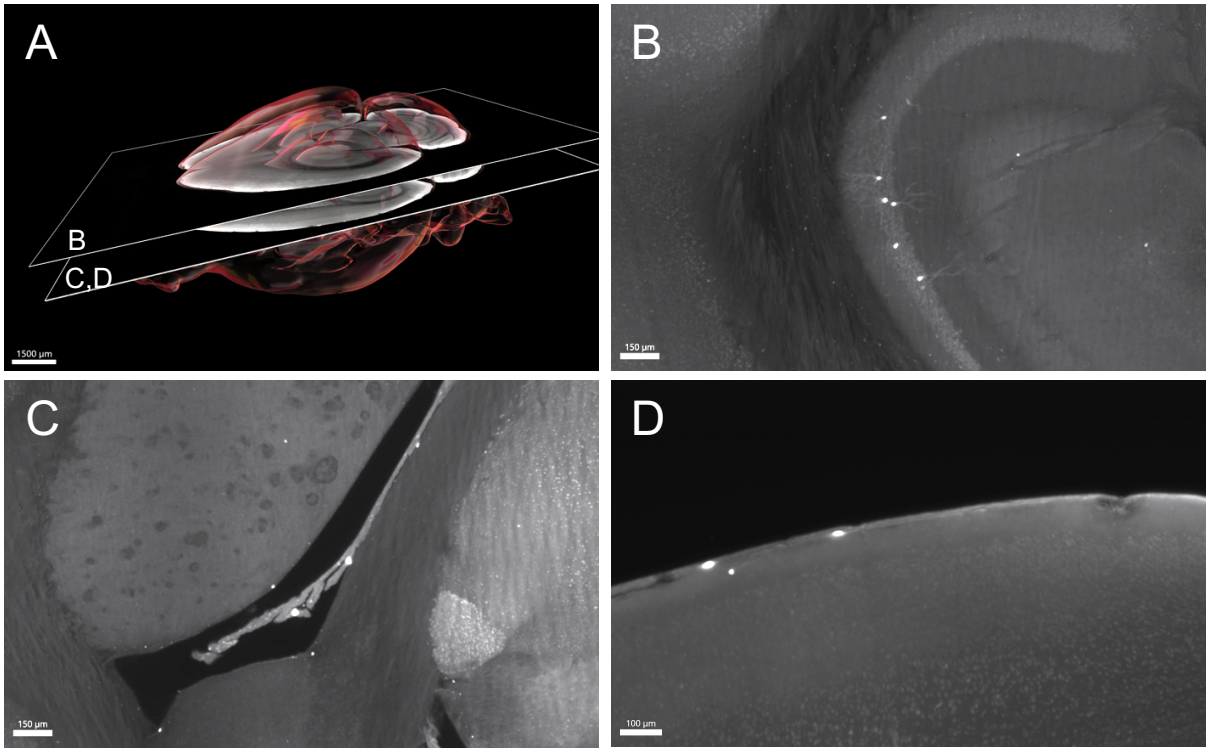

Figure 4-14 Some EYFP$^+$ cells are reproducibly identifiable in all investigated mice
All investigated mice had neuronal-shaped EYFP$^+$ cells e.g. in the hippocampus (cf. Figure 4-13), as in **B**, very bright and prominent cells of a circular or brick-like morphology in all four CPs (**C**) and relatively big, roundish or elongated cells in the (lepto-) meningeal regions (**D**). An overview of the three-dimensional brain including the horizontal sections, where the cells are located, is shown in **A**. Scale bars A 1.5 mm, B, C 150 µm, D 100 µm.

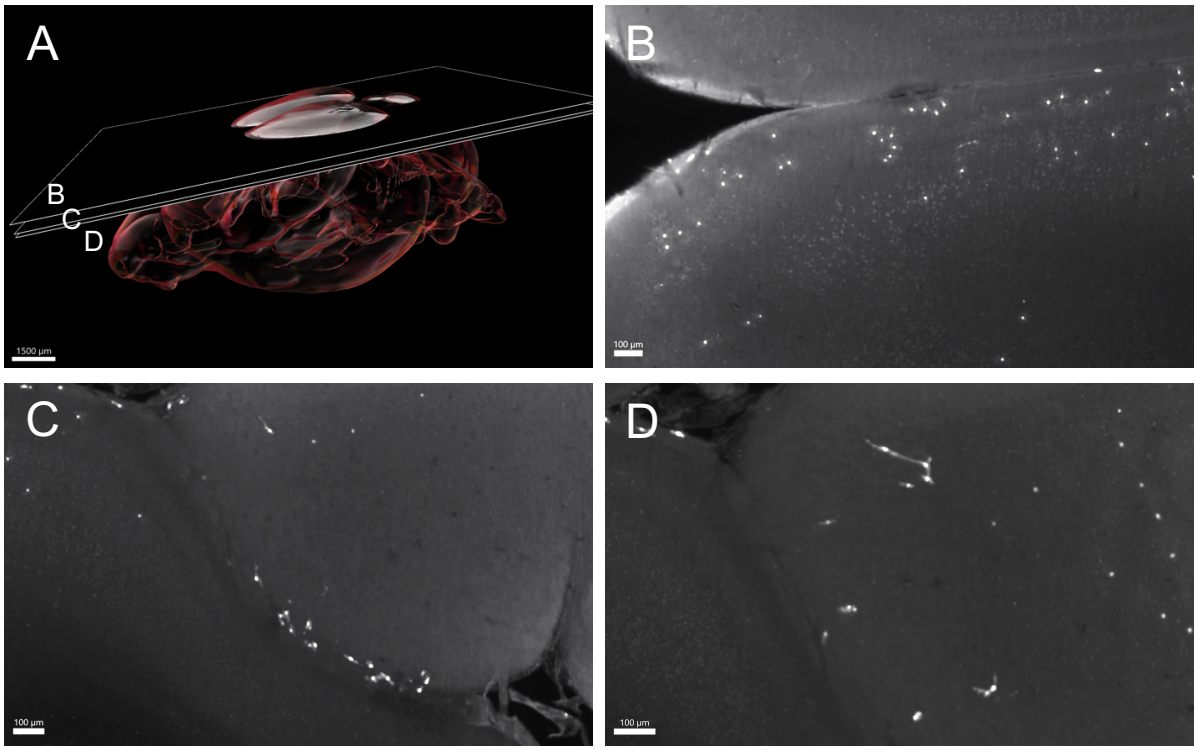

Figure 4-15 Some mice have additional EYFP$^+$ cells of varying morphology or localization
Only some mice had additionally EYFP$^+$ cells with an astrocyte-like appearance (**B**), preferably located in the cortex, egg-like EYFP$^+$ cells, preferably in surface regions (**C**) or endothelial cell-/pericyte-like EYFP$^+$ cells in varying brain regions (**D**). An overview of the three-dimensional brain including the horizontal sections, where the cells were identified, is shown in **A**. Scale bars A 1.5 mm, B, C, D 100 µm.

But surprisingly, when I stained cryosections of the Mcpt5-Cre EYFP mouse brains with AB/SO, only very few and single cells could be visualized by this dye combination. I could neither identify the same cell clusters as before with the LSFM nor could I observe a comparable number of AB/SO$^+$ cells on any of the slices.

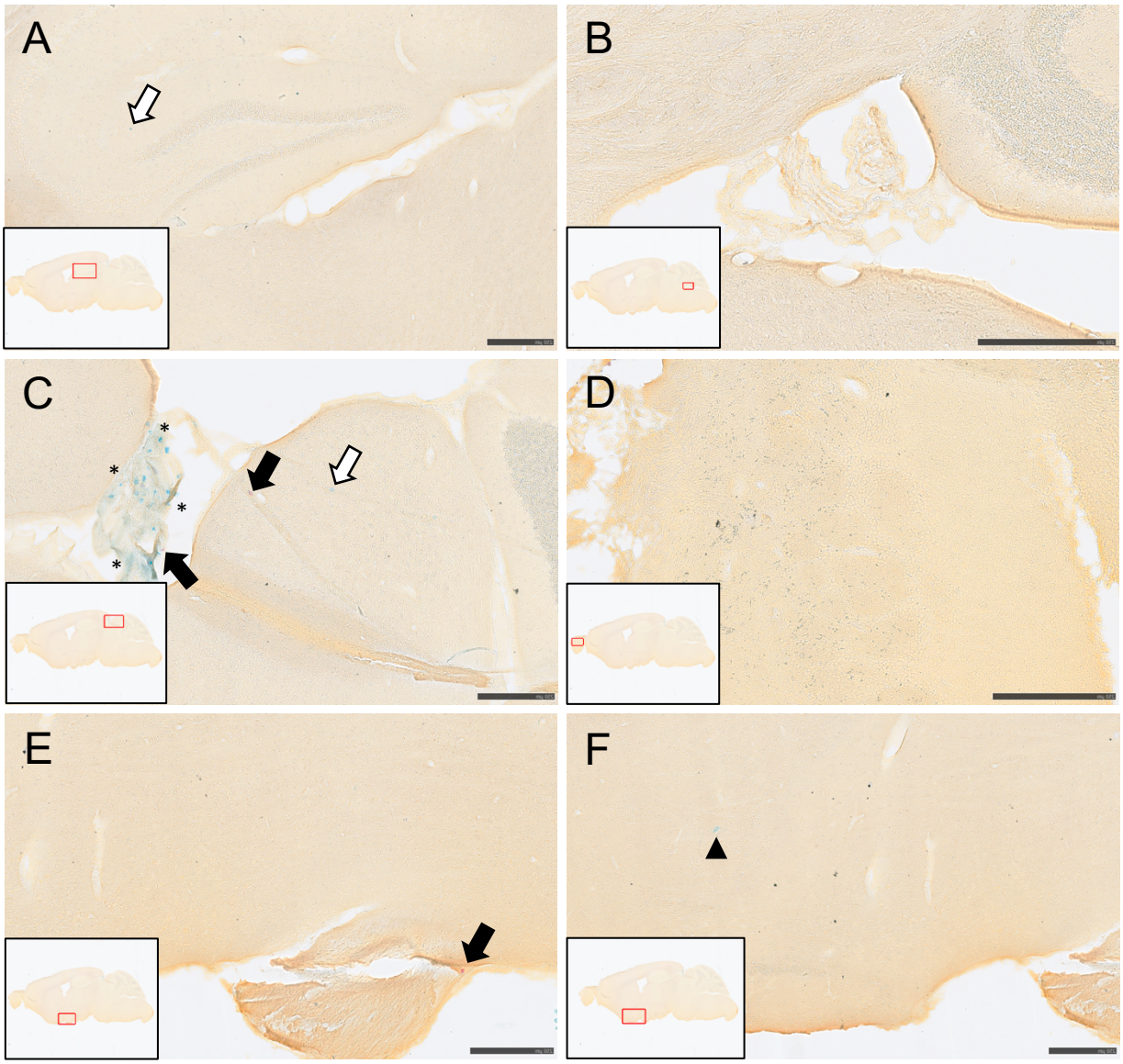

Figure 4-16 AB/SO staining on sagittal brain sections detects only few MCs

A comparable sagittal section of a female murine brain, stained with AB/SO revealed only very few and scattered single stained cells (AB^+ 'blue' or SO^+ 'red'). This sequential MC stain barely detected MCs in the hippocampus (**A**) or preoptic area (**F**), and not a single one in the CPs (**B**) or olfactory bulb (**D**). Few MCs could be detected in the leptomeninges surrounding the whole brain (**E**). Most of them were in the DM, the only area in which cell accumulations could be observed, (**C**). SO^+ cells are marked with a black arrow, AB^+ cells with a white arrow. Most of the DM MCs were AB^+ (inside the asterisks in C). The arrowhead in F marks a blue-stained structure which cannot clearly be identified as a cell due to an atypical morphology and contrast in the tissue. Scale bars 250 µm.

4.4 Mcpt5 expression in publicly available transcriptome data of murine brains

To my knowledge, the expression of Mcpt5 was not investigated yet in the murine brain, neither on RNA, nor on protein level (as of August 2022). Even Wasielewska *et al.* did not mention any investigations questioning the specificity in brain tissue, when using the Mcpt5-Cre mouse model for the first time in that organ [116]. I aimed to fill this gap of knowledge with the help of publicly available transcriptome data. The progress made in single cell transcriptome analyses over the last years and the ongoing open access publishing of comprehensive datasets, may help to discover Mcpt5 (*Cma1*) RNA expression in brain cells by reusing and reanalyzing publicly available data.

For this purpose, I found two appropriate datasets: Both van Hove and colleagues [57] and Zeisel and colleagues [205] performed single cell analyses of murine brains. Whereas van Hove *et al.* focused only on $CD45^+$ brain immune cells, Zeisel *et al.* included and investigated all brain cells. The biggest advantage of both was the deployment of an interactive online tool to easily explore every gene of interest in their data and therefore facilitate reanalyzing.

I first investigated the brain immune cells which were generated out of four different locations in wildtype homeostatic mouse brains [57]: CP, DM (peeled off calvaria), enriched subdural meninges (slice of the dorsal cortex using a 0.25 mm blade between bregma coordinates 2 mm and -4 mm, <1 mm thick) and whole brain (includes all brain tissues). In the CP (Figure 4-17**B**), they identified T cells (TCs), B cells (BCs), three dendritic cell (DC) subsets, monocytes (Mo), three NK cell subsets and two macrophage subsets. *Cma1* which is the official gene name for Mcpt5 could be detected in 2.5% of total cell numbers (94 cells). Highest expression was measured in three TCs. When searching for other MC genes (*Tpsb2, Mcpt4, Tpsab1*), the exact same cells have not been noticed within the TC population. Some few cells with low *Cma1* expression, which did not cluster within the population, were identified among the big macrophage cluster. But most of the $Cma1^+$ cells with moderate expression built up one of the NK cell clusters. Other MC genes were not detected within here, whereas NK cell genes as *Ncr1* or *Klrb1* were detected in all three annotated NK cell clusters on a comparable moderate level (not shown).
In the DM dataset (Figure 4-17**C**), 9% (461 cells) of the cells expressed *Cma1*. Most of them were scattered without clustering, only in the NK cell population, there seemed to be an enrichment of cells moderately expressing *Cma1*. Highest expression could be observed in the population “11” which was not annotated. Other MC genes (*Tpsb2, Mcpt4, Tpsab1*) showed the same scattered distribution pattern without obvious clustering but highest expression was observed again in the population “11” (not shown).

In the subdural meninges dataset (Figure 4-17**D**), only 0.6% (38 cells) of all cells expressed *Cma1*, but there was a clear enrichment of 31 of them in the NK cell cluster. The expression level reached from low to moderate.

The same could be observed in the whole brain dataset (Figure 4-17**A**). 1.4% of dataset, which were 85 single cells, expressed *Cma1*. A clear cluster was only visible in the NK/NKT cell population. In none of the NK cell clusters which showed *Cma1* expression, other MC genes (*Tpsb2, Mcpt4, Tpsab1*) could be detected (not shown).

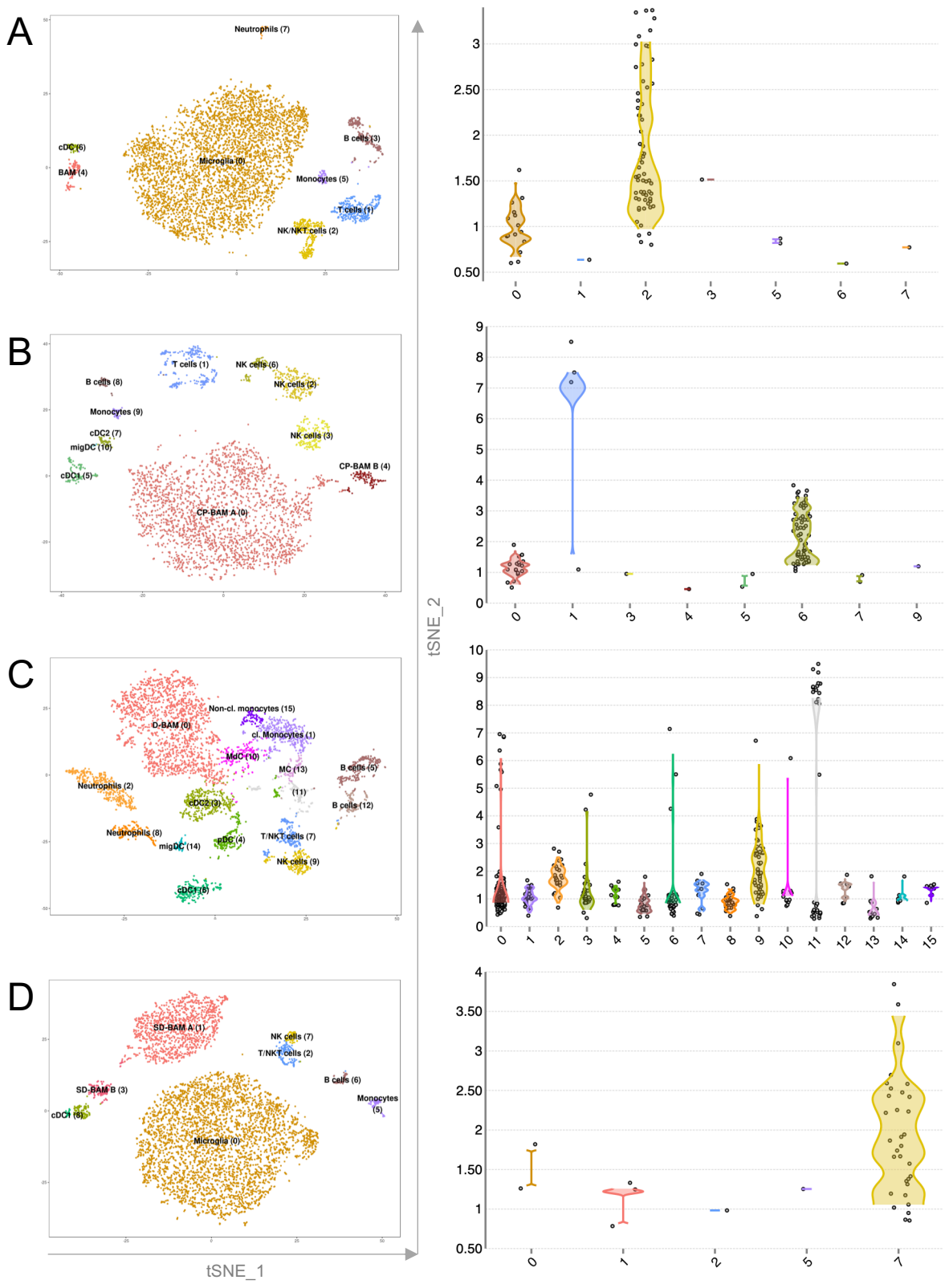

Figure 4-17 Single cell transcriptome data identified *Cma1* expression in non-MC immune cells

CD45^{+} immune cells of the murine whole brain (**A**), CPs (**B**), DM (**C**) and enriched subdural meninges (**D**) were isolated and measured using droplet-based single cell RNA sequencing [57]. On the left, t-SNE plots show the identified cell clusters in each tissue. On the right, *Cma1* expression was plotted against the cell clusters (color-coded and numbered), each dot representing a *Cma1* expressing cell

within a cluster. In whole brain, CP and subdural meninges, most of the *Cma1* expressing cells were identified in the NK cell cluster. In the meninges, highest *Cma1* expression was identified in cluster 11 which was not further annotated. NK cells were the second cell type in which moderately *Cma1* expressing cells were identified. Plots were generated with the interactive tool on brainimmuneatlas.org to discover the original dataset of [57].

In the whole brain single cell dataset of Zeisel and colleagues, in which all cerebral cell types were isolated and investigated, only a very small fraction was made up of immune cells. 5,425 cells out of 160,796 in total (3%) were identified as microglia populations. Since microglia build up the majority of brain immune cells, all others were probably too less to isolate, cluster or characterize them.

But surprisingly, in seven out of 262 non-immune cell clusters identified by the authors, *Cma1* expression was measurable, with four of them being neuronal clusters (Figure 4-18). Although, the expression level was low in all seven clusters (trinarization score $\leq$ 0.95), *Cma1* transcription may be sufficient to build enough Cre-recombinase for EYFP synthesis in the Cre reporter mouse. The non-neuronal, *Cma1* expressing cell clusters comprise of ependymal cells, astrocytes and pericytes as displayed in Figure 4-18 and Table 4-3.

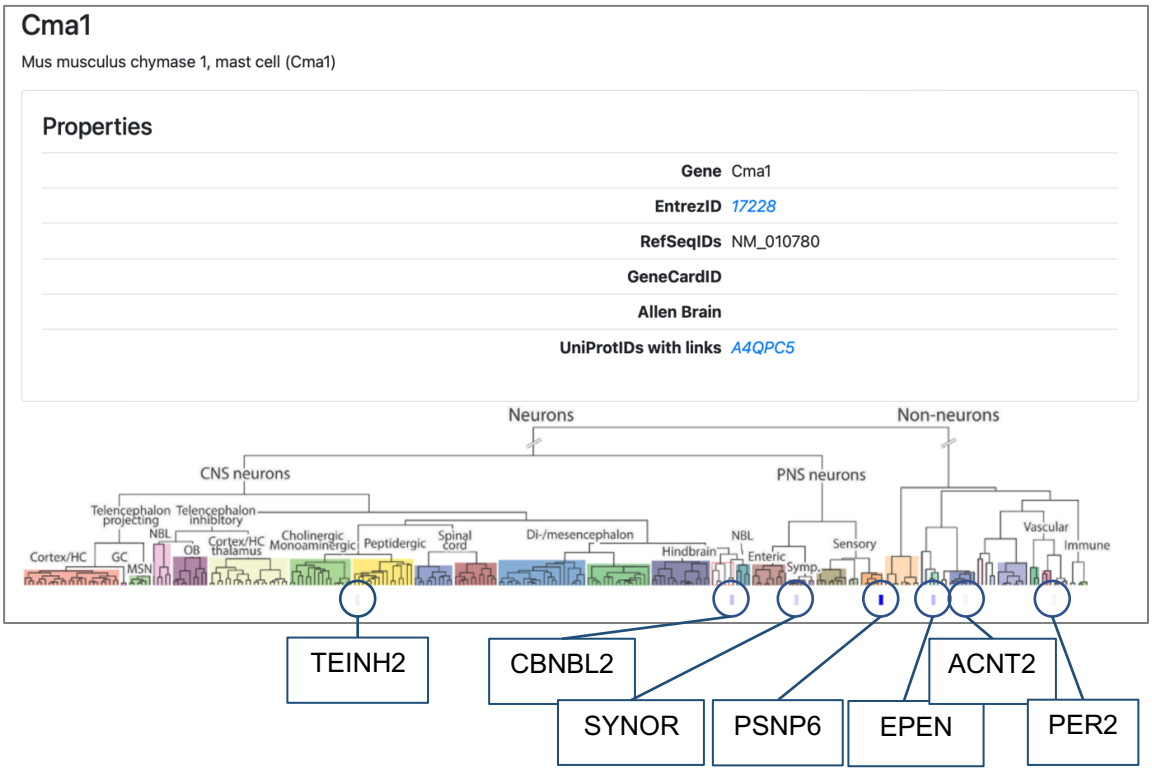

Figure 4-18 Single cell transcriptome data from whole mouse brain revealed *Cma1* expression in non-immune cells

Using droplet-based sequencing, Zeisel *et al.* investigated single cells from the mouse nervous system [205]. An interactive tool at mousebrain.org allowed to browse the dataset for *Cma1* expression. *Cma1*

expression was detected in the central nervous system and peripheral neurons, neuroblasts, ependymal cells, astrocytes and pericytes (cell types abbreviations are explained in Table 4-3 below). All of them had a trinarization score ≤ 0.95.

Table 4-3 Description of cell types and brain regions in Figure 4-18 according to [205]

Symbol	Cell type	Brain region
TEINH2	GABAergic inhibitory neurons	Striatum, septal nucleus
CBNBL2	Neuroblasts	cerebellum
SYNOR4	Noradrenergic erector muscle neurons	sympathetic ganglion
PSNP6	Non-peptidergic peripheral sensory neurons	Dorsal root ganglion
EPEN	Ependymal cells	Ependyma, brain
ACNT2	Non-telencephalon fibrous astrocyes	Hypothalamus, Thalamus, Midbrain dorsal, Midbrain ventral, Pons, Medulla, Spinal cord
PER2	pericytes	CNS

CNS – central nervous system, GABA – γ-aminobutyrate

4.5 Fluorescent protein expression is not restricted to MCs

The single cell transcriptome data by Zeisel *et al.* suggested that the EYFP$^+$ cells in the Mcpt5-Cre EYFP mice observed with LSFM were not exclusively CTMCs. As shown in Figure 4-13, there were clusters of cells with long and branched dendrites which were morphologically categorized as neurons. In order to confirm whether these EYFP$^+$ cells represent neurons, I made 30 µm cryosections of Mcpt5-Cre reporter mouse brains and stained them with a Nissl dye. Since the EYFP is a pH-sensitive fluorescent protein and always lost its fluorescence when counterstained with antibody or dye solutions for several hours, I used the Mcpt5-Cre tdT reporter mouse. The tdTomato is brighter, more stable when treated with staining solutions and buffers and emits at longer wavelength which improves the SNR due to less background fluorescence. Our technician, Kathleen Baumgart, stained the cryosections with NeuroTrace™ (Invitrogen™), a fluorescent Nissl dye for neuron detection, and TO-PRO™-3 iodide (Invitrogen™), a DNA intercalating dye.

Figure 4-19 displays three exemplary regions of such a brain section in which neuronal-shaped EYFP$^+$ cells were detected with LSFM before. And indeed, also in the Mcpt5-Cre tdT reporter mice of same sex and age, neuron-like fluorescent cells were detected in these areas. All of them were positive for NeuroTrace™, but as expected, not all of them cells were tdTomato$^+$ as well. These findings show that the reporter gene expression is probably not restricted to CTMCs.

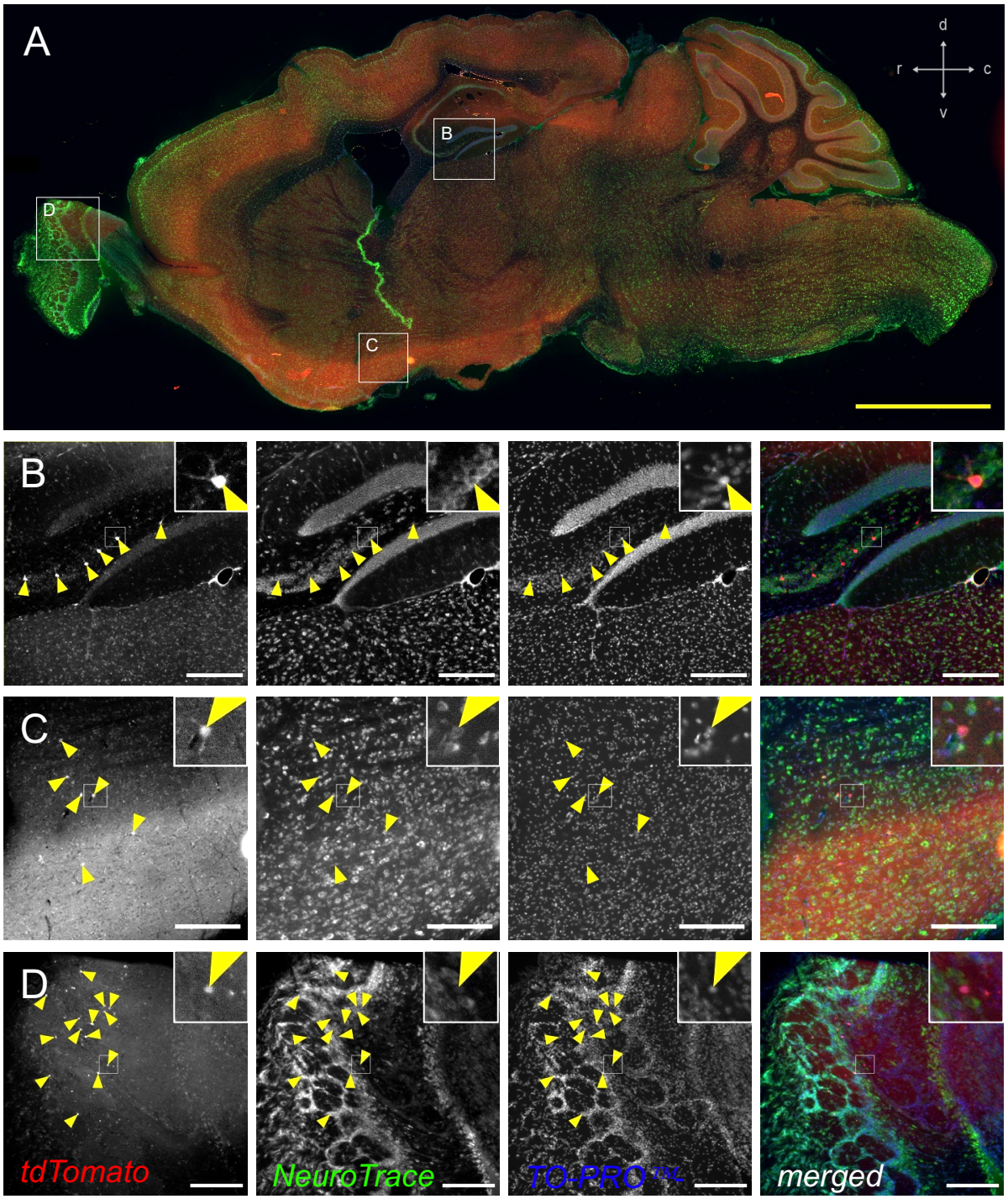

Figure 4-19 Mcpt5-Cre tdT brain sections were counterstained with a fluorescent Nissl dye

When counterstaining tdTomato$^+$ cells in the brain with a Nissl dye (NeuroTrace™, NT), colocalization of both dyes indicated that especially the cell clusters shown in Figure 4-13 comprised of *Cma1* expressing neurons. The regions marked in **A** correspond to the regions in Figure 4-13. **B** represents hippocampal tdTomato$^+$ cells, **C** shows tdTomato$^+$ cells in the preoptic area and **D** in the olfactory bulb. All of them stained additionally with NeuroTrace™. Single tdTomato$^+$ cells marked with yellow arrowheads were magnified in the upper right corner of each image. TO-PRO™-3 iodide was used as a nuclear stain (blue). Scale bars: yellow 2 mm, white 200 µm

As a next step, I aimed to distinguish MCs and non-MCs within the reporter mice. Since it is still under debate, whether all brain MCs express c-kit, which is a universal marker for most MC populations [79], I decided to use again the AB/SO staining. To combine both, the fluorescence-based and histological techniques, I first acquired images with a widefield fluorescent microscope and then removed carefully the cover glass, washed the slices with PBS and continued after drying with the AB/SO staining procedure as described above (3.12). The results are shown in Figure 4-20 and Figure 4-21. In Figure 4-20 brain surface areas are shown. The DM still enveloped the brain partially and homed most of the tdTomato$^+$ cells (Figure 4-20**A, B, C**). These cells had the typical egg-like shape of MCs, with low FP in the cytosol but a brighter tdTomato fluorescence around the nuclei. All of them were identified after histological staining as AB/SO$^+$ (Figure 4-20**A', B', C'**), except of one. Directly attached to the brain surface, in the pia mater region, one comparably big and strongly tdTomato$^+$ cell with an elongated shape is marked in Figure 4-20**A** on the right and identified as AB/SO$^-$ in **A'**. Figure 4-21**A-B'** revealed that neither the tdTomato$^+$ neurons in the hippocampus, nor the tdTomato$^+$ cells in the ependyma, the epithelium of the CP or around blood vessels in the parenchyma stained with AB/SO. On the other hand, Figure 4-21**C** and **C'** showed, that there were few AB/SO$^+$ cells which were not identified as tdTomato$^+$ before.

All in all, most of the AB/SO$^+$ cells were detected in the surrounding meninges, and appeared in either blue (AB$^+$) or red-blue (ABSO$^+$).

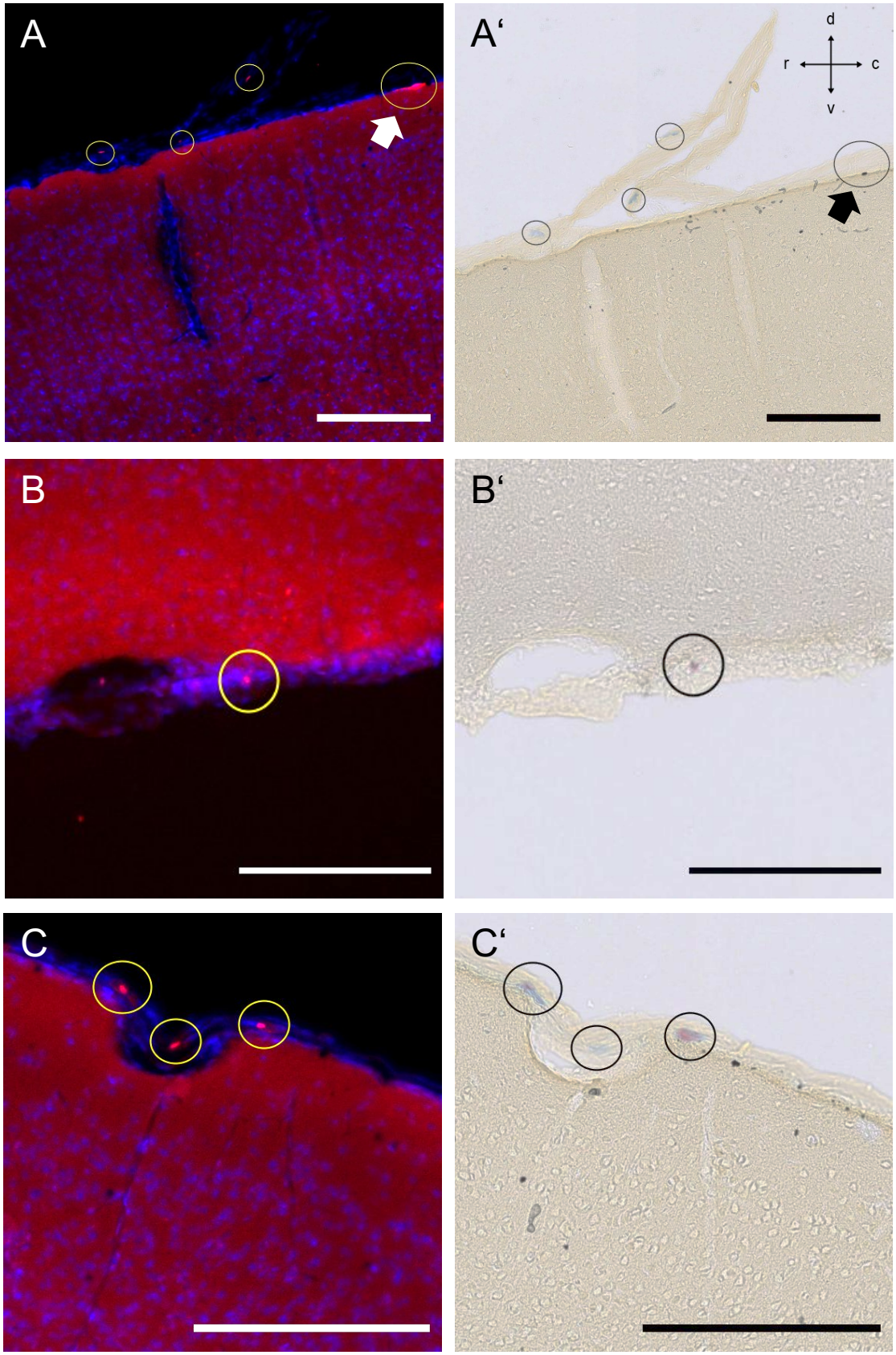

Figure 4-20 Fluorescence imaging of tdTomato⁺ cells in the meninges was followed by AB/SO staining

To investigate which and how many of the tdTomato⁺ cells in Mcpt5-Cre tdT murine meninges are MCs, brain sections were first acquired with a fluorescence microscope (**A, B, C**) and afterwards histologically

stained with the sequential MC stain AB/SO (**A', B', C'**). In the meninges covering the brain surface, tdTomato$^+$ cells stained red-blue (ABSO$^+$) or blue (AB$^+$) as well. Only very few, often bright tdTomato$^+$ cells (white arrow) did not stain with AB/SO (black arrow). Scale bars 200 µm. c – caudal, d – dorsal, r – rostral, v – ventral

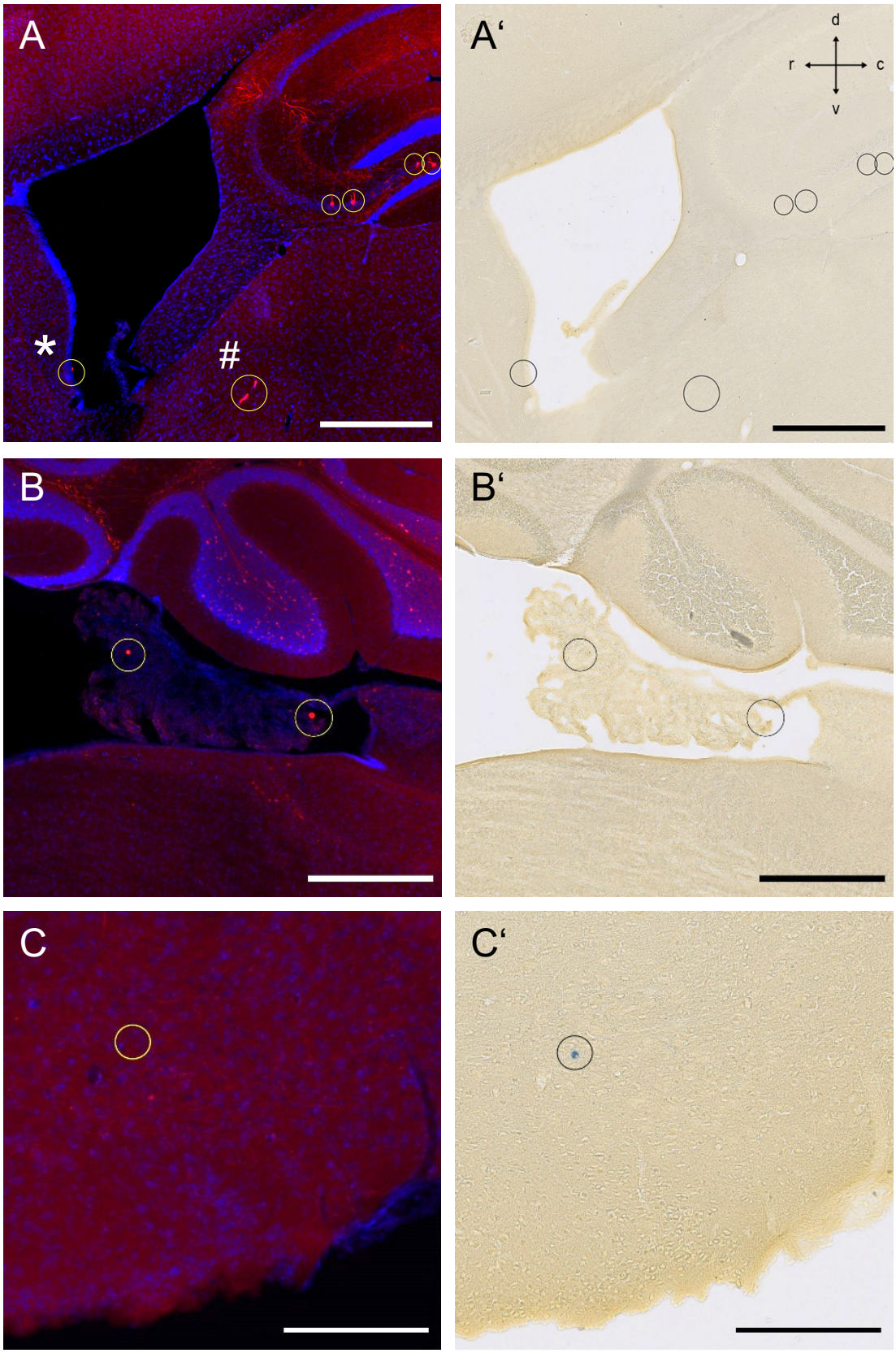

Figure 4-21 Fluorescence imaging of tdTomato⁺ cells in brain parenchyma was followed by AB/SO staining

To investigate which and how many of the tdTomato⁺ cells in Mcpt5-Cre tdT mouse brains are MCs, brain sections were first acquired with a fluorescence microscope (**A, B, C**) and afterwards histologically

stained with the sequential MC stain AB/SO (**A', B', C'**). In contrast to the meningeal cells in Figure 4-20, the hippocampal, as well as ependymal (*) and pericyte-like (#) tdTomato$^+$ cells (**B**) and the very bright brick-like tdTomato cells in the CP (**C**) could not be stained with AB/SO. On the other hand, very few AB$^+$ cells (**C'**) were detected which were tdTomato$^-$ (**C**). **A, A', C, C'** Scale bar 500 µm. **B, B'** Scale bar 200 µm.

When isolating the brain from skull for LSFM, the DM was partially or completely removed or ruptured due to its strong attachment to the calvaria. Thus, the DM had to be prepared separately for microscopy. I carefully removed the sensitive tissue from the inside of the calvaria bone and flattened them on slides. Due to their thinness and transparency, they could be stained and imaged as sections after drying. To address the question whether non-MCs are targeted in the Mcpt5-Cre reporter mice in the DM as well, we counterstained the isolated DM of the EYFP reporter mice with a c-kit antibody and in a second experiment repeated the combined IHC and AB/SO two-step microscopy as described in section 3.12.

As displayed in Figure 4-22, the EYFP fluorescence was barely detectable after antibody and Hoechst treatment. But c-kit$^+$ cells were abundant, scattered in a homogenous distribution over the whole explant while some being positioned like a bead chain alongside vessels.

Even in the second experiment, the EYFP fluorescence was barely detectable and vanished in the autofluorescence of the tissue, the subsequent histological staining revealed many AB/SO$^+$ cells. In contrast to the ABSO$^+$ cells in Figure 4-20, most of them were only AB$^+$ here (Figure 4-21). The distribution pattern seemed to be comparable to what was observed with the c-kit staining in Figure 4-22.

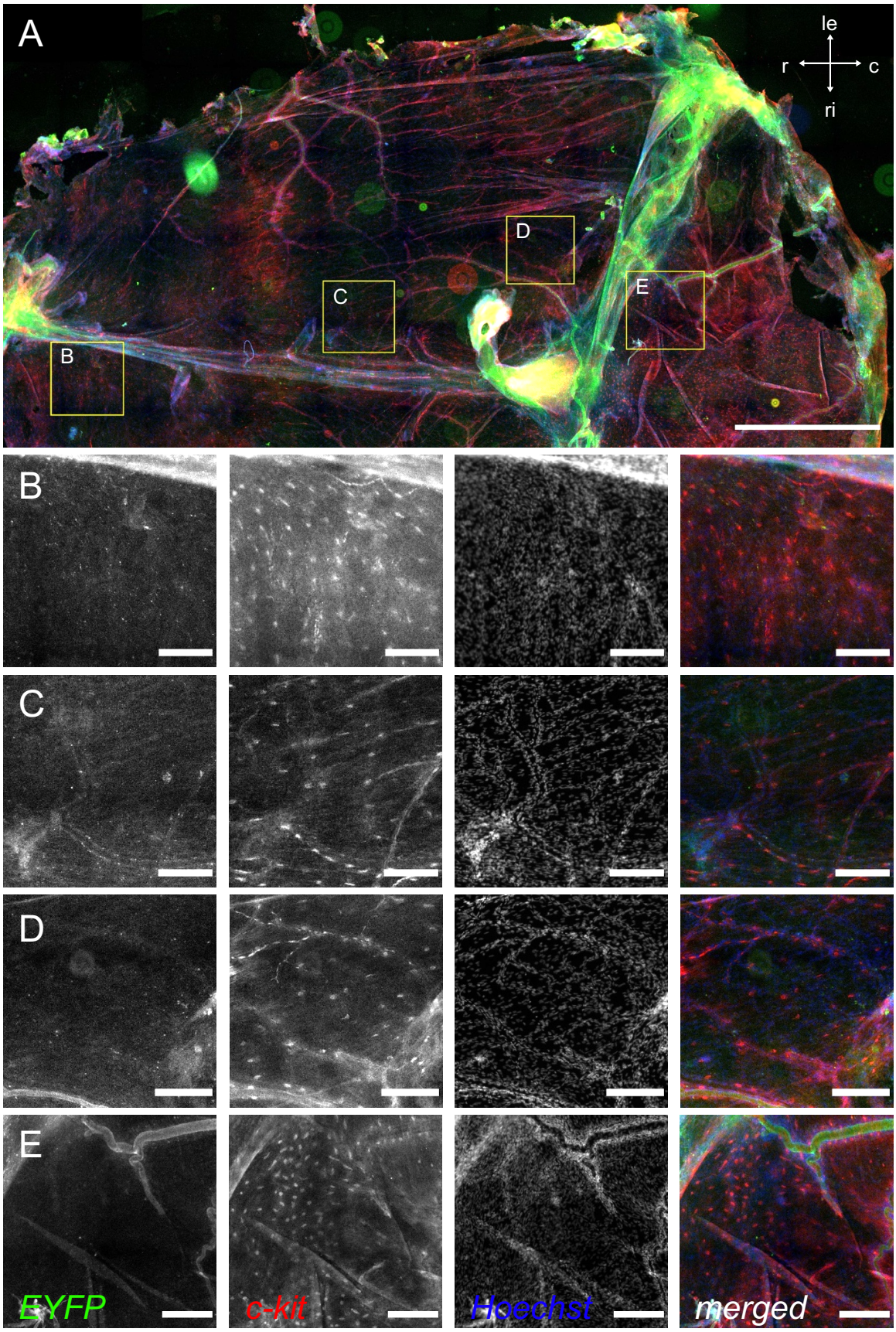

Figure 4-22 EYFP^{+} cells in the meninges were counterstained against c-kit

The DM was isolated and imaged separately from the brains of 10 weeks-old Mcpt5-Cre^{+} EYFP females. These whole-mount explants were counterstained with an anti-c-kit antibody and a Hoechst nuclear dye. The magnified areas from above the right (**B**) and left (**C** and **D**) hemisphere and the cerebellum (**E**) are

marked with yellow squares in **A**. EYFP fluorescence was barely detectable after antibody treatment, but all areas were rich in c-kit$^+$ cells. **A** Scale bar 2 mm. **B-E** Scale bar 250 µm. c – caudal, le – left, r – rostral, ri – right

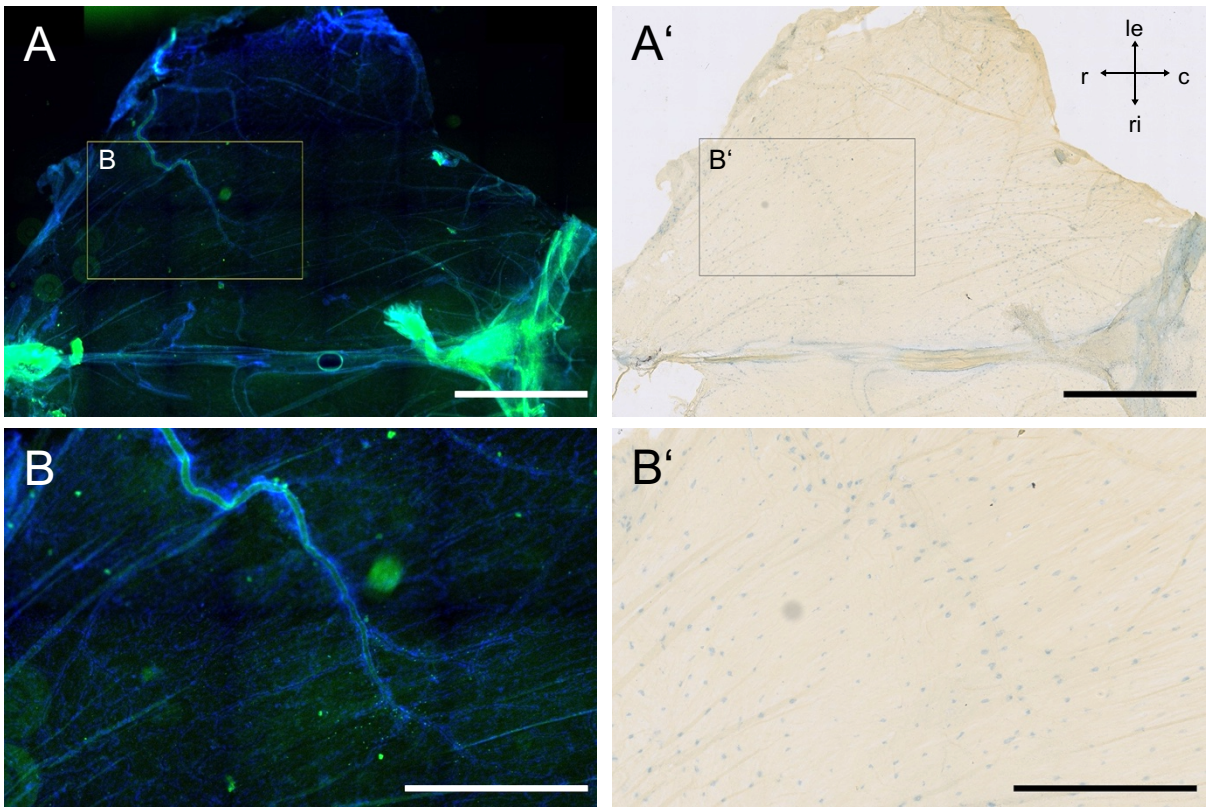

Figure 4-23 Fluorescence imaging of EYFP$^+$ cells in the DM was followed by AB/SO staining
When combining fluorescence microscopy of Mcpt5-Cre$^+$ EYFP DM (A, B) with subsequent AB/SO histological staining (A', B'), the whole DM explant seemed to be rich in AB$^+$ cells. Comparable to Figure 4-22, EYFP$^+$ cells were barely detectable (**B**), but many AB$^+$ cells (**B'**) populated the entire magnified area, marked in **A**. **A** Scale bar 2 mm **B** Scale bar 1 mm. c – caudal, le – left, r – rostral, ri – right

AB$^+$ cells using this AB/SO staining protocol were described as immature MCs or MMC-like. Both MC types lack the highly sulfated and strongly anionic heparin as GAG component in their granules [108, 113]. In contrast, MCs filled with heparin containing granules (mature CTMCs), stain red [108, 113]. Given this fact, the AB$^+$ DM MCs in Figure 4-23 seemed to contain no or less heparin. Thus, they cannot bind avidin as this is used to detect heparin containing CTMCs in the tissue. I tested this hypothesis by staining DM of Mcpt5-Cre tdT reporter mice with fluorescently labeled avidin (Figure 4-24). Surprisingly, most of the tdTomato$^+$ cells were additionally avidin$^+$. As observed before for c-kit$^+$ or AB/SO$^+$ cells, the avidin$^+$ cells were scattered homogenously in the whole specimen, while some were located alongside blood vessels like beads on a chain (Figure 4-24**D**). They were roundish or partially elongated in shape, some of them with the MC typical egg-like appearance. It seemed that all avidin$^+$ cells were tdTomato$^+$ as well. However, not all tdTomato$^+$ cells were avidin$^+$.

Interestingly, all cells with a divergent morphology and strongest tdTomato fluorescence could not be stained with avidin (Figure 4-24**D**, yellow arrows).

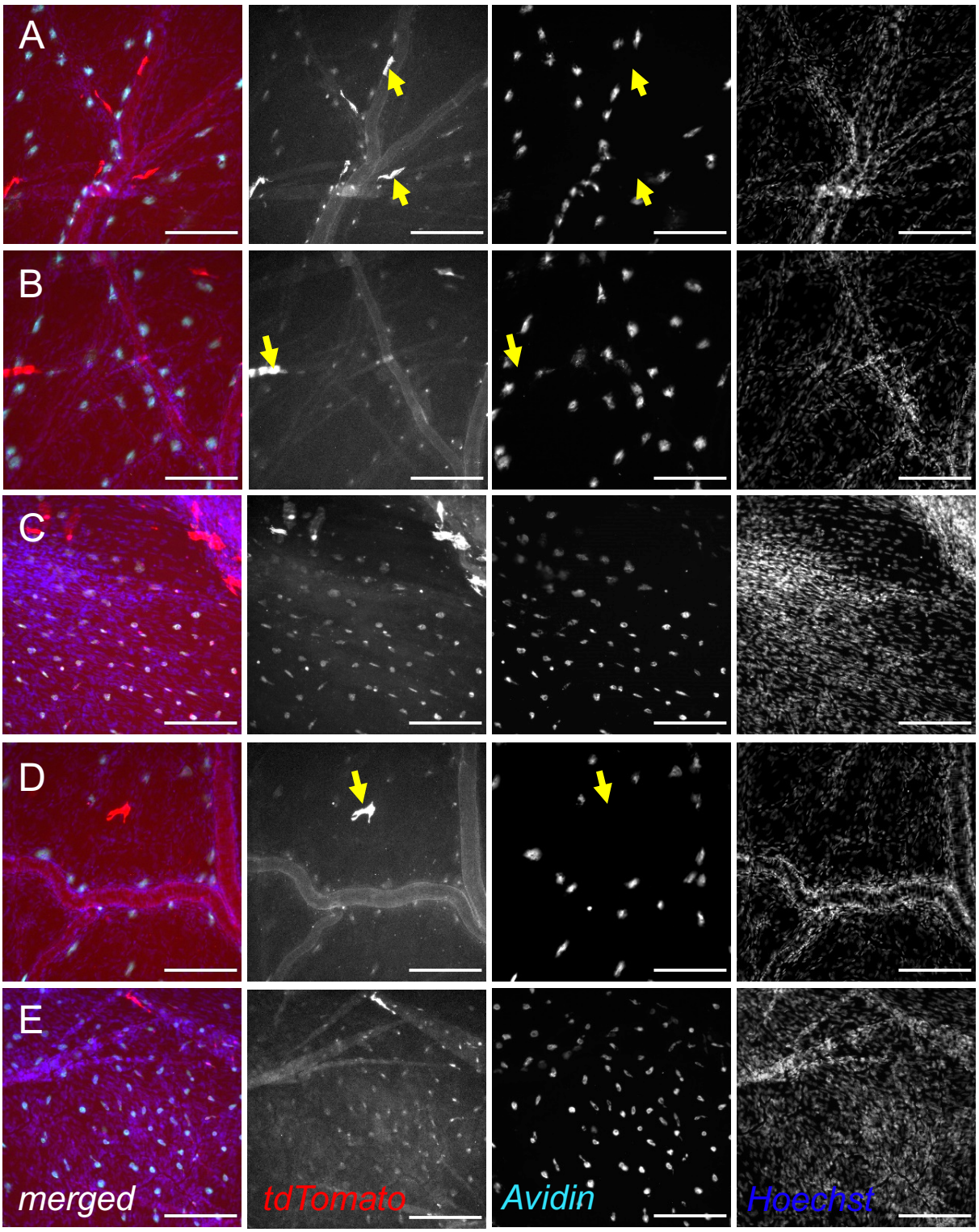

Figure 4-24 tdTomato⁺ cells were counterstained with fluorescently labeled avidin

Mcpt5-Cre tdT mice were stained with fluorescently labeled avidin (cyan). Most of the tdTomato⁺ cells were avidin⁺ as well (A-E). In **A, B** and **D**, double positive cells were located alongside vascular. In **C** and **E**, a high cell density was observed. Some cells, usually different in shape, larger and brighter in

fluorescence than all double positive cells were tdTomato$^+$ but avidin$^-$ (yellow arrows). Scale bar 200 µm

4.6 Quantification of dural MCs by classical staining methods

The co-occurrence of AB$^+$ and ABSO$^+$ cells within one tissue is surprising due to the fact that MCs either contain heparin and stain red (SO$^+$) *or* lack heparin and stain blue (AB$^+$) with AB/SO [166]. Indeed, when I repeated this experiment, I identified very few SO$^+$ cells. Thus, I decided to quantify these three types of AB/SO$^+$ cells (AB$^+$, SO$^+$, or mixed type (ABSO$^+$)) and, since most studies were performed in males or without considering sexes (in regard to the studies in Table 1-3) but I used females, I decided to include both sexes and analyze them separately afterwards. In addition to the cell counts, I determined the area in which these cells were detected in order to calculate the AB/SO$^+$ cells per mm^2. As displayed in Figure 4-25**A**, I noticed that the majority of AB/SO$^+$ cells were of the mixed type (ABSO$^+$), less were AB$^+$ and only very few SO$^+$ cells were identified. Figure 4-25**B** shows clearly that no sex difference could be observed in the total MC counts. However, the cell density in the DM covering the cerebellum was about twice than in the hemisphere-covering DM. No difference could be observed between right and left hemispheres. Whereas the ABSO$^+$ cells seemed to be homogenously distributed over the whole meninges, the SO$^+$ cells were detected mainly in the anterior and posterior areas and the AB$^+$ cells were located in the edges and along the sagittal and transverse sinus (Figure 4-25**C**).

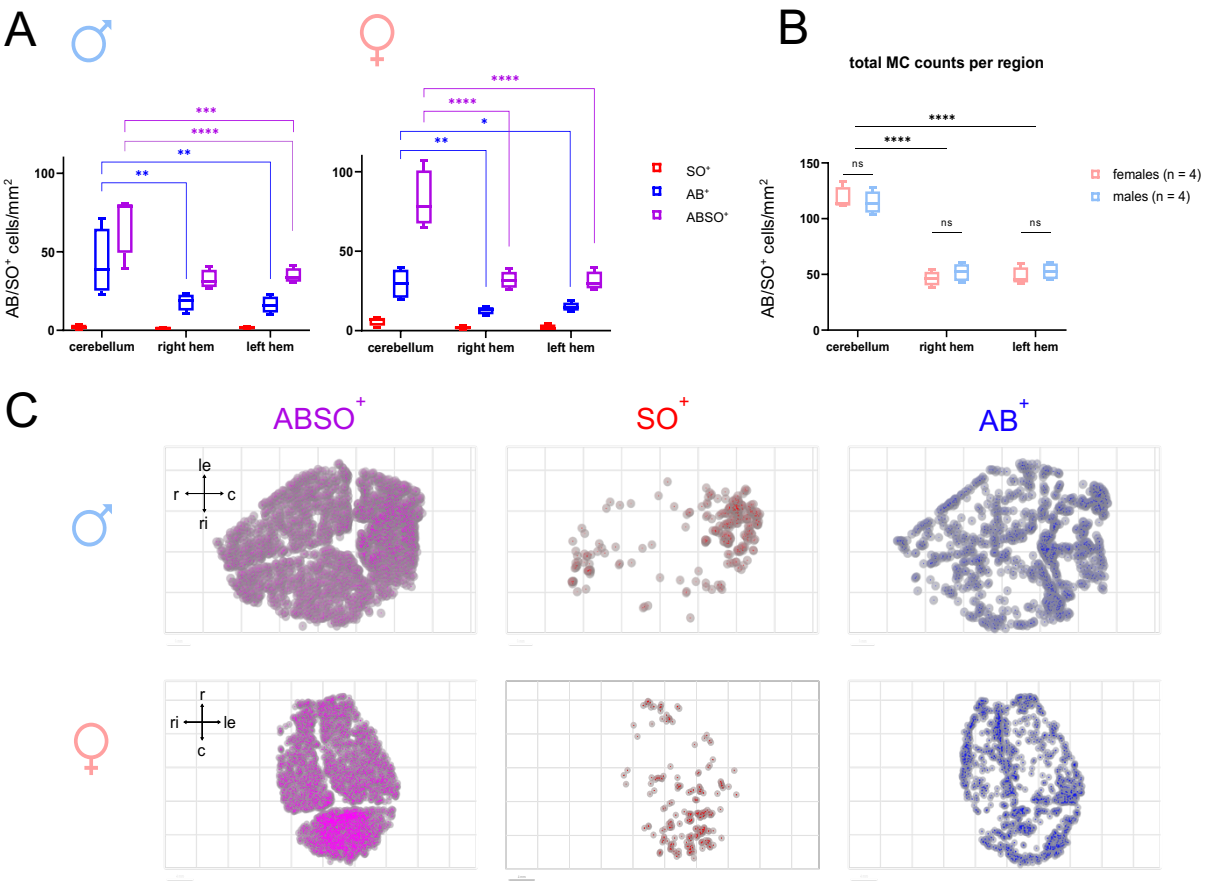

Figure 4-25 AB/SO staining of the DM detected AB⁺ 'blue' cells, SO⁺ 'red' cells and a 'red-blue' ABSO⁺ mixed type

Using the sequential MC stain AB/SO, MCs of the DM stained either red-blue (ABSO⁺), blue (AB⁺) or red (SO⁺). **A** In both females and males mainly ABSO⁺ cells (purple) were counted, less were AB⁺ (blue) and only very few SO⁺ (red). In the cerebellum-covering region, there were significantly more ABSO⁺ and AB⁺ cells compared to the regions above the hemispheres. **B** The total number of AB/SO⁺ cells per mm^2 revealed no differences between both sexes. Whereas total MC counts were equal between the left and the right hemisphere-covering regions, the MC density above the cerebellum was about twice as high ($\alpha < 0.0001$). **C** Interestingly, AB⁺ MCs could be detected preferentially in border regions – close to the sinuses and along the edges. AB – Astra blue, c – caudal, hem – hemisphere, le – left, ns – non significant ($\alpha \geq 0.05$), r – rostral, ri – right, SO – safranin O. * $\alpha < 0.05$, ** $\alpha < 0.01$, *** $\alpha < 0.001$, **** $\alpha < 0.0001$

4.7 Defining the nature of dural EYFP⁺ cells in Mcpt5-Cre reporter mice

As mentioned above, the AB/SO staining was developed to distinguish MMCs and CTMCs or immature and mature CTMCs. A mixed type has been rarely detected. Burton proposed in 1964 for rat MCs [113], that ABSO⁺ cells may represent a transitional form between the blue AB⁺ and the red SO⁺ types. To find out how these three MC types differ in their gene expression

profile, we performed single cell RNA sequencing of EYFP$^+$ cells from Mcpt5-Cre EYFP female DM. This method will allow to answer two questions: 1. whether the EYFP expression is restricted to MCs in the DM and 2. whether three different subtypes of MCs can be distinguished mirroring the AB/SO staining results.

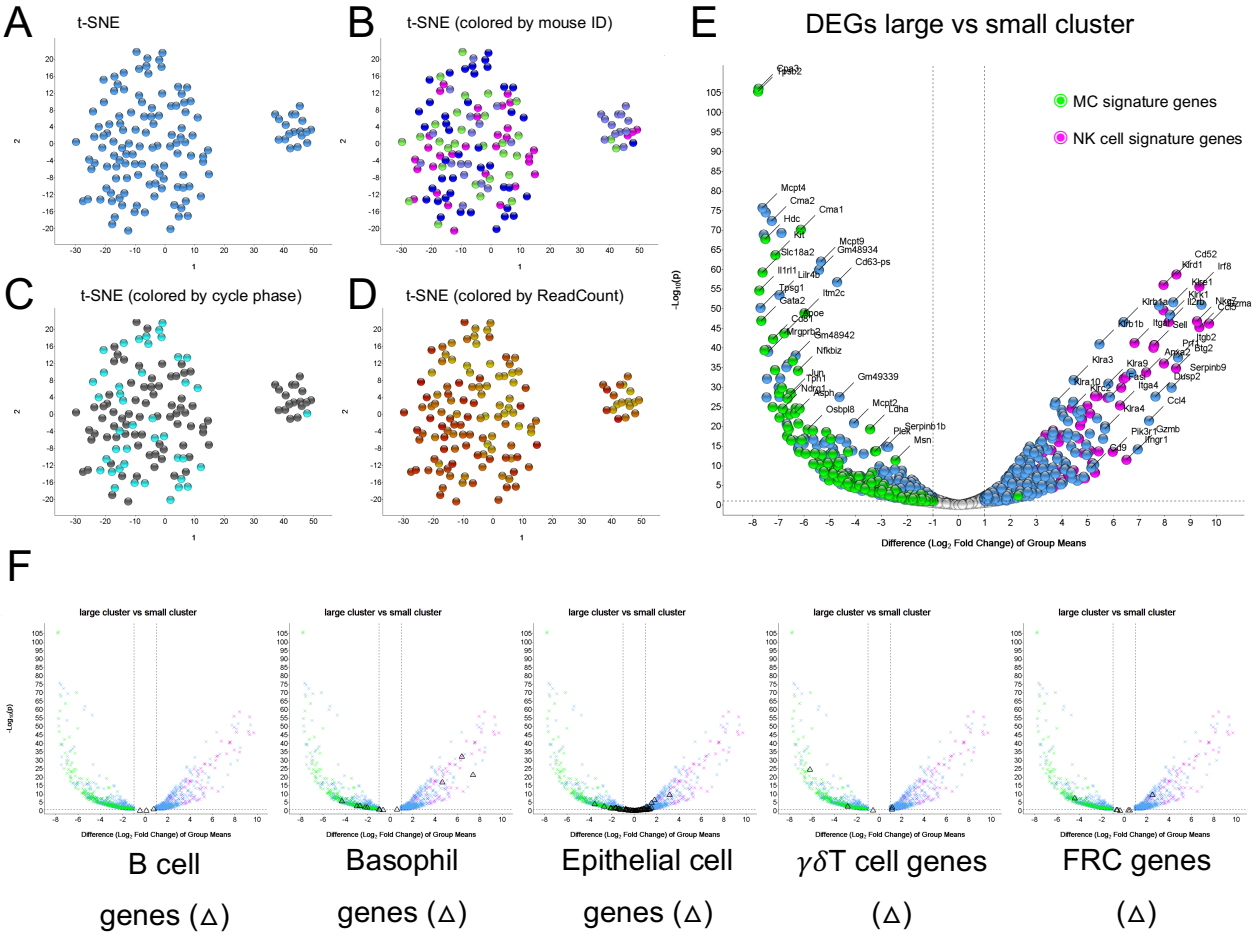

Figure 4-26 Single cell RNA sequencing from EYFP$^+$ cells in the DM

EYFP$^+$ cells were isolated out of Mcpt5-Cre$^+$ EYFP DM and single cells were sorted and sequenced. The resulting t-SNE plots revealed two distinct cell clusters (**A**). These two clusters could neither be explained by mouse ID (**B**), estrous cycle stage (with diestrus in light blue and estrus in grey) (**C**) nor ReadCounts (**D**). Low ReadCounts were labeled in yellow, high in red. **E** Two group comparison allowed to identify differentially expressed genes (DEGs) of both clusters, which were displayed in a volcano plot. MC signature genes (green) and NK cell signature genes (magenta) described the two populations best and thus, were highlighted. **F** No other immune cell signature genes were enriched in only one of the clusters. Signature genes for B cells, basophils, thymic epithelial cells, γδT cells, and fibroblast reticular cells (FRC) were added in the same volcano plot as black triangles. Immune cell signatures (cf. Supplemental Table 1) were identified and excerpted in a publicly available dataset of the Immunological Genome Project, ImmGen (GSE37448, [191]). Official gene names were used in E.

After prefiltering the resulting dataset which is described in section 3.13, two cell clusters could be distinguished clearly, as shown in Figure 4-26**A**. These clusters could neither been explained by the individual mice (Figure 4-26**B**), the estrous cycle stage (Figure 4-26**C**), nor the ReadCounts (Figure 4-26**D**), but may present two different cell types. In Figure 4-26**E**, the DEGs of both clusters were displayed in a volcano plot. To annotate these cell types, I used a publicly available transcriptome dataset (GSE37448, [191]) dealing with more than 30 different immune cell subsets and excerpted lists of signatures genes for different cell types (cf. Supplemental Table 1 and Supplemental Table 2). The volcano plot in **E** is colored by the best fitting gene lists: MC signature genes (green) and NK cell signature genes (pink). Since the MC genes were almost exclusively on the left side and the NK cell genes on the right, this labeling characterized the two clusters as MCs (large cluster) and NK cells (small cluster). In contrast, I marked exemplary BC, basophil, thymic epithelial, TC and fibroblast reticular cell signature genes as black triangles in the same volcano plot in Figure 4-26**F**. None of these signatures could be identified only on one side of the plot. Most of the genes were localized in the center and thus, have no impact on the clustering. This labeling method confirmed, that the EYFP expression in the DM of Mcpt5-Cre EYFP mice is not restricted to MCs. Once identified as MCs and NK cells, the two clusters colored by mouse IDs in Figure 4-26**B** revealed, that 2.4% (1 of 42 cells (dark blue)) to 42.9% (12 out of 28 cells (light blue)) of $EYFP^+$ cells sorted for this experiment were NK cells.

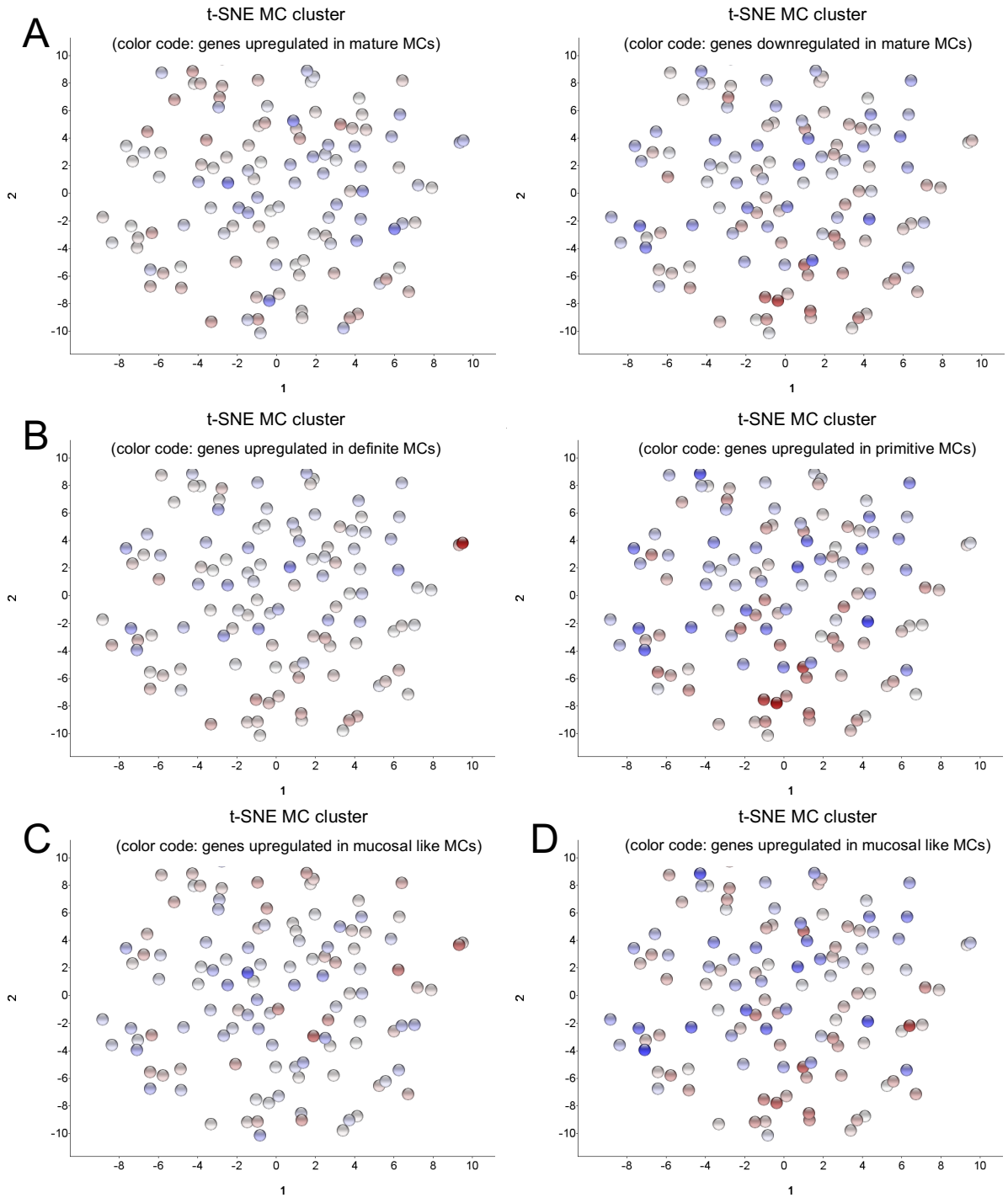

Figure 4-27 The MC population did not subcluster in terms of maturation state, hematopoietic origin or subtype

A Akula *et al*. [104] published a list of DEGs between mature and immature MCs. When color coding the MC population („large cluster“ in Figure 4-26) according to the lists, neither obvious subclustering could be observed nor an alternating color pattern between the left (mature MC genes) and right (immature MC genes) t-SNE plots. **B** The same appeared when coloring the MC cluster according to gene lists containing DEGs between MCs of definite (left) and primitive (right) hematopoietic origin (generated using the GSE104790 dataset by Gentek *et al.* [90]). **C, D** When coloring the t-SNE plots according to gene lists containing mucosal MC (MMC) genes, identified in two different studies ([206,

207]), the coloring patterns were expected to overlap for separating the MC cluster in two subtype populations. If the coloring shows no similarities, as observed here, the DM MCs probably will not subcluster in terms of subtype. Genes subsets are listed in Supplemental Table 3. Red – upregulation of the listed genes, Blue – downregulation of the listed genes

For further analysis of the MC cluster, the NK cells were excluded from the dataset. In order to identify subclusters which may explain the three populations observed with AB/SO staining, two different algorithms were applied on the MC cluster. But neither the unsupervised clustering algorithm kmeans (based on kmeans++ by Arthur and Vassilvitskii [208]), nor the Isomap dimensionality reduction (based on [209] and [210]) could identify subclusters. Consequently, I decided against unsupervised clustering and started a manual approach to explore the MC data. Since the AB/SO staining distinguishes either MMCs and CTMCs or immature and mature MCs, I searched for transcriptome studies and open accessible datasets, in which gene expression characteristics of these four MC subtypes were described. Akula *et al.* presented in [104] the differences in the gene expression pattern of mature (pMCs) and immature (BMMCs) MCs, whereas Kasakura *et al*. [207] and Yamaguchi *et al.* [206] both published genes upregulated in MMC-like cells. Additionally, I included a study in which the authors investigated the differences of primitive (yolk-sac-derived) and definite (HSC-derived) MC subsets, meaning MCs of varying hematopoietic origins [90] (all genes lists are available in Supplemental Table 3). From all of these studies I created gene lists of DEGs, which characterize the distinct MC subtypes and were identified by the authors in the certain study.
In Figure 4-27**A**, the MC cluster was labeled by genes, which were upregulated (left) or downregulated (right) in mature MCs according to Akula *et al.* [104]. If maturation played a role, the coloring patterns of both plots should behave alternating and most probably, the red or blue labeled cells should cluster. But both could not be observed. The same holds true for Figure 4-27**B**, in which the MC cluster was labeled by genes which were identified by Gentek *et al.* to be upregulated in definite MCs (left) or upregulated in primitive MCs (right) [90]. It seemed that the red cells accumulate on the bottom of the plot, but since the coloring patterns behave not alternating, it is unlikely that the MCs form subpopulations by different hematopoietic origins. In Figure 4-27**C** und **D**, the MC cluster is labeled by gene sets which were discovered to be upregulated in MMCs by Kasakura *et al*. [207] and Yamaguchi *et al*. [206]. It would be likely that both plots show a similar coloring pattern, if MMCs and CTMCs and a third, probably transitional state, are the subtypes observed after AB/SO staining, but there are too few similarities between the two plots to define any subpopulations.

During the MC counting and quantification process, I have made two observations, which may indicate a fourth alternative as a cause for the three AB/SO$^+$ populations. First, as shown in Figure 4-25**C**, the AB$^+$ MCs were located mainly on the edges and alongside the sinuses.

These regions are strongly attached to the skull bone. While removing them carefully from the skull bone, these areas are touched with forceps the most. Second, while the SO^+ cells were mainly small, definite, roundish and had a clear boundary, the AB^+ cells were bigger, irregularly shaped, look sometimes ruptured, or even lost their cellular morphology. Most of them lacked a clear cellular boundary. The $ABSO^+$ cells varied strongly in their appearance regarding shape and red-blue ratio, but showed a distinct arrangement of the dyes. While the red dye always bound inside, the blue dye bound in the border region of the cell. Therefore, I hypothesized that the blue, AB^+, cells might be activated and/or degranulated, but not emptied (the complete loss of all granules would make them invisible). The red, SO^+, cells might be inactive and intact, whereas the mixed type $ABSO^+$ cells might be partially degranulated. The pH outside of the cells, in the tissue, differs from the acidic pH inside the intact lysosome-like SG, which may lead to a stepwise altered staining characteristic from red to blue when the cells degranulate.
As a result, I repeated the analysis of subcluster identification in the MC cluster by using datasets dealing with MC activation. Two studies had analyzed how the gene expression changes in MCs after activation. In Figure 4-28**A**, a dataset of human cultured skin MCs, activated by FcεRI crosslinking was used for color-coding [211]. In Figure 4-28**B**, a list of genes upregulated in LPS-stimulated BMMCs was the basis for the coloring [104]. Since both studies differ in MC type, MC origin, species and activation stimulus, also the DEGs might differ in a way that subclusters could not be recognized. But surprisingly, in both plots in the upper left corner, red labeled cells seemed to accumulate. Those were only few but a tendency to cluster formation was visible and worth to be further investigated.

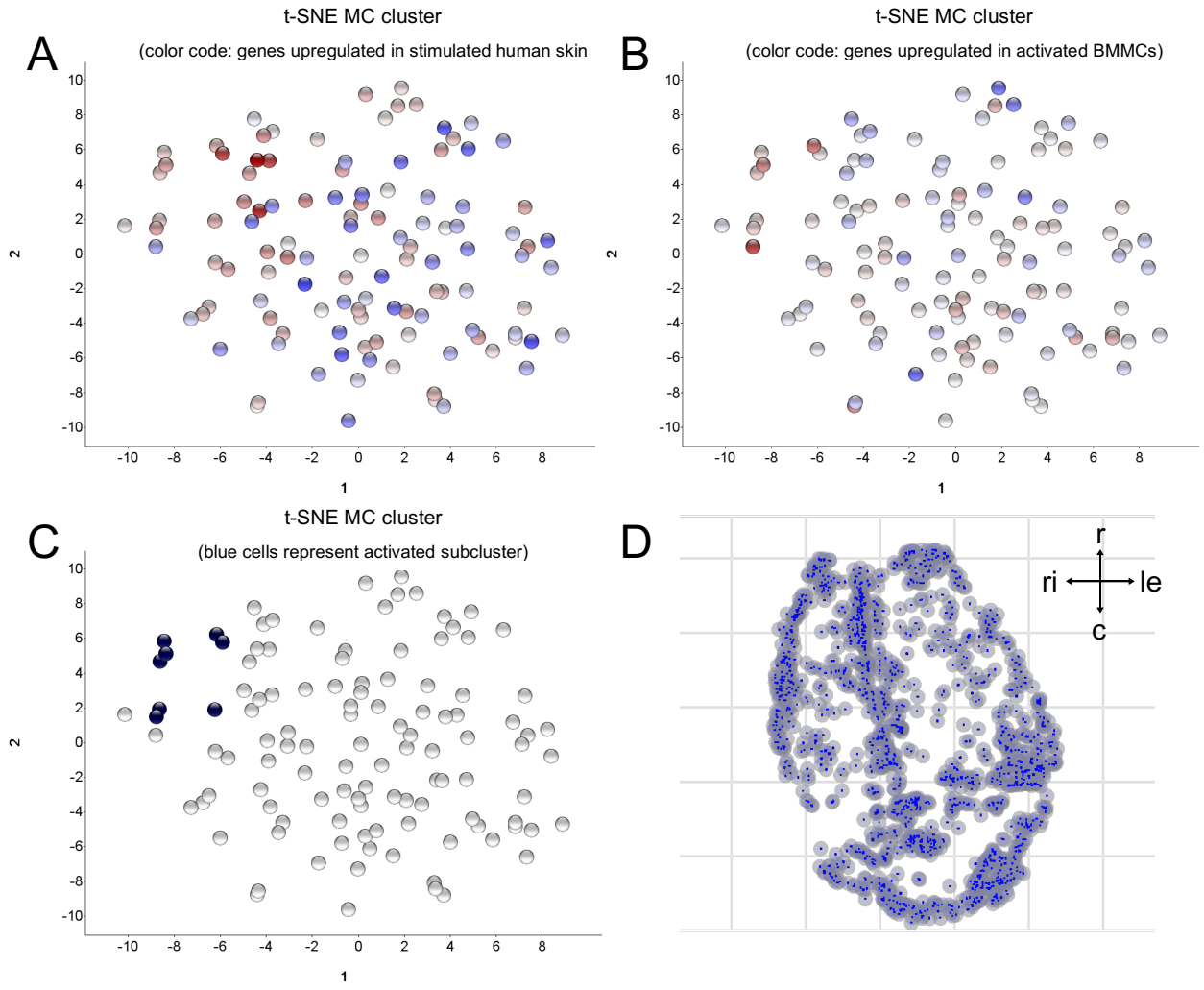

Figure 4-28 The MC population seemed to subcluster in terms of activation state

A, B When coloring the MC cluster („large cluster“ in Figure 4-26) according to gene lists composed of genes upregulated in activated MCs (taken from [104, 211], cf. Supplemental Table 4), the color patterns showed a similarity. In the upper left corner (dark blue cells marked in **C**), a subcluster of ‘reddish‘ cells appeared. These cells may have features of activated MCs. **D** reproduces one of the distribution patterns in Figure 4-25**C**, displaying the arrangement of AB^+ cells mainly in the outer DM regions and along the sinusoid structures. Red – upregulation of the listed genes, Blue – downregulation of the listed genes, BMMCs – bone marrow-derived mast cells, c – caudal, le – left, r – rostral, ri – right

4.8 CTMC-like dural MCs show different activation states

In order to test the hypothesis that AB/SO staining can display MC activation, I slightly adapted the DM isolation and fixation procedure from above (cf. Figure 3-4). Therefore, the mice were not perfuse-fixed prior to DM isolation (Figure 4-29**A**). The euthanized mice were quickly decapitated and the brain was carefully removed from the ventral side of the skull. The calvaria including the DM were directly placed in either 1xPBS (as a control), cromolyn sodium (a MC stabilizer) or A23187 solution (a calcium ionophore). In contrast to the MC stabilizer reagent which blocks MC degranulation [212], calcium ionophores are able to induce maximal degranulation responses in MCs in a dose-dependent manner [213, 214]. After 20 minutes of incubation, the skull was fixed, followed by DM isolation. The DM MCs were stained, counted and quantified as described in section 3.12 . Figure 4-29 shows the results as distribution patterns in **B** and summarized in bar charts in **C** and **D**. While the MC counts and percentages of the three populations did not differ significantly between PBS and cromolyn treatment, the calcium ionophore treatment decreased the intact (SO^+) and partially degranulated ($ABSO^+$) MCs significantly and increased the degranulated (AB^+) cell population. In addition, Figure 4-29**D**, which displays the total MC count per mm^2 shows a tendency that the total number of identifiable MCs might decrease as well.

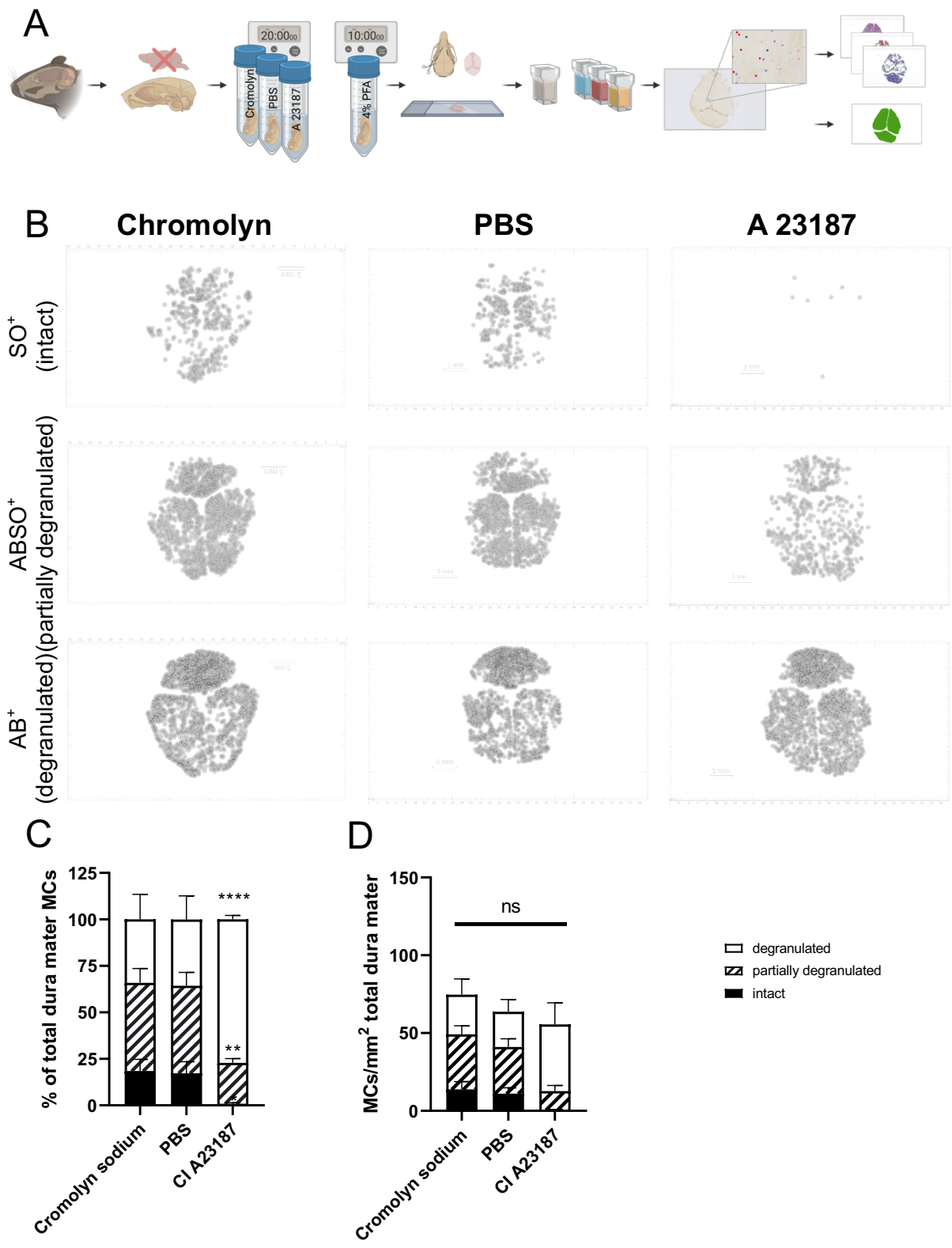

Figure 4-29 Differential AB/SO staining revealed activated MCs

A Non-fixed murine skulls rid of the brain, were incubated for 20 min in PBS, cromolyn or A23187, a calcium ionophore, prior to fixation. The staining and counting procedures were the same as for Figure 4-25. Created with Biorender.com **B** represents the resulting distribution patterns of SO^+ (only red, intact), $ABSO^+$ (red-blue, partially degranulated) and AB^+ (only blue, degranulated) MCs. The percentages of all three cell states for each treatment are summarized in stacked bar charts in **C**. **D**

displays the total MC numbers per mm^2. AB – Astra blue, CI – calcium ionophore, MC – mast cell, PBS – phosphate buffered saline, PFA – paraformaldehyde solution, SO – safranin O. **** $\alpha < 0.0001$, ns $\alpha > 0.05$

To sum this up, the utilization of AB/SO staining is not limited to distinguish MMCs and CTMCs or immature and mature CTMCs, but can display MC degranulation as well.

Taken together, I could detect EYFP expression in MCs and non-MCs in the brains of female Mcpt5-Cre EYFP reporter mice. By combining state-of-the-art three-dimensional fluorescence microscopy with classical MC stainings and transcriptome profiling, I investigated the Mcpt5 expression in the brain comprehensively. Hereby, it turned out, that the suitability of this transgenic mouse line for further studies of cerebral MCs is poor compared to the high specificity reported for peripheral tissues.

5 Discussion

This study aimed for investigating brain MCs at three intra-organ localizations. Due to the lack of suitable MC-specific mouse models so far, their functional role is not yet fully understood. In this thesis, the Mcpt5-Cre mouse model was used, known for its high MC-specificity in peripheral tissues. Considering that the usefulness and quality of a mouse model may vary depending on the organ, I investigated the brains of Mcpt5-Cre EYFP mice for the first time in order to assess their suitability for brain MC studies.

For macrophages in the brain, different subtypes can be discriminated, the stromal macrophages and epiplexus cells in the CP, the brain-resident microglia in the parenchyma and meningeal subpopulations. As these subtypes differ in their transcriptome and predicted functions [15, 44, 175], we herewith hypothesized that MCs from CP, meninges and parenchyma show molecular and functional differences as well. Aiming to discover those varieties, we performed bulk RNA sequencing of $EYFP^+$ cells from each of the three brain regions of Mcpt5-Cre EYFP mice. Bulk RNA Sequencing has the advantage to be less noisy than single cell sequencing, which facilitates to focus on intra-organ differences via DGE analysis. In addition, we compared the cerebral subsets with peritoneal $EYFP^+$ cells of the same mouse. These peritoneal $EYFP^+$ cells from the Mcpt5-Cre EYFP reporter line were previously confirmed to be connective-tissue type-like MCs (close to 100% c-$kit^+Fc\varepsilon RI\alpha^+$) [139]. Thus, it is not surprising that both dimensionality reduction plots and hierarchical clustering displayed a strong relation to the meningeal samples but less similarities with parenchymal and CP samples, respectively. The DM is rich in connective tissue and previous studies in rodents already identified CTMCs there, based on typical staining characteristics [122, 167, 215]. This is supported by more recent investigations of the meningeal immune cell transcriptome, publicly available at brainimmuneatlas.org [57]: Whereas CTMC genes (*Cma1*, *Tpsb2* and *Mcpt4)* were detected, the MMC genes *Mcpt1* or *Mcpt2* were not identified.
However, it turned out, that compared to the meningeal and peritoneal $EYFP^+$ cells, the parenchymal and CP samples showed reduced MC gene expression, and in two of the three CP samples, none of them were expressed at all. This may suggest that two subtypes exist in the CP with only one expressing the typical CTMC genes as *Cma1*, *Cpa3*, *Mcpt4*, *Tpsab1* and*Tpsb2*. But, in stark contrast, the CP samples showed no subclustering in PCA. Moreover, in the Pearson correlation matrix, CP samples displayed strongest clustering (> 0.99), which suggests a high uniformity in their overall transcriptome profile. From publicly available single cell transcriptome data, it is hard to suppose whether different subtypes may exist. Dani *et al*. detected MCs only in embryonic but not in adult CPs and except of low *Kit* and intermediate *Gata2* expression, they did not investigate particularly MC marker genes. The same applied

for the adult murine CPs investigated by van Hove *et al.* [57] without identifying any MCs. Only when mice were infected, the same group detected very few MCs in the CP [216]. However, none of them expressed *Cma1*, *Tpsb2, Tpsab1* or *Mcpt4* and only a subpopulation showed *Cpa3* expression.

In order to validate that the discrepancy in the CP transcriptome profiles is not an artefact of the method or the single experiment, we repeated the sorting of 50 EYFP$^+$ cells from the same four body locations and subsequently quantified the expression of selected MC genes via qPCR. Control samples from splenocytes (negative ctrl), BM (BMMCs, immature and cMMCs, MMC-like) and skin (CTMCs) were included to compare with the brain samples. The peritoneal MCs expressed all CTMC genes (*Cma1, Tpsb2, Mcpt4, Kit, Fcer1a*), but highest *Tpsb2*, *Cma1* and *Mcpt4* as observed by Akula *et al.* in a recent study as well [107]. All of the five MC genes could be detected in all brain samples except of, interestingly, one CP and one meningeal sample. In these last-mentioned, the housekeeping gene expression (*Rps18*) was not altered compared to all other samples, but none of the selected MC genes could be determined, which is in accordance with what was observed in the RNA sequencing analysis. In the negative control (CD3ε^+ splenocytes), no MC genes were detected except of one showing low *Cma1* expression. Surprisingly, *Cd3e* was detected only in 50% of the splenocyte samples even if the translated protein was the basis for sorting these cells. It can be, that the transient number of transcripts at the timepoint of sorting was too low to detect them in these cells. The same can cause the absence of detectable amounts of either *Tpsb2*, *Kit* or *Fcer1a* in few of the skin samples. In some of them, single genes were not detectable, but in three out of six samples, transcripts of all of the targeted genes were measured. *Mcpt4* is not expressed in the BMMCs, which confirms their immature state [89]. In cMMCs, *Mcpt2* can be detected, as supposed [97], and in addition in one meningeal sample. The latter is in accordance with the observation that meningeal MCs upregulate *Mcpt2* when activated [217]. Notably, *Cd3e* expression was detected in the negative controls, as expected, but additionally in two of the six skin samples. This is surprising since *Cd3e* expression is generally thought to be exclusive for T lymphocytes. There is only few evidence that *Cd3e* is also expressed by NK cells or cerebellar Purkinje cells [218, 219].

All in all, a clear MC-typical profile, as observed in previous studies when MC subsets were described elsewhere, cannot be identified here. I concluded that these are either atypical MC subsets or a mixture of at least two different cell types in changing compositions. With the last-mentioned, I consider the limitation of the method. The pooling of cells for bulk RNA sequencing or qPCR results in mixing their transcriptome profiles. This reduces the noise of single cells on the one hand, but creates an artificial profile as soon as the cells are not pure

in terms of a specific population. And indeed, although this mouse model is often used in MC studies due to its high specificity compared to kit mutant mice and other transgenic mouse models, an unspecific targeting was observed before. Non-MC recombination in the Mcpt5-Cre EYFP mice was shown in NK cells in the blood (12% $EYFP^+NK1.1^+CD49b^+$) [1] and spleen (30%$EYFP^+NK1.1^+NKp46^+$) [146], and < 20% of splenic $CD11b^+$ cells ($EYFP^+CD11b^+$) [146]. Whether the *Cd3e* expression in the two skin samples result from $EYFP^+$ NK cells as well needs to be further elucidated. But it seems likely given that a small number of $EYFP^+$ non-MCs (2.7% $EYFP^+CD117^-Fc\varepsilon RI\alpha^-$) were detected before in ear skin cell suspensions of these mice [1].
Interestingly, a single cell transcriptome dataset of brain immune cells, identified *Cma1* to be expressed primarily in NK cells of whole brain, meninges and CP as well [57].

In accordance with this, the bulk sequencing analysis revealed lymphocyte genes to be upregulated in all parenchymal, meningeal, one peritoneal and interestingly, one CP sample which lacked any detectable MC gene expression. In all of these samples *Gzma* (expressed in cytotoxic CD8 T cells), *Ncr1* and three Klr genes (all expressed in NK cells) were upregulated. To my knowledge, MCs do not express *Ncr1* and neither Akula *et al.* [107] nor van Hove *et al.* [57] detected this gene in MCs and *Gzma* was described as almost undetectable [107]. This underlines the hypothesis of an inhomogeneous composition of the bulk samples, containing both $EYFP^+$ MCs and non-MCs.

Of note, the transient presence of mRNA transcripts is always an issue to keep in mind when interpreting the results of transcriptome studies. Due to a constant RNA turnover inside the cells, one should consider that every transcriptome profile is a snapshot of a cell state and may not represent the full characteristic and functionality. Especially under stress conditions when dissociated from the tissue, the cells degrade more mRNAs and adjust their transcription in parallel, which may result in a biased output [220, 221]. Consequently, I carefully surveyed every sample and selected with the help of experts only those for further analysis, which showed no abnormalities in QC tests (RNA sequencing) and a comparable housekeeping gene expression (qPCR).

All in all, I detected MC genes in the $EYFP^+$ cells of Mcpt5-Cre EYFP mouse brains. However, with these bulk RNA based methods, the MC-specificity of Mcpt5-Cre in the brain cannot be assessed.

With the use of different fluorescence microscopy techniques, the ectopic EYFP expression could be visualized. Therefore, an organic clearing protocol for LSFM was developed, based

on the ethyl cinnamate clearing by Klingberg *et al.* [188]. In contrast to what the authors observed when treating kidneys of CD11c-EYFP mice with the organic solvent, I could not preserve the endogenous fluorescence in Mcpt5-Cre EYFP reporter mouse brains. Thus, I enhanced the endogenous FPs with the use of nanobodies as suggested by Cai *et al.* in the vDisco protocol [58]. Further improvements in regard of nanobody penetration were proposed by the same group (SHANEL protocol for human organs) [202]. But it failed for my purpose due to significantly reduced nuclei staining quality. Finally, I noticed that the quality and penetration of the nanobodies varied depending on the manufacturer and the coupled fluorophore. This phenomenon was recognized by the authors of the vDisco method as well and was documented for different batches on their website as a consequence [222].

Interestingly, with the final clearing protocol, I observed substantially more EYFP$^+$ cells per mouse than isolated in the previous FACS experiment. On the one hand, the expression pattern of the fluorescent cells was comparable for some regions (mainly olfactory bulb (glomerular layer), preoptic area, hippocampus, brain surface, CP and ependyma) among the four female mouse brains investigated. On the other hand, I detected single or clustering morphologically different fluorescent cells in varying brain regions. Such cells occurred only in some but not all brains and in varying amounts and locations. In order to distinguish MCs and non-MCs, I used the classical sequential MC staining AB/SO on brain slices in addition. Herewith, I refused the option to co-stain brain slices with the widely used generic MC marker c-kit, since Wasielewska *et al*. recently detected c-kit$^+$ neurons in the hippocampus of mice, which may distort the picture [116].

The EYFP$^+$ cells forming big clusters (mainly in hippocampus, preoptic area, olfactory bulb) had a neuronal shape with one or several dendrites around a bright and defined cell body. Whereas they did not stain with AB/SO, they could be co-stained with NeuroTrace™, a fluorescent Nissl dye. This group of basic dyes stain the so-called Nissl substance in neurons [223, 224] and thus, confirm their neuronal nature. However, it should be considered that Nissl dyes do not detect specific neuronal marker proteins. The staining is based on electrostatic interactions with the basophilic Nissl substance in neuronal cell bodies, which is mainly composed of rough endoplasmic reticulum [223]. Therefore, highly metabolically active cells, like cells of the CP, can also stain with Nissl dyes [225]. And this was certainly the case on my brain slices as well. Nevertheless, the distinct neuronal cell shape with long dendrites supports that these EYFP$^+$ cells are neurons. Moreover, Zeisel *et al.* studied the transcriptome profile of single murine brain cells and surprisingly, discovered in four types of neurons *Cma1* expression [205]. Even if the expression was low or described as not very likely (trinarization

score ≤ 0.95), the transcription may be strong enough to induce Cre-recombinase and subsequently EYFP expression in neuronal subpopulations of Mcpt5-Cre EYFP mice.
Of note, although that many neurons were detected with LSFM, they were excluded by the special cell isolation protocol for FACS for the bulk RNA Sequencing. This was approved by Lorena Morton (Institute for Inflammation and Neurodegeneration, OvGU Magdeburg, data not shown) when developing the protocol and hence, may explain the discrepancy of cell numbers observed between both methods.

Intriguingly, Zeisel *et al.* identified *Cma1* expression not only in neurons, but also in ependymal cells, astrocytes and pericytes [205]. This is in accordance with the $EYFP^+$ cells I detected in only some of the mouse brains. They were morphologically neither neurons, nor MCs, but astrocyte- or pericyte-like in shape, rare in cell numbers and could not be stained with AB/SO. Also, in the ependyma, a few cells in all investigated mouse brains were always $EYFP^+$, but AB/SO^- either.
The transcriptome dataset of van Hove *et al.* further supports the hypothesis of non-MC *Cma1* expression [57]. Despite the detection in NK cells, the authors determined low *Cma1* expression in a very small percentage of microglia and in fractions of all immune cell subsets in the meninges. This may explain the presence of single $EYFP^+$, but AB/SO^- cells in the parenchyma of some of the brains investigated. Moreover, it may account for fluorescent cells in the meninges which were neither detectable with AB/SO nor with avidin. Single cell RNA sequencing of the $EYFP^+$ cells in Mcpt5-Cre DM confirmed the recombination in NK cells but none of the other *Cma1* expressing immune cells by van Hove *et al*. [57].
In the CPs of all brains, I detected very bright and prominent $EYFP^+$ cells, which can barely be described morphologically due to the low resolution. Whereas previous studies identified MCs on histological preparations of CPs [124, 165, 166], it seems contradictory that recent transcriptome analyses could not detect MCs in CPs of adult mice [53, 57] and I could not stain them with AB/SO either. But the histological preparations by Dropp [124] and Fritscher *et al.* [170] reveal that MCs are attached to the CP and the ventricular lining. This loose interaction may be sensitive to the preparation procedure and tissue treatment in general and accounts for the contradictory findings. As a consequence, the $EYFP^+$ cells in the CPs of the Mcpt5-Cre mice, which seem to be integrated in the tissue, may not be MCs. It could be, that this is the very small percentage of macrophages expressing very low levels of *Cma1*, as detected in the dataset by van Hove *et al.* [57].
Although single cell datasets are informative and explorative, the annotation of the cell clusters is not perfect. Van Hove *et al.* identified three cells in the CP with very abundant *Cma1* expression but also *Mcpt4* and *Tpsb2* [57]. These cells were annotated as T cells, which strongly suggests being undetected doublets. Doublets can appear in droplet sequencing

studies when two (or more) cells accessed one droplet by chance resulting in a mixed-type profile of the single cell transcriptome. Consequently, it cannot be ruled out, that some of the *Cma1* transcripts detected were accidentally ascribed to non-MCs.
Nonetheless, all transcriptome analyses underline the ectopic EYFP expression in the brains, revealed by different microscopy techniques.

Whether the $EYFP^+$ cells in the Mcpt5-Cre EYFP brains currently express Cre under the control of Mcpt5 or synthesized the recombinase in their past cannot be assessed from the data above. Since some cells (as MCs and neurons) have a long lifetime and FPs can survive inside cells for quite a long time as well [226], it can be that the Mcpt5 (*Cma1*) promotor was only temporarily active at a previous cell state during development. Indeed, Parenti *et al.* observed a more than 180-fold increase (log2 fold change 7.5) in *Cma1* expression (adjusted p-value: $1.5x10^{-7}$) in extraembryonic endoderm stem cells compared to embryonic fibroblasts when performing DGE analysis with mice [227] (accessible online at [228]). However, the role of *Cma1* activation during development was not part of this study and was therefore not further investigated. In accordance with this, Walker *et al.* detected strongly upregulated *Cma1* expression in neural precursor cells of the mouse hippocampus (log2 fold change 7, adjusted p-value: $9x10^{-13}$) compared to niche cells (non-precursor neuronal cells) [229] (accessible online at [230]). The assumption that *Cma1* is only activated temporarily in some cells during development is underlined by the fact, that *Cma1* mRNA was not detectable in one meningeal and one CP samples in qPCR although the 50 cells per sample were sorted based on EYFP fluorescence and housekeeping gene expression was normal.
In contrast, Meyer *et al*. could show that Mcpt5 (*Cma1*) in non-MCs is not only transiently expressed during development. The authors demonstrated that a subset of uterine NK cells actively express and secrete the chymase to remodel blood vessels during pregnancy [67]. But for all other cells targeted by the Mcpt5-Cre, the timepoint and the mechanism of Cre induction remain to be elucidated.
Another very interesting idea how off-target effects may occur in a MC mouse model was summarized by Moon *et al.* [231]. As other cells, MCs are able to use exosomes in addition to granules to communicate with their environment [231, 232]. Besides proteins, exosomes store mRNA and microRNA. Both nucleic acid molecules can be transferred between MCs and other cells and were shown to control the recipient's gene expression. Up to 15% of the donor cell mRNA content was determined in such extracellular particles [233]. Imagine that Cre recombinase transcripts are transferred as well and will be translated in others than MCs, the foreign enzyme may be able to induce ectopic EYFP expression. Whether this mechanism acts in the Mcpt5-Cre EYFP or related mouse models as well, needs to be further investigated.

The combination of different microscopy techniques, together with the transcriptome studies revealed contradictory results for meningeal MCs, apart from the mouse model specificity: The expression of *Cma1*, *Mcpt4* and *Tpsb2* in the EYFP$^+$ cells of Mcpt5-Cre reporter meninges, together with the presence of heparin in Mcpt5-Cre targeted cells and previous investigations of rodent meninges [122, 167, 215] assumed that DM MCs are CTMCs. In line with this, single cell RNA sequencing of the EYFP$^+$ cells in the DM identified MCs of a CTMC phenotype [104, 106], with highest expression of *Cpa3*, *Tpsb2* and *Mcpt4*.
In stark contrast, the AB/SO staining on DM whole mounts detected primarily blue (AB$^+$) and red-blue (ABSO$^+$, mixed type) MCs, representing either MMCs or less mature CTMCs [110, 113, 122, 166]. Red (SO$^+$) cells, which are usually referred to as CTMCs [108, 110, 113] formed the smallest population.
These contradictory findings may result from the rare description or explanation of ABSO$^+$ double positive cells in previous studies. Most authors use AB/SO staining to distinguish CTMCs and MMCs [79, 108, 122], but I could not observe subclustering of the single cell transcriptomes in MMC- or CTMC-like MCs. Some authors noticed a red-blue mixed type, but did not comment on it [234, 235]. When Burton described that mixed type in 1964, he hypothesized a transitional state between immature and mature MCs [113], which was affirmed by others years later [236-239]. But when analyzing the MC cluster of the single cell sequencing in the light of maturation genes, no subpopulations become visible either.

Dimitriadou *et al.* were the first using the sequential staining to identify MC activation in 1991 [240], followed by [241] and [172], respectively. Surprisingly, the authors have not been explained why, but the following observations indicated an activation effect in my data as well. First, I noticed that the AB$^+$ “blue” cells were not randomly distributed but preferably located at the edges and along the sinuses in the MC distribution patterns. The sinusoid and border regions are, where the DM is connected tighter to the calvaria bone. Although they have been carefully removed or loosened, they have to be touched with the scissors. Even though the tissue is quickly perfuse-fixed *in vivo* before, this fixation may be incomplete or the pressure of the scissors may damage or break the cell membranes and release some granules. Second, the AB$^+$ cells had less defined cell surfaces, as it was observed by Duque-Wilckens *et al.* [22] in activated DM MCs as well. And third, the single cell RNA sequencing identified the MMC-related MC protease *Mcpt2* to be upregulated in the meningeal MCs, which was reported in activated DM MCs before by Brown and Weinberg [217].
In order to test, whether a subpopulation of the DM MCs may be activated, I used again the manual subcluster identification approach, using one dataset of activated human skin MCs in cell culture [211] and one of LPS-treated murine BMMCs [104]. Both systems were far from physiological, but unexpectedly, I observed a subcluster of cells which showed an enrichment

in genes related to MC activation. With the subsequent activation assay, I could confirm that AB/SO staining is sensitive to the MC activation status as well. Consequently, it is likely that the DM isolation itself causes degranulation of the MCs, either partially or massive. Due to the perfuse-fixation procedure, it is unlikely that the MCs actively degranulate when the tissue is removed. Either the tissue handling “degranulates” the MCs by mechanically interrupting cell membranes, or the stress when the mice were euthanized may cause MC degranulation. It was shown in various studies with rodents, that DM MCs react very sensitive to physiological and psychological stress [22, 72, 167].
Hence, a proper fixation and handling as well as appropriate controls are recommended when using the AB/SO staining. The results may be interpretated carefully, considering that the ability to indicate MC activation as well affects the reliable detection of MC subtypes on the other hand. A mix of CTMCs and MMCs in different maturation or activation states within the same specimen may not be distinguishable and other staining or biomarker detection methods should be considered and utilized in addition. The interpretation of the AB/SO staining is therefore not as straight-forward as generally communicated in MC staining reviews [79, 108].

Apart from the activation status, the AB/SO staining was used to count the DM MCs in three regions, separately for the left and right hemisphere, as well as the cerebellum. Hereby, no differences between males and females were detected, which is different from MC counts in the neuropil of rats. They show both sex- and side-specific variations in MC numbers [122, 163]. A recent study, which was conducted at the same time, counted TB-stained MCs in the DM, but in a smaller rectangular area [22]. They determined 50 MCs/mm^2 above the hemispheres as well. Above the cerebellum, they counted between 50 and 100 MCs/mm^2, which is slightly less than I quantified (100 – 125 MCs/mm^2). This variance may be either the result of the different staining or, more likely, the extrapolation of the cell density in the entire area based on the counted square. Therewith, the density of MCs in the DM seems to be as high as in the skin. In the dermis of C57BL/6 mice, about 60 MCs/mm^2 were estimated by Hart *et al.* and even less in other mouse strains [242]. However, in human skin biopsies, 77 to 108 MCs/mm^2 were identified by Janssens *et al.* [243].

6 Conclusion

With this work, I confirm the presence of MCs in the CNS. Aiming to find a suitable mouse model for further investigations on how brain MCs function and interact in a complex neuro-immune cell network, the Mcpt5-Cre EYFP mouse was investigated. By combining state-of-the-art three-dimensional microscopy and classical MC staining techniques, I identified MCs in the murine meninges and very few within the parenchyma. Bulk RNA sequencing results presume their existence additionally in the CP although this was not reproduced with microscopy.

Comprehensive investigations of the cerebral EYFP$^+$ cells in the Cre/*loxP* based mouse model revealed ectopic expression of the FP in primarily neurons, but also astrocytes, pericytes, microglia or NK cells. Since MCs cannot be detected reliable by a single marker, I combined a lot of different techniques to validate this finding. By this, I can now confirm the expression of Mcpt5 in non-MCs, what was already observed 2011 by Dudeck *et al*. [1], 2014 by Abram *et al.* [146] and 2017 by Meyer *et al*. [67]. Publicly available transcriptome data were revisited in this thesis and support the above finding as well [57, 205, 227, 229, 244]. Whether the ectopic expression of EYFP may be the result of transient or permanent Mcpt5-Cre expression in non-MCs, needs to be further elucidated. However, it displays that caution is needed when using Cre based mouse models. Their quality and specificity may vary between mouse lines and organs. This should be considered especially when using the Mcpt5-Cre R-DTA mouse as the corresponding constitutive MC deficiency model. These mice lack cells targeted by the Mcpt5-driven Cre expression and it cannot be excluded that they show deficiency in certain neurons, meningeal NK or other cells as well. It is also very likely that the Mcpt5-Cre iDTR or Mcpt5-Cre TNF mouse lines may be affected and potential off-target effects in varying tissues of these mice are still understudied. Thus, Mcpt5-Cre mouse models face limitations, at least when used in brain studies. It is recommended to test their specificity for every organ or tissue separately and for every combination with a new *loxP* locus. Implicit extrapolations from one organ or one mouse line to another should be avoided and it is important to suspect systemic effects as well.

Apart from a detailed investigation of the mouse model, this study presents a transcriptome profile for DM MCs, which shows their CTMC-like phenotype. Gene exploration analyses of the MCs combined with an activation assay, revealed that the sequential MC staining AB/SO can differentiate activated and quiescent MCs. Thus, the blue color is not only attributable to immature MCs or MMCs as generally taught [79, 108], but may indicate an activated CTMC as well.

7 Outlook

The present study shows that the Mcpt5-Cre mouse model cannot be used without restrictions to address brain MC functions. It demands a consequent implementation of appropriate controls as well as detailed investigations with state-of-the-art techniques on how the model can be used for a specific scientific issue. Therefore, a sophisticated study design is equally important as an open handling of limitations.

Nonetheless, I can recommend the mouse model for further brain MC approaches. Recent advantages in single cell transcriptome methods may allow to repeat the single cell RNA sequencing for $EYFP^+$ cells from whole brain. It may give insights in the entirety of MCs in the brain and further elucidates which cell types are targeted in addition. Spatially resolving transcriptome methods, as recently brought on the market by companies as 10XGenomics (Visium Spatial Gene Expression) or NanoString (CosMx™ Spatial Molecular Imager), may provide information on how cerebral MCs differ among varying brain areas to suggest local functionalities. Combining proteome or multiome information can complete the picture. Additionally, deep learning algorithms (as CellChat [245], CellPhoneDB [246] or NicheNet [247]) were developed, which predict cell-cell interactions or even networks based on gene expression data [248, 249]. What a few authors observed on tissue preparations decades ago by chance (MC-astrocyte contacts [117], MC-neuron interactions [167]) may be confirmed thanks to the advancement of computational tools and power.

Finally, it would be interesting to investigate the exosomes of Mcpt5-Cre EYFP MCs itself and the exchange mechanism within their environment. The results of scientific approaches may be interpretated even more cautious if the Cre recombinase itself as a protein or its transcript is transferred to other cells and affect the acceptor’s gene expression.

8 List of Publications

1. Dudeck, A., et al., *Mast cells are key promoters of contact allergy that mediate the adjuvant effects of haptens.* Immunity, 2011. **34**(6): p. 973-84.
2. Dudeck, J., et al., *Mast-Cell-Derived TNF Amplifies CD8(+) Dendritic Cell Functionality and CD8(+) T Cell Priming.* Cell Rep, 2015. **13**(2): p. 399-411.
3. Beaven, M.A., *Our perception of the mast cell from Paul Ehrlich to now.* Eur J Immunol, 2009. **39**(1): p. 11-25.
4. Goldmann E, E., *Die aussere und innere Sekretion des gesunden und kranken Organismus im Liche der "vitalen Farbung".* Beitr. Klin. Chir., 1909. **64**: p. 192-265.
5. Goldmann, E.E., *Vitalfärbung am Zentralnervensystem: Beitrag zur Physio-Pathologie des Plexus chorioideus und der Hirnhäute*. 1913: Königl. Akademie der Wissenschaften.
6. Saunders, N.R., et al., *The rights and wrongs of blood-brain barrier permeability studies: a walk through 100 years of history.* Front Neurosci, 2014. **8**: p. 404.
7. Bentivoglio, M. and K. Kristensson, *Tryps and trips: cell trafficking across the 100-year-old blood-brain barrier.* Trends Neurosci, 2014. **37**(6): p. 325-33.
8. Barker, C.F. and R.E. Billingham, *Immunologically privileged sites.* Adv Immunol, 1977. **25**: p. 1-54.
9. Billingham, R.E. and T. Boswell, *Studies on the problem of corneal homografts.* Proc R Soc Lond B Biol Sci, 1953. **141**(904): p. 392-406.
10. Engelhardt, B., P. Vajkoczy, and R.O. Weller, *The movers and shapers in immune privilege of the CNS.* Nat Immunol, 2017. **18**(2): p. 123-131.
11. Shechter, R., A. London, and M. Schwartz, *Orchestrated leukocyte recruitment to immune-privileged sites: absolute barriers versus educational gates.* Nat Rev Immunol, 2013. **13**(3): p. 206-18.
12. Hong, S. and L. Van Kaer, *Immune privilege: keeping an eye on natural killer T cells.* J Exp Med, 1999. **190**(9): p. 1197-200.
13. Silver, R., et al., *Mast cells in the brain: evidence and functional significance.* Trends in Neurosciences, 1996. **19**(1): p. 25-31.
14. Hickey, W.F., B.L. Hsu, and H. Kimura, *T-lymphocyte entry into the central nervous system.* J Neurosci Res, 1991. **28**(2): p. 254-60.
15. Rua, R. and D.B. McGavern, *Advances in Meningeal Immunity.* Trends Mol Med, 2018. **24**(6): p. 542-559.
16. Ibrahim, M.Z.M., *The mast cells of the mammalian central nervous system: Part 1. Morphology, distribution and histochemistry.* Journal of the Neurological Sciences, 1974. **21**(4): p. 431-478.
17. Olsson, Y., *Mast Cells in the Nervous System*, in *International Review of Cytology*, G.H. Bourne, J.F. Danielli, and K.W. Jeon, Editors. 1968, Academic Press. p. 27-70.
18. Dropp, J.J., *Mast cells in mammalian brain.* Acta Anat (Basel), 1976. **94**(1): p. 1-21.
19. Louveau, A. and J. Kipnis, *Dissection and immunostaining of mouse whole-mount meninges.* 2015.
20. Aspelund, A., et al., *A dural lymphatic vascular system that drains brain interstitial fluid and macromolecules.* J Exp Med, 2015. **212**(7): p. 991-9.
21. Kataru, R.P., et al., *Regulation of Immune Function by the Lymphatic System in Lymphedema.* Front Immunol, 2019. **10**: p. 470.
22. Duque-Wilckens, N., et al., *Early life adversity drives sex-specific anhedonia and meningeal immune gene expression through mast cell activation.* Brain Behav Immun, 2022. **103**: p. 73-84.
23. Benakis, C., G. Llovera, and A. Liesz, *The meningeal and choroidal infiltration routes for leukocytes in stroke.* Ther Adv Neurol Disord, 2018. **11**: p. 1756286418783708.
24. Liddelow, S.A., *Fluids and barriers of the CNS: a historical viewpoint.* Fluids Barriers CNS, 2011. **8**(1): p. 2.
25. Coles, J.A., et al., *Where are we? The anatomy of the murine cortical meninges revisited for intravital imaging, immunology, and clearance of waste from the brain.* Prog Neurobiol, 2017. **156**: p. 107-148.
26. Kinaci, A., et al., *Histologic Comparison of the Dura Mater among Species.* Comp Med, 2020. **70**(2): p. 170-175.
27. Dorrier, C.E., et al., *Emerging roles for CNS fibroblasts in health, injury and disease.* Nat Rev Neurosci, 2022. **23**(1): p. 23-34.

28. Abbott, N.J., et al., *The role of brain barriers in fluid movement in the CNS: is there a 'glymphatic' system?* Acta Neuropathol, 2018. **135**(3): p. 387-407.
29. Au - Leda, A.R., et al., *Mouse Microsurgery Infusion Technique for Targeted Substance Delivery into the CNS via the Internal Carotid Artery.* JoVE, 2017(119): p. e54804.
30. Richardson, E. *A Surgical Approach to Induce Local Reversal of Blood Flow to Assess Plasticity of Segmented Endothelium in the Mouse Ear*. 2018; Available from: http://nrs.harvard.edu/urn-3:HUL.InstRepos:39010117 (accessed online: 25.08.2022).
31. Rustenhoven, J., et al., *Functional characterization of the dural sinuses as a neuroimmune interface.* Cell, 2021. **184**(4): p. 1000-1016.e27.
32. Gao, Y.R. and P.J. Drew, *Effects of Voluntary Locomotion and Calcitonin Gene-Related Peptide on the Dynamics of Single Dural Vessels in Awake Mice.* J Neurosci, 2016. **36**(8): p. 2503-16.
33. Bacyinski, A., et al., *The Paravascular Pathway for Brain Waste Clearance: Current Understanding, Significance and Controversy.* Front Neuroanat, 2017. **11**: p. 101.
34. Quintana, F.J., *Astrocytes to the rescue! Glia limitans astrocytic endfeet control CNS inflammation.* J Clin Invest, 2017. **127**(8): p. 2897-2899.
35. Bedussi, B., et al., *Paravascular channels, cisterns, and the subarachnoid space in the rat brain: A single compartment with preferential pathways.* J Cereb Blood Flow Metab, 2017. **37**(4): p. 1374-1385.
36. Bedussi, B., et al., *Clearance from the mouse brain by convection of interstitial fluid towards the ventricular system.* Fluids Barriers CNS, 2015. **12**: p. 23.
37. Schaeffer, S. and C. Iadecola, *Revisiting the neurovascular unit.* Nat Neurosci, 2021. **24**(9): p. 1198-1209.
38. Abbott, N.J. and A. Friedman, *Overview and introduction: the blood-brain barrier in health and disease.* Epilepsia, 2012. **53 Suppl 6**: p. 1-6.
39. Stratman, A.N., et al., *Interactions between mural cells and endothelial cells stabilize the developing zebrafish dorsal aorta.* Development, 2017. **144**(1): p. 115-127.
40. Erickson, M.A. and W.A. Banks, *Neuroimmune Axes of the Blood-Brain Barriers and Blood-Brain Interfaces: Bases for Physiological Regulation, Disease States, and Pharmacological Interventions.* Pharmacol Rev, 2018. **70**(2): p. 278-314.
41. Silver, R. and J.P. Curley, *Mast cells on the mind: new insights and opportunities.* Trends Neurosci, 2013. **36**(9): p. 513-21.
42. Natale, G., et al., *Glymphatic System as a Gateway to Connect Neurodegeneration From Periphery to CNS.* Frontiers in Neuroscience, 2021. **15**.
43. Wolburg, H. and W. Paulus, *Choroid plexus: biology and pathology.* Acta Neuropathol, 2010. **119**(1): p. 75-88.
44. Ghersi-Egea, J.F., et al., *Molecular anatomy and functions of the choroidal blood-cerebrospinal fluid barrier in health and disease.* Acta Neuropathol, 2018. **135**(3): p. 337-361.
45. Liddelow, S.A., *Development of the choroid plexus and blood-CSF barrier.* Front Neurosci, 2015. **9**: p. 32.
46. Dohrmann, G.J., *Dark and light epithelial cells in the choroid plexus of mammals.* J Ultrastruct Res, 1970. **32**(3): p. 268-73.
47. Kaur, C., G. Rathnasamy, and E.A. Ling, *The Choroid Plexus in Healthy and Diseased Brain.* J Neuropathol Exp Neurol, 2016. **75**(3): p. 198-213.
48. Schwerk, C., et al., *The choroid plexus-a multi-role player during infectious diseases of the CNS.* Front Cell Neurosci, 2015. **9**: p. 80.
49. van Deurs, B. and J.K. Koehler, *Tight junctions in the choroid plexus epithelium. A freeze-fracture study including complementary replicas.* J Cell Biol, 1979. **80**(3): p. 662-73.
50. MacAulay, N., R.F. Keep, and T. Zeuthen, *Cerebrospinal fluid production by the choroid plexus: a century of barrier research revisited.* Fluids Barriers CNS, 2022. **19**(1): p. 26.
51. Christensen, O., M. Simon, and T. Randlev, *Anion channels in a leaky epithelium. A patch-clamp study of choroid plexus.* Pflugers Arch, 1989. **415**(1): p. 37-46.
52. Damkier, H.H., P.D. Brown, and J. Praetorius, *Cerebrospinal fluid secretion by the choroid plexus.* Physiol Rev, 2013. **93**(4): p. 1847-92.
53. Dani, N., et al., *A cellular and spatial map of the choroid plexus across brain ventricles and ages.* Cell, 2021. **184**(11): p. 3056-3074.e21.
54. Lein, E.S., et al., *Genome-wide atlas of gene expression in the adult mouse brain.* Nature, 2007. **445**(7124): p. 168-176.
55. Bakker, R., P. Tiesinga, and R. Kötter, *The Scalable Brain Atlas: Instant Web-Based Access to Public Brain Atlases and Related Content.* Neuroinformatics, 2015. **13**(3): p. 353-366.
56. Miyata, S., *New aspects in fenestrated capillary and tissue dynamics in the sensory circumventricular organs of adult brains.* Frontiers in Neuroscience, 2015. **9**: p. 390.

57. Van Hove, H., et al., *A single-cell atlas of mouse brain macrophages reveals unique transcriptional identities shaped by ontogeny and tissue environment, interactive data exploration online available https://www.brainimmuneatlas.org/wt-homeostatic.php.* Nat Neurosci, 2019. **22**(6): p. 1021-1035.
58. Cai, R., et al., *Panoptic imaging of transparent mice reveals whole-body neuronal projections and skull-meninges connections.* 2019. **22**(2): p. 317-327.
59. Herisson, F., et al., *Direct vascular channels connect skull bone marrow and the brain surface enabling myeloid cell migration.* Nat Neurosci, 2018. **21**(9): p. 1209-1217.
60. Cugurra, A., et al., *Skull and vertebral bone marrow are myeloid cell reservoirs for the meninges and CNS parenchyma.* Science, 2021. **373**(6553).
61. Brioschi, S., et al., *Heterogeneity of meningeal B cells reveals a lymphopoietic niche at the CNS borders.* Science, 2021. **373**(6553).
62. Mapunda, J.A., et al., *How Does the Immune System Enter the Brain?* Frontiers in Immunology, 2022. **13**.
63. Engelhardt, B., *T cell migration into the central nervous system during health and disease: Different molecular keys allow access to different central nervous system compartments.* Clinical and Experimental Neuroimmunology, 2010. **1**(2): p. 79-93.
64. Baunbæk Egelund, G., et al., *Cerebrospinal fluid pleocytosis in infectious and noninfectious central nervous system disease: A retrospective cohort study.* Medicine (Baltimore), 2017. **96**(18): p. e6686.
65. Dudeck, A., et al., *Mast cells as protectors of health.* Journal of Allergy and Clinical Immunology, 2019. **144**(4): p. S4-S18.
66. Magnúsdóttir, E.I., et al., *Mouse connective tissue mast cell proteases tryptase and carboxypeptidase A3 play protective roles in itch induced by endothelin-1.* Journal of Neuroinflammation, 2020. **17**(1): p. 123.
67. Meyer, N., et al., *Chymase-producing cells of the innate immune system are required for decidual vascular remodeling and fetal growth.* Sci Rep, 2017. **7**: p. 45106.
68. Weller, C.L., et al., *Mast cells in health and disease.* Clin Sci (Lond), 2011. **120**(11): p. 473-84.
69. Ragipoglu, D., et al., *Mast Cells Drive Systemic Inflammation and Compromised Bone Repair After Trauma.* Front Immunol, 2022. **13**: p. 883707.
70. Kroner, J., et al., *Mast Cells Are Critical Regulators of Bone Fracture-Induced Inflammation and Osteoclast Formation and Activity.* J Bone Miner Res, 2017. **32**(12): p. 2431-2444.
71. Norrby, K., *Mast cells and angiogenesis.* Apmis, 2002. **110**(5): p. 355-71.
72. Nurkhametova, D., et al., *Activation of P2X7 Receptors in Peritoneal and Meningeal Mast Cells Detected by Uptake of Organic Dyes: Possible Purinergic Triggers of Neuroinflammation in Meninges.* Front Cell Neurosci, 2019. **13**: p. 45.
73. Conti, P., et al., *Progression in migraine: Role of mast cells and pro-inflammatory and anti-inflammatory cytokines.* Eur J Pharmacol, 2019. **844**: p. 87-94.
74. Sobiepanek, A., et al., *The Multifaceted Roles of Mast Cells in Immune Homeostasis, Infections and Cancers.* International Journal of Molecular Sciences, 2022. **23**: p. 2249.
75. Hoppe, A., et al., *Mast cells initiate the vascular response to contact allergens by sensing cell stress.* J Allergy Clin Immunol, 2020. **145**(5): p. 1476-1479.e3.
76. West, P.W. and S. Bulfone-Paus, *Mast cell tissue heterogeneity and specificity of immune cell recruitment.* Front Immunol, 2022. **13**: p. 932090.
77. Klein, O. and R. Sagi-Eisenberg, *Anaphylactic Degranulation of Mast Cells: Focus on Compound Exocytosis.* J Immunol Res, 2019. **2019**: p. 9542656.
78. Blank, U., et al., *Vesicular trafficking and signaling for cytokine and chemokine secretion in mast cells.* Front Immunol, 2014. **5**: p. 453.
79. Grigorev, I.P. and D.E. Korzhevskii, *Modern Imaging Technologies of Mast Cells for Biology and Medicine (Review).* Sovrem Tekhnologii Med, 2021. **13**(4): p. 93-107.
80. Wernersson, S. and G. Pejler, *Mast cell secretory granules: armed for battle.* Nature Reviews Immunology, 2014. **14**(7): p. 478-494.
81. Varricchi, G., et al., *Are Mast Cells MASTers in Cancer?* Front Immunol, 2017. **8**: p. 424.
82. Noto, C.N., S.G. Hoft, and R.J. DiPaolo, *Mast Cells as Important Regulators in Autoimmunity and Cancer Development.* Front Cell Dev Biol, 2021. **9**: p. 752350.
83. Forsythe, P., *Mast Cells in Neuroimmune Interactions.* Trends in Neurosciences, 2019. **42**(1): p. 43-55.
84. Vangansewinkel, T., et al., *Mast cells promote scar remodeling and functional recovery after spinal cord injury via mouse mast cell protease 6.* Faseb j, 2016. **30**(5): p. 2040-57.
85. DeBruin, E.J., et al., *Mast cells in human health and disease.* Methods Mol Biol, 2015. **1220**: p. 93-119.

86. Feyerabend, T.B., et al., *Loss of histochemical identity in mast cells lacking carboxypeptidase A.* Mol Cell Biol, 2005. **25**(14): p. 6199-210.
87. Plum, T., et al., *Human Mast Cell Proteome Reveals Unique Lineage, Putative Functions, and Structural Basis for Cell Ablation.* Immunity, 2020. **52**(2): p. 404-416.e5.
88. Kim, H.S., et al., *Recent advances in mast cell activation and regulation.* F1000Res, 2020. **9**.
89. Leist, M., et al., *Membrane-bound stem cell factor is the major but not only driver of fibroblast-induced murine skin mast cell differentiation.* Exp Dermatol, 2017. **26**(3): p. 255-262.
90. Gentek, R., et al., *Hemogenic Endothelial Fate Mapping Reveals Dual Developmental Origin of Mast Cells.* Immunity, 2018. **48**(6): p. 1160-1171.e5.
91. Li, Z., et al., *Adult Connective Tissue-Resident Mast Cells Originate from Late Erythro-Myeloid Progenitors.* Immunity, 2018. **49**(4): p. 640-653.e5.
92. Wolf, A.A. and H.S. Goodridge, *Mast Cells Reveal Their Past Selves.* Immunity, 2018. **48**(6): p. 1065-1067.
93. Krystel-Whittemore, M., K.N. Dileepan, and J.G. Wood, *Mast Cell: A Multi-Functional Master Cell.* Frontiers in Immunology, 2016. **6**.
94. Baccari, G.C., et al., *Chapter one - Mast Cells in Nonmammalian Vertebrates: An Overview*, in *International Review of Cell and Molecular Biology*, K.W. Jeon, Editor. 2011, Academic Press. p. 1-53.
95. Enerbäck, L., *Mast cells in rat gastrointestinal mucosa. 2. Dye-binding and metachromatic properties.* Acta Pathol Microbiol Scand, 1966. **66**(3): p. 303-12.
96. Siraganian, R.P., *Mast Cells*, in *Encyclopedia of Immunology (Second Edition)*, P.J. Delves, Editor. 1998, Elsevier: Oxford. p. 1667-1671.
97. Derakhshan, T., et al., *Lineage-specific regulation of inducible and constitutive mast cells in allergic airway inflammation.* J Exp Med, 2021. **218**(1).
98. Jiménez, M., et al., *Responses of Mast Cells to Pathogens: Beneficial and Detrimental Roles.* Front Immunol, 2021. **12**: p. 685865.
99. Valent, P., et al., *Mast cells as a unique hematopoietic lineage and cell system: From Paul Ehrlich's visions to precision medicine concepts.* Theranostics, 2020. **10**(23): p. 10743-10768.
100. Pejler, G., et al., *Mast cell proteases: multifaceted regulators of inflammatory disease.* Blood, 2010. **115**(24): p. 4981-90.
101. Hunt, J.E., et al., *Natural disruption of the mouse mast cell protease 7 gene in the C57BL/6 mouse.* J Biol Chem, 1996. **271**(5): p. 2851-5.
102. Frossi, B., et al., *Is it time for a new classification of mast cells? What do we know about mast cell heterogeneity?* Immunol Rev, 2018. **282**(1): p. 35-46.
103. Weidner, N. and K.F. Austen, *Heterogeneity of mast cells at multiple body sites. Fluorescent determination of avidin binding and immunofluorescent determination of chymase, tryptase, and carboxypeptidase content.* Pathol Res Pract, 1993. **189**(2): p. 156-62.
104. Akula, S., et al., *How Relevant Are Bone Marrow-Derived Mast Cells (BMMCs) as Models for Tissue Mast Cells? A Comparative Transcriptome Analysis of BMMCs and Peritoneal Mast Cells.* Cells, 2020. **9**(9).
105. Pejler, G., *Novel Insight into the in vivo Function of Mast Cell Chymase: Lessons from Knockouts and Inhibitors.* Journal of Innate Immunity, 2020. **12**(5): p. 357-372.
106. Dwyer, D.F., N.A. Barrett, and K.F. Austen, *Expression profiling of constitutive mast cells reveals a unique identity within the immune system.* Nat Immunol, 2016. **17**(7): p. 878-87.
107. Akula, S., et al., *Quantitative In-Depth Analysis of the Mouse Mast Cell Transcriptome Reveals Organ-Specific Mast Cell Heterogeneity.* Cells, 2020. **9**(1).
108. Ribatti, D., *The Staining of Mast Cells: A Historical Overview.* Int Arch Allergy Immunol, 2018. **176**(1): p. 55-60.
109. Theoharides, T.C., *Mast cells: the immune gate to the brain.* Life Sci, 1990. **46**(9): p. 607-17.
110. Strobel, S., H.R. Miller, and A. Ferguson, *Human intestinal mucosal mast cells: evaluation of fixation and staining techniques.* J Clin Pathol, 1981. **34**(8): p. 851-8.
111. Bergholt, N.L., et al., *A Standardized Method of Applying Toluidine Blue Metachromatic Staining for Assessment of Chondrogenesis.* Cartilage, 2019. **10**(3): p. 370-374.
112. Mutsaddi, S., et al., *Comparison of histochemical staining techniques for detecting mast cells in oral lesions.* Biotech Histochem, 2019. **94**(6): p. 459-468.
113. Burton, A.L., *HISTOCHEMICAL STUDIES ON DEVELOPING MAST CELLS.* Anat Rec, 1964. **150**: p. 265-9.
114. Tsai, M., P. Valent, and S.J. Galli, *KIT as a master regulator of the mast cell lineage.* J Allergy Clin Immunol, 2022. **149**(6): p. 1845-1854.
115. Shin, J.Y., et al., *High c-Kit expression identifies hematopoietic stem cells with impaired self-renewal and megakaryocytic bias.* J Exp Med, 2014. **211**(2): p. 217-31.

116. Wasielewska, J.M., et al., *Mast cells increase adult neural precursor proliferation and differentiation but this potential is not realized in vivo under physiological conditions.* Sci Rep, 2017. **7**(1): p. 17859.
117. Shanas, U., et al., *Brain mast cells lack the c-kit receptor: immunocytochemical evidence.* J Neuroimmunol, 1998. **90**(2): p. 207-11.
118. Bergstresser, P.R., R.E. Tigelaar, and M.D. Tharp, *Conjugated avidin identifies cutaneous rodent and human mast cells.* J Invest Dermatol, 1984. **83**(3): p. 214-8.
119. Gaudenzio, N., et al., *Genetic and Imaging Approaches Reveal Pro-Inflammatory and Immunoregulatory Roles of Mast Cells in Contact Hypersensitivity.* Front Immunol, 2018. **9**: p. 1275.
120. Dudeck, J., et al., *Directional mast cell degranulation of tumor necrosis factor into blood vessels primes neutrophil extravasation.* Immunity, 2021. **54**(3): p. 468-483.e5.
121. Boes, T. and D. Levy, *Influence of sex, estrous cycle, and estrogen on intracranial dural mast cells.* Cephalalgia, 2012. **32**(12): p. 924-31.
122. Lenz, K.M., et al., *Mast Cells in the Developing Brain Determine Adult Sexual Behavior.* J Neurosci, 2018. **38**(37): p. 8044-8059.
123. Mackey, E., et al., *Sexual dimorphism in the mast cell transcriptome and the pathophysiological responses to immunological and psychological stress.* Biol Sex Differ, 2016. **7**: p. 60.
124. Dropp, J.J., *A COMPARATIVE STUDY OF VENTRICULAR MAST CELLS WITHIN THE VERTEBRATE BRAIN.* Proceedings of the Pennsylvania Academy of Science, 1978. **52**(1): p. 17-20.
125. Michaloudi, H.C. and G.C. Papadopoulos, *Mast cells in the sheep, hedgehog and rat forebrain.* J Anat, 1999. **195 (Pt 4)**(Pt 4): p. 577-86.
126. Pearce, F.L., *Functional heterogeneity of mast cells from different species and tissues.* Klin Wochenschr, 1982. **60**(17): p. 954-7.
127. Majeed, S.K., *Mast cell distribution in rats.* Arzneimittelforschung, 1994. **44**(3): p. 370-4.
128. Hendrix, S., et al., *The majority of brain mast cells in B10.PL mice is present in the hippocampal formation.* Neurosci Lett, 2006. **392**(3): p. 174-7.
129. Karhausen, J. and S.N. Abraham, *How mast cells make decisions.* The Journal of Clinical Investigation, 2016. **126**(10): p. 3735-3738.
130. Kitamura, Y., S. Go, and K. Hatanaka, *Decrease of mast cells in W/Wv mice and their increase by bone marrow transplantation.* Blood, 1978. **52**(2): p. 447-52.
131. Waskow, C., et al., *Rescue of lethal c-KitW/W mice by erythropoietin.* Blood, 2004. **104**(6): p. 1688-95.
132. Cable, J., et al., *Effects of mutations at the W locus (c-kit) on inner ear pigmentation and function in the mouse.* Pigment Cell Res, 1994. **7**(1): p. 17-32.
133. Galli, S.J., N. Gaudenzio, and M. Tsai, *Mast Cells in Inflammation and Disease: Recent Progress and Ongoing Concerns.* Annu Rev Immunol, 2020. **38**: p. 49-77.
134. Grimbaldeston, M.A., et al., *Mast cell-deficient W-sash c-kit mutant Kit W-sh/W-sh mice as a model for investigating mast cell biology in vivo.* Am J Pathol, 2005. **167**(3): p. 835-48.
135. Sayed, B.A., et al., *Meningeal mast cells affect early T cell central nervous system infiltration and blood-brain barrier integrity through TNF: a role for neutrophil recruitment?* J Immunol, 2010. **184**(12): p. 6891-900.
136. Reber, L.L., T. Marichal, and S.J. Galli, *New models for analyzing mast cell functions in vivo.* Trends Immunol, 2012. **33**(12): p. 613-25.
137. Feyerabend, T.B., et al., *Cre-mediated cell ablation contests mast cell contribution in models of antibody- and T cell-mediated autoimmunity.* Immunity, 2011. **35**(5): p. 832-44.
138. Lilla, J.N., et al., *Reduced mast cell and basophil numbers and function in Cpa3-Cre; Mcl-1fl/fl mice.* Blood, 2011. **118**(26): p. 6930-8.
139. Scholten, J., et al., *Mast cell-specific Cre/loxP-mediated recombination in vivo.* Transgenic Res, 2008. **17**(2): p. 307-15.
140. Lyon, M.F. and P.H. Glenister, *A new allele sash (Wsh) at the W-locus and a spontaneous recessive lethal in mice.* Genet Res, 1982. **39**(3): p. 315-22.
141. Berrozpe, G., et al., *The W(sh), W(57), and Ph Kit expression mutations define tissue-specific control elements located between -23 and -154 kb upstream of Kit.* Blood, 1999. **94**(8): p. 2658-66.
142. Reitz, M., et al., *Mucosal mast cells are indispensable for the timely termination of Strongyloides ratti infection.* Mucosal Immunology, 2017. **10**(2): p. 481-492.
143. Schubert, N., et al., *Unimpaired Responses to Vaccination With Protein Antigen Plus Adjuvant in Mice With Kit-Independent Mast Cell Deficiency.* Front Immunol, 2018. **9**: p. 1870.
144. Sawaguchi, M., et al., *Role of mast cells and basophils in IgE responses and in allergic airway hyperresponsiveness.* J Immunol, 2012. **188**(4): p. 1809-18.

145. Dahdah, A., et al., *Mast cells aggravate sepsis by inhibiting peritoneal macrophage phagocytosis.* J Clin Invest, 2014. **124**(10): p. 4577-89.
146. Abram, C.L., et al., *Comparative analysis of the efficiency and specificity of myeloid-Cre deleting strains using ROSA-EYFP reporter mice.* J Immunol Methods, 2014. **408**: p. 89-100.
147. Cheng, L.E., et al., *Perivascular mast cells dynamically probe cutaneous blood vessels to capture immunoglobulin E.* Immunity, 2013. **38**(1): p. 166-75.
148. Dudeck, J., et al., *Mast cells acquire MHCII from dendritic cells during skin inflammation.* J Exp Med, 2017. **214**(12): p. 3791-3811.
149. Knight, P.A., et al., *Delayed expulsion of the nematode Trichinella spiralis in mice lacking the mucosal mast cell-specific granule chymase, mouse mast cell protease-1.* J Exp Med, 2000. **192**(12): p. 1849-56.
150. Tchougounova, E., G. Pejler, and M. Abrink, *The chymase, mouse mast cell protease 4, constitutes the major chymotrypsin-like activity in peritoneum and ear tissue. A role for mouse mast cell protease 4 in thrombin regulation and fibronectin turnover.* J Exp Med, 2003. **198**(3): p. 423-31.
151. Abonia, J.P., et al., *Mast cell protease 5 mediates ischemia-reperfusion injury of mouse skeletal muscle.* J Immunol, 2005. **174**(11): p. 7285-91.
152. Shin, K., et al., *Mouse mast cell tryptase mMCP-6 is a critical link between adaptive and innate immunity in the chronic phase of Trichinella spiralis infection.* J Immunol, 2008. **180**(7): p. 4885-91.
153. Sternberg, N. and D. Hamilton, *Bacteriophage P1 site-specific recombination. I. Recombination between loxP sites.* J Mol Biol, 1981. **150**(4): p. 467-86.
154. Sauer, B., *Functional expression of the cre-lox site-specific recombination system in the yeast Saccharomyces cerevisiae.* Mol Cell Biol, 1987. **7**(6): p. 2087-96.
155. Sauer, B. and N. Henderson, *Site-specific DNA recombination in mammalian cells by the Cre recombinase of bacteriophage P1.* Proc Natl Acad Sci U S A, 1988. **85**(14): p. 5166-70.
156. Song, A.J. and R.D. Palmiter, *Detecting and Avoiding Problems When Using the Cre-lox System.* Trends Genet, 2018. **34**(5): p. 333-340.
157. Schmidt-Supprian, M. and K. Rajewsky, *Vagaries of conditional gene targeting.* Nat Immunol, 2007. **8**(7): p. 665-8.
158. Rajewsky, K., et al., *Conditional gene targeting.* J Clin Invest, 1996. **98**(3): p. 600-3.
159. Srinivas, S., et al., *Cre reporter strains produced by targeted insertion of EYFP and ECFP into the ROSA26 locus.* BMC Dev Biol, 2001. **1**: p. 4.
160. Dong, H., X. Zhang, and Y. Qian, *Mast cells and neuroinflammation.* Med Sci Monit Basic Res, 2014. **20**: p. 200-6.
161. Traina, G., *The role of mast cells in the gut and brain.* J Integr Neurosci, 2021. **20**(1): p. 185-196.
162. Xanthos, D.N., et al., *Central nervous system mast cells in peripheral inflammatory nociception.* Mol Pain, 2011. **7**: p. 42.
163. Goldschmidt, R.C., et al., *Mast cells in rat thalamus: nuclear localization, sex difference and left-right asymmetry.* Brain Res, 1984. **323**(2): p. 209-17.
164. Kim, D.Y., D. Jeoung, and J.Y. Ro, *Signaling pathways in the activation of mast cells cocultured with astrocytes and colocalization of both cells in experimental allergic encephalomyelitis.* J Immunol, 2010. **185**(1): p. 273-83.
165. Nautiyal, K.M., et al., *Serotonin of mast cell origin contributes to hippocampal function.* Eur J Neurosci, 2012. **36**(3): p. 2347-59.
166. Fedorova, E.A., et al., *[Mast cells of the human pineal gland.].* Adv Gerontol, 2018. **31**(4): p. 484-489.
167. Rozniecki, J.J., et al., *Morphological and functional demonstration of rat dura mater mast cell-neuron interactions in vitro and in vivo.* Brain Res, 1999. **849**(1-2): p. 1-15.
168. Khalil, M., et al., *Brain mast cell relationship to neurovasculature during development.* Brain Res, 2007. **1171**: p. 18-29.
169. Arac, A., et al., *Evidence that meningeal mast cells can worsen stroke pathology in mice.* Am J Pathol, 2014. **184**(9): p. 2493-504.
170. Fritscher, J., et al., *Mast Cells Are Activated by Streptococcus pneumoniae In Vitro but Dispensable for the Host Defense Against Pneumococcal Central Nervous System Infection In Vivo.* Front Immunol, 2018. **9**: p. 550.
171. Dong, H., et al., *Stabilization of Brain Mast Cells Alleviates LPS-Induced Neuroinflammation by Inhibiting Microglia Activation.* Front Cell Neurosci, 2019. **13**: p. 191.
172. Wang, Y., et al., *The Mast Cell Is an Early Activator of Lipopolysaccharide-Induced Neuroinflammation and Blood-Brain Barrier Dysfunction in the Hippocampus.* Mediators Inflamm, 2020. **2020**: p. 8098439.

173. Desbiens, L., et al., *Significant Contribution of Mouse Mast Cell Protease 4 in Early Phases of Experimental Autoimmune Encephalomyelitis.* Mediators Inflamm, 2016. **2016**: p. 9797021.
174. Vangansewinkel, T., et al., *Mouse mast cell protease 4 suppresses scar formation after traumatic spinal cord injury.* Sci Rep, 2019. **9**(1): p. 3715.
175. Mildenberger, W., S.A. Stifter, and M. Greter, *Diversity and function of brain-associated macrophages.* Current Opinion in Immunology, 2022. **76**: p. 102181.
176. Martin, M., *Cutadapt removes adapter sequences from high-throughput sequencing reads.* 2011, 2011. **17**(1): p. 3.
177. Andrews, S., *FastQC: a quality control tool for high throughput sequence data. Available online at: http://www.bioinformatics.babraham.ac.uk/projects/fastqc.* 2010.
178. Schindelin, J., et al., *Fiji: an open-source platform for biological-image analysis.* Nat Methods, 2012. **9**(7): p. 676-82.
179. Hao, Y., et al., *Integrated analysis of multimodal single-cell data.* Cell, 2021. **184**(13): p. 3573-3587.e29.
180. Liao, Y., G.K. Smyth, and W. Shi, *The R package Rsubread is easier, faster, cheaper and better for alignment and quantification of RNA sequencing reads.* Nucleic Acids Res, 2019. **47**(8): p. e47.
181. Dobin, A., et al., *STAR: ultrafast universal RNA-seq aligner.* Bioinformatics, 2013. **29**(1): p. 15-21.
182. Madisen, L., et al., *A robust and high-throughput Cre reporting and characterization system for the whole mouse brain.* Nature neuroscience, 2010. **13**(1): p. 133-140.
183. Byers, S.L., et al., *Mouse estrous cycle identification tool and images.* PLoS One, 2012. **7**(4): p. e35538.
184. Mrdjen, D., et al., *High-Dimensional Single-Cell Mapping of Central Nervous System Immune Cells Reveals Distinct Myeloid Subsets in Health, Aging, and Disease.* Immunity, 2018. **48**(2): p. 380-395.e6.
185. Düsedau, H.P., et al., *p75(NTR) regulates brain mononuclear cell function and neuronal structure in Toxoplasma infection-induced neuroinflammation.* Glia, 2019. **67**(1): p. 193-211.
186. Love, M.I., W. Huber, and S. Anders, *Moderated estimation of fold change and dispersion for RNA-seq data with DESeq2.* Genome Biol, 2014. **15**(12): p. 550.
187. AppliedBiosystems. *Guide to Performing Relative Quantitation of Gene Expression Using Real-Time Quantitative PCR*. 2004; Available from: https://biotech.illinois.edu/sites/biotech.illinois.edu/files/uploads/Guide%20to%20relative%20quantitation.pdf (accessed online: 18.11.2022).
188. Klingberg, A., et al., *Fully Automated Evaluation of Total Glomerular Number and Capillary Tuft Size in Nephritic Kidneys Using Lightsheet Microscopy.* J Am Soc Nephrol, 2017. **28**(2): p. 452-459.
189. Kobler, O., et al., *A quick and versatile protocol for the 3D visualization of transgene expression across the whole body of larval Drosophila.* Journal of Neurogenetics, 2021. **35**(3): p. 306-319.
190. Picelli, S., et al., *Smart-seq2 for sensitive full-length transcriptome profiling in single cells.* Nat Methods, 2013. **10**(11): p. 1096-8.
191. Elpek, K.G., et al., *The tumor microenvironment shapes lineage, transcriptional, and functional diversity of infiltrating myeloid cells.* Cancer Immunol Res, 2014. **2**(7): p. 655-67.
192. Arac, A., et al., *Meningeal Mast Cells as Key Effectors of Stroke Pathology.* Front Cell Neurosci, 2019. **13**: p. 126.
193. Kuo, C.H., et al., *Role of CCL7 in Type I Hypersensitivity Reactions in Murine Experimental Allergic Conjunctivitis.* J Immunol, 2017. **198**(2): p. 645-656.
194. Jo, K., et al., *Inferring transcriptomic cell states and transitions only from time series transcriptome data.* Scientific Reports, 2021. **11**(1): p. 12566.
195. Chang-Hui, S., *Chapter 7 - Detection and Analysis of Nucleic Acids*, in *Diagnostic Molecular Biology*, S. Chang-Hui, Editor. 2019, Academic Press. p. 167-185.
196. Chen, J.Z., L.A. Herzenberg, and L.A. Herzenberg, *Heparin inhibits EcoRI endonuclease cleavage of DNA at certain EcoRI sites.* Nucleic Acids Res, 1990. **18**(11): p. 3255-60.
197. Cora, M.C., L. Kooistra, and G. Travlos, *Vaginal Cytology of the Laboratory Rat and Mouse: Review and Criteria for the Staging of the Estrous Cycle Using Stained Vaginal Smears.* Toxicol Pathol, 2015. **43**(6): p. 776-93.
198. Birnbaum, M.E., et al., *Molecular architecture of the αβ T cell receptor-CD3 complex.* Proc Natl Acad Sci U S A, 2014. **111**(49): p. 17576-81.
199. Susaki, E.A., et al., *Advanced CUBIC protocols for whole-brain and whole-body clearing and imaging.* Nat Protoc, 2015. **10**(11): p. 1709-27.
200. Jing, D., et al., *Tissue clearing of both hard and soft tissue organs with the PEGASOS method.* Cell Res, 2018. **28**(8): p. 803-818.

201. Becher, B., A. Waisman, and L.F. Lu, *Conditional Gene-Targeting in Mice: Problems and Solutions.* Immunity, 2018. **48**(5): p. 835-836.
202. Zhao, S., et al., *Cellular and Molecular Probing of Intact Human Organs.* Cell, 2020. **180**(4): p. 796-812.e19.
203. Hendrix, S., et al., *Mast cells protect from post-traumatic brain inflammation by the mast cell-specific chymase mouse mast cell protease-4.* Faseb j, 2013. **27**(3): p. 920-9.
204. Irani, A.M. and L.B. Schwartz, *Mast cell heterogeneity.* Clin Exp Allergy, 1989. **19**(2): p. 143-55.
205. Zeisel, A., et al., *Molecular Architecture of the Mouse Nervous System, interactive data exploration online available http://mousebrain.org/adolescent/.* Cell, 2018. **174**(4): p. 999-1014.e22.
206. Yamaguchi, T., et al., *The role of galanin in the differentiation of mucosal mast cells in mice.* Eur J Immunol, 2020. **50**(1): p. 110-118.
207. Kasakura, K., et al., *Cooperative Regulation of the Mucosal Mast Cell-Specific Protease Genes Mcpt1 and Mcpt2 by GATA and Smad Transcription Factors.* J Immunol, 2020. **204**(6): p. 1641-1649.
208. Arthur, D. and S. Vassilvitskii, *k-means++: the advantages of careful seeding*, in *Proceedings of the eighteenth annual ACM-SIAM symposium on Discrete algorithms*. 2007, Society for Industrial and Applied Mathematics: New Orleans, Louisiana. p. 1027–1035.
209. Tenenbaum, J.B., V.d. Silva, and J.C. Langford, *A Global Geometric Framework for Nonlinear Dimensionality Reduction.* Science, 2000. **290**(5500): p. 2319-2323.
210. Nilsson, J., et al., *Approximate geodesic distances reveal biologically relevant structures in microarray data.* Bioinformatics, 2004. **20**(6): p. 874-80.
211. Motakis, E., et al., *Redefinition of the human mast cell transcriptome by deep-CAGE sequencing.* Blood, 2014. **123**(17): p. e58-67.
212. Wang, Y.J., et al., *Cromolyn inhibits the secretion of inflammatory cytokines by human microglia (HMC3).* Sci Rep, 2021. **11**(1): p. 8054.
213. Demo, S.D., et al., *Quantitative measurement of mast cell degranulation using a novel flow cytometric annexin-V binding assay.* Cytometry, 1999. **36**(4): p. 340-8.
214. Hosokawa, J., et al., *Role of Calcium Ionophore A23187-Induced Activation of IkappaB Kinase 2 in Mast Cells.* International Archives of Allergy and Immunology, 2013. **161(suppl 2)**(Suppl. 2): p. 37-43.
215. Michaloudi, H., et al., *Developmental changes of mast cell populations in the cerebral meninges of the rat.* J Anat, 2007. **211**(4): p. 556-66.
216. De Vlaminck, K., et al., *Differential plasticity and fate of brain-resident and recruited macrophages during the onset and resolution of neuroinflammation.* Immunity, 2022. **55**(11): p. 2085-2102.e9.
217. Brown, M.A. and R.B. Weinberg, *Mast Cells and Innate Lymphoid Cells: Underappreciated Players in CNS Autoimmune Demyelinating Disease.* Front Immunol, 2018. **9**: p. 514.
218. Lanier, L.L., et al., *Expression of cytoplasmic CD3 epsilon proteins in activated human adult natural killer (NK) cells and CD3 gamma, delta, epsilon complexes in fetal NK cells. Implications for the relationship of NK and T lymphocytes.* J Immunol, 1992. **149**(6): p. 1876-80.
219. Nakamura, K., et al., *CD3 and immunoglobulin G Fc receptor regulate cerebellar functions.* Mol Cell Biol, 2007. **27**(14): p. 5128-34.
220. Mattei, D., et al., *Enzymatic Dissociation Induces Transcriptional and Proteotype Bias in Brain Cell Populations.* Int J Mol Sci, 2020. **21**(21).
221. Denisenko, E., et al., *Systematic assessment of tissue dissociation and storage biases in single-cell and single-nucleus RNA-seq workflows.* Genome Biology, 2020. **21**(1): p. 130.
222. Erturk, A. *TISSUE CLEARING AND PROCESSING RESOURCE CENTER*. [Website] [cited 2023 february 18]; Available from: http://discotechnologies.org
223. Kádár, A., et al., *Improved method for combination of immunocytochemistry and Nissl staining.* J Neurosci Methods, 2009. **184**(1): p. 115-8.
224. Nievel, J.G. and J.N. Cumings, *Nissl Substance and Ribosomal Aggregates.* Nature, 1967. **214**(5093): p. 1123-1124.
225. Casoni, F., et al., *ZFP423 regulates early patterning and multiciliogenesis in the hindbrain choroid plexus.* Development, 2020. **147**(22).
226. Geoffroy, C.G. and O. Raineteau, *A Cre-lox approach for transient transgene expression in neural precursor cells and long-term tracking of their progeny in vitro and in vivo.* BMC Dev Biol, 2007. **7**: p. 45.
227. Parenti, A., et al., *OSKM Induce Extraembryonic Endoderm Stem Cells in Parallel to Induced Pluripotent Stem Cells.* Stem cell reports, 2016. **6**(4): p. 447-455.
228. EMBL-EBI(1). *Expression Atlas*. [Website] [cited 2023 february 19]; Available from: https://www.ebi.ac.uk/gxa/experiments/E-GEOD-77550/Results.

229. Walker, T.L., et al., *Lysophosphatidic Acid Receptor Is a Functional Marker of Adult Hippocampal Precursor Cells.* Stem cell reports, 2016. **6**(4): p. 552-565.
230. EMBL-EBI(2). *Expression Atlas*. [Website] [cited 2023 february 19]; Available from: https://www.ebi.ac.uk/gxa/experiments/E-GEOD-68270/Results.
231. Moon, T.C., A.D. Befus, and M. Kulka, *Mast Cell Mediators: Their Differential Release and the Secretory Pathways Involved.* Frontiers in Immunology, 2014. **5**.
232. Carroll-Portillo, A., et al., *Mast cell synapses and exosomes: membrane contacts for information exchange.* Front Immunol, 2012. **3**: p. 46.
233. Ekström, K., et al., *Characterization of mRNA and microRNA in human mast cell-derived exosomes and their transfer to other mast cells and blood CD34 progenitor cells.* J Extracell Vesicles, 2012. **1**.
234. Gersch, C., et al., *Mast cells and macrophages in normal C57/BL/6 mice.* Histochem Cell Biol, 2002. **118**(1): p. 41-9.
235. Harris, W.H., et al., *Mast cells of the bovine trachea: staining characteristics, dispersion techniques and response to secretagogues.* Can J Vet Res, 1999. **63**(1): p. 5-12.
236. Michaloudi, H., et al., *Mast cells populations fluctuate along the spinal dura mater of the developing rat.* Brain research, 2008. **1226**: p. 8-17.
237. Zucker-Franklin, D., et al., *The Presence of Mast Cell Precursors in Rat Peripheral Blood.* Blood, 1981. **58**(3): p. 544-551.
238. Zhuang, X., A.J. Silverman, and R. Silver, *Distribution and local differentiation of mast cells in the parenchyma of the forebrain.* J Comp Neurol, 1999. **408**(4): p. 477-88.
239. Wulff, B.C., et al., *Mast Cells Contribute to Scar Formation during Fetal Wound Healing.* Journal of Investigative Dermatology, 2012. **132**(2): p. 458-465.
240. Dimitriadou, V., et al., *Trigeminal sensory fiber stimulation induces morphological changes reflecting secretion in rat dura mater mast cells.* Neuroscience, 1991. **44**(1): p. 97-112.
241. Fouilloux, I., et al., *Mast cell activation and degranulation occur early during induction of periosteal bone resorption.* Bone, 2006. **38**(1): p. 59-66.
242. Hart, P.H., et al., *Age-related changes in dermal mast cell prevalence in BALB/c mice: functional importance and correlation with dermal mast cell expression of Kit.* Immunology, 1999. **98**(3): p. 352-6.
243. Janssens, A.S., et al., *Mast cell distribution in normal adult skin.* J Clin Pathol, 2005. **58**(3): p. 285-9.
244. Schaum, N., et al., *Single-cell transcriptomics of 20 mouse organs creates a Tabula Muris, interactive data exploration online available https://tabula-muris.ds.czbiohub.org.* Nature, 2018. **562**(7727): p. 367-372.
245. Jin, S., et al., *Inference and analysis of cell-cell communication using CellChat.* Nature Communications, 2021. **12**(1): p. 1088.
246. Efremova, M., et al., *CellPhoneDB: inferring cell–cell communication from combined expression of multi-subunit ligand–receptor complexes.* Nature Protocols, 2020. **15**(4): p. 1484-1506.
247. Browaeys, R., W. Saelens, and Y. Saeys, *NicheNet: modeling intercellular communication by linking ligands to target genes.* Nat Methods, 2020. **17**(2): p. 159-162.
248. Hou, R., et al., *Predicting cell-to-cell communication networks using NATMI.* Nat Commun, 2020. **11**(1): p. 5011.
249. Liu, Z., D. Sun, and C. Wang, *Evaluation of cell-cell interaction methods by integrating single-cell RNA sequencing data with spatial information.* Genome Biology, 2022. **23**(1): p. 218.

Appendix

Supplemental Table 1 Signature genes of selected immune cells

Cell type	Gene symbol	q-value
B cells	*Bank1*	2.84E-55
	Cd19	1.40E-91
	Cd38	9.18E-23
	Cd79b	5.96E-80
	Fcmr	5.50E-114
	H2-Ob	6.48E-40
	Isoc1	1.89E-13
	Ms4a1	4.87E-163
	Smim14	7.66E-15
	Tmem243	1.90E-14
	Tnfrsf13c	6.04E-71
Basophil genes	*Adgrg1*	2.47E-31
	Adgrg3	2.28E-17
	Aqp9	1.08E-68
	Ccl3	2.73E-14
	Ccl4	4.71E-24
	Chst15	1.64E-30
	Csf1	4.38E-20
	Fads1	1.54E-19
	Far2	4.64E-85
	Hgf	1.32E-86
	Hist1h1c	1.39E-20
	Ifitm1	2.00E-66
	Igf1r	1.43E-34
	Il18rap	1.31E-14
	Jak2	5.49E-22
	Lpxn	6.15E-13
	Plp2	9.14E-36
Epithelial cells	*1700025G04Rik*	4.10E-34
	1810011O10Rik	2.73E-35
	Ache	8.62E-42
	Adm	1.20E-48
	Ahcyl2	5.74E-34
	Akt3	6.38E-17
	Alas1	8.89E-28
	Alcam	3.60E-39
	Anxa4	9.73E-27

	Anxa5	4.01E-28
	Aplp2	1.46E-14
	Apobec3	2.86E-13
	Arf1	3.57E-21
	Ascl1	2.11E-36
	Atp1b1	1.43E-23
	Atp6v0a1	1.12E-35
	Atpif1	1.94E-37
	Bmp2k	2.61E-20
	Calcb	2.22E-24
	Calr	3.55E-22
	Canx	4.91E-15
	Ccl11	1.90E-12
	Ccl25	8.19E-23
	Ccser2	1.88E-33
	Cd2ap	3.44E-21
	Cd40	4.00E-16
	Cd74	2.09E-52
	Cdh1	5.56E-84
	Cldn1	2.01E-47
	Cnn3	2.41E-26
	Copz2	3.27E-31
	Crip3	1.03E-16
	Csn2	9.07E-21
	Csrp1	3.20E-20
	Cstb	2.56E-34
	Ctsl	1.13E-22
	Cxcl10	1.90E-36
	Dnajb1	5.29E-18
	Dram1	1.22E-34
	Dsc3	5.89E-70
	Dsg2	3.70E-39
	Dsp	8.33E-66
	Dstn	1.45E-29
	Emp2	6.51E-24
	Epcam	1.60E-83
	Etv6	6.15E-21
	Eya1	4,28E-43
	Eya2	5.92E-52
	Fabp5	7.47E-54
	Fezf2	5.46E-42
	Foxn1	1.48E-51
	Fscn1	1.31E-23

	G6pc2	1.39E-29
	Gas6	5.31E-23
	H2-Aa	1.20E-48
	H2-Ab1	2.24E-55
	H2-DMa	1.14E-57
	H2-Eb1	9.15E-42
	H2-Oa	4.36E-34
	Hadh	1.08E-20
	Hagh	2.07E-41
	Hsp90aa1	6.60E-26
	Hsp90b1	2.48E-23
	Hspb1	1.48E-17
	Icosl	2.73E-35
	Ifitm3	9.00E-30
	Igfbp5	9.03E-23
	Il13ra1	4.21E-62
	Irf7	1.15E-11
	Itgb8	4.44E-48
	Jup	7.62E-17
	Kcnip3	8.05E-38
	Kcnj15	1.15E-65
	Kcnk6	9.92E-27
	Krt14	4.60E-34
	Krt17	1.02E-80
	Krt18	1.67E-65
	Krt5	2.20E-24
	Krt7	1.12E-56
	Krt8	3.31E-93
	Lacc1	1.50E-32
	Lad1	4.53E-13
	Lifr	8.12E-19
	Lima1	3.78E-29
	Lman1	1.02E-19
	Lypd8	1.79E-17
	Maged1	1.58E-34
	Mreg	1.90E-56
	Mt1	1.34E-11
	Mt2	5.53E-19
	Nampt	2.75E-36
	Ndufa11	8.56E-21
	Ndufc2	1.86E-20
	Nectin1	3.11E-57
	Nfix	2.19E-18

	Npas2	9.83E-32
	Oasl2	1.91E-57
	Oat	3.31E-16
	Parm1	8.33E-36
	Parp12	1.42E-29
	Parp8	4.81E-13
	Pdia3	4.31E-18
	Pdia4	3.35E-20
	Pdpn	1.03E-16
	Perp	1.72E-51
	Pip5k1b	9.94E-24
	Plagl1	1.64E-40
	Pld1	1.32E-40
	Prdx2	6.45E-34
	Prnp	1.75E-42
	Prokr2	5.82E-30
	Ptprq	9.16E-40
	Romo1	1.67E-30
	Rtp4	1.63E-16
	S100a1	1.11E-38
	S100a16	3.20E-27
	Sfn	1.49E-49
	Sfrp1	1.30E-60
	Sgpl1	5.97E-45
	Sgpp1	3.18E-55
	Sirt1	5.70E-15
	Slc24a4	5.91E-41
	Slco2a1	1.38E-51
	Slfn5	1.27E-24
	Sncg	1.99E-16
	Spib	6.11E-44
	Spint1	5.30E-60
	Spint2	1.95E-51
	Sprr1a	4.17E-24
	Stat3	2.14E-13
	Sumo2	1.46E-24
	Syngr2	4.24E-27
	Syt1	1,71E-41
	Tbata	3.60E-39
	Tmc4	1.50E-73
	Tmem176b	2.28E-15
	Tnc	3.64E-34
	Tns3	2.49E-25

	Trafd1	2.51E-25
	Trim29	3.54E-42
	Tsc22d1	2.55E-25
	Tuba1a	1.55E-22
	Ucma	1.01E-21
	Uqcrc2	9.96E-13
	Usp18	1.79E-51
	Vcam1	9.69E-24
	Zfp706	7.14E-17
FRCs	*Abi3bp*	1.27E-41
	Adh1	3.59E-38
	Aebp1	3.59E-21
	Angptl2	1.38E-14
	Antxr1	1.55E-14
	C3	2.37E-36
	C4b	1.04E-17
	Ccl19	7.13E-46
	Cdh11	8.61E-44
	Chrdl1	2.30E-11
	Clu	5.17E-25
	Cpxm1	8.07E-93
	Cxcl12	3.55E-61
	Cxcl13	3.96E-23
	Cygb	1.51E-18
	Dcn	1.58E-11
	Des	7.75E-22
	Dpt	6.33E-32
	Fmod	8.53E-37
	H6pd	4.94E-41
	Hmgcs2	1.15E-65
	Htra1	1.56E-31
	Igfbp3	3.77E-63
	Il33	8.99E-67
	Inmt	2.11E-23
	Itih5	8.15E-48
	Lix1l	1.52E-16
	Mfge8	3.54E-21
	Mmp14	4.92E-22
	Mmp2	2.51E-12
	Nrp1	8.99E-16
	Olfml3	1.75E-30
	Osmr	8.38E-20
	Pam	1.05E-20

	Pcolce	2.47E-17
	Pdgfra	4.02E-80
	Plpp1	2.05E-14
	S1pr3	6.08E-30
	Serping1	1.06E-11
	Slc1a5	2.47E-15
	Svep1	9.81E-45
	Thbs2	3.18E-34
	Vtn	8.38E-40
γδ T cells	*Blk*	1.33E-121
	Cd247	1.78E-15
	Cd3g	5.37E-16
	Cdk6	1.49E-15
	Etv5	8.45E-35
	Lat	5.00E-13
	Ncbp1	3.74E-12
	Nt5c3b	1.71E-21
	Pdcd1	1.67E-27
	Rasgrp1	1.20E-19
	Rnf167	3.25E-12

Data extracted from the Immunological Genome Project (ImmGen) dataset GSE37448 [191].

Supplemental Table 2 MC and NK cell signature genes

Cell type	Gene symbol	q-value	difference
MC signature genes (gene list is restricted to the 50 most different genes compared to NK cells)	*Cpa3*	9.62E-23	12090.0361
	Pmp22	6.57E-11	8262.2373
	Ccl2	2.10E-11	8125.44385
	Hdc	9.98E-07	8107.00732
	Tpsb2	7.53E-14	7738.19385
	Kit	4.45E-11	7644.3999
	Rgs18	9.80E-12	7410.17236
	Ccl7	0.00023277	7217.06738
	Fcer1a	7.95E-08	7070.22266
	Il1rl1	6.03E-11	6894.1709
	Cd81	8.26E-13	5958.81885
	Vim	3.58E-08	5874.93994
	Slc6a4	4.93E-09	5354.22607
	Slc7a8	6.50E-07	5349.83447
	I830077J02Rik	1.44E-10	5227.41992
	Papss2	1.67E-13	5168.62354
	Osbpl8	2.59E-14	4945.44971
	Pla2g7	4.96E-05	4647.74902

	Ndrg1	0.0012854	4646.86621
	Slc31a2	1.85E-07	4533.33252
	Srgn	1.59E-09	4522.9375
	Tph1	4.28E-07	4439.97412
	Ctsg	1.15E-09	4403.77344
	Dapp1	4.39E-09	4295.52979
	Maob	1.38E-12	4293.13037
	Ndst2	1.12E-08	4152.44727
	Lilrb4a	2.56E-07	4147.13379
	Slc18a2	6.53E-10	4144.54443
	Tcn2	1.89E-11	4120.50879
	Ednra	8.95E-11	4082.08057
	Ms4a2	4.43E-11	4020.70947
	Cma1	5.02E-14	3983.94507
	Ecm1	1.09E-07	3917.49829
	Myadm	7.75E-12	3874.43359
	Anpep	7.94E-08	3846.68823
	Alox5	6.77E-05	3821.27466
	Cited2	2.80E-06	3694.12988
	Ftl1	3.82E-05	3683.33008
	Anxa5	2.30E-06	3599
	Meis2	1.14E-11	3576.58203
	Cyp11a1	2.41E-06	3517.12109
	Dusp1	0.03124415	3476.4541
	Apoe	1.15E-07	3378.20117
	Sla	0.00019414	3357.0874
	Bmpr2	1.63E-10	3308.31372
	Slc7a5	4.22E-07	3306.67261
	Cyb5a	1.51E-07	3306.36987
	Rab27b	4.93E-13	3296.1499
	Gata2	1.47E-10	3254.85278
NK cell signature genes (gene list is restricted to the 50 most different genes compared to MCs)	*Actb*	1.71E-06	-3548.27
	Adamts14	1.09E-09	-1775.834
	Ccl5	5.43E-32	-13804.492
	Nkg7	4.40E-22	-10860.618
	Ncr1	7.12E-19	-9279.4541
	Il2rb	1.33E-16	-7351.6421
	Ccl3	4.86E-07	-6769.6455
	Cd52	1.37E-17	-6123.5767
	Cd7	3.96E-19	-6025.8047
	Sell	1.92E-11	-5743.0972
	Klrd1	1.74E-19	-4964.8833
	Rpl18	4.77E-14	-4851.9775

	Selplg	5.40E-14	-4570.8374
	Rplp0	2.55E-12	-4533.4248
	Klrc1	1.82E-28	-4177.5737
	Xcl1	5.02E-09	-4162.5703
	Prf1	1.12E-19	-4158.6299
	Eef1a1	7.82E-09	-4112.5728
	Gzma	5.37E-17	-3981.8184
	Lck	8.62E-18	-3847.7029
	Rps5	8.74E-12	-3817.5425
	Ctsw	5.74E-21	-3797.8901
	Tmsb4x	1.28E-09	-3717.4526
	Cnn2	1.50E-12	-3713.9412
	Ifngr1	6.57E-11	-3704.7219
	Fau	1.22E-13	-3692.4524
	Gimap4	2.56E-26	-3646.5945
	Rpl19	1.13E-14	-3572.5649
	Rpl9	8.56E-17	-3538.3708
	Rpl21	2.83E-09	-3510.8
	B4galnt1	2.27E-16	-3439.3254
	Ifng	5.95E-12	-3417.1113
	Rpl5	2.18E-16	-3360.248
	Rpl18a	3.69E-09	-3323.76
	Car2	1.86E-07	-3265.093
	Itga4	1.21E-10	-3249.8655
	Gimap6	1.06E-11	-3172.8784
	Ptprc	6.66E-13	-3140.5325
	Tpt1	4.05E-10	-3135.2275
	Irf8	1.55E-10	-3109.6492
	Rack1	5.92E-17	-3103.26
	Bin2	3.00E-11	-3081.7405
	Rps11	6.71E-16	-3079.8525
	Il12rb2	1.84E-08	-3072.5989
	Rpl37a	1.22E-09	-3065.9448
	Cd2	1.13E-14	-3062.4094
	Jak1	3.75E-10	-3056.728
	Uba52	5.13E-14	-3044.3425
	Chsy1	1.52E-13	-3005.9985
	Lsp1	3.62E-24	-2982.6047

Data extracted from the Immunological Genome Project (ImmGen) dataset GSE37448 [191].

Supplemental Table 3 Signature genes of MC subtypes

Cell type	Gene symbol
Akula *et al.* 2020(2) [104] – DEGs, upregulated in mature MCs (pMCs compared to BMMCs)	*Adamts9*
	C2
	Cma1
	CtsE
	Gfra2
	Hdc
	Il3ra
	Mcpt4
	Meis2
	Milr1
	Mrgprb2
	Myb
	Serpinb1a
	Tarm1
	Tpsb2
Akula *et al.* 2020(2) [104] – DEGs, downregulated in mature MCs (pMCs compared to BMMCs)	*Csf2rb*
	Ahrr
	Akr1c12
	Anpep
	Aqp8
	Aqp9
	Avil
	Birc5
	Calca
	CD200r4
	CD300lf
	CD96
	Cited
	Clnk
	CTLA2a
	Cyp4a12a
	Dnm3
	Dtx4
	F13a1
	F2r
	Gab2
	Gfi1b
	Glipr1
	Gpr174
	Greb1
	IL-4ra

	IL10ra
	Il1b
	Il2ra
	Il6
	Kcnn4
	Krba1
	Lif
	Lpar6
	Mthfd2
	Nampt
	Neb
	Nlrp3
	Nrop3
	Pgr
	Pik3cd
	Ptger4
	Rab38
	Rhof
	Rnase6
	Rnf128
	Sema4d
	Serpina3g
	Spns3
	Stap1
	Stk19
	Tbxas1
	Tgfbr1
	Tmem233
	Treml2
	Ulbp1
Gentek *et al.* 2018 [90] – DEGs, upregulated in definite MCs	*Ccl7*
	Adrb2
	Apod
	Apoe
	Atp6v0d2
	Avpi1
	C2
	Ccl2
	Cd14
	Clec10a
	Cnr1

	Csf1
	Esyt3
	F2r
	Fcer1a
	Gfra2
	H2-Aa
	H2-Ab1
	H2-DMa
	H2-Eb1
	Il15
	Il1rap
	Ltbr
	Ly6a
	Lyz1
	Lyz2
	Mill2
	Mrgprx1
	Nrp1
	S100a4
	S100a6
	Tubb6
	Vasn
	Vegfc
Gentek *et al.* 2018 [90] – DEGs, upregulated in primitive MCs	*Alox5*
	Arvcf
	Asns
	Ccr8
	Cmah
	Cx3cr1
	Dlk1
	Epha2
	Fbp1
	Fbp2
	Glb1
	Gpx3
	Grm6
	H19
	Heyl
	Hif3a
	Ifitm1
	Igf2bp1
	Igf2bp3
	Igf2r

	Lgr4
	Lst1
	Mest
	Mreg
	Nrep
	Plcd3
	Plxnc1
	Prss34
	Ptgir
	Smo
	Smpx
	Tac1
	Tnfrsf9
	Uck2
Kasakura *et al.* 2020 [207] – genes upregulated in MMC-like cells	*Gata1*
	Gata2
	Il1rl1
	Mitf
	Ms4a2
	Smad2
	Smad3
	Smad4
	Spi1
	Syk
	Tgfb
Yamagucchi *et al.* 2020 [206] – genes upregulated in MMC-like cells	*Galr2*
	Galr3
	Gpr162
	Gpr65
	Il5ra
	Il9r
	Ltc4s
	Npy1r
	Ptgds

Supplemental Table 4 Signature genes of activated MCs

Cell type	***Gene symbol***
Akula *et al.* 2020(2) [104] – DEGs, upregulated in LPS-treated BMMCs	*Calca*
	Gzmb
	Gzmc
	Hdc
	Il13

	Il1b
	Il6
	Mgat5
	Milr1
	Nfkbiz
	Tmem63b
	Tnfrsf9
Motakis *et al.* 2014 [211] – DEGs, upregulated in activated human skin MCs	*Aqp2*
	Ccl3
	Ccl4
	Ccl7
	Cnn1
	Crtam
	F2rl2
	Fasl
	Hoxb9
	Il11
	Il13
	Il3
	Il31
	Inhba
	Ly6g6c
	Nrg1
	Rai2
	Raph1
	Slc16a14
	Tnfsf18
	Trim6
	Xirp1

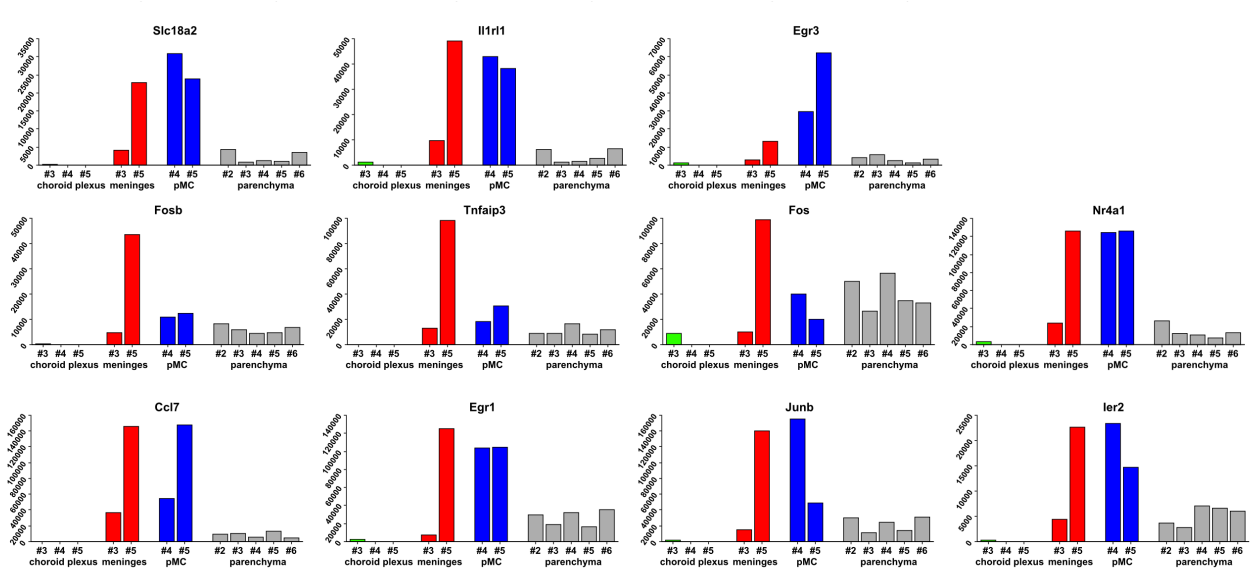

Supplemental Figure 1 Downregulated genes in CP samples of bulk RNA Sequencing

The remaining non-MC genes out of the 17 genes downregulated in two of the CP samples (bulk RNA sequencing) are displayed here. Normalized fragment counts were plotted.

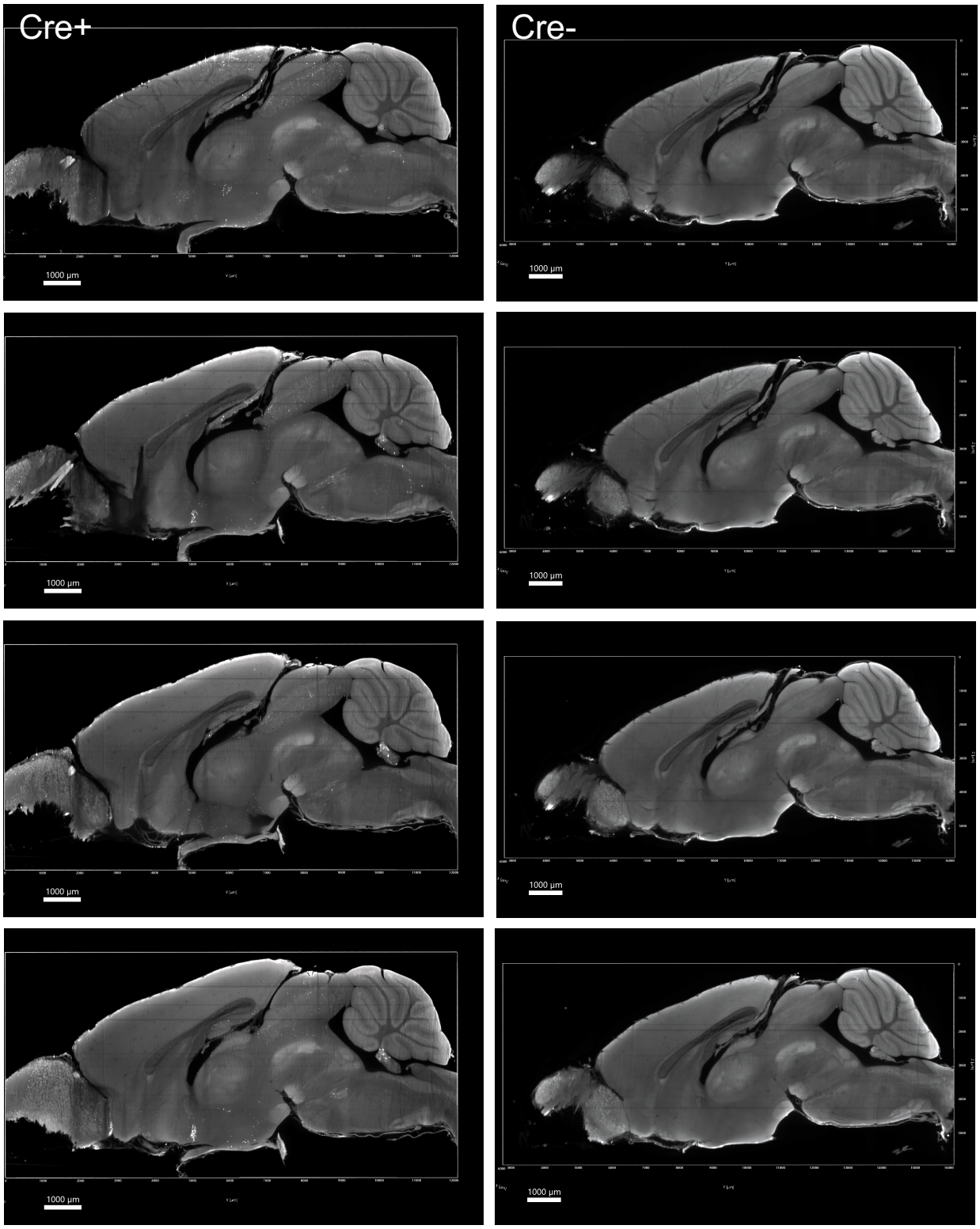

Supplemental Figure 2 Left hemispheres of Mcpt5-Cre^{+} and Mcpt5-Cre^{-} EYFP mouse brains

The corresponding right hemispheres are displayed in Figure 4-11. Scale bar 1 mm

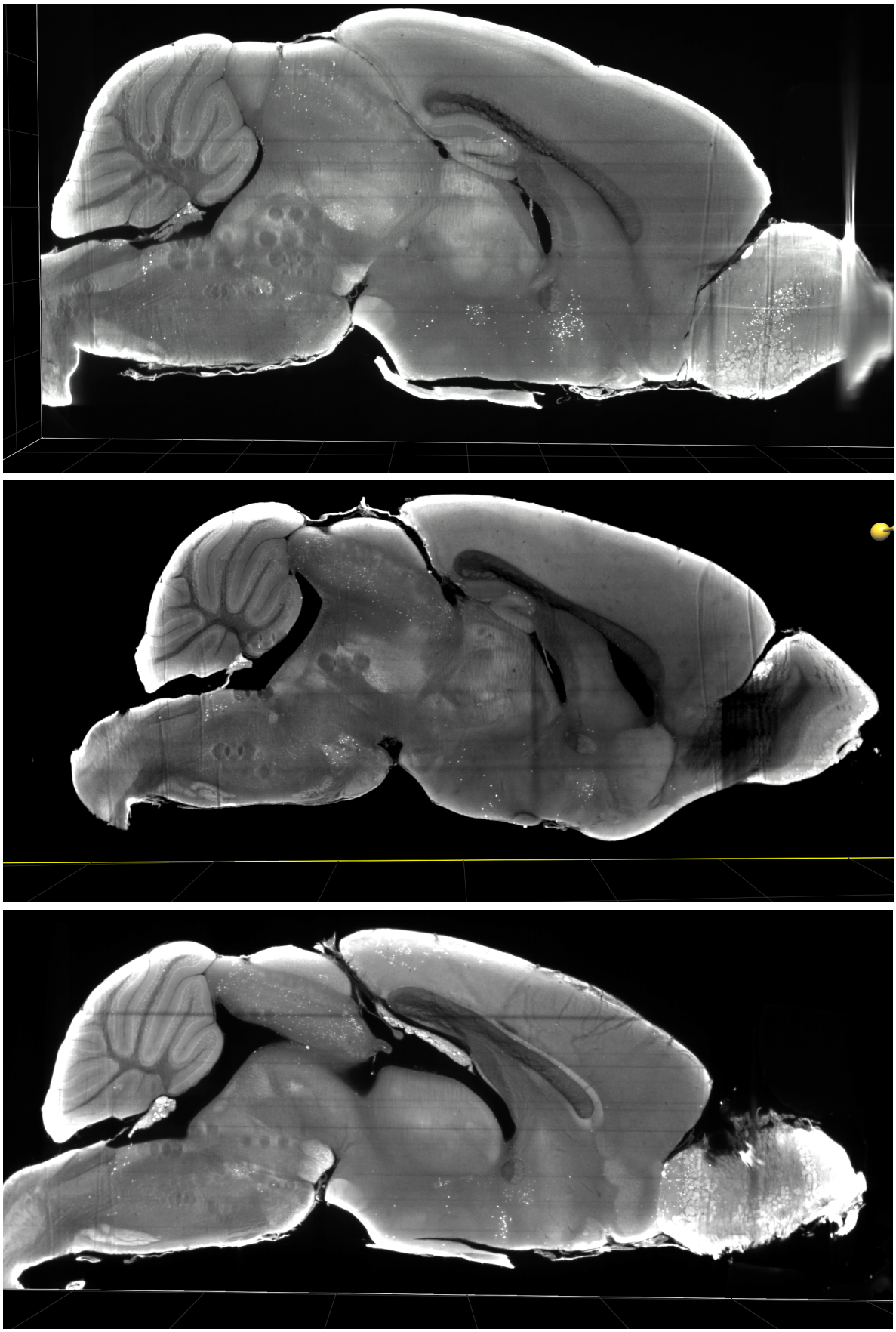

Supplemental Figure 3 Virtual brain slices of different Mcpt5-Cre^{+} EYFP mice

Representative images from the other three brains investigated via LSFM are shown. Grid size 1 mm

Declaration of Honor

I hereby declare that I prepared this thesis without impermissible help of third parties and that none other than the indicated tools have been used; all sources of information are clearly marked, including my own publications.

In particular I have not consciously:
- Fabricated data or rejected undesired results
- Misused statistical methods with the aim of drawing other conclusions than those

warranted by the available data
- Plagiarized external data or publications
- Presented the results of other researchers in a distorted way

I am aware that violations of copyright may lead to injunction and damage claims of the author and also to prosecution by the law enforcement authorities.
I hereby agree that the thesis may be reviewed for plagiarism by mean of electronic data processing.

This work has not yet been submitted as a doctoral thesis in the same or a similar form in Germany or in any other country. It has not yet been published as a whole.

Location, Date, Signature